GKSS
FORSCHUNGSZENTRUM
in der HELMHOLTZ-GEMEINSCHAFT

# On the wave field propagating over an uneven sea bottom observed by ground based radar

**(Vom Department Geowissenschaften der Universität Hamburg als Dissertation angenommene Arbeit)**


**Author:**

***S. Flampouris***



ISSN 0344-9629


HELMHOLTZ
| GEMEINSCHAFT

wissen
schafft
nutzen


GKSS 2010/6

GKSS 2010/6

# On the wave field propagating over an uneven sea bottom observed by ground based radar

**(Vom Department Geowissenschaften der Universität Hamburg als Dissertation angenommene Arbeit)**

**Author:**

***S. Flampouris***

**(Institute of Coastal Research)**

**GKSS-Forschungszentrum Geesthacht GmbH • Geesthacht • 2010**

Die Berichte der GKSS werden kostenlos abgegeben.
The delivery of the GKSS reports is free of charge.

*Anforderungen/Requests:*

GKSS-Forschungszentrum Geesthacht GmbH
Bibliothek/Library
Postfach 11 60
21494 Geesthacht
Germany
Fax.: +49 4152 87-17 17

*Druck: GKSS-Hausdruckerei*



ISSN 0344-9629

GKSS-Forschungszentrum Geesthacht GmbH · Telefon (04152) 87-0
Max-Planck-Straße 1 · 21502 Geesthacht / Postfach 11 60 · 21494 Geesthacht

GKSS 2010/6

# On the wave field propagating over an uneven sea bottom observed by ground based radar

*(Vom Department Geowissenschaften der Universität Hamburg als Dissertation angenommene Arbeit)*

Stylianos Flampouris

*207 pages with 112 figures and 10 tables*


## Abstract

This dissertation focuses on the microwave scattering by sea waves during high-wind conditions in the littoral zone, based on measurements by Dopplerized, horizontally polarized, ground-based X-band radar. The purpose is to determine the local bathymetry and current field, as well as to estimate the deterministic and stochastic properties of individual waves and of the wave field as it propagates over and interacts with an inhomogeneous sea bottom. The wave field is monitored with two different function modes of the radar: imaging with a rotating antenna and scanning with a fixed direction.

The imaging radar data are analyzed for the extraction of the bathymetry and current field by inverse modeling of the wave field using two different and already established methods: the Dispersive Surface Classificator – DiSC, based on linear wave theory, and Bell's method, based on modified solitary theory. Among the main achievements of this investigation are: the validation of the DiSC and its discussion in comparison with Bell's method by analyzing the same radar data, their accuracy is up to 90 %; the non-linear extension of the DiSC with three non-linear wave theories and the oceanographic application of the method for monitoring the bathymetry and the current field during the trespassing of a low pressure front, which balances the tidal phase and causes motion of 50000 $m^3$ ± 10 % of sediment.

From the same instrument, the normalized radar cross-sections and the Doppler velocities are estimated from the coherent data and they are analyzed with existing and innovative algorithms for the extraction of oceanographic information. The methodological steps for the application of those data are clearly defined. Data from four different wave conditions, from 2 m to 5 m significant wave heights, are presented. The oceanographic results are the indirect calculation of the phase velocity based on the rate of appearance in time and space of the scatterers. The radar scattering and the ongoing oceanographic processes are classified by the NRCS and the Doppler velocities. In this experiment, the Doppler sea-surface velocities are proven to be the sum of the velocities of the wind drift and the orbital motion of the waves. The frequency of the propagating wave group is almost constant in the littoral zone and the Doppler velocity is decreased as a function of the local bathymetry. Based on the measured components of the Doppler velocity, the wave-energy decay along the radar radius is estimated. The comparison of the spectra of the Doppler velocities with the spectra from the wave riders proved that the establishment of a transfer function between the two quantities is possible, because the frequency is identical and the power density of the peak frequency proved to be approximately 40 % higher than that measured from the buoy, independent of the actual wave conditions. A separation of the scatterer's velocity from the propagating and wave-breaking related phenomena is achieved and the velocity of the breakers is determined to be in the same order of magnitude as the phase velocity.

# Untersuchung zur Beobachtung propagierender Wellenfelder über inhomogener Bathymetrie mit landgestütztem Radar

## Zusammenfassung

Diese Dissertation untersucht die Radar Rückstreuung an Sturmwellen im Küstenraum anhand von Messungen, die mit Dopplerisierten horizontal polarisierten, Land gestütztem X-Band Radar erfasst wurden. Ziel ist, zum einen die Beobachtung der Bathymetrie und des Strömungsfeldes über Invertierung der Abbildungen der Wellenfelder und zum andern die Untersuchung der Wechselwirkungen zwischen den deterministischen und stochastischen Eigenschaften individueller Wellengruppen mit inhomogener, litoraler Bathymetrie. Hierzu wurde das Wellenfeld mit zwei unterschiedlichen Verfahren beobachtet: Abbildung mit drehender Antenne, wobei das Wellenfeld innerhalb des Beobachtungsfensters synoptisch abgebildet wird und die radiale Abtastung entlang eines Strahles mit fester Antennenblickrichtung und hoher zeitlicher Auflösung.

Bei der Bathymetrie und Strömungsabschätzung wurden zwei bereits etablierte Invertierungs-Methoden anhand desselben Datensatzes miteinander verglichen: die Methode „DiSC", die auf der linearen Wellentheorie basiert und die Methode nach Proudman Oceanographic Laboratory, die nach einer modifizierten „Solitary Theorie" vorgeht. Aus zwei Beispielen wurden die Ergebnisse der mit einem nicht linearen Ansatz erweiterten Methode „DiSC" mit denjenigen von drei weiteren nicht linearen Modellen verglichen. Die Genauigkeiten der Messungen der Strömungsfelder, die während des Durchzugs einer Sturmfront genommen wurden – wobei der Tidestrom durch Wind und Luftdruck nahezu kompensiert (geblockt) war –, stimmen bis zu 90 % überein. Aus einem etwa zeitgleich genommenen Radar-Datensatz wurde im Untersuchungsgebiet eine Sandbewegung von +50.000 $m^3$ ± 10 % ermittelt.

Aus den komplexen Radarrückstreuwerten wurden mit vorhandenen und neu entwickelten Algorithmen die Dopplergeschwindigkeiten und die Rückstreuquerschnitte ermittelt und erläutert. Beide Größen wurden bei vier unterschiedlichen Seezuständen, mit signifikanten Wellenhöhen zwischen 2 m und 5 m verglichen und klassifiziert. Es wurde gezeigt, dass die erfasste Dopplergeschwindigkeit der Summe der Geschwindigkeiten aus Winddrift und Orbitalbewegung der Wellen entspricht und dass die Frequenz der im Flachwasser propagierenden Wellen konstant bleibt, wohingegen die Dopplergeschwindigkeit bei abnehmender Wassertiefe ebenfalls abnimmt. Aus den ermittelten Doppler Komponenten wurde die Abnahme der Seegangsenergie entlang des Radarstrahles abgeschätzt und aus den Spektren der Dopplergeschwindigkeiten zusammen mit denjenigen aus Bojenmessugen eine Übertragungsfunktion ermittelt. Unabhängig vom aktuellen Seezustand wurde bei jeweils identischer Frequenz des Energiemaximums, die Energiedichte der aus Radar ermittelten Spektren um jeweils etwa 40 % höher als aus den Bojen ermittelten Energien berechnet. Die Trennung der Geschwindigkeiten der Rückstreuflächen bei normaler Wellenpropagation von denjenigen, die während Brechern auftreten, ist gelungen, wobei die Geschwindigkeiten im Brecherbereich in der Größenordnung der Phasengeschwindigkeit der Wellen ermittelt wurden.

*Manuscript received / Manuskripteingang in TFP: 30. Juli 2010*

## Acknowledgments

Over the last 3 years, I have had the chance and honor to meet, discuss and cooperate with several people, who have influenced my way of thinking and approach to the scientific problems in this dissertation.

I would like to express my sincere gratitude to Dr. F. Ziemer of GKSS for giving me the opportunity to work in the Department of Radar Hydrography (KOR) at the GKSS Research Center. His continuous support in all possible ways, with help and guidance and long edifying conversations made me feel comfortable to focus on my research. I enjoyed this learning experience and I hope that he feels the same.

I would like to acknowledge my supervisor, Prof. Dr. Detlef Stammer for giving me the opportunity to perform this study in the University of Hamburg. I would also like to thank the three members of the doctoral committee from the University of Hamburg, Prof. (emer.) Dr. Werner R. Alpers, Prof. Dr. Dirk Gajewski and Dr. Gerhard Peters.

Heartfelt thanks to my scientific companion, Dr. Joerg Seemann from KOR for sharing his knowledge, experience, constructive criticism and comments; it is a spiritual and scientific pleasure working with him. I extend my thankfulness to Gottfried Schymura from KOR for his dedication keeping several radar stations operational and to acquire high-quality field data; without his contribution, this work could not have been implemented. I also want to thank my colleagues Marius Cysewski, Stephan Sedlacek (KOR) and Dr. Alexander Bezuglov from St. Petersburg Electrotechnical University in Russia, for their support with different parts of the thesis, whenever I needed it.

I would like to thank Dr. Paul Bell from Proudman Oceanographic Laboratory for hosting me and giving me the opportunity to work with his radar analysis system; the period of our cooperation was stimulating and productive. Dr. Stamatis Dostoglou from University of Missouri was always available for me, despite the distance, and I have to thank him for helping me believe that the sky is indeed the limit.

I would like to acknowledge Dr. Christian Senet, who made me feel comfortable with his multistep and complicated algorithms with humor and self-sarcasm; Martina Heineke and Dr. Rolf Riethmueller from KOK for sharing their in-situ bathymetric data. Also from GKSS, I would like to thank Dr. Jens Meywerk and Dr. Hermann Kuhn from KIO for the 24/7 support of the computational servers; Dr. Walter Puls from KSS for his quiet company during the most productive hours at the office and our relaxing conversations; Dr. Gerhard Gayer from KSD for his scientific remarks; Peter Perthun and Dr. Clivia Haese from KOK. Moreover, I have to acknowledge the contribution of several agencies that provided oceanographic data: the Bundesamt fuer Seeschifffahrt und Hydrographie, Hamburg; the Deutscher Wetterdienst-Seewetteramt; the Landesbetrieb fuer Kuestenschutz, Nationalpark and Meeresschutz Schleswig-Holstein, Husum and the Wasser- und Schifffahrtamt, Toenning. This investigation was partially sponsored in the frame of FINO3 - Forschungsplattformen in Nord- und Ostsee Nr. 3, by Ministerium für Wissenschaft, Wirtschaft und Verkehr des Landes Schleswig-Holstein, the Bundesministerium für Umwelt, Naturschutz und Reaktorsicherheit and the European regional development fund.

I would like to express my thankfulness to Georgia Kakoulaki, now at University of Massachusetts, for her support and help, for being there and being essential to me.

Finally, after all these years, I have to admit that I have a great precept to follow, my sister, Dr. Stella Flampouri, who sets me an example of how to enjoy life and handle each moment. Finally, I would like to thank my parents, who are the permanent and fanatic supporters of my dreams, decisions and actions; without them I could not have managed anything.

# Table of Contents

## List of Figures

## List of Tables

## List of Symbols

$A_e$ effective aperture area of the antenna

$a_j$ scatter amplitude of the j[th] scatter element

$c$ wave celerity

$c_g$ group velocity

$c_p$ speed of the scattering object on the water surface

$c_s$ speed of light

$D$ total wave group dissipated energy

$D_b$ dissipated energy due to wave breaking

$D_c$ dissipated energy due to current impact

$D_f$ dissipated energy due to bottom friction

$D_w$ energy gain due to wind

$f_D$ Doppler frequency

$G$ maximum antenna gain

$G_t$ antenna gain

$g$ gravitational acceleration

$g_H$ horizontal polarization

$E$ energy density

H height

$h$ local depth

$K$ complete elliptic functions of the first kind

$k_0$ wave number of the electromagnetic radiation

$L$ wave length

$M$ total modulation

$M_{hydro}$ modulation due to hydrodynamics

$M_{shadow}$ modulation due to the shadowing

$M_{tilt}$ modulation due to tilt

$M_{wind}$ modulation due to wind

$m$ modulus of the elliptic functions

$P_r$ radar received signal power

$P_t$ radiated signal power

$R$ distance from radar

$R_r$ known distance from the radar

$r_{br}$ distance of the breaking zone from the radar

$S_D(f)$ Doppler spectrum

$U$ amplitude of the complex signal

$U_r$ Ursell parameter

$u_c$ current velocity

$u_{orb}$ orbital wave motion

$u_w$ wind drift

$\Delta r$ length of grid cell

$\Delta t$ time step

$E$ complete elliptic functions of the second kind

$\eta$ instantaneous wave height

$\theta_g$ local grazing angle of sensor

$\theta_0$ incidence angle

$\lambda_{rad}$ wavelength of the electromagnetic signal

$\mu$ dynamic viscosity

$v(u,v,w)$ velocity of the unit water mass

$\rho$ water density

$\sigma$ target cross section

$\sigma_0$ normalized radar cross section

$\sigma_r$ known reflectivity per unit area

$\tau$ wave period

$\tau_p$ pulse width

$\phi$ width of the antenna swath

$\phi_j$ the phase of the $j^{th}$ scatter element

$\psi$ power spectral density of the surface

$\omega$ angular frequency

## List of Abbreviations

A/D analog/digital converter

ADCP Acoustic Doppler Current Profiler

BSH Bundesamt fuer Seeschifffahrt und Hydrographie

BWK Berliner Wetterkarte

CST Composite Surface Theory

DGPS differential global positioning system

DiSC Dispersive Surface Classificator

DTM digital terrain model

DWD Deutscher Wetterdienst

GK Gauss–Krueger coordinate system

HH horizontally polarized signal transmission and reception

IF intermediate amplifier

LGA Low Grazing Angle

MTF modulation transfer function

NN Normal Zero reference level (in German, Normal Null)

NRCS Normalized Radar Cross Section

PRF pulse repetition frequency

RCS Radar Cross Section

RTI Range-Time-Intensity, referred to plots

RTV Range-Time -Doppler Velocity, referred to plots

SWA Seewetteramt

U.N. United Nations

UNCED United Nations Conference on Environment and Development

VV vertically polarized signal transmission and reception

# CHAPTER 1

## 1.1 Introduction

Coastal zones are under increasing environmental pressure and exhibit environmental changes as a consequence of population growth and often conflicting human activity, climate change and the physical processes that govern the coastal environment. Since 45% of the global population reside within 150 km of the ocean, with this tendency increasing, McGranahan (1999), understanding of the processes involved in coastal areas is relevant, not only for the scientific community; it also fulfills society's need for protection, sustainable development and the management and prediction of the evolution of coastal, natural and urban systems, Salomons et al. (2005). The role of the scientific community is declared as precautionary action, which involves a sophisticated recognition of the problems and issues posed, U.N. (1993) (UNCED, Agenda 21). With these perspectives in mind, the dominant physical processes in the littoral zone and its related phenomena have to be monitored. On the one hand to identify their mechanisms, in spatial and temporal scale, and on the other hand to develop mathematical and numerical approaches for the long-term, from global to local scale modeling and monitoring concepts, and to support decision-making.

The littoral areas are highly complex with spatial and temporal fluctuations of the coastal and oceanic dynamics varying from seconds (eddies) to decades (sea level change) and from centimeters (capillary waves) to thousands of kilometers (seiches), Massel (1996). The long-term goal of coastal research is to obtain a predictive understanding of the processes at work and their dependence on offshore and local conditions.

It has been demonstrated that remote sensing techniques provide important information in the investigation of these phenomena. More specifically, radar imaging of the sea surface provides reliable information about the spatial behavior of wave fields, Hasselmann and Hasselmann (1991). Commercial products for wave monitoring have been on the market for 50 years. One of the latest innovations has been developed at GKSS Research Center, Geesthacht, Germany, which is in operational use, Borge et al. (1999). The system is based on a nautical X-band radar for providing a time series of radar backscattered images from the ocean's surface. The radar technique thereby allows measurement under most weather conditions. With extant installations of nautical radar systems in all marine structures, platforms and ships, the measurements may be implemented in a very cost-efficient way, even during severe meteorological conditions. In the context of this thesis, this radar system is extended.

## 1.2 The physical mechanisms in the littoral zone

The nearshore zone is the most energetic region of the coastal environment, where the processes related with the propagation of the wave field take place. Waves are the prime movers for littoral processes along the shoreline; ocean waves shoal and interact with the local environment. For the most part, they are generated by the action of the wind over water and transport the energy imparted to them over vast distances. When they approach an open shoreline from deep water, undergoing processes impact the wave field, the wave height increases until the wave breaks and the wind-derived energy is dissipated and cross-shore and longshore currents are generated, Dean and Dalrymple (2004). The cumulative action of nearshore hydrodynamics initiates the sediment dynamics, which have a direct impact on the local bathymetry and the shape of the coast.

Conversely, the hydrodynamic components are influenced by changes of the actual bathymetry, which occur on time scales as short as hours, due to the presence of large storms, or as low-frequency motions, caused by epochal or other long-term phenomena. The dissipation of the wave energy and the transformation of the wave propagating over an uneven bottom towards the shore has been the subject of study for decades. However, understanding the mechanism of wave formation and deformation, the way in which waves travel across the ocean and their dissipation mechanism is by no means complete. Part of the reason is because observations of wave characteristics at sea are difficult, but also because mathematical models of waves are based on the dynamics of idealized conditions, and ocean waves do not conform precisely to these assumptions.

The wave energy dissipation is a known and intensively-discussed problem, due to the importance of the phenomenon of the nearshore circulation and the modeling of wave propagation in shallow areas. A common and reasonable assumption, Dingemans (1997), Guenther and Rosenthal (1995), Schneggenburger et al. (1997) and many others, is of the energy balance:

$$\nabla(c_g E) + D = 0 \qquad (1.1)$$

where $c_g$ is the group velocity, $E$ is the energy density and $D$ is the dissipated power of the wave field over sandy coastlines.

$D$ is the sum of various contributions and it assumes the validity of:

$$D = D_b + D_f + D_c - D_w \qquad (1.2)$$

where $D_b$ is the dissipated energy due to the wave breaking, $D_f$ the dissipated energy due to bottom friction, $D_c$ the dissipated energy due to the current impact and $D_w$ the gain in power due to the wind (hence its negative effect on the dissipation of energy). The above assumption is taken into account in both theoretical and practical approaches to the subject. Over short distances any dissipation due to the wind is impossible to identify, because of the limited observation time and/or fetch; hence (1.2) is simplified to:

$$D = D_f + D_c + D_b \qquad (1.3).$$

These three factors and the related hydrodynamic phenomena comprise the main subject of interest in this dissertation.

## 1.3 Experimental efforts

The collection of observational data at the nearshore regions is essential for the study of coastal phenomena and the development and set up of hydro- and sediment-dynamic models, Prandle et al. (2000). The high temporal and spatial resolution of the littoral processes, wave and current field formation, propagation and wave breaking, requires fine observations in both dimensions. Extended spatial sampling requires the instrument is moved to different locations or an array of instruments deployed for the acquisition of instantaneous sampling. This incurs logistical and practical problems (number of sensors, installation and maintenance costs) due to high wave energy in the nearshore and surf zone environments.

Series of experiments have been conducted since the 60s, indicative for wave tank experiments: Battjes and Janssen (1978), Smith and Kraus (1990), Dette et al. (1998) and for field surveys such as Thornton and Guza (1983), Prandle et al. (2000) and Herbers et al. (2006) the DUCK94 project, to answer what happens to the wave energy. In the best of the cases, DUCK94, there are less than twenty five sensors measuring wave properties over a length of approximately 2 km. The collection of the appropriate data of those quantities is especially difficult and costly, depending on the actual meteorological and oceanographic situation during the measurements. Nevertheless, the conditions with large waves or strong currents represent the most energetic periods for hydro- and morpho-dynamics and so attract the greatest of scientific interest.

The traditional in-situ techniques provide high temporal sampling rates, but only at one spot, which are insufficient for the observation of totality of the coastal processes. The deployment of an array of instruments provides a partial solution to the problem, but the spatial resolution is usually coarser than the investigated phenomena; the spatial coverage is limited and the instruments themselves influence the properties of the observed processes, therefore the monitoring of area-wide processes, such as current and wave field propagation, is impossible. In addition, the satellite and airborne remote sensing techniques have sampling periods several times larger than the phenomena themselves or the measurements are sporadic and their spatial resolution is usually lower than that required.

From the above presentation, it turns out that monitoring of the dominant phenomena in the coastal zone remains insufficiently sampled by using in-situ measurements. Recently this problem has begun to be countered by using ground-based remote sensing techniques, which provide large spatial coverage with a wide range of user-defined spatial and temporal resolutions, e.g. from cameras, a review from Holman and Stanley (2007) or from radar systems, for a review see section 4.1.

## 1.4 Area of investigation

The selection of an area of research was an important step in the current investigation, due to the fact it is based on the observation of a developed or locally generated wave field and its interactions with the local bathymetry and conditions. The northern tip of Sylt Island satisfied the selection criteria. The island of Sylt is the most northern sandy barrier island of the Frisian island chain on the German North Sea coast; it is located about 30 km off the mainland, close to the Danish border. The shape of the island is oblong, with a length of approximately 40 km and a width varying from a few hundred meters to 13 km; its surface area covers 99 km$^2$. From a geological point of view, the island contains a core of Saalian (380–126 ka BP, Gibbard et al. (2005) and Elsterian (480–420 ka BP) moraines, as well as reworked early Cenozoic sediments, Schwarzer (1984).

This study focuses on the large sandy spit system at the northern end of the island, West and Southwest List, which was formed during the Holocene, Dietz and Heck (1952). The thickness of the sand extends to several meters on the coast of Sylt, Koester (1974 ); the contemporary surface geological formation is based on the periodic growth and migration of sand dunes, Lindhorst et al. (2008), which propagate towards the tidal channel system to the north and the leeward side of the island. Nowadays, since 1978, the shoreline is stabilized by regular beach nourishment, approximately every second year, Doddy et al. (2004).

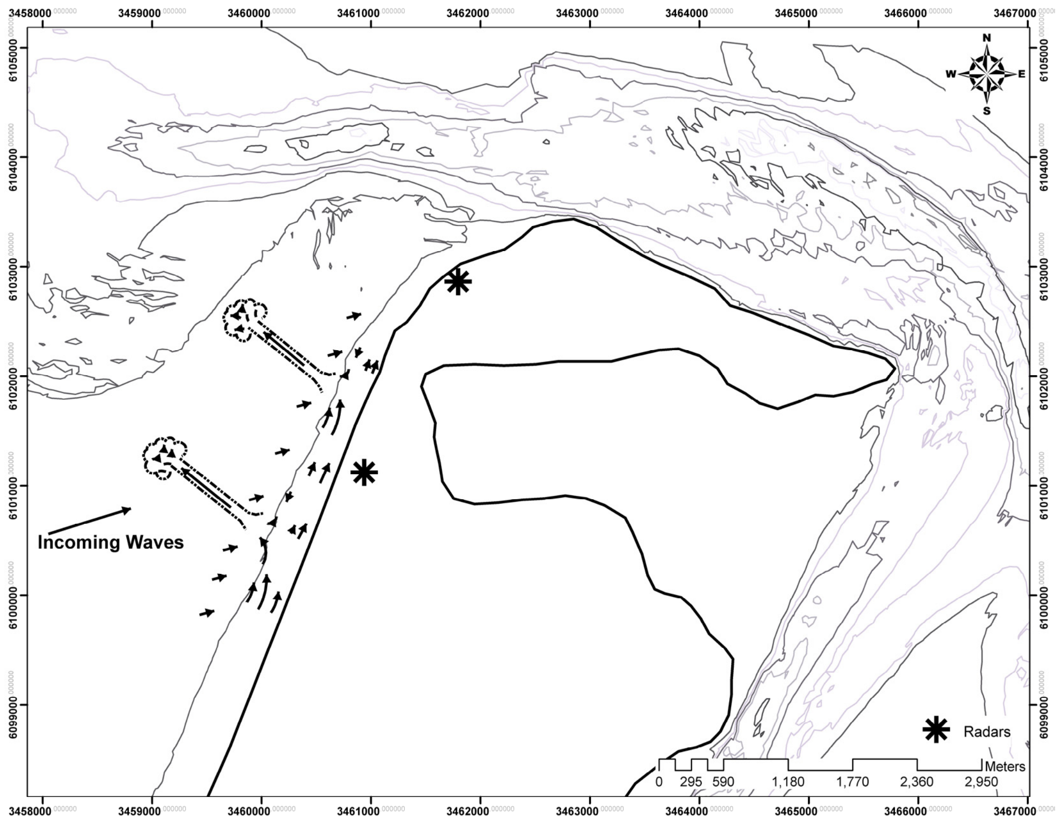


**Figure 1.4-1. The area of investigation: the northern tip of the island of Sylt, the general nearshore circulation is sketched and the isobaths every 5 m are plotted on the bathymetric survey of BSH in 2008.**

On the north side of the island, there is a main shipping channel, Lister Tief. The width of this tidal channel is 2.5 km and its depth exceeds 30 m. At the bottom of it, there are sand dunes having a 200-500 m wavelength and 5-10 m height and migrating about 80 m per year, Hennings et al. (2004). The west side of the island, towards the open sea, is characterized as strand plain, but at the isoline of 3 m there is a longshore bar, which has great seasonal, annual and hyper-annual variability in time and space. In addition, on the north-western side of the island, there is a relatively shallow, maximum depth 12 m shipping channel, the Lister Land Tief. Between the two channels there are several shoals, where the wave field is refracted and the waves break. Therefore, the tidal inlet is considered wave protected.

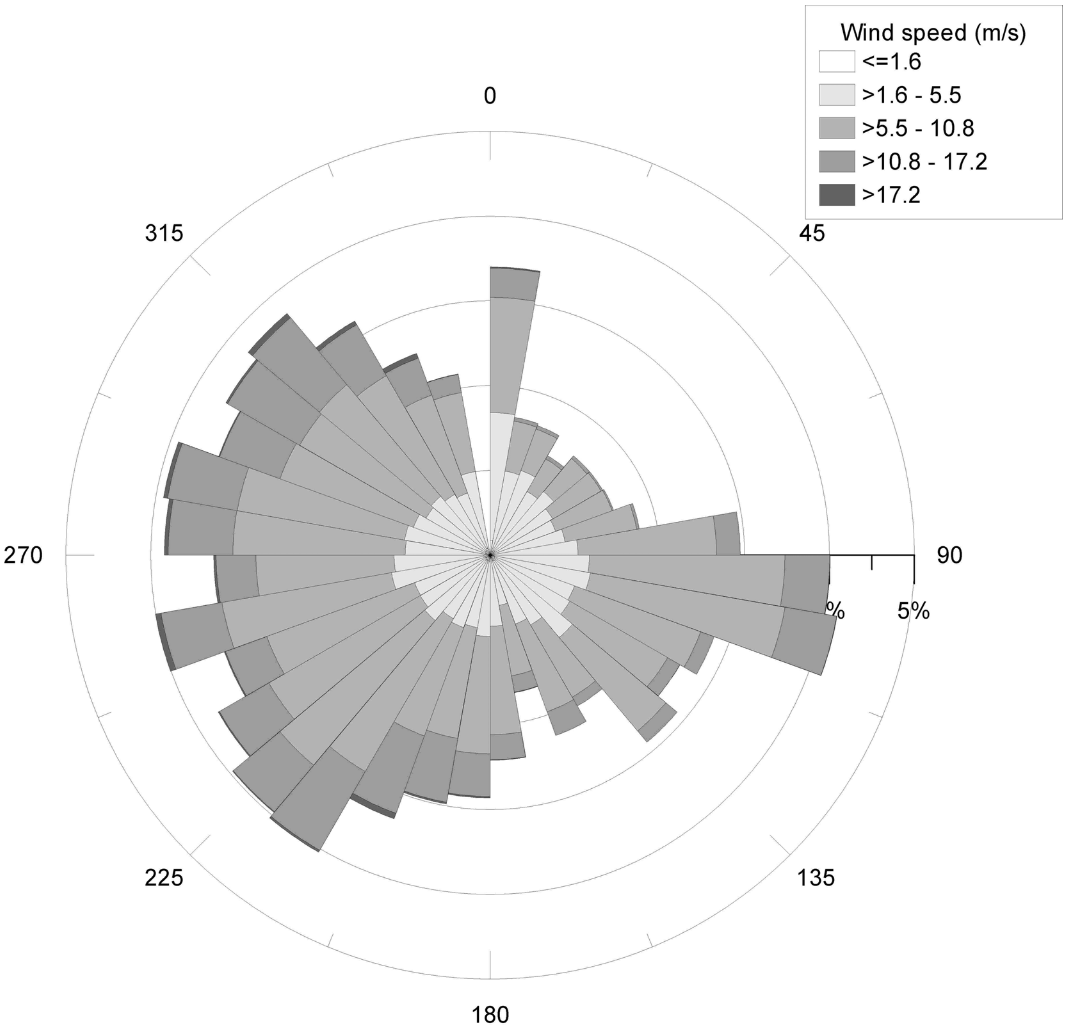


**Figure 1.4-2. Wind climate at List West, rose plot of the wind speed and direction 2000-2007. The plot shows that the wind directional spread was primarily from south-west to west.**

The typical hydrodynamics of the island are dominated by a semidiurnal lower to upper mesotidal regime as defined by Hayes (1979) with a tidal range of 1.8–2.2 m, Backhaus et al. (1998). In the deep traffic channels to the west of List West, the current velocities measured by ADCP of between 0.2 and 1.2 m/s with a moderate breeze condition (3-4 Beaufort), Cysewski (2003); these velocity readings are in accordance with the analog measurements taking place on a pile at Hoernum, southern Sylt. Similar measurements, at the tidal inlet and in the tidal channel at the north of Ellenbogen, demonstrated a maximum near surface current velocity of 2.0 m/s. High resolution radar ship-based measurements have shown the significant impact of the bathymetry and of the submarine geostructures on the current field, Kakoulaki (2009), the Lister Tief shows large morphological changes due to strong tidal current velocities, Sedlacek (2007).

For meteorological conditions more severe than a strong breeze (6 Beaufort), in-situ measurements are unavailable; there are only ground-based radar current measurements. During flooding, inflow velocity vectors over the shallower area are significantly higher than in the deeper part and channel area; the maximum current velocity exceeds 2.3 m/s. During ebbing, outflow current velocities were comparatively low and tend to increase at the tidal mouth, where the maximum velocity reaches 1.7 m/s, Chowdhury (2007). The surface current field measurement during severe meteorological conditions is also part of the present study and discussed in section 4.8.

The statistical analysis of the wind measurements from 2000 to 2007, confirmed previous studies that westerly winds are dominant, Mueller (1980), Ahrendt (2001), figure 1.4-2. The wave measurements at a depth of 12 m offshore Westerland have shown that the dominant wave direction is west-southwest during normal conditions and west during storm conditions. The mean wave height is calculated from the available data as 1.5 m, with a maximum value of 5 m, BSH (2009).

In the inlet, the tidal currents cause cross shore transport through the channel between the barrier islands. At the west side of the island, tidal and wave-induced currents are dominant seaward of the longshore bar, resulting in sediment suspension and transport to the north, Sistermans and Nieuwenhuis (2004). The longshore transport along the coast depends on the approaching angle of the waves to the shore. With foreshore normal or slightly oblique waves and a longshore variation in wave height, a cell circulation system is generated. Judging from the orientation of the coast and the lack of embayment and cusps along the beach, it seems that usually the waves break with an appreciable angle with respect to the shore, therefore the flow is dominated by a longshore directed current and the circulation cells have not been observed in the spatial scale of the experiment, figure 1.4-1. In general, the nearshore flow is the complex, synergic result of the waves and tides; in any case the impact of the water circulation is the continuous erosion and movement of the sediment offshore and to the northern end of the island.

## 1.5 Aims and objectives

The present investigation focuses on the applicability of microwave ground-based imaging of the wave field for the investigation and monitoring of the local hydrodynamics and aims to answer two major scientific questions:

1. Could inverse wave modeling be applied for the accurate determination of local bathymetry and current field during severe meteorological and oceanographic conditions?

2. What information about the wave field transformations and wave energy dissipation in the littoral zone can be extracted by imaging the surface waves with Dopplerized X-band radar?

To answer those two questions, several objectives have been set:

- The validation of the bathymetry extracted with the linear dispersion relation by the DiSC method and the determination of the source of error.
- The examination of the performance of modified solitary dispersion, inversed with a similar algorithm and comparison with the linear DiSC.
- The expansion of DiSC with the inversion of two more non-linear wave theories: modified cnoidal and modified Stokes theories, for more accurate bathymetric assessment.
- The demonstration of DiSC applications by determining the impact of a 10-day storm on the bathymetry of a coastal area and by identifying the impact of the “inverted barometer” effect on the surface current field.
- The development of a concrete methodology for the wave field scanning under low grazing angle conditions for the extraction of wave-related information.
- The separation of the backscattered signal according to wave breaking or not situation.
- The measurement and the estimation of deterministic and stochastic properties of the littoral wave field from the sea surface Doppler velocity and the normalized radar cross section.

## 1.6 Dissertation Structure

The previously mentioned scientific questions are answered throughout the dissertation, which is organized as following. In chapters 2 and 3, the basic theoretical background about the applied wave theories, in the context of the current study and radar imaging of the sea surface, are briefly presented. In chapters 4 and 5 the achievements of the current thesis are presented. Chapter 4 is dedicated to the inversion of the wave field propagation by analyzing the incoherent radar signal and chapter 5 is dedicated to monitoring of the wave field with Dopplerized X-band radar, figure 1.6-1.

At the beginning of both chapters, the related literature is reviewed. In §4.3, the DiSC algorithm is described, Senet et al. (2008); in §4.4 the linear DiSC is validated with multibeam echosounder data, Flampouris et al. (2007) and Flampouris et al. (2008b). In the following section, §4.5, the performance of a similar, but non-linear method, Bell's method, is examined and in §4.6 the bathymetric results of the two methods are compared, Flampouris et al. (2009a). In §4.7, the extension of DiSC with three non-linear wave theories is presented, Flampouris et al. (2009b). In §4.8, two oceanographic applications of the DiSC are demonstrated, Flampouris et al. (2008a) and Flampouris et al. (2008c). This is the first time that this kind of the experiment has been carried out, so the experimental setup and conditions are extensively described in §5.2 and 5.3. In §5.4 the compilation of the multistep methodology for the data analysis is presented, partially published by Flampouris et al. (2009c), the results of those approaches are demonstrated, validated and interpreted in §5.5 to 5.9, Flampouris et al. (2010). In chapter 6, the achievements of the current investigation are summarized, the main conclusions are highlighted and the outlook with suggestions for further research is given.

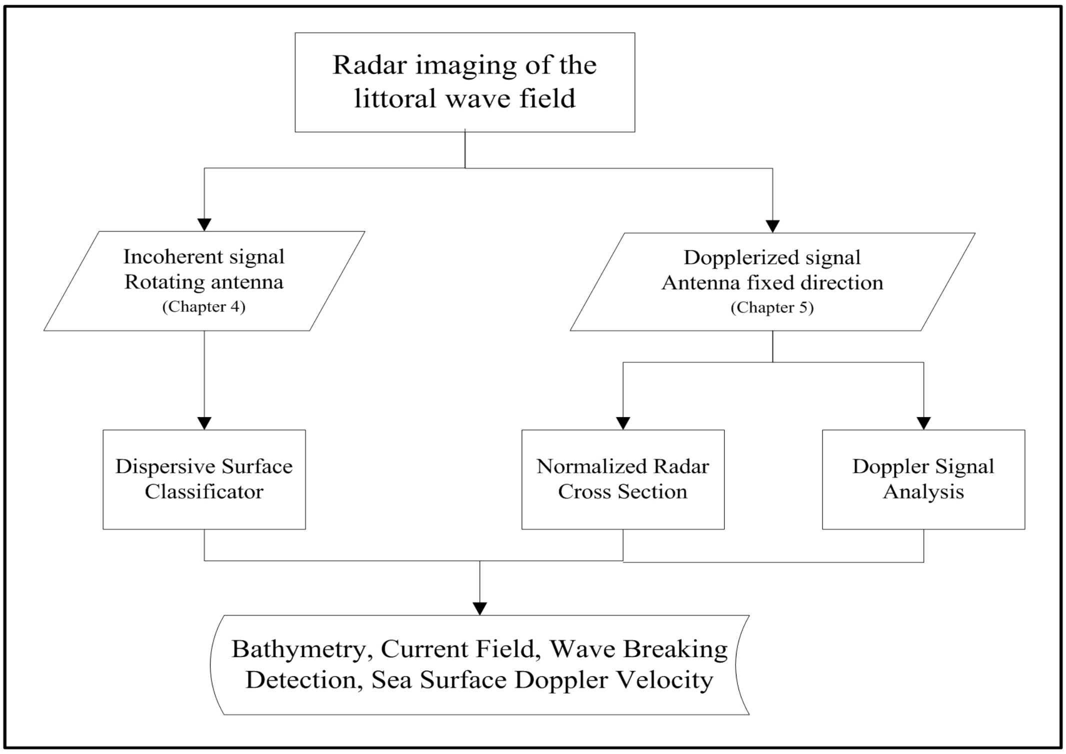


**Figure 1.6-1. General flowchart of the study. More detailed flowcharts of chapters 4 and 5 are illustrated in figures 4.3-1 and 5.4-1.**

# CHAPTER 2

## 2 Sea surface waves in the littoral zone

The wave-centric consideration of the nearshore zone defines it as the region between the shoreline and a fictive offshore limit, where the depth becomes so large that it no longer influences the waves, Svendsen (2006). This definition is practical, because the influence of the bottom on the wave field is the most important mechanism in nearshore hydrodynamics. A wave is a local oscillation that propagates through space and time, usually with transference of energy. The more frequently observed waves, and the subject of the present investigation, are the sea-waves, which are the oscillation of water mass around a rest position. The relation between the spatial and temporal wave parameters wavelength, $L$, and wave period, $\tau$, is a function of parameters describing matter, such as density, viscosity and surface tension. The function describing the relation between $L$ and $\tau$ depending on the free physical parameters is the dispersion relation.

The determination of the dispersion relation in nearshore hydrodynamics has been the subject of theoretical investigation for approximately 200 years. Stokes (1847) published the first linear and non-linear wave theory, which is often referred as Stokes' waves, summarized in Stokes (1880). Over the following decades, a consistent approximation for non-linear waves in shallow water was developed by Boussinesq (1872), to fill the gap of the nearshore failure of the Stokes theory. The Boussinesq theory was expanded further with the determination of analytical solutions, Korteweg and DeVries (1895), which are known as cnoidal and solitary waves. Since then, these mathematical models of the wave theories have been used with several different approximations, but in areas near the onset of wave breaking, the wave shape is of non-permanent form and can change quickly, which makes the determination of the wave characteristics in this region ambiguous; thus, for domains that span the shoaling and breaking zones they are not universally applicable and empirical formulations must often be called upon, e.g. Hedges (1976), Kirby and Dalrymple (1986). The dynamics and kinematics of water waves are discussed in several textbooks, for instance by Svendsen (2006), and Dingemans (1997), but at the same time it remains a hot topic among several investigators, such as Le Roux (2007), Catalan and Haller (2008), Hedges (2009).

The present chapter aims to provide a brief overview of the principles of wave theories that are applied in individual parts of this thesis. In this study, the applied wave theories are already established and well tested. For readers with an interest in the subject, there are dedicated books for long and deep discussions about these theories and their applications. In the following paragraphs the generation of the waves is ignored and they focus on the propagation of mature wave groups over uneven sea bottoms.

## 2.1 Sea Surface Waves

A wave is an oscillation of the sea surface, resulting from different forces and having different spatial and temporal properties. The wave period is a useful way to classify the waves. The smallest water waves with a period of 0.1 s are called capillary waves. Locally generated waves, called chop, have periods of approximately 1 s and ocean swell about 10 s. Tsunamis have a period of the order of minutes and are associated with seismic sea waves, while seiches are associated with the back-and-forth sloshing of water in closed or semi-closed basins and have periods that range from minutes to hours. The energy distribution versus length scale is given in figure 2.1-1. Ocean surface waves are also classified by their driving or restoring forces.

The wind is the dominant cause for the development of sea surface waves, capillary waves and sea swell. In addition, tidal waves are generated by the gravitational forces of the moon, the sun and the solar planets. Seiches are created by natural or eigen oscillations in semi-enclosed or closed areas, such as harbors, whereas tsunamis are created by earthquakes. The restoring forces are surface tension for the short capillary waves and the earth’s gravitation for almost all the rest. This thesis focuses on wind-generated waves with a gravitational restoring force.

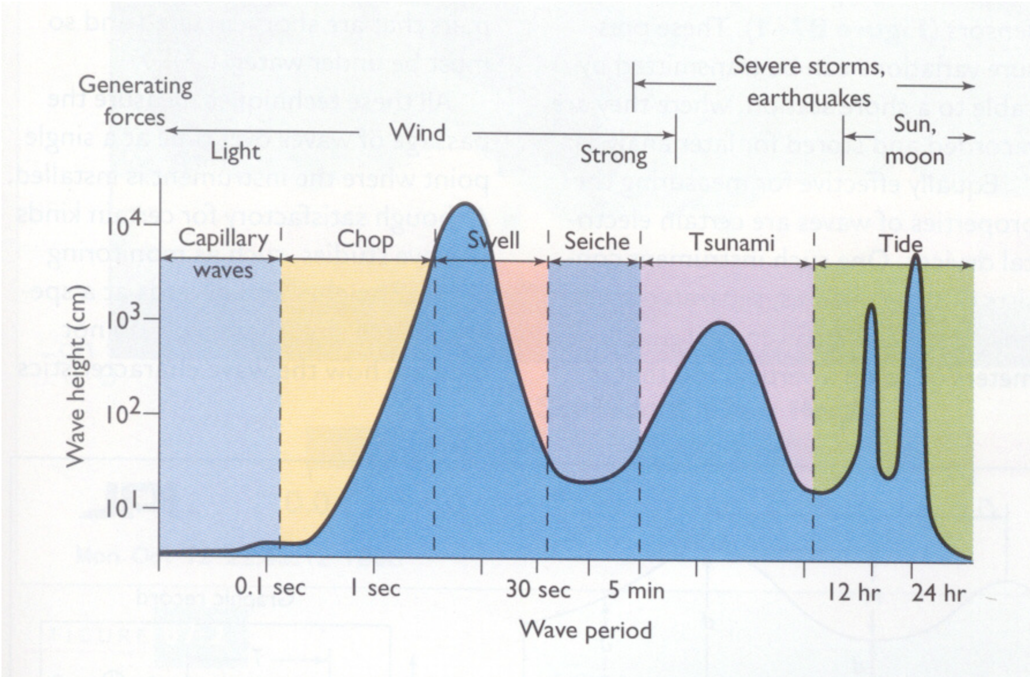


**Figure 2.1-1. Classification of sea waves according to their wave period. The scales of wave height and wave period are logarithmic, Pinet (1999).**

## 2.2 Characteristics of waves

Sea-surface waves are deformations at the air-sea boundary and are characterized by the wavelength, $L$, or reciprocally by the wavenumber $k = 2\pi / L$ and height, H, and the water depth over which they are propagating, $h(x)$. In figure 2.2-1, a two-dimensional diagram of a wave propagating in the $x$ direction is shown. $L$ is defined as the horizontal distance between two successive wave crests and it is related to the water depth $h(x)$ and the wave period, $\tau$, or reciprocally to the angular frequency $\omega = 2\pi / \tau$), which is the time required for two successive crests to pass a particular point. From the above, the speed of the wave, celerity, is defined as the distance $L$ that the wave moves in time $\tau$; in mathematical terms $c = L / \tau$. The instantaneous elevation of the water surface, heave, is defined as the function of position and time, $\eta(x,t)$.

The typical wave form is sinusoidal, see figure 2.2-1, which is an idealistic representation and propagates only in one direction. It has been proven that the actual wave heave in different environments, in the middle of the ocean or in the littoral zone, is the superposition of a large number of sinusoidal waves, Pierson et al. (1955), which has been generalized and rephrased to the summation of such solutions for different values of $k$ also remains a solution of the system, Dingemans (1997).

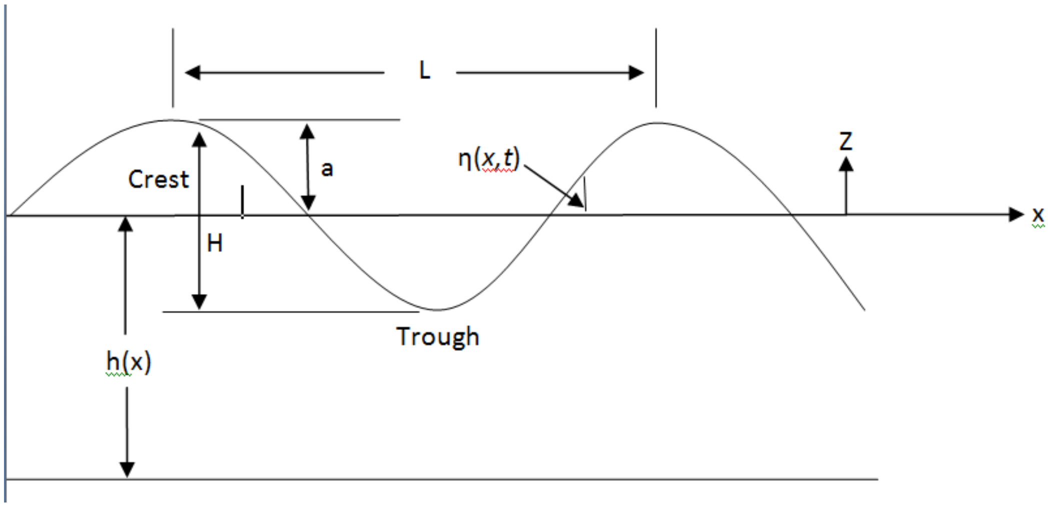


**Figure 2.2-1. Regular, symmetrical waves are described by their height, wavelength and period, propagating over a finite depth, Dean and Dalrymple (2004).**

## 2.3 Refraction of sea surface waves

The interaction of sea surface waves with obstacles changes the wave parameters. The sea bottom in shallow waters, the coast and coastal structures are all considered as obstacles, which cause refraction, diffraction and reflection; in this case the focus is on wave refraction, because it is essential for the determination of the local bathymetry by DiSC.

In shallow water, where the wavelength is substantially larger than the water depth, the wave propagation depends on depth; the smaller the depth, the slower waves propagate. A wave field approaching the coast at an angle will propagate at different velocities according to depth. The part of the crestline which is in the shallowest water propagates more slowly than the part of the crest further offshore. Hence, further away from the coast the crestline moves faster shoreward than that closer to the coast. This implies that the crestline rotates towards a parallel to the shore. This phenomenon is known as refraction. In case of a non-uniform seabed, the refraction also distributes the wave energy non-uniformly over the littoral zone, Dronkers (2005).

## 2.4 The Ursell parameter

Since 1847, it has been proven the significance of the parameter $HL^2 / h^3$, as a measure of the shallow water limit, Stokes (1847). The theoretical note of Ursell (1953) shows that this ratio is important in distinguishing between the three different long wave cases governing nearshore hydrodynamics, the parameter is also called the Ursell parameter after him:

$$U_r \equiv \frac{HL^2}{h^3} \begin{cases} << O(1) & \text{linear shallow water waves} \quad (2.1.a) \\ = O(1) & \text{cnoidal and solitary waves} \quad (2.1.b) \\ >> O(1) & \text{nonlinear shallow water waves} \quad (2.1.c) \end{cases}$$

In figure 2.4-1, the Ursell number is plotted as function of the wave steepness and it illustrates the validity of the analytical wave theories.

Based on this categorization, the current existence and the wave breaking effect on the dispersion equation of the waves in the littoral zone, the linear theory, the modified cnoidal by Svendsen and Buhr Hansen (1976), a modified composite model based on Hedges (1976) and Booij (1981) and the composite model presented in Kirby and Dalrymple (1986), are used in the following chapters. For the sake of simplicity and easier comprehension, the monochromatic approaches of the four wave theories are summarized in the following paragraphs, where it also describes extensively the reasons why those approximations fit to the Stokes parameter and are applicable in this study.

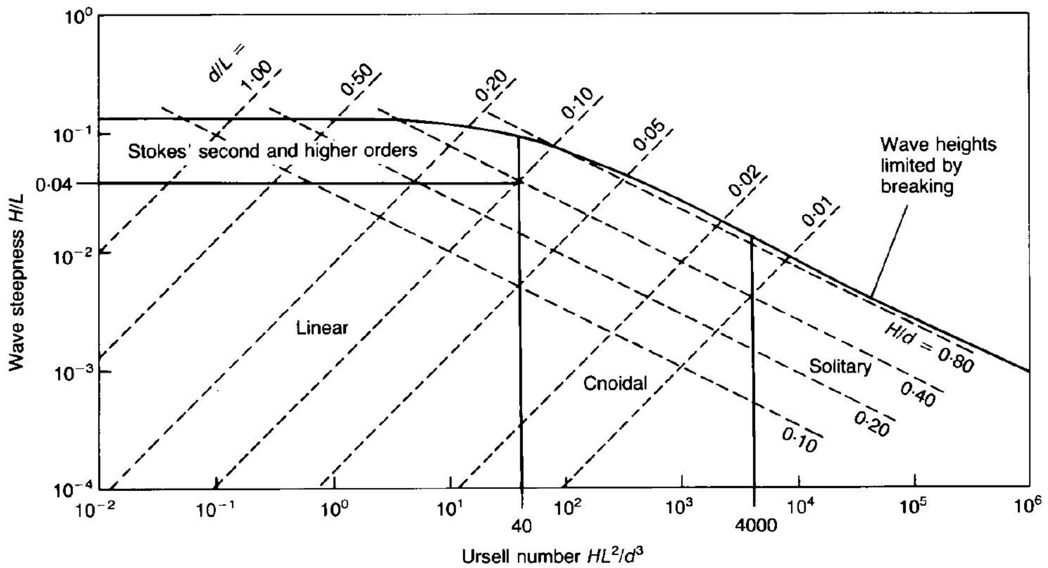


**Figure 2.4-1. Approximate regions of validity of analytical wave theories, Hedges (1995).**

## 2.5 Principles of Hydrodynamics

This section summarizes the basic hydrodynamic principles and laws on which the entire analysis of nearshore wave dynamics are based on. The content of this paragraph is trivial for the mathematical fluid mechanics and here only the necessary basic knowledge and principles are presented without any mathematical proofs. For further study of the subject there are several textbooks, e.g. Chorin and Marsden (2000). The dynamics of fluid flow are governed by the three conservation principles; the conservation of mass, momentum and energy.

In the case of an incompressible flow and homogeneous liquid of constant density $\rho$ and under the assumption that the forces on the water particle are the sum of the gravitational acceleration, the surface forces and stresses in the fluid, and are expressed as a function of the pressure $p$ , the fluid motion is mathematically described by the Navier-Stokes set of equations:

$$\frac{\partial v}{\partial t} + (v \cdot \nabla)v = -\frac{1}{\rho}\nabla p + g + \frac{\mu}{\rho}\nabla^2 v \qquad (2.2)$$

Where $v(u,v,w)$ is the velocity of a unit water mass, the ratio $\mu / \rho$ is the kinematic viscosity ($\mu$ is the dynamic viscosity), an indicator of the magnitude of the total stresses on the body, and $g$ is the gravitational acceleration. And together with the continuity equation:

$$\nabla \cdot v = 0 \text{ or } \frac{\partial u}{\partial x} + \frac{\partial v}{\partial y} + \frac{\partial w}{\partial z} = 0 \qquad (2.3)$$

They represent a system of partial differential equations for the flow with unknowns the $v$ and $p$ .

The system of partial differential equations (2.2) and (2.3) is unsolved; therefore there are numerous approximate and analytical solutions. Four of them are the main subject of the following paragraphs and are introduced in relation to the Ursell parameter.

## 2.6 Linear Theory

The linear wave theory emerges as a solution to the most simplified version of the general equations of motion. This solution occurs under the following simplifications and approximations: The wave height $H$ is much smaller than the wave length $L$, it satisfies the equation (2.1a), the motion is two dimensional, restricted to the plane $(x,z)$ and the viscous and turbulent stresses are neglected, so the motion is considered as irrotational. The depth is considered constant, $h$ and the waves are periodic with period $\tau$. The displacement of the water surface from the mean water level is specified as $z=\eta(x,t)$ and it is expressed as a sinusoidal function: $\eta(x,t)=a\cos(\omega t-kx)$, where $\omega=2\pi/\tau$ is the radian frequency and $a$ is the wave amplitude.

The linearized solution of the set of the differential equations (2.2) and (2.3) is the dispersion relation of the gravitational, wind-generated, sea surface waves:

$$\omega^2 = gk\tanh kh \qquad \text{or equally} \qquad c^2 = \frac{g}{k}\tanh kh \qquad (2.4)$$

The water particles move in elliptical orbits, which can be decomposed into the horizontal and vertical velocity components $u$ and $w$ as follows:

$$u(x,z,t) = a\omega\frac{\cosh k(h+z)}{\sinh kh}\cosh(kx-\omega t) \qquad (2.5.a)$$

$$w(x,z,t) = a\omega\frac{\sinh k(h+z)}{\sinh kh}\sinh(kx-\omega t) \qquad (2.5.b).$$

### *2.6.1 Wave modification by currents*

In the littoral zone, the tidal-dominated region where secondary phenomena cause currents, the most important currents are horizontal and they have a horizontal extension that is of the order of the wave length or even larger. The presence of the currents changes the waves. For the study of this impact, the common assumption is the wave motion on a locally steady current, uniform both over depth and in the horizontal plane; hence it can be proved that the dispersion relation is:

$$\omega = \sqrt{gk\tanh kh} + \vec{k}\cdot\vec{u}_c \qquad (2.6)$$

Where $\vec{u}_c$ is the near surface current. The term $\omega_D = \vec{k}\cdot\vec{u}_c$ is called the Doppler frequency and it indicates the effect of the near-surface current, leading to a frequency shift of $\omega$. If a current is flowing in a direction opposing the wave, the absolute (in the inertial coordinate system of the observer) frequency of the wave is decreased and vice versa. The deformation of the dispersion relation due to the Doppler effect is illustrated in figure 2.6-1.

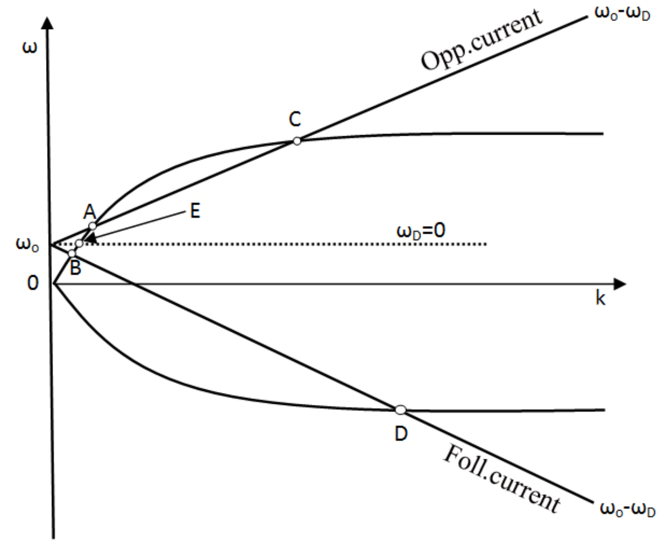


**Figure 2.6-1. Visualization of the current existence and impact on linear dispersion, from Jonsson (1990).**

### *2.6.2 Evaluation of the linear theory according to the depth*

For deep-water waves, defined by the condition $h >> L$, the approximation $\tanh(kd) \approx 1$ holds and the deep-water wave dispersion is independent of the depth:

$$\omega(k) = \sqrt{gk} \qquad (2.7)$$

This case is not of interest, because it is not valid in the nearshore areas.

In shallow waters, where $h$ is small compared to $L$, $h << L$, it implies that $\tanh(kh) \approx kh$ from which the shallow-water dispersion relation occurs:

$$\omega(k) = k\sqrt{gh} \qquad (2.8)$$

which shows a direct relation between the local water depth and the speed.

## 2.7 Non-linear wave approximations

In coastal regions and for long waves in intermediate and small depths, the ratio of the depth over the wavelength becomes relative small for the application of the linear approach. Based on the fact that in shallow waters both wave amplitude and water depth affect the radian frequency, against the equation (2.8), Boussinesq (1872) developed another wave theory with the assumption that the $h/L$ is small. The main characteristic of the phase-speed models, such as linear or Boussinesq, is that they are derived for either breaking or non-breaking waves; to plug this gap, composite, empirical models have been introduced, focusing on the transition from non-breaking to breaking waves at the intermediate depth of the shoaling regions, such as the coastal zone.

### *2.7.1 Boussinesq wave theory*

A full presentation of the Boussinesq wave theory is beyond the scope of this section and the final non-linear dispersion equation is applied without further analysis. Therefore only a few elements from the theory are presented here. There are several reference text books and hundreds of scientific publications for details on the theory development, analysis and application; for the compilation of the current section the books by Dingemans (1997) and Svendsen (2006) were used.

Taking the assumption that the governing equations are weakly dispersive and weakly non-linear in shallow water, Peregrine (1967) proved from the classical Boussinesq wave equations that the $U_r \approx O(1)$. For the case of waves traveling in only one direction, the analytical solution for the celerity of periodic waves of constant form is given by:

$$c = \sqrt{gh[1 + \frac{H}{mh}(2 - m - 3\frac{E}{K})]} \qquad (2.9)$$

Where $K, E$ are the complete elliptic functions of the first and second kind, respectively, and $m$ is the modulus of the elliptic functions and with a known Ursell number is calculated by $m = \frac{3}{16K^2}U_r$.

Svendsen and Buhr Hansen (1976), with the assumption that the deviation of equation (2.9) from the linear shallow water speed is expected to be in the order of $H/h$ simplified (2.9) to the following equation:

$$c = \sqrt{gh(1 + f(m)\frac{H}{h})} \qquad (2.10).$$

It is proven in the same publication that the accuracy of the equations (2.9) and (2.10) is comparable if the calculation cost is also taken into consideration. Holland (2001) calibrated the $f(m)$ term to a single value and defined that for the coastal zone, the $f(m)$ varies between 0.42 and 0.48; similarly, Bell et al. (2004), defined it equal to 0.4. The waves described with those equations are called cnoidal, in analogy to sinusoidal waves, because the surface profile is described by the elliptic cnoidal-function. The cnoidal wave theory is asymptotic to linear, periodic shallow theory when $U_r \to 0$ and it is asymptotic to the solitary, aperiodic wave theory when $U_r \to \infty$.

### 2.7.2 *Composite models*

Composite models have been introduced and attempt to span the transition from non-breaking to breaking waves in the intermediate depth of the shoaling regions, Catalan and Haller (2008). Specific scientists have focused on the subject and produced a range of different dispersion relations; over the last three decades these include Hedges (1976) and Kirby and Dalrymple (1986).

With reference to Hedges (1976), the celerity equation arising from the linear wave theory is modified to agree with the equivalent solitary wave expression as shallow water conditions are reached. This modification is based on the inclusion of the wave height in the linear dispersion relation:

$$c^2 = \frac{g}{k} \tanh k(h + Z) \qquad (2.11)$$

Where $Z = \alpha H$. The factor $\alpha$ was introduced by Booij (1981) and he empirically calibrated it as equal to 0.5. The equation (2.11) agrees with the usual linear theory expression for deep water conditions and the solitary theory solution in shallow water. In the intermediate range there is a reasonable agreement between the results calculated from this simple equation and those arising from the complex cnoidal wave expression, which involves complete elliptic integrals of the first and second kind. The model of Hedges was extended by Kirby and Dalrymple to include a wider range of relative water depths. The phase speed is given by the following set of equations:

$$c^2 = \frac{g}{k}\left[1 + f_1\left(\frac{kH}{2}\right)^2 D\right]\tanh\left[kh + f_2\left(\frac{kH}{2}\right)\right]$$

$$D = \frac{8 + \cosh 4kh - 2\tanh^2 kh}{8\sinh^4 kh} \qquad (2.12.a\text{-}d)$$

$$f_1 = \tanh^5 kh$$

$$f_2 = \left(\frac{kh}{\sinh kh}\right)^4$$

This method extended the effects of non-linear dispersion in a monochromatic Stokes wave model into water depths that are too shallow for the Stokes theory to retain validity and provides a smooth match between the Stokes theory and the empirical shallow water dispersion (2.11). The model collapses to linear when $H \to 0$ and it tends asymptotically to the Hedges model when $f_1 \to 0$ and $f_2 \to 1$.

# CHAPTER 3

# 3 Theory of real aperture radar ocean imaging

In this chapter, the basics of real aperture radar are described; further details can be retrieved from radar dedicated books, e.g. Skolnik (1990) and this chapter partially is based on Dankert (2004). The necessary detailed literature overviews on specific subjects, which are applied in the context of this study, are extensively presented as introductory paragraphs in the following chapters, specifically sections 4.1 and 5.1.

A radar echo from the sea surface is defined as sea clutter and it is function of several parameters, some of which indicate a complicated interdependence; thus a detailed (qualitative and quantitative) description of its characteristics with a great deal of confidence and precision presents a difficult task. In a proper sea clutter measurement, the polarization, radar frequency, grazing angle and resolution cell size have to be specified. In addition to these four parameters, geophysical conditions play a major role in the interaction of electromagnetic waves with the sea waves. The meteorological conditions and the conditions at the atmospheric boundary layer have a strong impact on the backscattering, Wetzel (1990b).

## 3.1 Radar equation

The most compact and comprehensive description of the factors influencing radar performance is the radar equation, which provides the range dependency of radar backscatter in terms of radar characteristics. The radar equation relates the range of a radar to the characteristics of the transmitter, receiver, antenna, target and environment, Skolnik (2001).

One form of this equation gives the received signal power $P_r$ as:

$$P_r = \frac{P_t G_t}{4\pi R^2} \times \frac{\sigma}{4\pi R^2} \times A_e \qquad (3.1)$$

The right side has been written as the product of three factors to represent the physical processes evolved. The first factor is the power density at a distance $R$ meters from a radar that radiates a power of $P_t$ (Watts) from an antenna of gain $G_t$. The numerator of the second factor is the target cross section $\sigma$ in square meters. The denominator accounts for the divergence on the return path of the electromagnetic radiation with range and is the same as the denominator of the first factor, which accounts for the divergence on the outward path. The product of the first two terms represents the power per square meter returned to the radar. The antenna of effective aperture area $A_e$ intercepts a portion of this power in an amount given by the product of the three factors.

## 3.2 Radar characteristics

The radar frequency, the polarization, the grazing angle and the resolution cell size are defined by the construction of the radar system hardware and the installation of the radar antenna. Monitoring of the sea surface has been implemented in a broad range of frequencies; from HF (3 MHz) to $K_a$-band (40 GHz). The utilization of different bands has several advantages and depends on the target. The X-band, used in this study, has the advantage that the radar wavelength permits the detection of each individual wave crest, Werle (1998). In addition X-band radars have a convenient size and weight, making them suitable for mounting on different platforms and serving different ends, another benefit of the system is the relatively low cost, Skolnik (1990).

The polarization of the electromagnetic wave is defined by the orientation of the oscillation of the electrical field; in the case that the radar transmits (horizontal or vertical) and receives at the same polarization is called co-polar (HH or VV), otherwise is called cross-polar. Since the 1950s, it has been proven that the differences in the echo from targets viewed with different polarizations might be used for distinguishing one from another and this has been proved correct also for monitoring of different scatterers of sea clutter, especially at low grazing angles. Since the very first observations, Pidgeon (1968), it has been observed that the amplitude of a radar cross-section and the Doppler frequency of an imaged sea surface with the two different polarizations have different properties. For instance, Lee et al. (1995b) demonstrated that for a grazing angle of $6^{o}$, the return loss spectral density of the time-integrated Doppler spectrum for VV polarization has approximately -30 dB in comparison with HH polarization and the Doppler spectrum of the data with HH polarization has a peak at a 4 times higher Doppler frequency than the Doppler spectrum of the VV polarized data. In this study, a horizontally polarized radar system is used, because it has proven to relate well with the breakers, which are dominant in the surf zone.

The grazing angle is used to describe the aspect that the clutter is viewed from and is defined with respect to a tangent of the surface; commensurately the incidence angle is defined with respect to the normal surface. The two notions are used as complements. The observations according to the grazing angle are divided into high, low ($1.5^o$- $10^o$) and very low ($<1.5^o$), Wetzel (1990a). The shore-based radar measurements belong to the last two categories. As already mentioned, at a low grazing angle (LGA) polarization plays a major role in the imaging of waves, Lewis and Olin (1980). Moreover, the wind influence is the parameter with the greater impact, Trizna (1988). At the LGA, backscattering is influenced by shadowing and multipath propagation. The shadowing of the troughs of the waves by the crests prevents low-lying scatterers from being illuminated. Multipath reduces the energy propagating at low angles, because of the cancelation of the direct energy by out-of-phase surface-reflected energy, Skolnik (2001).
In summary, all four properties of the radar system, radar frequency, the polarization, the grazing angle and the resolution cell size, have significant effects on the radar measurements, due to their interconnections and influence on the imaging of the sea surface under different oceanographic conditions.

## 3.3 Speckle

Radar images are affected by a granular appearance, called speckle, if the roughness of the ocean surface is within the order of the electromagnetic wave length. This small-scale fluctuating component of the radar backscatter is caused by a coherent sending signal and the interference of many individual scattering elements within a radar resolution cell, analog to a laser optic, Goodman (1976). The resulting complex scatter amplitude A is given by:

$$A = \sum_{j=1}^{N} a_j e^{i\phi_j} \tag{3.2}$$

where $a_j$ is the scatter amplitude and $\phi_j$ the phase of the j$^{th}$ scatter element. The phases are uniformly distributed over [0, 2π]. From the central-limit theorem, it follows that for a sufficient number of scatterers (N →∞) the components of $\mathrm{A}_i (i \in C)$ are Gaussian. In an incoherent radar, such as nautical radar, the radar pulse is also coherent, but only the modulus of the complex scatter amplitude $a = |\mathrm{A}|$ is detected, which is Raleigh distributed.

These considerations are for homogeneous surfaces. If the ocean surface is modulated by the sea state, the sea clutter statistic becomes non-Gaussian, maybe due to the few scatterers, as a result of the strong shadowing. Different statistical distributions have been fitted to the radar backscatter under grazing incidence, Ward (1988), Trizna (1988), Sekine and Mao (1990). The backscattered signal is a product of two components, Alpers and Hasselmann (1982). The first one is a temporally and spatially large scale component and is caused by modulation of the radar cross-section (RCS) by the sea state. The second one is a temporally and spatially small-scale component, the speckle, with a de-correlation time of *O(10)* ms. With an antenna rotation period of 2 s this signal is uncorrelated. The speckle component causes noise in the radar images.

## 3.4 Modulation mechanisms

The sea state is imaged by radar, because the RCS is modulated by the long ocean surface waves. The modulation of the RCS is mathematically described by the modulation transfer function (MTF), Alpers et al. (1981), which is a sum of four contributing processes: the geometrical effects of shadowing and tilt, hydrodynamic modulation, and wind modulation:

$$M = M_{shadow} + M_{tilt} + M_{hydro} + M_{wind} \tag{3.3}$$

Under grazing incidence, parts of the imaged sea surface cannot be seen by the radar; as the wave crests shadow the wave troughs. In this case the maximum antenna height is 36 m, the effect is strong and has a great impact on the data acquisition; the countering of this problem is discussed in section 5.4.5.

Tilt modulation is a purely geometric effect, which leads to a higher radar backscatter from a wave front which is propagated towards the radar. The long ocean waves tilt the facets from the horizontal plane towards and away from the radar. This leads to a change of local incidence angles and therefore to a change of radar backscatter, which increases with decreasing incidence angle. The azimuth has a strong influence on tilt modulation. Thereby the strongest modulation occurs when the antenna is viewing directly in the wave-travel direction or at 180° to it, whereas when parallel to the crests of single wave components, there is no modulation contribution, Moore (1985).

Hydrodynamic modulation describes the modulation of the amplitude and phase of the capillary waves by the interaction with the orbital velocity field of the long surface waves. This effect is indicated by convergence zones on the wave fronts and divergence zones on the wave backs. Under grazing incidence with HH polarization, the discrete scattering elements mainly contribute to the RCS of the ocean surface. These elements are increased by hydrodynamic modulation, Shyu and Phillips (1990).

Wind modulation is based on the variation of wind-induced friction velocity along the ocean surface. Estimates of the modulation of friction velocity have been carried out by Hara and Plant (1994). They found that the influence of wind modulation on Bragg waves is stronger than on the longer ocean waves. Further investigations on wind modulation have been performed by Wright and Keller (1980), Smith (1990), Romeiser et al. (1997) and others.

# CHAPTER 4

# 4 Inversion of the wave field for observation of bathymetry and current field

## 4.1 Literature review

In the following paragraphs, wave field imaging by ground based radars and its applications are reviewed by following a historical sequence of achievements and focusing mainly on depth extraction.

The determination of bathymetry in coastal environments by utilizing ocean wave shoaling photographic imagery and the observed reduction of ocean wave phase speed with decreasing water depth has been used since WW-II, Williams (1946); thus far this basic idea has been applied successfully, especially since the development of operational ground based video imagery systems, Stockdon (2000), mainly the Argus, see Holman and Stanley (2007) for a review; similar techniques have also been applied in wave flume experiments for the determination of the local bathymetry, e.g. Catalan and Haller (2008). In addition, significant results on this topic have been acquired from airborne optical measurements, Piotrowski and Dugan (2002), Dugan et al. (2003).

In parallel with these video based methods, microwave imaging of the wave field has been developed. For operational marine radar, backscatter of the transmitted signal by elements of the sea surface often places severe limits on the detection ability of returns from ships, aircraft, navigation buoys, and other targets sharing the radar resolution cell with the sea. These interfering signals are commonly referred to as sea clutter or sea echo, Wetzel (1990b).

The oceanographic community of remote sensing started digging into the presumed noise of the signal, leading to an accumulation of a large amount of useful information about scattering from the sea and how this scattering relates to oceanographic variables. Grazing incidence radars have been built and used for research purposes, leading to a broader understanding of the physics of sea clutter, which underpins the interpretation of image data captured from marine radars, Wetzel (1990a).

Crombie (1955) was the first to record the phenomenon of radar backscattering from sea waves, after which it became a main investigation issue when Wright (1966) published his oceanographic observations based on ground based radars. Both researchers hypothesized that a resonant interaction was occurring between radar waves and surface gravity waves. Since then, radar wave scattering from the ocean surface has been studied theoretically and experimentally for many years, Barrick (1968), Hasselmann (1971), Krishen (1971), Plant (1977), Alpers and Hasselmann (1978) and the complete first 30 years of research were then summarized by Hasselmann et al. (1978).

The scattering properties can be explained by using Bragg type scattering, mainly at moderate incidence angles. Bragg scattering is basically a resonant reflection mechanism from surface waves and also accounts for the local tilt of the surface. It has been proven that at least four processes: tilt, roughness, hydrodynamic and shadowing modulation influence the imaging mechanism, Valenzuela (1974), Elachi and Brown (1977), Valenzuela (1978a), Heathershaw et al. (1979). Subsequently, complex backscattering models answering specific problems have been presented and still there is ongoing research; indicative publications include Lee et al. (1995b), Hyunjun and Johnson (2002), Haller and Lyzenga (2003), Catalán et al. (2008).

Even though the backscatter mechanism has been obscure, the first application of the wave field monitoring was published in early 1960s, by Oudshoorn (1961), who was monitoring the wave field in the challenging area of the harbor mouth at Rotterdam. After him, Wright (1965), Wills and Beaumont (1971), Evmenov et al. (1973) and probably others have published photographs of radar scopes showing waves. The analysis of these kind of photos for the quantitative extraction of wave properties was introduced by Mattie and Lee (1978) and ameliorated by Heathershaw et al. (1979). Making use of digitized radar images, the 2-dimensional, Hoogeboom and Rosenthal (1982), and 3-dimensional spectra of spatial radar images were calculated, Young et al. (1985). The development of stable spectral analysis was originally applied to ship-based radar data by Ziemer and Rosenthal (1987) and gradually led to the development of the Wave Monitoring System, WaMoS, Ziemer (1991), Ziemer and Dittmer (1994) and Ziemer (1995). Similar systems have been presented by several research groups or companies, for instance Hirakuchi and Ikeno (1990 ), Gronlie (1995), Borge et al. (1999), Reichert et al. (2007).

Since the early 1980s, with the broad expansion of civil radar applications, there are several theoretical approaches to the radar imaging mechanism of sea bottom topography, see Alpers and Hennings (1984), Shuchman et al. (1985), Zimmerman (1985), Hennings (1990), Romeiser et al. (1997), Vogelzang et al. (1997), which are summarized by Hennings (1998)

and more recently Hennings and Herbers (2006), who presented the interaction of the marine sand waves with small scale hydrodynamic phenomena.
Nevertheless, during the last decade, with the establishment of effective methodologies for the monitoring of the wave field and the measurement of the spectral wave parameters, as well as the broad commercialization of different ground-based radar systems and mainly the exponential increase of computational power; several methodologies for bathymetry reckoning have been published. All these methods for the determination of bathymetry are based on two basic approaches. The first is similar to video based methods, time averaged radar sequences are calibrated according to the underlying bathymetry, e.g. Ruessink et al. (2002), Takewaka (2005 ), McNinch (2007), because in those methods the backscatter intensity (related mainly to the wave breakers) is important, the actual depth information refers mainly to the position of sand bars or other geomorphological structures; this property has been used successfully for the assimilation of radar data in hydrodynamic modeling, van Dongeren et al. (2008), but this approach is beyond our interest.
The second method is by measurement of the wave celerity and inverting an established wave theory the local depth is calculated. With reference to Bell (1999), the motion of the wave crests is traced by a spatial cross correlation in time, the distribution of the wave phase speeds is estimated and the depth is calculated by using the linear dispersion relation, the tidal signal is clearly identified and validated with in-situ data; these results inspired the worldwide radar community. In a publication by Senet et al. (2000b), the surface current field was taken into consideration and by applying 3D spectral filtering on the 3D complex image spectrum, they isolated the interesting spectral parts of the wave field, which were inverted in local scale for the determination of the bathymetry; even though it lacked a result validation, this contribution was an important and innovative approach. A similar method with different algorithmic implementation, also accepting the validity of the linear wave theory, is presented in the work of Hessner et al. (2006); the result is validated with spot in-situ measurements, which show phase agreement, but differences in the magnitude. Trizna (2001) extensively discussed the observed ambiguities from the inversion of the linear theory for the determination of the bathymetry. In a work by Hasan and Takewaka (2007 ), a similar method is presented, its main difference to the previous investigations is the calculation of the wavenumber is based on the maximum entropy method; the resulted bathymetry seems reasonable, but some of the validation data are approximately 20 years old, which is not

reasonable for areas with such high variations, according to the conclusions of Galal and Takewaka (2008). In Bell (2004), the wave dispersion relation of Hedges (1976) is inverted with significant results and since then this algorithm has been ameliorated and validated several times: e.g., Bell (2008a), Hessner and Bell (2009), Flampouris et al. (2009a); the results of this last validation are presented in paragraph 4.5.1 and form a part of this thesis.

The expansion of radar based systems for monitoring of hydro- and sediment dynamics, forced the funding of European Union projects for the operational monitoring and the integration of different observation techniques, see e.g. PROMISE, Prandle (2000), ODON, She and al. (2004), EDIOS, Verduin (2004) and among them the OROMA - Operational Radar and Optical Mapping in monitoring hydrodynamic, morphodynamic and environmental parameters for coastal management. One of the final products of OROMA was a quasi-operational observing system, a combination of existing hardware consisted by a nautical radar system for the acquisition of data and development of software, Dispersive Surface Classificator, DiSC, as a processing method for the determination of local depth and the current field, Ziemer et al. (2004). In the context of this project, a series of investigations into the localization of wave energy and ita inverse in local scale for the determination of local depth and the current vector have been published, Senet et al. (2000a), Senet et al. (2000c), Seemann et al. (2000a), Seemann et al. (2000c), Senet and Seemann (2002a), Senet and Seemann (2002b), Senet (2004; Senet and Seemann (2002a), an alternative method combining the advantages of the previous investigations was recently presented, Senet et al. (2008), which is the most recently presented methodology for the determination of the bathymetry from radar image sequences. The method analyzes inhomogeneous image sequences of dynamic dispersive boundaries to determine the physical parameters (bathymetry and current field) based on deformation of the wave spectrum and its reformation in local scale by using linear wave theory. The algorithm of DiSC is utilized in this dissertation and it is partially the subject of research, therefore it is presented briefly in section 4.3 and more extensively at appendix A. This methodology is mature enough and currently utilized quasi-operationally, but remains under development, e.g. Flampouris and Ziemer (2006), Chowdhury (2007), Alamsyah (2008). The accuracy of the linear version of DiSC is of the order $O(10\%)$ in comparison with echosoundings, Flampouris et al. (2008b). To increase the accuracy of the method, the DiSC has been extended for non-linear wave theories, Flampouris et al. (2009b), both of these subjects are the main topics of this thesis, sections 4.4 and 4.6 respectively.

## 4.2 DiSC Experiment

The complexity of the natural environment requires synergetic monitoring by several systems. In the following paragraphs, the details of the instrumentation for a series of experiments and the recorded data are presented.

### *4.2.1 Experimental setup*

The monitoring station was mounted near the lighthouse List West on the island of Sylt in the German Bight, figure 4.2-1.

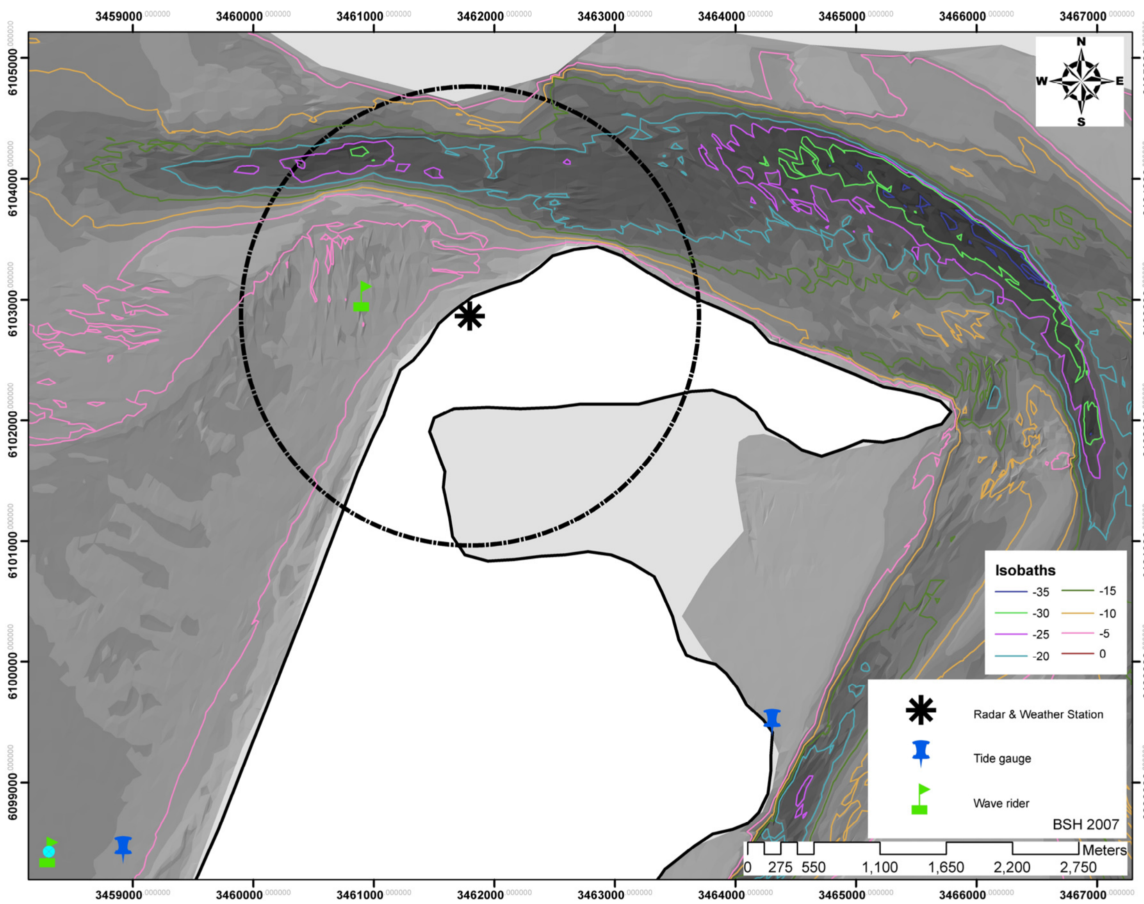


**Figure 4.2-1. Area of investigation. The black star points the position of the radar, the two blue pins the positions of the tidal gauges and the green flags the positions of the wave buoys. The two sensors at the west side of Sylt are moored a few kilometers to the south.**

The radar radius covered Lister Landtief, and part of the Lister Tief. The instrument used for acquisition of the sea surface is a software-hardware combination described in many publications, for example Borge et al. (1999), as part of the Wave Monitoring System (WaMoS), consisting of a Furuno FR 1201 nautical radar, a WaMoS II analog-digital converter and a WaMoS II software package for the acquisition of the radar images. The instrument used for observation is ground-based nautical X-band radar, figure 4.2-2, with horizontal polarization, mounted 25 m above the Normal Zero reference level (in German, Normal Null, NN). The radar is mounted with some interruptions for about 9 years.

**Figure 4.2-2. The image on the left illustrates the radar at List West station, next to the lighthouse of the List West, and on the right the mast of the radar Furuno FR 1201, above the meteorological station, which is a few meters lower (Image source: KOR, GKSS).**

### *4.2.2 Radar Data*

Sequences of radar data are acquired on an hourly basis. The sequences consisted of 256 individual images with an interval of 1.8 s between successive images; determined by the antenna rotation time. The antenna period may be impacted by the wind, therefore the total duration of the sampling varies, but it is approximately 8 minutes. The polar images cover a radius of a nautical mile and are interpolated to a Cartesian grid with a cell size of 7 m x 7 m, corresponding to the spatial resolution of the radar. The size of one image is 576 pixels x 576 pixels. The exact specifications of the Cartesian grid for the nautical radar image sequences are listed in table 4-1.

**Table 4-1. Specification of the Cartesian grid for the nautical radar image sequences.**

| | |
|---|---|
| Number of pixels in x-direction (west-east) Nx | 288 |
| Cartesian-grid pixel resolution in x-direction (west-east) $\Delta x$ | 6.82m |
| Spatial length in x-direction (west-east) X | 982m |
| Number of pixels in y-direction (south-north) Ny | 288 |
| Cartesian-grid pixel resolution in y-direction (south-north) $\Delta y$ | 6.82m |
| Spatial length in y-direction (south-north) Y | 982m |
| Number of images per image sequence Nt | 256 |
| Temporal resolution (antenna-rotation time) $\Delta t$ | 1.8s |
| Temporal length of an image sequence T | 460s |

To complete this approach to the subject, it is essential to mention the reasons why radar data was not available for all nine years, even though the radar was functioning. First of all, it is a well-known and commonly accepted fact that the most difficult part of marine sciences is the collection of data; rough and often unforeseen circumstances influence or destroy the equipment, for example, lightning is one of the most common causes of radar destruction. A second reason is the huge storage capacity that it is necessary for the raw radar data, each sample used to need about 90 Mb and now approximately 700 Mb. Only lately has technology permitted small volume high storage capacity, which is useful in this field. In addition, the archiving of terabytes of raw data involves several problems, mostly in the hardware; sometimes data was corrupted by hardware malfunction.

The transformation of the coordinates in the radar data from polar to Cartesian was realized by the use of existing software in PV-Wave, Seemann and Senet (1999). The algorithm in the software is the nearest neighbor interpolation method. For each cell of the polar coordinates, the distance between the cell and the center of the image, and the angle between the line that connects each cell with the center and the y-axis are calculated. So for each cell there is a pair of coordinates, (distance and angle) and the whole grid is filled with values. By using the nearest neighbor algorithm all these pairs are matched to the Cartesian grid. All the radar image sequences analyzed in this thesis are geocoded and oriented northward. The exact geographical coordinates are known by the Gauss–Krueger (GK) coordinate system. The radar antenna's position, height, and view direction are determined by a differential global positioning system (DGPS). The grazing incidence angle varies between $1^o$ and $5^o$, depending on the distance from the radar; therefore the radar measurement is considered as a low grazing angle measurement.

### *4.2.3 Wave riders*

The wave heave and direction was measured in two positions. The first buoy is moored by GKSS in the range of the radar at the depth of approximately 5.5 m positioned at 55°03.26N, 08°23.42E. The device is a directional waverider Mark II with a 0.9 m diameter. It is moored at a fixed position to ensure sufficient symmetrical horizontal buoy response; essential in this case as it lays in an area with complex geomorphology. The second buoy is a similar one operated by BSH and positioned at $54^o55.03$N, $8^o13.30$E, where the local water depth is 13 m, 16 km south of the area of investigation. The positions of both of them are illustrated in figure 4.2-2.

### *4.2.4 Tidal gauges*

The tide level data were acquired by gauges in the coastal area of Westerland, at 54°54.14N, 08°16.38E, 16 km south of the area of investigation, which is considered open sea and at the Port of List, approximately 10 km inside the tidal basin and the settled area in the Wadden Sea, see figure 4.2-2. The time shift for both measuring points from the area of investigation is known from the tidal calendar.

### 4.2.5 Meteorological station

The weather parameters were measured by the meteorological weather station, manufactured by Siggelkow Geraetebau GmbH mounted on the radar mast, approximately 3 m below the radar antenna. Minimum, maximum and mean values of six meteorological parameters are stored continuously with a period of 6 s. The useful parameters for this study are wind magnitude and direction, air pressure, temperature. By applying the logarithmic law, the wind speed at 10 m height was calculated.

For the period of the experiments, the data of wind speed and direction and the air pressure are acquired at the Port of List by the Seewetteramt Hamburg part of the Meteorological Service for Germany, and are used for the cross validation of the meteorological measurements and for filling gaps in the time series.

### 4.2.6 Multibeam Echosounder

The bed relief of the surveyed area was mapped by coupling a multibeam survey technique with high-accuracy positioning. The bed survey was carried out by means of a multi-beam echosounder EM 3000™ from Simrad-Kongsberg. This system is designed to work in water depths from 3 m to 200 m and it operates at a frequency of 300 kHz with a ping repetition rate of 15 Hz. The nominal apex angle is 1.5° along-track and 120° across-track during transmission, and 30° along-track and 1.5° across-track during receiving. This results in an array of 127 individual beams with an effective 1.5 x 1.5° apex angle per single beam, arranged with some overlaps over an arc of 120°. The three-dimensional sonar head positions and orientations were finally fixed by combining antenna position (Trimble 4000 ssi™), gyro-compass (Anschütz 20™, 4™) and motion sensor (DMS-05™, TSS UK LTD) data. The accuracy of ship position accuracy is in the order of centimeters and the relative positions of all components onboard the ship were measured to an accuracy of millimeters.

The multibeam echosounder measurements were further processed by a digital terrain model (DTM). The DTM employed used the "Seabed" algorithm, Anonymous (2003). With this method, for each grid cell, a surface paraboloid is computed from a weighted fit through all data points within a user-definable search radius. The altitude of each DTM cell is defined by the value of the parabolic surface at each grid point. The grid size of the terrain model is

2 m × 2 m. All results shown in the following are based on this DTM and each grid cell contains 25 to 50 data points.

The multi beam echosounder's data for the present investigation were acquired on August 25, 2003, two days before a storm and the spatial grid cell resolution of the data is 2 m x 2 m; for the comparison with the DiSC results, the echosoundings have been averaged spatially in the radar grid with resolution 42 m × 42 m or 60 m × 60 m, depending on the resolution of the radar deduced bathymetry, figure 4.2-3.

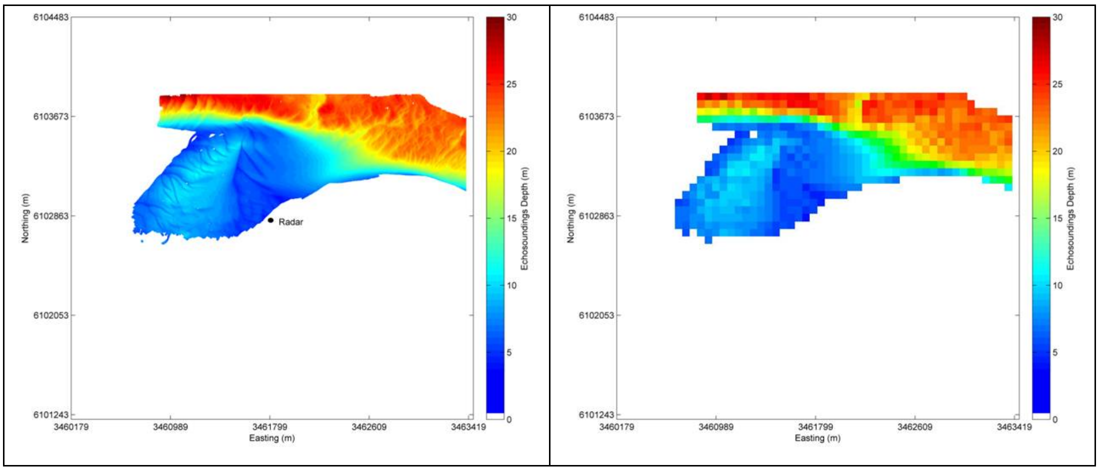


**Figure 4.2-3. Multibeam echosounder bathymetric data. Left: Spatial resolution of grid 2 m. Right: Spatial resolution of grid 42 m.**

## 4.3 Dispersive Surface Classificator – DiSC

The local changes of the wave field contain information on the local bathymetry and the shearing currents, so the determination of the bathymetry and current field is possible by an inversion of the imaged wave group. This simple idea requires a complicated implementation. In this section the basics steps of the Dispersive Surface Classificator are presented; see appendix A for an extended version of the DiSC methodology.

The assumption of DiSC is stationarity of the wave field during the measurement period. The DiSC is a multi-step method. The radar data system acquisition yields image sequences in polar coordinates, to minimize computational time the discrete raw-image sequences are transferred to Cartesian coordinates. The first step of the algorithm is an estimation of the 3D spectrum of the image sequence. By using filtering techniques, the complex-valued image spectrum is decomposed and the wave signal is separated from the noise. Simultaneously the direction and dispersion of the complex-valued spectrum is separated into spectral bins of 2D wavenumber planes of constant frequencies.

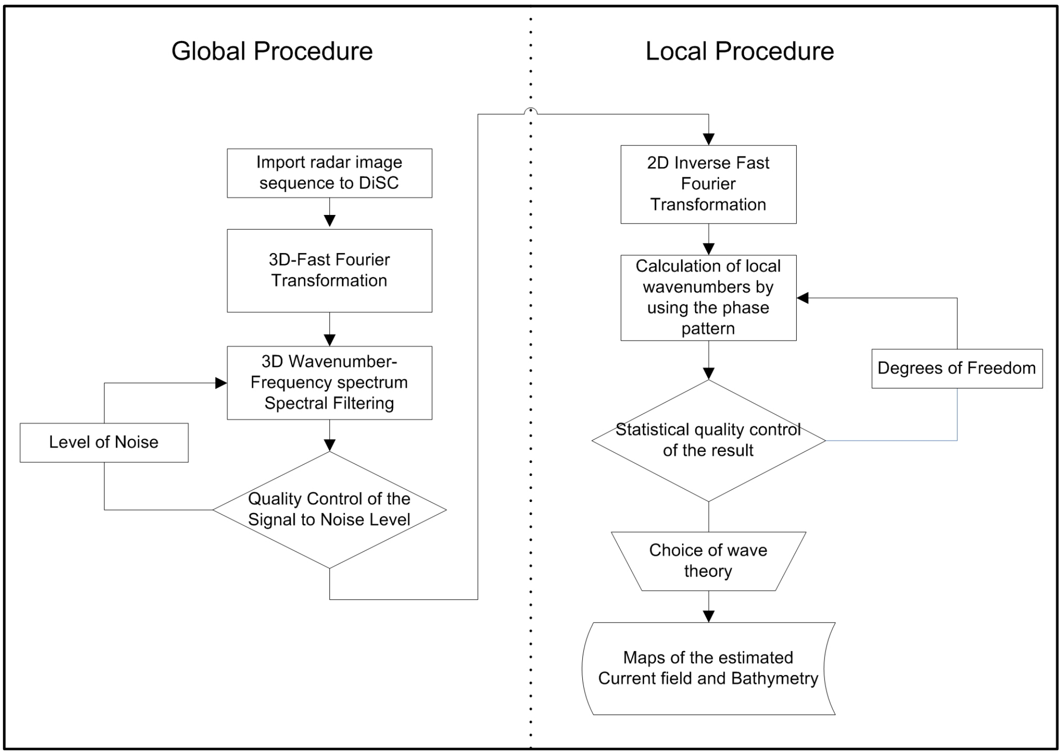


**Figure 4.3-1. Flowchart of DiSC processing. This is an extended version of the left branch of the flowchart in figure 1.6-1. The main steps in the process are: calculation of the 3D spectrum of the whole image sequence, separation of the frequency bandwidths corresponding to dispersive waves, local determination of the wavenumbers, and choice of inversed wave theory; the results are maps of the bathymetry and the current field.**

The next step is a 2D inverse Fast Fourier Transformation of the spectral bins, yielding complex-values to one-component spatial maps in the spatio-frequency domain, which are used for the calculation of spatial maps of local wavenumbers from the one-component images of constant frequency The resulting, one-component local wavenumbers are compiled into maps of known frequency to local 3D spectra and finally using the spatial maps of local wavenumber vectors and power for the calculation of spatial hydrographic-parameter maps. As the next step in the scope of this dissertation, four different wave theories are applied. The number of the local wavenumbers from the one-component images is counted and used as criterion for the results significance. In summary, skipping the technical details, the frequency of the wave components is estimated from the whole image sequence as a global procedure and the wavenumber is determined in subareas of the images; by having estimated these two properties, an inversion for the determination of the bathymetry and current field is possible.

This method was applied on several 12-hour datasets of radar image sequences. To increase the degrees of freedom, all DiSC maps of each tidal cycle were averaged after correction by the tidal gauge measurement, since it is assumed to be statistically independent measurements.

## 4.4 Validation of DiSC bathymetry

The most important step in the application of DiSC is a validation of the method. The DiSC results are compared with the bathymetric data acquired by multibeam echosounder, section 4.2.6. The fact that the delay between the acquisitions of the two datasets is less than 48 hours makes those two datasets worldwide unique, therefore several attempts with different methodological approaches or analytical settings are analyzed.

### *4.4.1 Oceanographic conditions*

The minimum wind strength during the radar observation should be higher than force 5 Beaufort so that there are waves, the backscatter energy is significant and the wave field is long enough to carry bathymetric information.

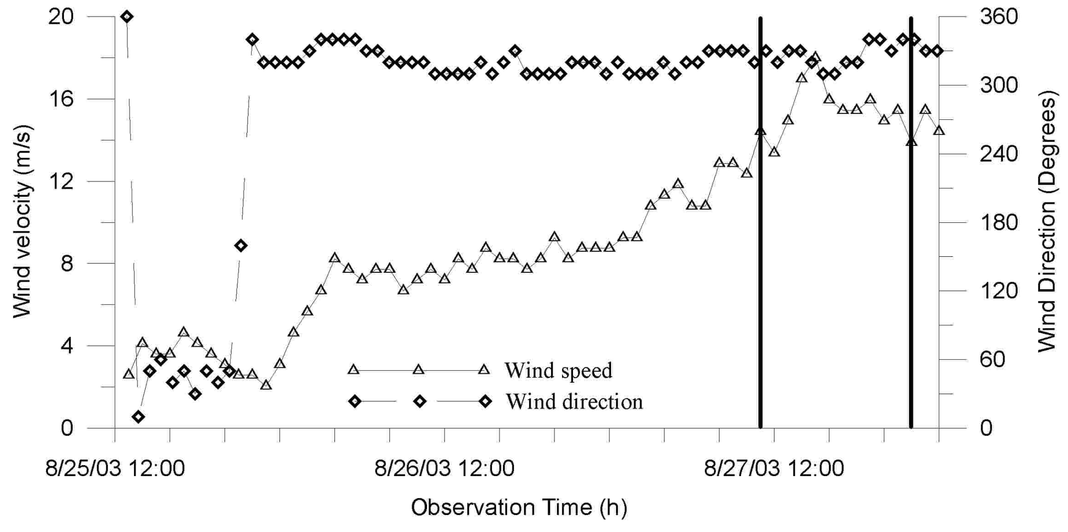


**Figure 4.4-1. The hourly average wind speed and direction during radar data acquisition, the period of radar observation is indicated by the 2 perpendicular solid lines, the wind magnitude is the average during the first 10 minutes of each hour.**

In this part of the study, the DiSC method is applied to a dataset collected over a 12-hour period, between August 26, 2003 at 23:00 and August 27, 2003 at 10:00. The wind was blowing for more than 24 hours before the data acquisition from WSW and during the data acquisition the wind direction was varying between WNW. The wind speed was higher than 8 m/s and was increasing up to 18 m/s during the data acquisition period, figure 4.4-1. During the same period, the significant wave height varied between 1.2 m and 1.7 m and the tide had a normal period of 12.3 h and approximately 2 m range, figure 4.4-2.

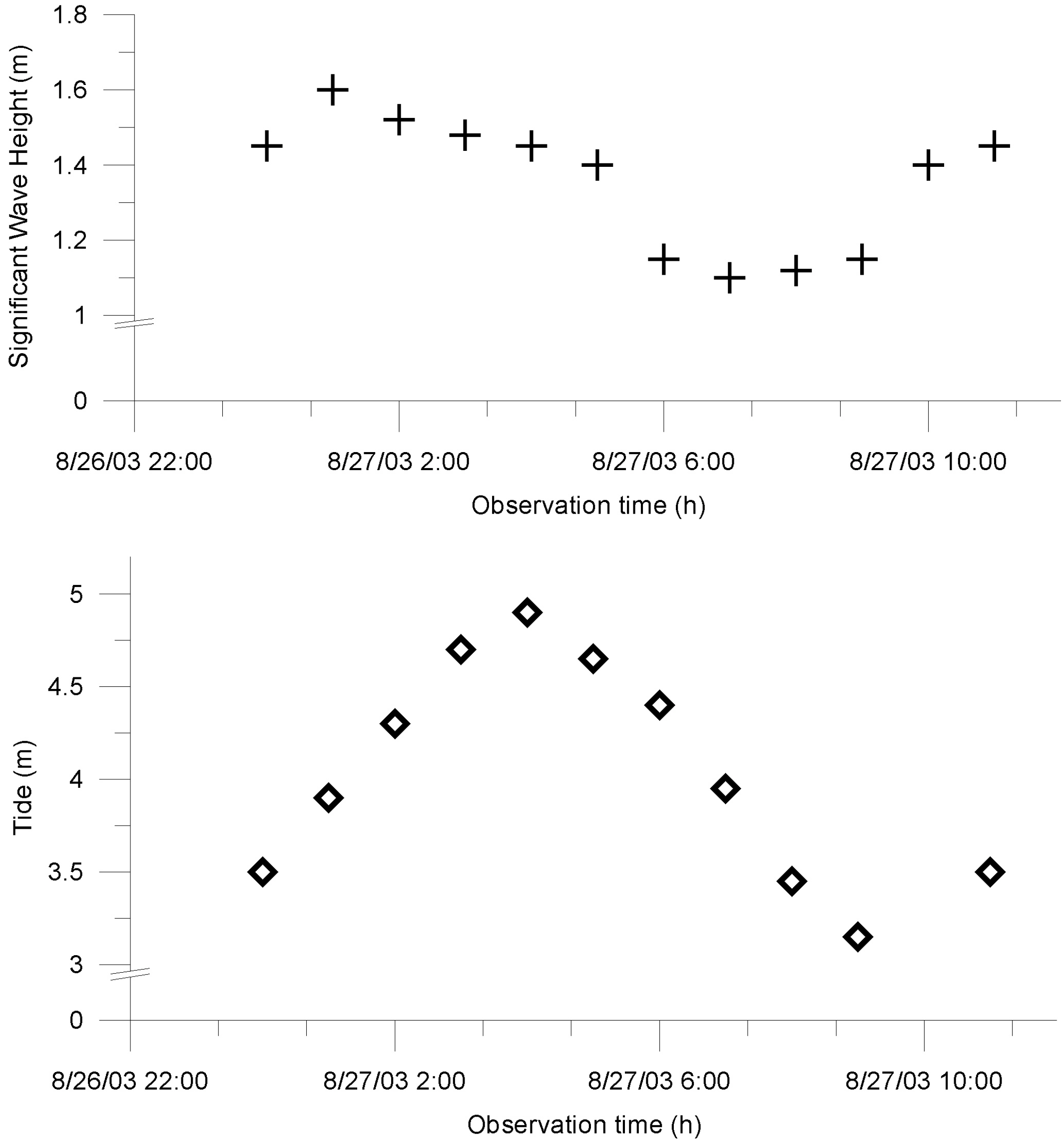


**Figure 4.4-2. Top: The measured significant wave height in the area of radar range during radar data acquisition. Bottom: the tide signal from the tidal gauge of Westerland, 10 nm to the south, the time offset was calculated from the tidal calendar.**

### 4.4.2 Results of validation

Hourly bathymetric maps, with a grid cell resolution of 40 m x 40 m, have been produced for the period of a 12-hour tidal cycle. The current field observation, as a co-product of the analysis, is overlapped and shown in figure 4.4-3, during flooding at 08.27.2003 03:00 UTC. To increase the significance of the result, the twelve maps were averaged. To define a common reference level between the average DiSC bathymetry and the echosounder's, a tide gauge correction was applied.

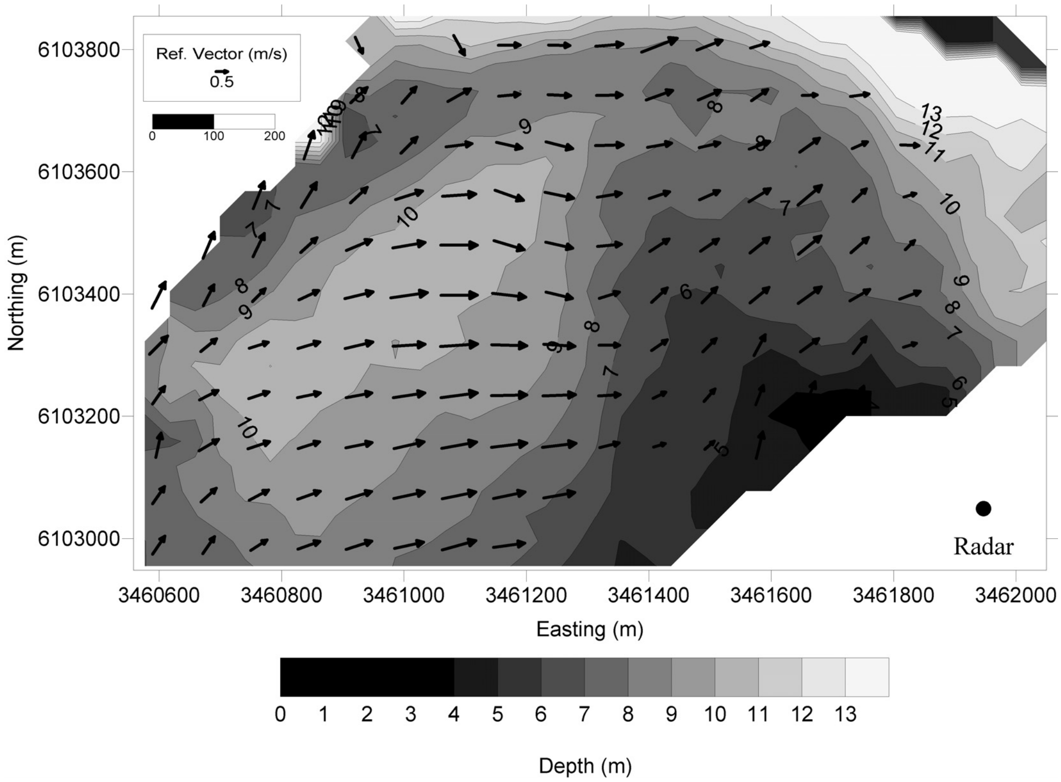


**Figure 4.4-3. Results of DiSC on August 27, 2003 at 03:00 UTC. Isolines of the instantaneous bathymetry and arrows for the current field during flooding.**

The averaged bathymetric values of the DiSC show insignificant correlation with the echosounder bathymetry, even though the main part of them present a one-to-one linear trend, figure 4.4-4. The uncorrelated data consist of two clusters; the first is a systematic overestimation of the depth by DiSC across the whole dataset, the second cluster is an underestimation of the bathymetry in the areas deeper than 12 m. About the main part of the data, the data are markedly offset towards shallower radar retrieval in shallow areas for depths less than 6 m.

The spatial plot of the error illustrates its spatial clustering. For this reason the relative error is plotted over the actual bathymetry surveyed by the multibeam echosounder, figure 4.4-5.

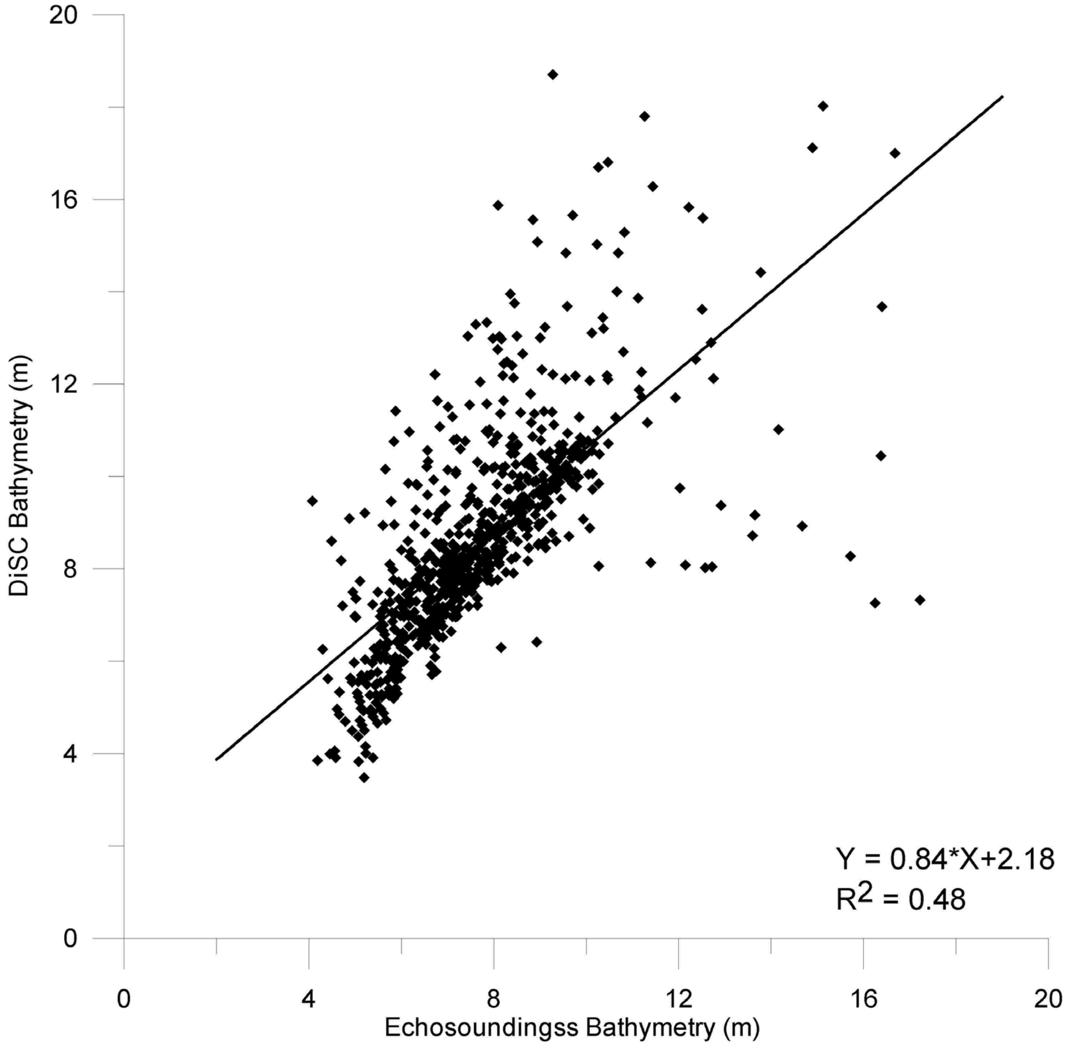


**Figure 4.4-4. Multibeam echosounder bathymetry versus 12-hour averaged DiSC deduced bathymetry. The regression line is a straight line fit across the data and it is estimated by a least squares fit.**

The circles indicate an error of ± 25%, which is the accuracy of a preliminary validation effort in 2002 by Senet and Seemann (2002b). The gray color indicates a negative error (overestimation of the depth) in contrast to the black color, which indicates a positive error (underestimation of the depth). In both cases the triangles indicate errors between 25% and 70% and the squares indicate errors between 70% and 100%.

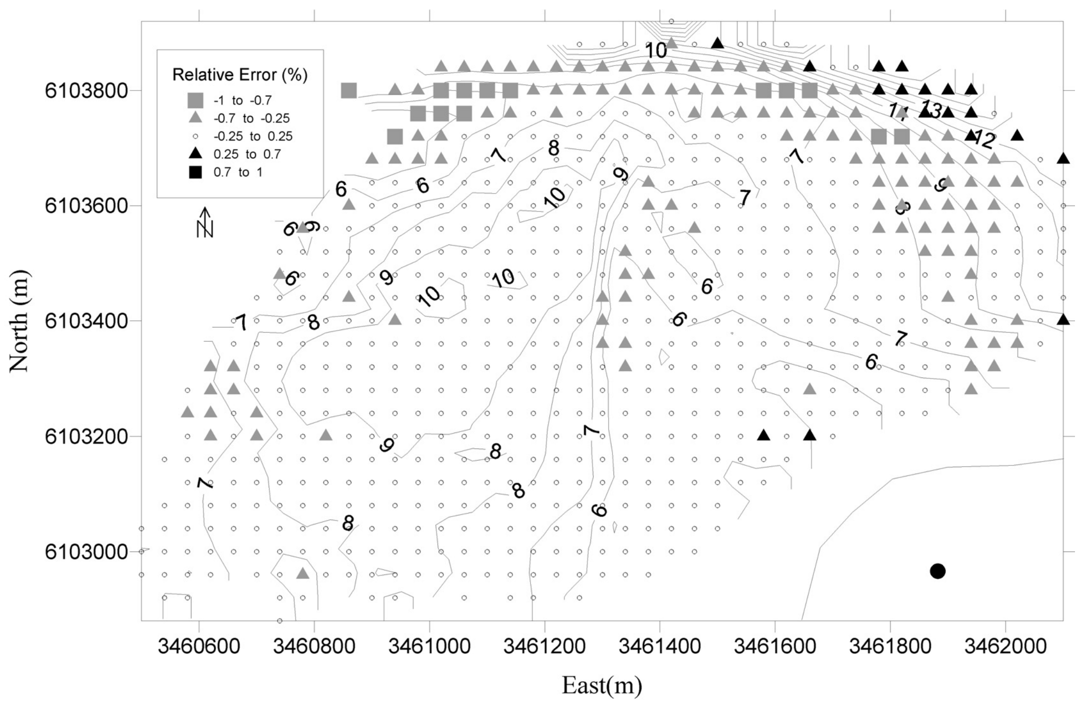


**Figure 4.4-5. Overlay of the multibeam echosounder bathymetry (isolines) with the relative error of the DiSC deduced bathymetry; the gray color is used for the negative (overestimation) values and the black for the positive (underestimation).**

More specifically, on the northeast side, deep (d >12 m) area, the error is positive and up to 70%. In the deeper parts, the wave length is smaller than the depth, therefore the error increases as a function of depth, but it is not possible to identify the mathematical relation, because of the high variability of the error. The highest values of the error occur over the grid cells with a high bathymetric gradient. By using the absolute relative error, the data was separated into groups with a step width of $0.05^{o}$. The plot of the mean value of the relative error of each group versus the mean value of the water depth as deduced by DiSC proves a correlation between those two parameters, figure 4.4-6. As the main error source, it identifies the influence of the bottom slope on the wave field; the question is about the error propagation between the grid cells.

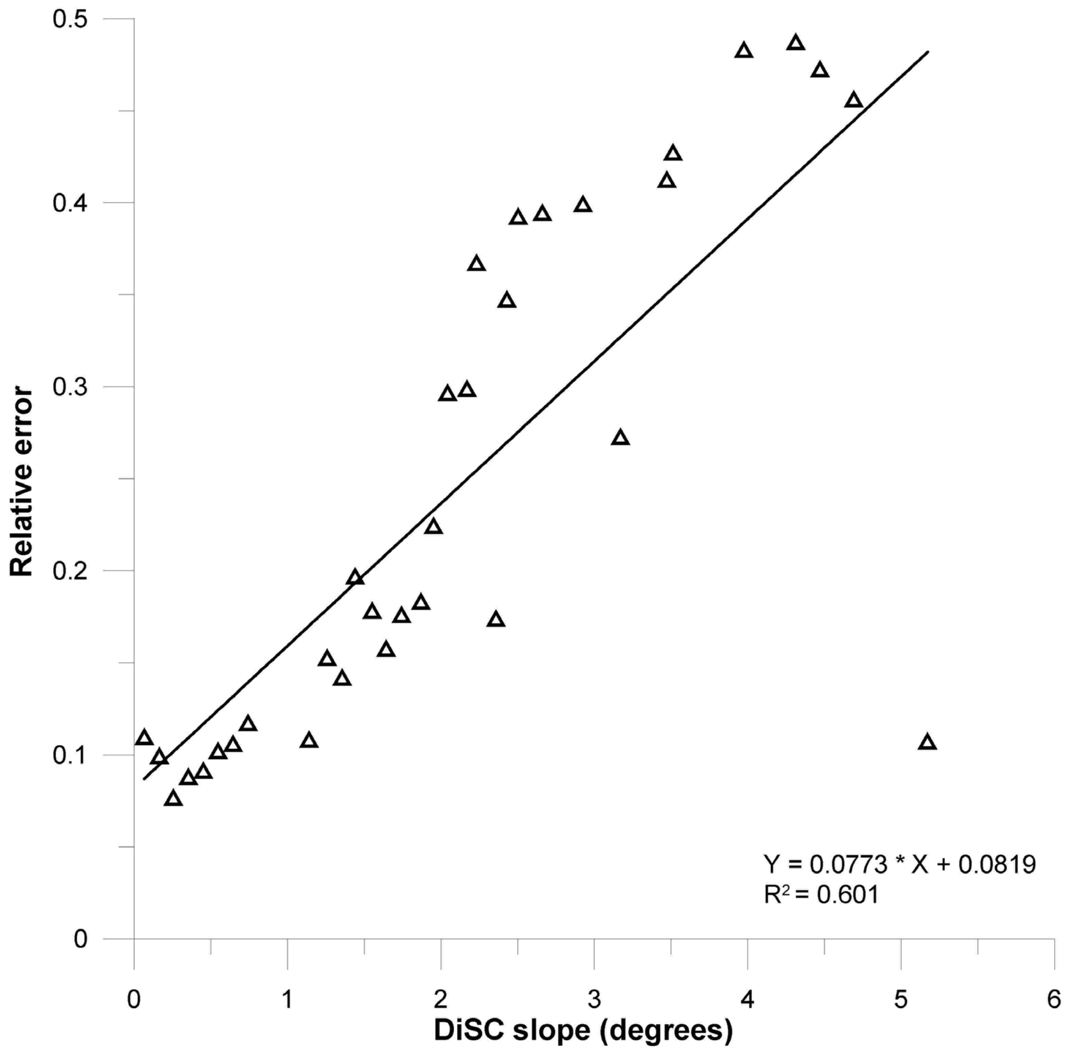


**Figure 4.4-6. Scatter plot of the relative error versus the sea bottom slope, as it is estimated by DiSC.**

The spatial correlation of the error, figure 4.4.-7, shows that the error of the depth in each grid cell has a significant correlation only with one neighboring grid cell. The disclosure of this correlation is a non-significant spatial correlated error has the same direction as the propagating wave field.

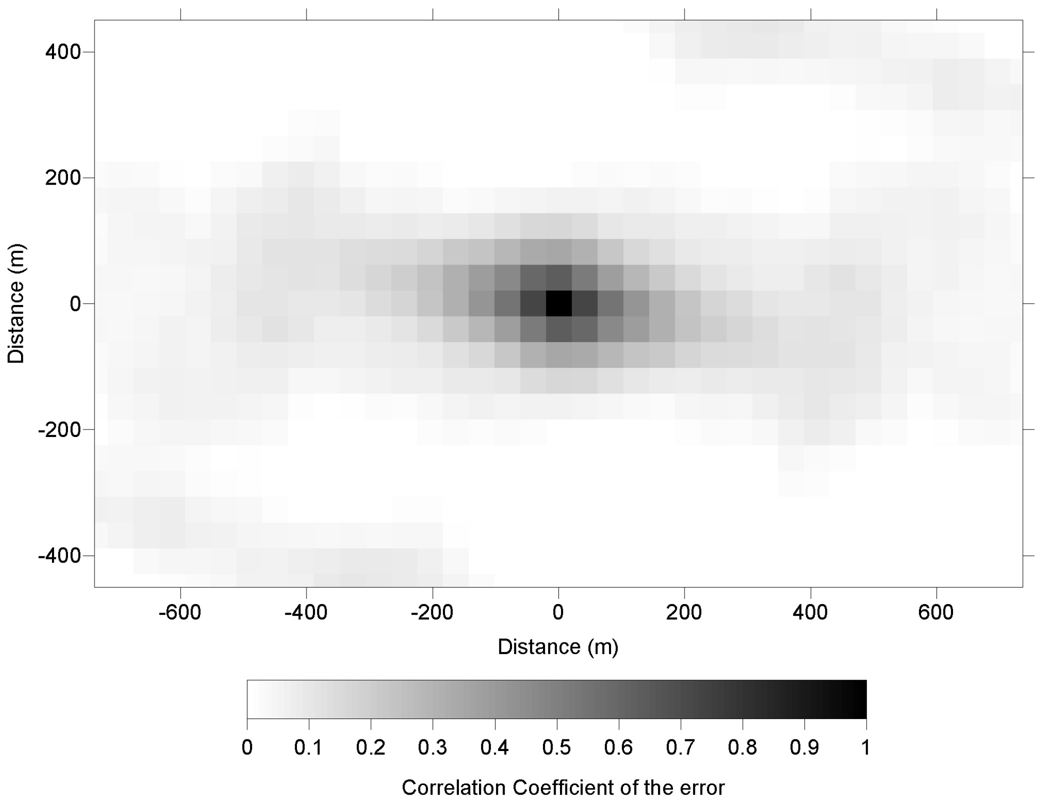


**Figure 4.4-7. Spatial correlation of the relative error within the bathymetric grid.**

The previously mentioned observations initiated the development of a method for the determination of the significance of the DiSC results and the filtering out of non-significant results. By using the number of fitting wave components, which influences the accuracy of the results, and compiling the knowledge that the error is not propagating within the grid, each grid cell bathymetry has been filtered; the minimum of regression points is defined as 30. In addition a second selection filter has been applied; the second filter is arranged according to the bathymetric gradient, the grid cells having DiSC deduced slope over $2^{o}$, have been filtered out. The remaining averaged bathymetric values of the DiSC have been plotted against the echosounder data, figure 4.4-8. The main characteristics are similar to the scatter plot in figure 4.4-4, except the minimization of the scatter. The frequency distribution of the relative error, figure 4.4-9, and the mean value proves a systematic underestimation of depth by DiSC of approximately less than 10%.

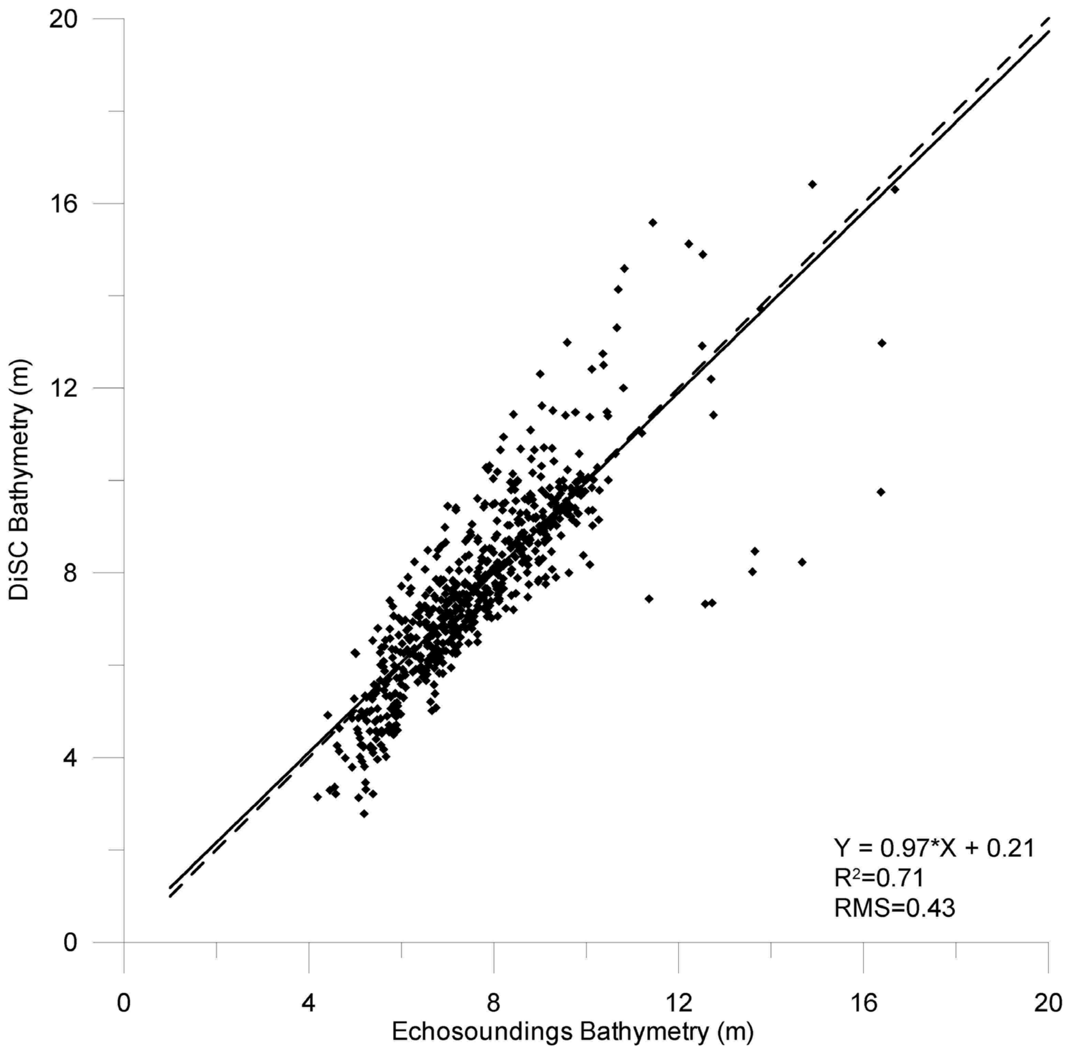


**Figure 4.4-8. Multibeam echosounder bathymetry versus DiSC deduced bathymetry, after the identification of error sources. The regression line is a straight line fit across the data and it is estimated by a least squares fit. The dashed line is the y=x line.**

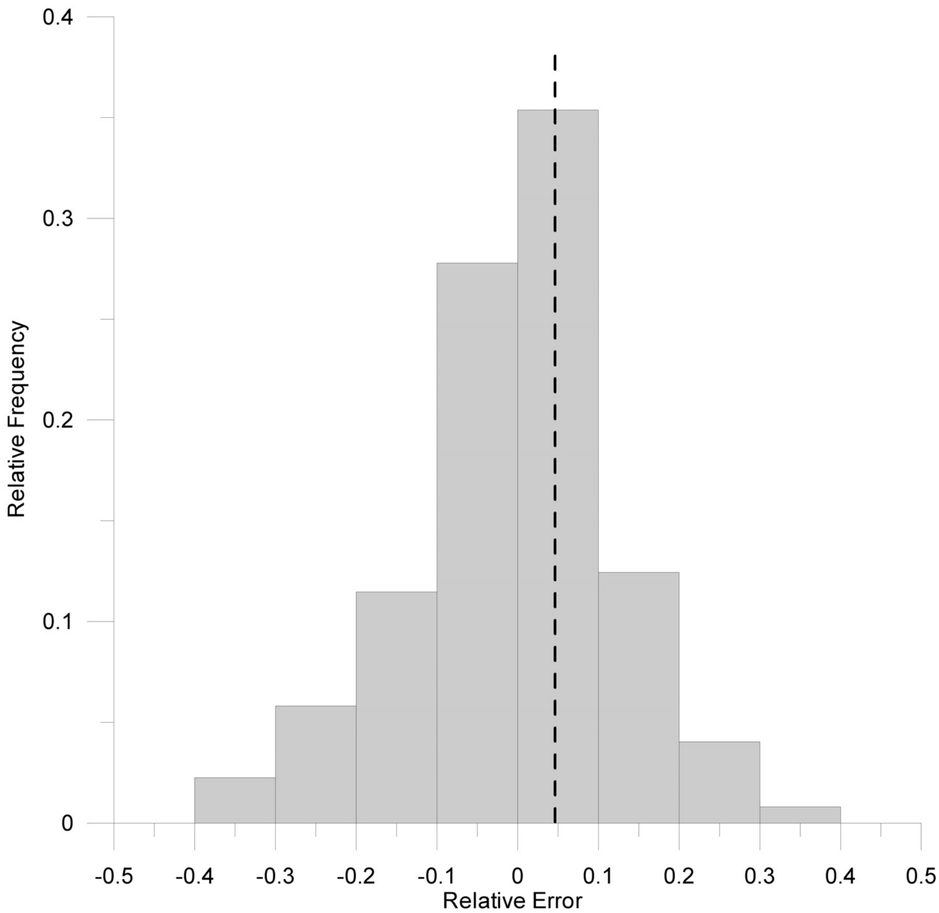


**Figure 4.4-9. A histogram of the relative error. An error of more than 80% of the grid cells is less than 20%. The dashed line indicates the mean error of all the grid cells, the standard deviation is 0.13.**

### *4.4.3 Discussion about DiSC accuracy*

The validation of the Dispersive Surface Classificator over optimal meteorological and wave conditions confirms the validity of using the linear dispersion relation for depth extraction in nearshore areas. The hourly results of the bathymetry and the current field, give a first assessment of the instantaneous depth and current. In previous investigations, Senet and Seemann (2002b), it was proven that the mean bias in the hourly results is approximately 0.4 m. For an increase in significance of the depth results, an average bathymetry is calculated over a tidal cycle in this approach.

The general comment is that DiSC underestimates the bathymetry approximately 10%. The precision of 80% of the DiSC results is lower, but comparable with high-resolution multibeam echosounding coupled with high accuracy positioning, e.g. Ernstsen et al. (2006), considering the spatial resolution of the two methods and the coverage density of the two systems. The

main error source is a change of bathymetric gradient, but the error is not propogated along the grid, as is proved from its spatial correlation, figure 4.4-7.
The histogram of the bias of the depth estimation, figure 4.4-9, shows that the mean error is less than 10%; the Dispersive Surface Classificator overestimates the depth and the standard deviation approximately 15%. The most probable physical reason for the error that appears on the highest point of the slope is the impact of bathymetric inhomogeneity on the waves; when approaching shallow areas, the impact of the seafloor and the bathymetric gradient transform the geometry of the waves, shoaling them. The wave crests become steeper, the wave height increases, which increases the backscattering on the wave crest and in turn influences the imaging of the wave field and causes an overestimation of the depth.
In addition, figures 4.4-4 and 4.4-8, demonstrate that in shallow areas, nominally less than 4 m, DiSC does not produce meaningful results. During the specific conditions, the wave field is strongly non-linear, because the waves are breaking due to the shoaling; therefore the applied linear physical model fails to model the actual wave conditions there and its inversion is impossible. As the method is based on linear wave theory, by assuming the depth, $h$, is comparably small compared to the wavelength, $L$, and the $\vec{u}_c$, the dispersion relation is transformed into $\omega(\vec{k}) = \sqrt{|g|h}$, which is the lower limit of the method.
In practice, the lower limit of the method depends on the radar resolution, in this case 7 m; therefore the shortest observed waves have approximately 28 m of length. In the scatter plots, it is obvious that DiSC underestimates the depth between 4 m and 6 m, which is due to the first, weak, impact of shoaling, which by itself is a non-linear phenomenon of waves approaching a shore.
The majority of DiSC deduced bathymetry between 6 m and 10 m, presents significant correspondence with the echosounder data with an accuracy of higher than 90%. The accuracy of the result for this cluster is similar to the accuracy of Holland (2001). The main source of error is a systematic underestimation of the depth, which exceeds in a small number of cases 40% and is obvious as a cloud of regression points parallel to the fit line. The geo-coding of the results and the overlapping with the multibeam bathymetry in figure 4.4-5 illustrates that the underestimation is caused mainly in the deeper areas where the waves are too short to be influenced by the bathymetry, DiSC underestimates approximately 90% of the areas deeper than 11 m. The limited available depth grid cells do not permit making general

statements about the error source under the specific wave conditions during data acquisition and the geomorphology of the area, but the decrease of the accuracy seems reasonable.

Any limitation of the method's application depends on the wave conditions. For the determination of a theoretical limit, assuming $h >> L$, so $\tanh(|\vec{k}|L) \approx 1$ holds, substituted in the dispersion relation $\omega(\vec{k}) = \sqrt{gk}$, independent of the depth; therefore the result of the inversion is ambiguous. In this case the upper limit of the method is approximately 13 m depth, but the distance from the radar and low backscattered energy determine the practical limitations.

The scatter plot, figure 4.4-6, of the absolute relative error versus the bathymetric gradient, as it is calculated from the DiSC results, indicates a significant correlation between these two quantities. The error presents two main clusters and one outlier as a function of the slope, the first cluster is between $0^{o}$ and $2^{o}$ and the second cluster lies between $2^{o}$ and $6^{o}$; in addition the difference between the two clusters is a constant offset of 0.1. A geo-coding of the error, figure 4.4-5, shows that the highest error is coming from the areas with high seafloor gradient, mainly in the shallow borders of the traffic channel. The erroneous results are presented in the areas with high gradient and one neighboring grid cell. The strongest example indicates that the error depends on the bottom slope, lies approximately among (6103200, 3461200) and (6103500, 3461350), where the error is doubled in comparison with the neighboring grid cells.

### *4.4.4 Conclusions of the linear DiSC validation*

During recent decades several efforts on the determination of bathymetry by inverse modeling wave propagation, approached by linear or non-linear models, have been published. However, few of them have extensive validations and discussions on the errors. The Dispersive Surface Classificator should be considered a state-of-the art method for bathymetric monitoring of coastal areas; because its significant accuracy is proven by this study and it has a high temporal and spatial resolution.

In the homogeneous areas, where there is not a high variation in the bathymetry (slope less than $2^{o}$), the error is approximately 7%. By comparison with the multibeam echosounding data, the radar deduced bathymetry has a similar accuracy with the assumption of a common grid cell. In the areas with high bathymetric variability the error is about 40%. The two main sources of error are the high bathymetric gradient (slope steeper than 2°), which influence the geometry of the waves and the linear wave dispersion, which is no longer applicable when the wavelength is too small to be influenced by the seafloor. The error is strongly correlated with the inhomogeneity of the sea bottom, which has the main non-linear impact on the waves. The error within each grid cell is significantly correlated with a neighboring grid cell, located in the direction of the wave field.

In general, the DiSC method is an alternative remote sensing method for coastal water monitoring, which has satisfactory and comparable accuracy with in-situ measurements, such as echosoundings, and it is applicable in areas of high interest where it is essential to constantly monitor with high resolution over time and during critical weather conditions. The current state of method permits operational application in areas of important activities, such as ship navigation, tracking sediment movement, for model validation and for data assimilation in real-time forecasting, because the inversion of the above conclusions and the knowledge of error sources permit the production of confidence maps of DiSC bathymetry, figure 4.4-10.

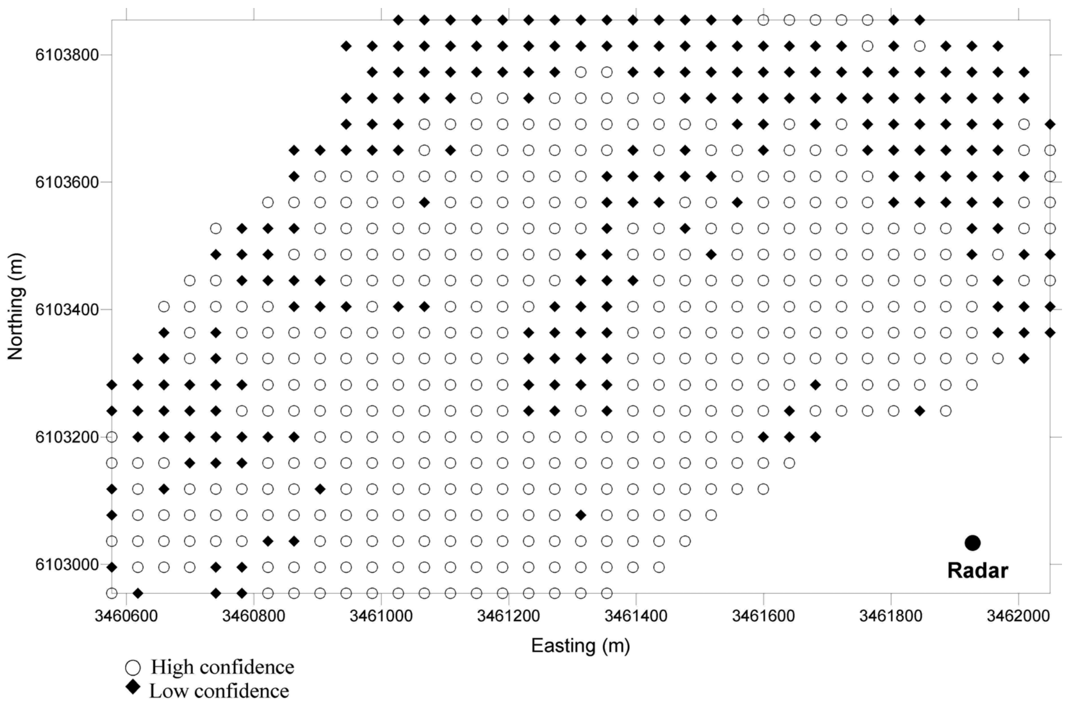


**Figure 4.4-10. Map of confidence. The values of depth corresponding to the circles are more reliable then the depth values corresponding to the diamonds.**

## 4.5 The performance of Bell's method

In the previous section, it was proven that the main error source of DiSC bathymetry is the non-linearity introduced by the interaction of the wave field with and the sea bottom. The question raised is how the inversion of non-linear wave theories performs for the extraction of the bathymetry. The most experienced researcher, who applies non-linear theories for the determination of the bathymetry by ground based X-band radar is Paul Bell from Proudman Oceanographic Laboratory in Liverpool. His example inspired the idea of a comparison of DiSC based on linear wave theory using Bell's method, Bell (2004), based on a modified cnoidal theory of Hedges (1976) and Booij (1981). The funding of a proposal for this comparison was approved by European Union under the ENCORA project; the contract number is TG-2008-DE-02. In the following paragraphs, the results are presented.

### *4.5.1 Bell's algorithm*

The details of Bell's algorithm are not described extensively in any publication, but the basics of the approach were presented in two papers, Bell (2004), Bell (2008b).

The analysis of radar data begins with a conversion from the polar coordinates, in which the raw data is recorded, to a geo-referenced Cartesian grid. The location of the radar, and hence the origins of the polar conversions, were determined by DGPS. No slant range to horizontal range correction was applied, because the differences this would make to the final images are a fraction of the final grid pixel sizes. A Fourier transform was carried out on each pixel through time in the image sequences to isolate individual wave frequencies. Each frequency layer within the transform was then analyzed, to map the variations in wavelength across the area viewed by the radars using a discrete 2D Fourier transform technique that isolates the strongest wave signal in the sub-images. Small subsections of the Fourier layer were used for this analysis, of a maximum size of 32 pixels x 32 pixels or 240 $m^2$. In order to make best use of the resolution of the system, this area is automatically halved if the number of wavelengths in the sub-image area exceeded 4. The size of the analysis area was chosen to allow a minimum of one wavelength of the longest period waves in the deepest areas viewed by the respective radars.

The wavelengths calculated from this analysis were then used in a least squares fit to find the water depth at each pixel, calculated from the non-linear wave dispersion equation, Hedges (1976), that approximates the effects of amplitude dispersion of the waves in shallow water, also as a function of the wave height, for more details see section 2.7.3.
In these instances, the offshore significant wave height $H_s$ was used as the waves observed in the field are spectral in nature and not of a single frequency as might be found in laboratory experiments. In this case, $0.4H_s$ was used as a correction factor of the non-linear dispersion shell and was found to produce significant results across the full range of depths.

### *4.5.2 Results of validation*

The approach is similar to the DiSC validation, paragraph 4.4.2. The results of the analysis are 12 hourly bathymetries and maps of the current field. In order to increase the statistical significance of the extracted bathymetry, they have been averaged, figure 4.5-1. The spatial resolution for Bell's method is 60 m. The water depths determined by this analysis were compared with the in-situ survey data by computing the relative error. The spatial distribution of the error is illustrated in figure 4.5-2.
A scatter plot of the Bell's bathymetry against the echosoundings is illustrated in figure 4.5-3. The method provides bathymetric data in the whole area covered by the radar image and it is obvious that the in-situ survey of the bathymetry is impossible for the whole area of investigation due to ship safety reasons.
For the identification of a correlation between the errors of the radar deduced bathymetry and the bathymetric gradient, a scatter plot between those two quantities is plotted, figure 4.5-4. In addition, the spatial correlation of the error of the radar bathymetry in each grid cell was calculated, figure 4.5-5. Each grid cell has significant correlation with six neighboring grid cells, in the direction of the wave field propagation. The frequency distribution of the relative error, figure 4.5-6, and the mean value proves a systematic underestimation of the depth in the order of 20%.

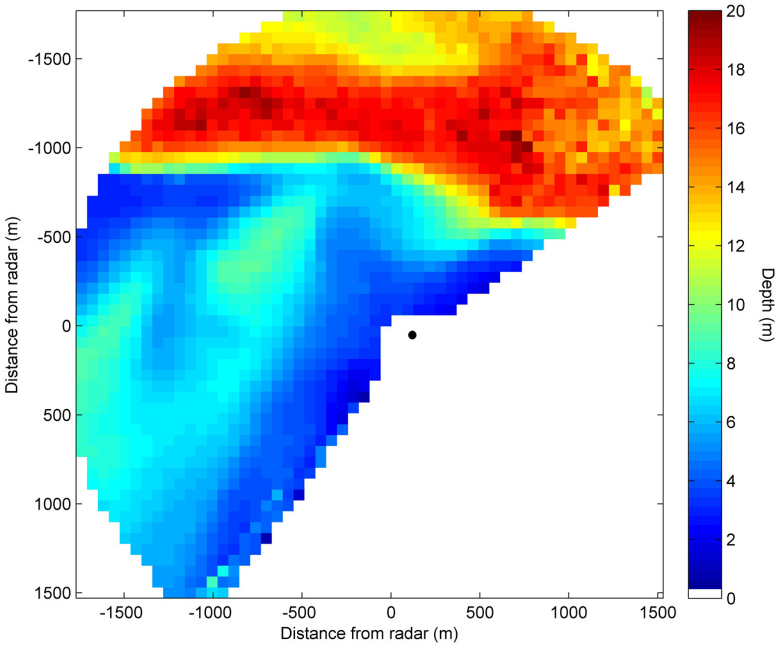


**4.5-1. Averaged bathymetry over 12 hours produced by Bell's method. The spatial resolution is 60 m. The black dot illustrates the position of the radar.**

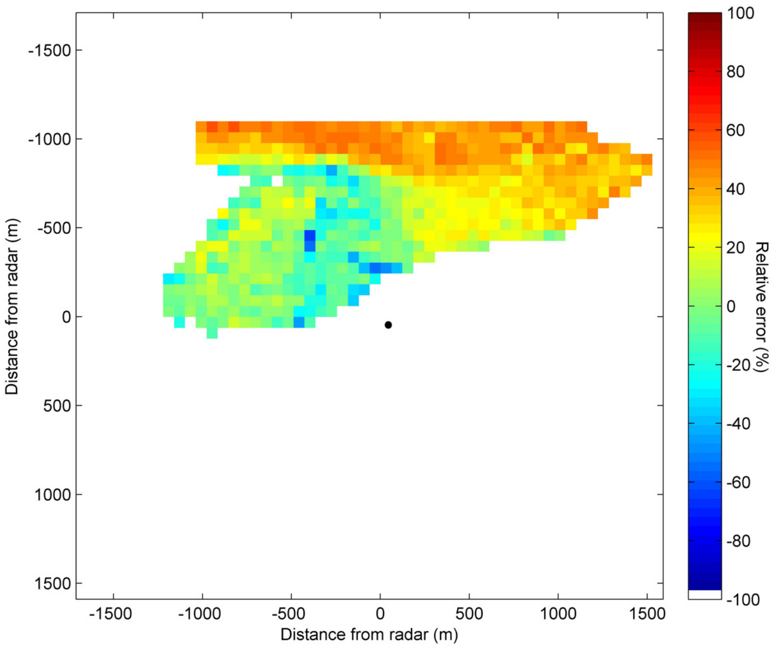


**4.5-2. Map of the relative error of the Bell's method. The spatial resolution is 60 m. The black dot illustrates the position of the radar.**

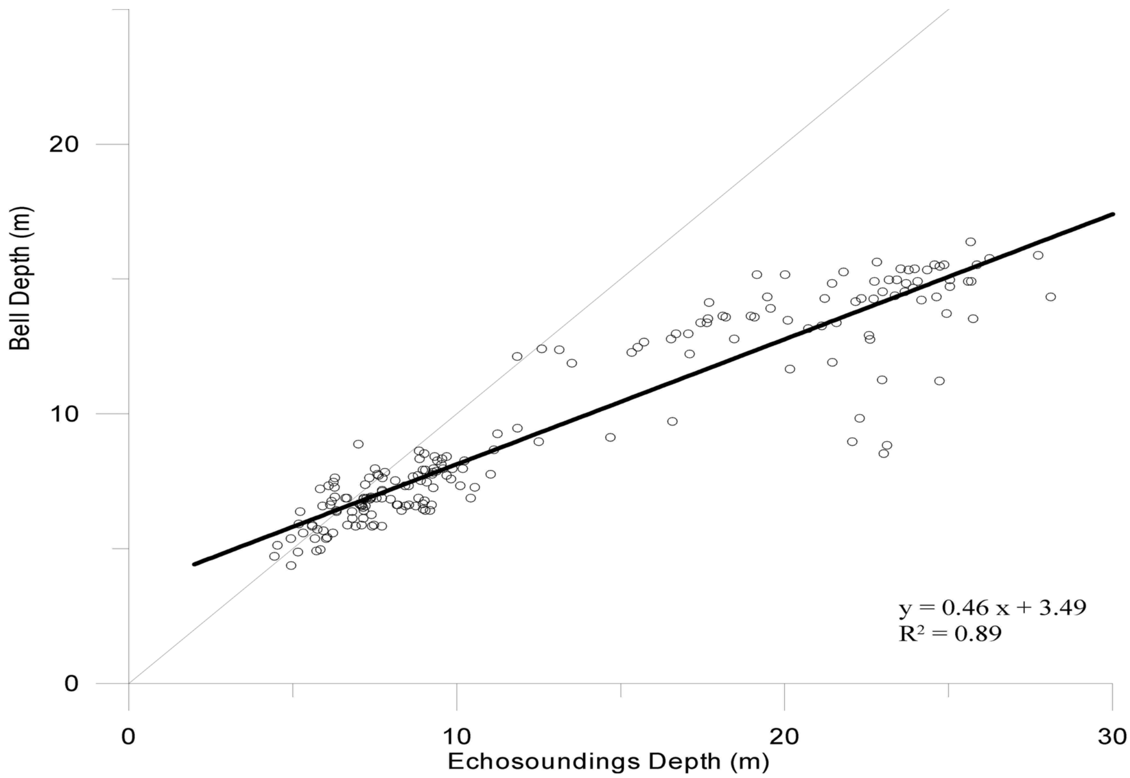


**4.5-3. Multibeam echosounder depth versus Bell's extracted depth. The regression line is a straight line fit across the data and is estimated by least squares fit. The faint line is the y=x line.**

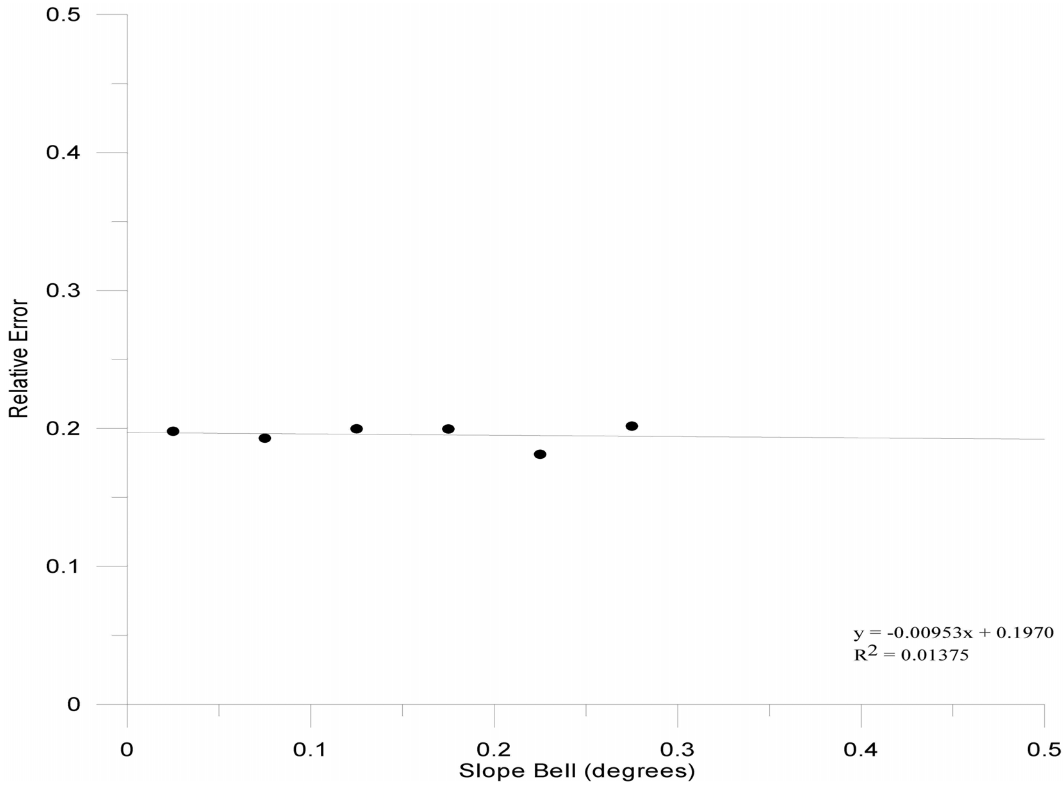


**4.5-4. Scatter plot of the relative error versus the sea bottom slope, as it is estimated by Bell's method. The error is independent of the local bathymetric gradient.**

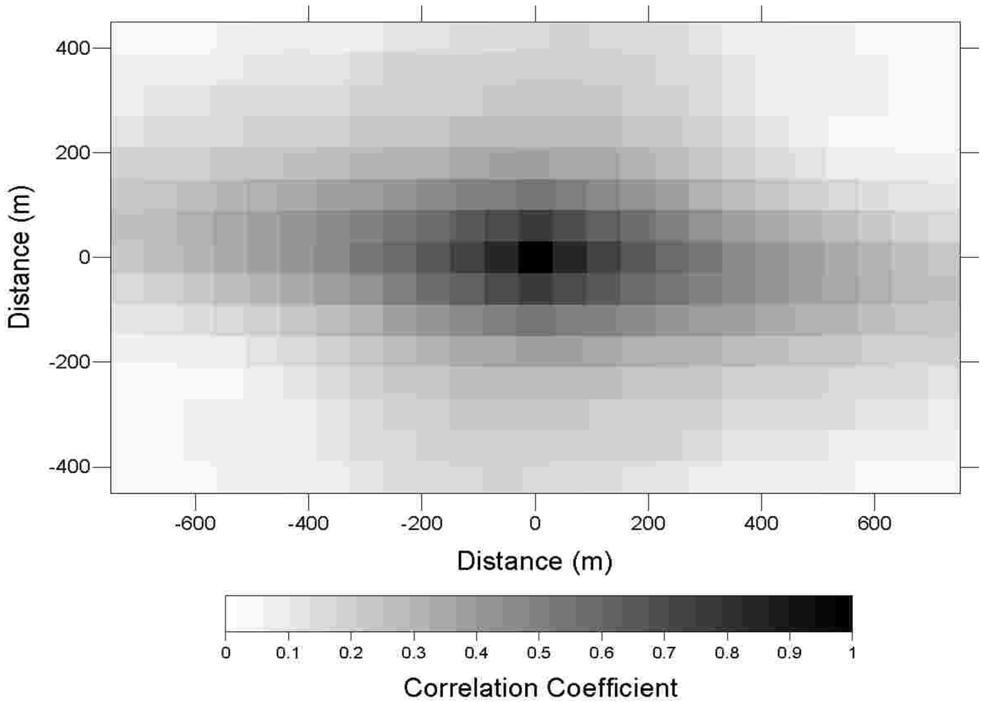


**4.5-5. Spatial correlation of the relative error of the Bell method within the bathymetric grid.**

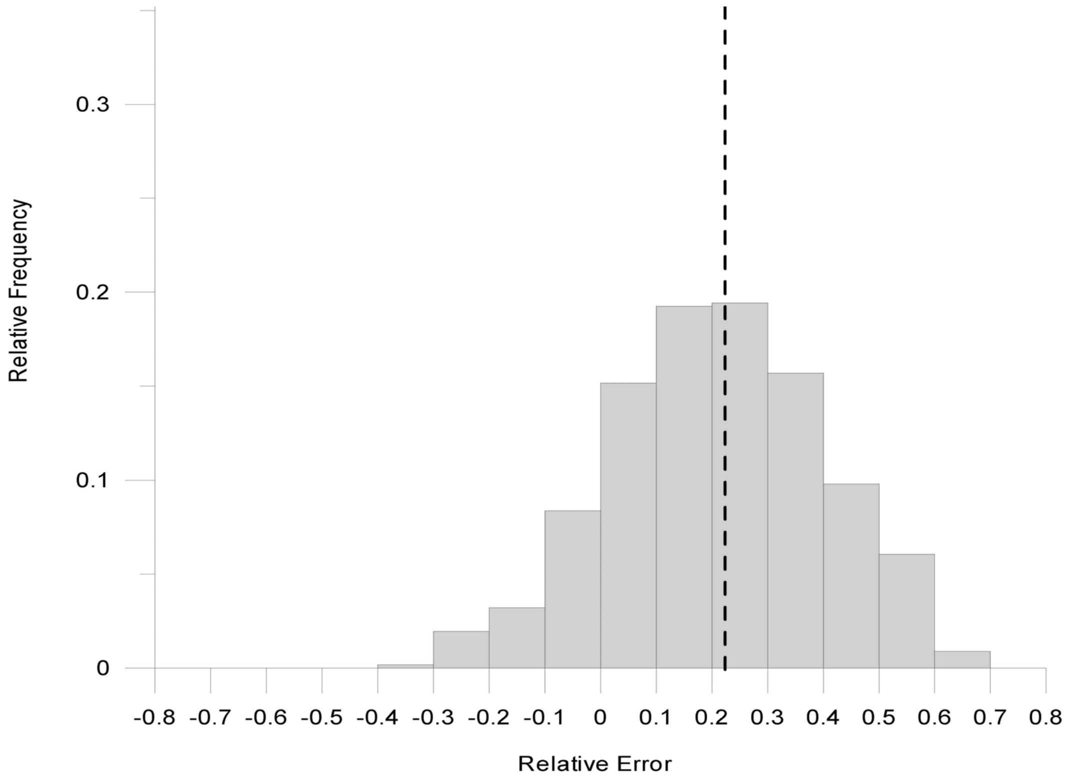


**4.5-6. Histogram of the relative error of Bell's method; 50% of the grid cells have a relative error less than 20%. The dashed line indicates the mean error, 0.22, of all the grid cells, the standard deviation is approximately 0.25.**

### 4.5.3 Discussion about the accuracy of Bell's method

An analysis of the radar data set with Bell's algorithm, as a method based on the cnoidal dispersion modified by linear theory, demonstrates the applicability of the inversion of non-linear theories for the determination of the local bathymetry.

The average bathymetry, figure 4.5-1, exposes the bed relief of the whole area of radar coverage. Despite the lack of in-situ echosounder data for the whole area, an optical comparison of the result with the nautical chart from the same year demonstrates that the method provides significantly good results. The overall impression is that the radar method underestimates the actual bathymetry by approximately 20%, as is proven by the histogram of relative error, figure 4.5-6, but it does reveal the actual sea bottom morphology.

The scatter plot between the echosoundings and the radar deduced bathymetry shows there are two clusters. The first cluster lies between 4.5 m and 8 m; the lower limit depends on the available echosounder bathymetry. In this cluster the method presents a significant correlation with the surveyed bathymetry. The second cluster is formed from depths over 8 m, where there is a clear underestimation of the depth due to the actual wave length. The underestimation of the deeper areas is the main reason for the inclination of the trend line from the y=x line. The second cluster depends on the actual wave conditions and the applied wave model. The waves are too short to be influenced by the bed relief and the applied theory is not valid for such depths.

The spatial distribution of the error illustrates the main sources of the error. The bathymetry for areas deeper than 11 m is clearly underestimated, due to the lack of long waves. The bathymetric gradient is the second source of the error. Bell's method has a reduced accuracy over the steep sides of the shipping channel and in the areas with sand dunes; which is obvious by comparing the map of a high resolution survey, figure 4.2-3, with the error map. Nevertheless, it is remarkable that the error is independent to the local steepness of the sea bottom, figure 4.5-4; the reason is the size of the resultant bathymetry, which smoothes the bathymetric variability. Finally, the error in each grid cell has a strong correlation with six neighboring grid cells, therefore the isolation of bathymetric grid cells with a lower accuracy is impossible.

## 4.6 Comparison of DiSC and Bell's method

The validation of the Dispersive Surface Classificator and the Bell's method raised a series of questions about the accuracy of the algorithms. Any comparison of the performance of the two wave theories is not a straightforward process due to the fact that the numerical implementations of the two algorithms differ. In addition, the two methods were developed to cover different monitoring orientations. On the one hand, the development of DiSC was based on the need to monitor the bathymetry in the littoral zone and tidal inlets, where there is a smooth bathymetric gradient and the tidal range is in the order of 2 m. The method has been demonstrated only for the coastal zone of the North Sea. On the other hand, Bell's method was originally developed for monitoring the Dee estuary, where the tidal range is in the order of 10 m and the currents are dominated by either the strong flow in the estuary or the tide. Bell's method has been applied mainly to areas with similar characteristics, e.g. the Atlantic coast of Spain, Bell (2004). Obviously, different needs have driven the focus of the methodologies' implementations.

Nevertheless, it is still possible to comment on some aspects of the overall performance of the two methods by comparing the results of the same dataset with the two algorithms.

A time series of instant water level at the deepest point subtracted from the mean of each time series has been plotted against the tidal gauge, figure 4.6-1. A comparison of the hourly results with the tidal gauge demonstrates that although neither of the two methods is precise at the hourly determination of the water level, the results of Bell's method has a higher correlation with the measured water level, due to the model used. The Hedge's dispersion function includes the significant wave height, therefore the impact of actual wave conditions is reduced in comparison to the linear dispersion used in DiSC.

Both methods have limitations due to their fundamental theoretical basis, the observation and inversion of the wave field; thus the maximum retrieved depth depends on the wave conditions. There is therefore a systematic underestimation of the actual bathymetry for areas deeper than approximately 12 m for DiSC and 11 m for Bell's method. Moreover, the accuracy of the methods depends on the bed relief. For DiSC, it is proven that there is strong correlation of the method's error to the gradient of the bathymetry, figure 4.4-6; in contrast, for the Bell's approach it seems that the error is independent of the local bed slope, figure 4.5-4, but it increases as a function of the bathymetric variability, figure 4.5-2.

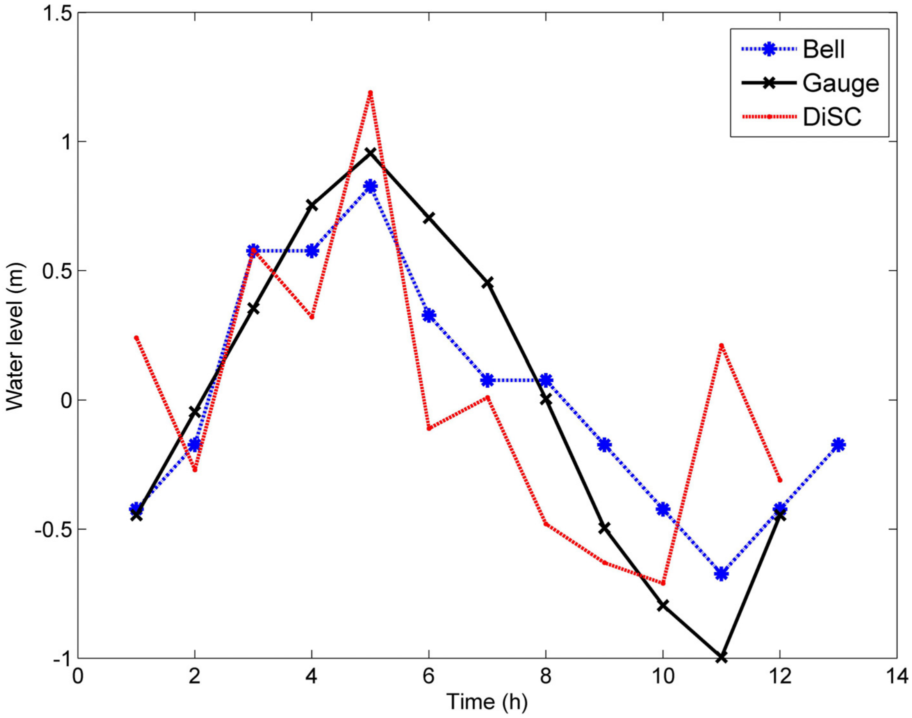


**Figure 4.6-1. The time series of water levels as calculated with Bell's method and DiSC in the deepest part of the tidal channel against the measured water level.**

On the DiSC side, the spatial correlation of the error proved that the error of each individual grid cell is neither propagating nor influences more than one neighboring grid cell. Whereas on the Bell's method side, it proved that a significant correlation exists among six grid cells. In practice, the error in Bell's method is spatially homogeneous. The use of the two characteristics of the DiSC error, bathymetric gradient and insignificant spatial correlation, permit their inverse use as independent valuators of the bathymetric result in each grid cell and for the exclusion of ambiguous values, but this is impossible with Bell's method.

Summarizing the conclusions of the previous sections, DiSC has a high accuracy in homogeneous areas and lower over sea bottom slopes and sand reefs, while Bell's method has a lower accuracy in deeper areas and homogeneous channels, but provides more accurate results over the shoals and the bed relief slopes due to an adapted wave model. However, the mean accuracy of the DiSC is higher with approximately 90%, figure 4.4-9, whereas the Bell's algorithm is approximately 80%, figure 4.5-6. In any case, both methods retrieve the actual bathymetry during storm conditions and the general sea bottom morphology, at times when in-situ measurements are not feasible and with an accuracy comparable to the echosounder's accuracy.

## 4.7 Non-linear extension of DiSC

As demonstrated in paragraph 4.6, an inversion of non-linear wave theories can improve a determination of bathymetry from radar image sequences in areas where linear wave theory is not strongly valid. In addition, using a large amount of field data from a cross-shore array of pressure sensors, Holland (2001) showed that in shallow water errors in the estimated depths using a linear dispersion relation commonly exceeded 50% and were correlated to the offshore wave heights. Those two were clear indications of the importance of finite amplitude effects for depth inversions.

Therefore, DiSC was further extended by the non-linear wave models described in chapter 2: The linear theory (LWT), the modified cnoidal (MCN) by Svendsen and Buhr Hansen (1976), modified composite model (CHB) based on Hedges (1976) and Booij (1981) and the composite model (CKD) presented from Kirby and Dalrymple (1986), were also inverted, see table 4-2. In all cases, it is assumed that the wave field is the sum of the individual wave components modeled by the four different wave theories, similar assumptions have been applied to investigations by Walker (1976), Headland and Chu (1984)and, Holland (2001), Bell (2008b).

### *4.7.1 Results of non-linear DiSC*

Hourly bathymetric maps with all four models have been produced for the period of a tidal cycle of 12 hours. The spatial resolution of the result is 40 m x 40 m and they are geo-referenced according to the position of the radar. To increase the significance of the result, each of the 12 bathymetries were averaged in time and a common reference level between the average DiSC and the echosounder's bathymetries has been established by applying a tide gauge correction, figure 4.7-1-4.7-4.

**Table 4-2. Overview of the inversed wave theories, see chapter 2 for details**

| Model | Abbreviation | Celerity Equation |
| --- | --- | --- |

| | | |
|---|---|---|
| Linear | LWT | $c^2 = \frac{g}{k}\tanh kh$ |
| Modified Cnoidal | MCN | $c^2 = gh(1 + m\frac{H}{h})$ |
| Modified Linear with solitary | CHB | $c^2 = \frac{g}{k}\tanh k(h + \gamma H)$ |
| Modified Stokes | CKD | $c^2 = \frac{g}{k}\left[1 + f_1\left(\frac{kH}{2}\right)^2 D\right]\tanh\left[kh + f_2\left(\frac{kH}{2}\right)\right]$ |

All four models provided reasonable bathymetries in comparison with the echosoundings; the main geomorphological features are mapped precisely. The shoaling at the northwestern side, the edge of the main shipping channel to the north, the secondary channel in the middle of the area of investigation and, in general, the bathymetric gradient across the whole region.

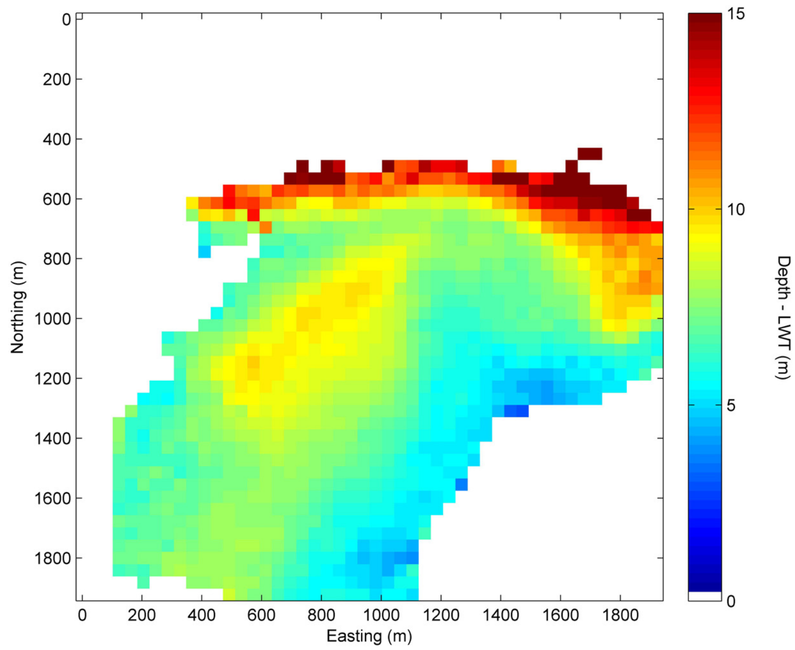


**Figure 4.7-1. DiSC bathymetry in meters based on LWT. The image is north oriented and the radar coordinates are (1800, 1800).**

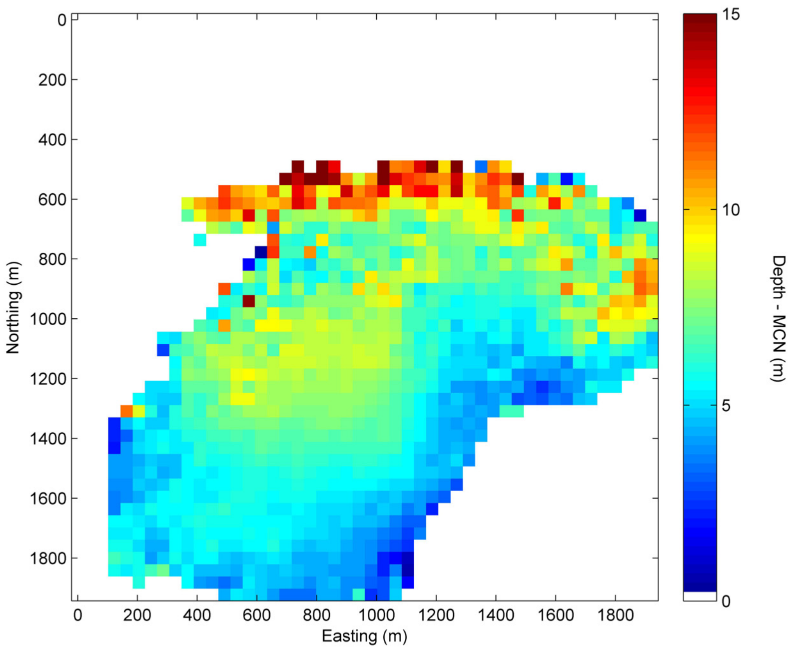


**Figure 4.7-2. DiSC bathymetry in meters based on MCN. The image is north oriented and the radar coordinates are (1800, 1800).**

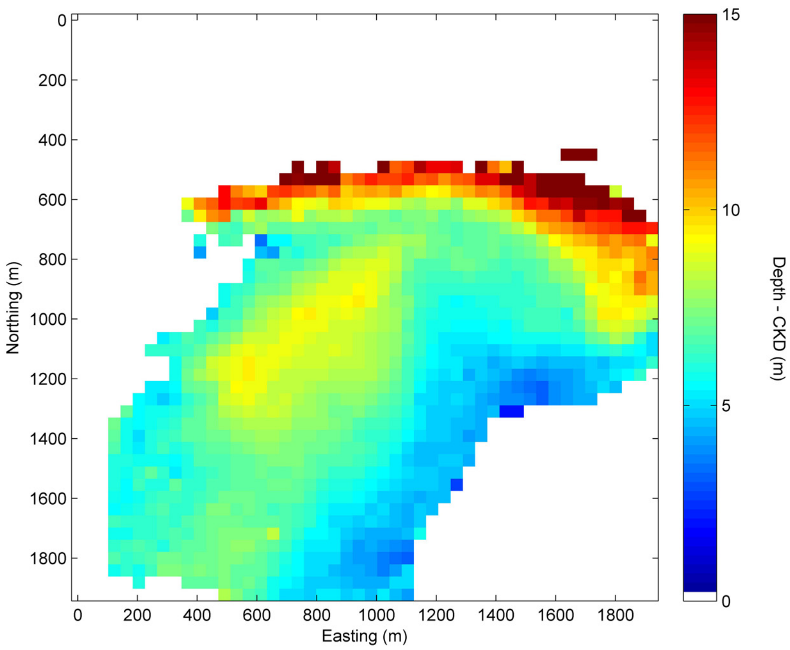


**Figure 4.7-3. DiSC bathymetry in meters based on CHB. The image is north oriented and the radar coordinates are (1800, 1800).**

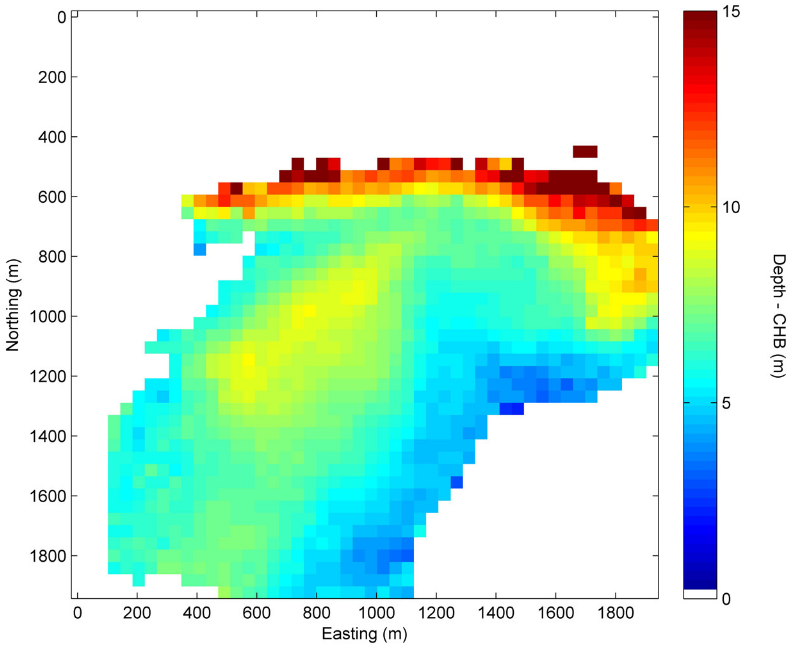


**Figure 4.7-4. DiSC bathymetry in meters based on CKD. The image is north oriented and the radar coordinates are (1800, 1800).**

The comparison of DiSC bathymetries shows that inversion of LWT provides on average a deeper estimation of the whole area, while MCN provides the shallowest bathymetry of the four models. With none of the models is it possible to determine the bathymetry of the northern deep shipping channel, due to the length of the propagating waves.

The performance of each model for the extraction of bathymetry is validated against the truth data, figure 4.7-5. The correlation of LWT, CHB and CKD DiSC bathymetries is significant; the scatter plots of these three methods demonstrate a clustering of the results. The first cluster lies between 4.5 m (the lower limit depends on the available echosounder bathymetry) and approximately 12 m; for this cluster all methods present significant correlation with the surveyed bathymetry. The second cluster is formed from the depths above 10 m, where there is a clear underestimation of the depth due to the actual wave length. The underestimation of the deeper areas is the main reason for the inclination of the trend lines from the y=x line.

The regression lines show a constant shift of the bathymetry from echosounding data, but the slope of all of them is constant, approximately 0.65. The common plot of the three regression lines confirms the expected behavior of the three models; the line corresponding to the LWT (black dashed line) is almost parallel to the one corresponding to the CHB (blue coarse dashed line), but the trend line of the CKD (red dashed line) in shallow waters is identical with the CHB and in the deeper areas is identical with the LWT. The CHB and CKD require the local wave height as input, in this case the significant wave height measured from the wave buoy is considered as a global value for both dispersion equations; this caused the offset between the LWT and the two composite models. The MCN model has also the expected trend from the theory, as the dispersion shell is dependent only to the depth and not the wavenumber. The slope of the regression line is 0.27, a fact that proves that the model performs well only at the shallow areas and systematically underestimates significantly the areas over 7 m.

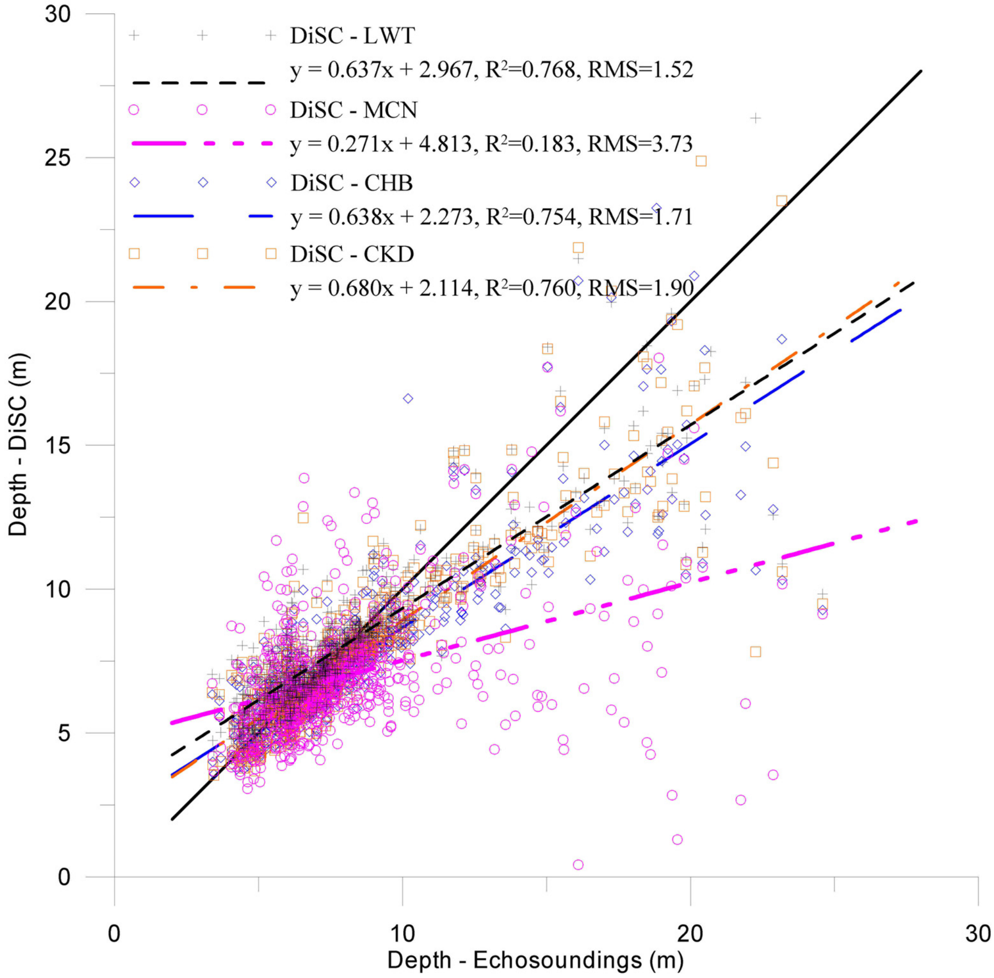


**Figure 4.7-5. Multibeam echosounder bathymetry versus the four DiSC extracted bathymetries. The regression lines are linear fits across the data and estimated by least squares fit. The solid black line is the y=x line. The LWT, CHB and CKD have similar performances, but the MCN almost fails.**

The relative error of the four methods was calculated and spatially plotted in order to define the error sources, figure 4.7-6 – 4.7-9. The spatial distribution of the error illustrates the main sources of errors. In the LWT, CHB and CKD cases, the bathymetry for areas deeper than 12 m is underestimated due to the lack of long waves; similarly MCN underestimates all areas deeper than 7 m. The bathymetric gradient is the second source of the error. The accuracy of all the methods is reduced over the steep sides of the ship channels and in areas with sand dunes. The error of LWT over the slopes exceeds 40% and is spread over a larger area in comparison with CHB and CKD, which have low accuracies only over the steepest of slopes and cover just two grid cells (80 m). In addition the two composite models have a higher accuracy in the shoal area and closer to the coast, due to the adapted wave model; in contrast LWT overestimates the mean bathymetry in the ship channel by less than 5%.

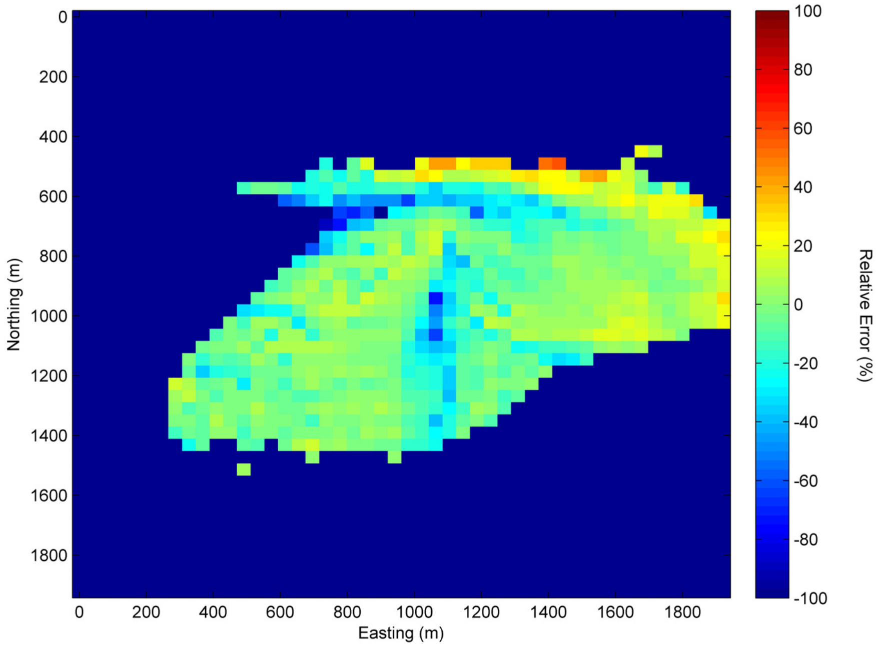


**Figure 4.7-6. The relative error of DiSC–LWT bathymetry as percentages. The image is north oriented and the radar coordinates are (1800, 1800).**

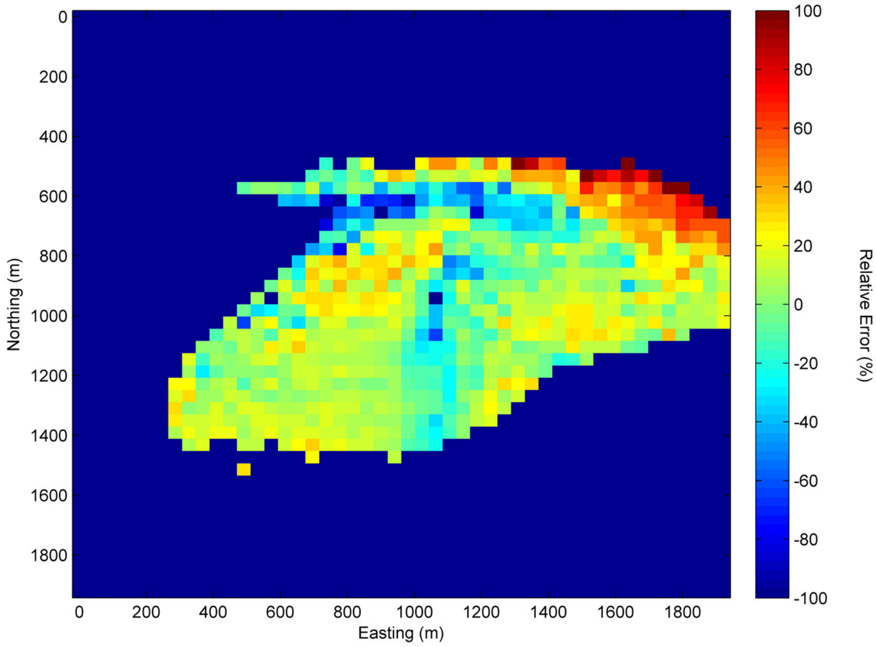


**Figure 4.7-7. The relative error of DiSC–MCN bathymetry as percentages. The image is north oriented and the radar coordinates are (1800, 1800).**

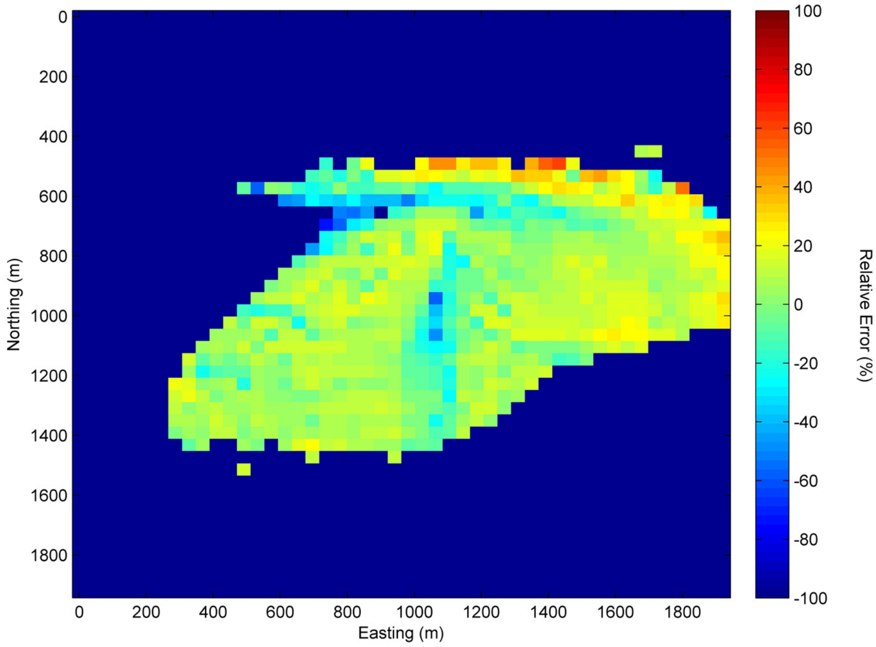


**Figure 4.7-8. The relative error of DiSC–CHB bathymetry as percentages. The image is north oriented and the radar coordinates are (1800, 1800).**

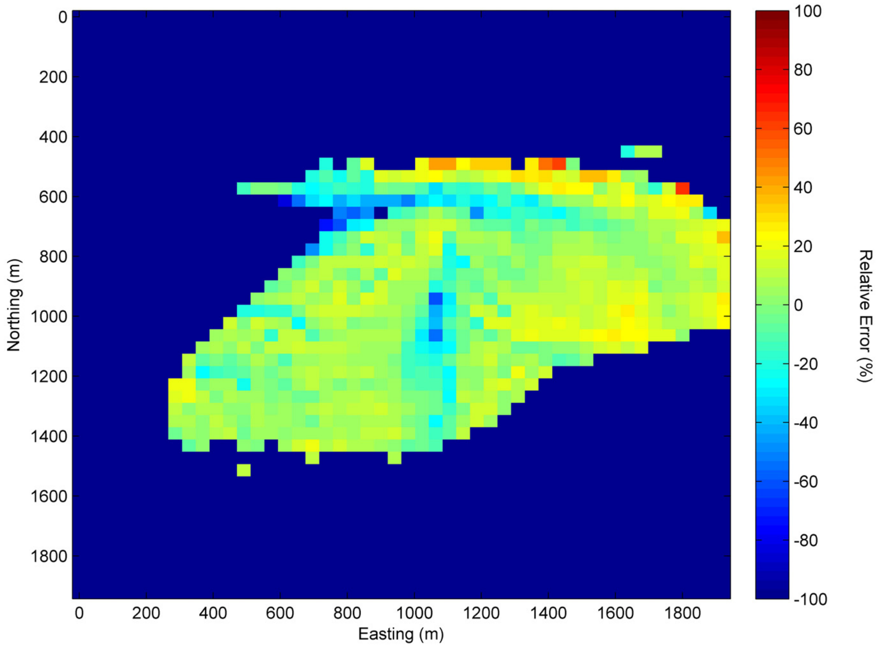


**Figure 4.7-9. The relative error of DiSC–CKD bathymetry as percentages. The image is north oriented and the radar coordinates are (1800, 1800).**

### *4.7.2 Conclusions from the comparison of the four inverted wave theories*

The inversion of four different wave theories, according to previously mentioned assumptions, proved that a determination of the local bathymetry is possible by inverting the wave field propagation in the nearshore zone. The performances of the first order Stokes (LWT), modified solitary based on the linear dispersion (CHB) and its extension to third order Stokes (CKD) are comparable and all three produced significant bathymetries. In general, their performance depends on actual wave conditions, wave directional spread and wave length, but their individual performance depends on the selected dispersion equation. The inversion of LWT provides more accurate results in the deeper areas, compared to the inversion of the CHB and CKD, which determine with higher accuracy the depth over the steeper slopes and in the shallower areas. MCN bathymetry is significant only in areas shallower than 7 m.

The criterion for adoption of one of the models should be the geomorphology and the hydrodynamics of the monitored area. In coastal regions that are deep with extended fetch and are steep near to the shore, e.g. the west side of Sylt Island, the linear model applied best with significant results. In contrast, in the shallow, protected areas with limited fetch, e.g. the Watten Sea, the cnoidal model should be applied. In the intermediate regions, probably one of the composite models would provide significant results. Regardless of the accuracy of the method it is a prodigious achievement to combine more than two wave theories, depending on the local conditions, and to further develop the algorithm to include local effects to ameliorate it, for example the wave heights.

## 4.8 Storm impact on bathymetry and on the current field on local scale

The extended validation of DiSC permits an application of the method for the monitoring of bathymetry and the current field. In this section of the investigation, oceanographic and meteorological observations are integrated for the identification of a 10-day storm's impact on the local bathymetry and on the current field during the trespassing of a low atmospheric pressure system across the coastal area of northern Sylt. The spatial resolution of the results is 40 m x 40 m and the temporal resolution is 30 minutes; simultaneous acquisition of data for the bathymetry and the current field with this high spatial and temporal resolution are reported for the very first time.

### *4.8.1 The motivation*

In 1997, by using mathematical models, Spiegel concluded that due to the variability of tidal range, currents and the degree of human intervention in different basins, the applicability of current models were doubtful and proposed physically-based stability criteria of the tidal basin, Spiegel (1997). Previously this approach has been impractical, due to limited knowledge of the processes in the coastal area. The fine scale in time and space of hydro- and sediment- dynamic phenomena are undersampled. Several efforts, Oost and Boer (1994), Louters and Gerritsen (1995); Kappenberg et al. (1998), for the monitoring of the German Bight barrier islands system have not clarified the circulation mechanisms and the impact of the storms on them; hence the results of numerical modeling of the tidal inlets, Ridderinkhof (1989), were impossible to be verified, even in areas of intense and long term monitoring, such as the Texel Island in Netherlands, Sha (1989). Bathymetric surveys require the use of an echosounder on a ship, which is expensive due to the long shipping times necessary and practical only during calm weather conditions in the coastal areas; as a consequence, the temporal evolution of highly morphodynamic areas is almost always undersampled by echosoundings measurements, and the critical motion of sand, for example during storm events, is not monitored.

The impact of air pressure variation on the water level has been broadly discussed; the first description of the phenomenon as “a 1 mbar decrease in atmospheric pressure very nearly produces a 1 cm rise in sea level” was by Ross (1854) and subsequently by many other researchers, such as Wunsch and Stammer (1997), who summarized, Doodson (1924), who introduced the terminology “inverted barometer response”; Proudman (1929), who gave a formal discussion of load responses in various special basins and more recent contributions include those of Munk and MacDonald (1960), Wunsch (1972), Brown et al. (1975), Dickman (1988), Ponte (1994), involving theory or observations, or both to varying degrees; and by using satellite altimetry Fu and Pihos (1994).

The aim of this study is to answer all three problems stated in the previous paragraphs, the spatial monitoring of the current field in the littoral zone, and the bathymetric survey during storm conditions and a description of the impact of the inverted barometer phenomenon on the current field in the littoral zone.

### *4.8.2 Meteorological and oceanographic conditions*

During nine years of radar data acquisition, see section 4.2.1, a broad variety of different meteorological and oceanographic conditions have been observed. The focus of this study is on one of the most severe storms of the last decade, which happened over the last 10 days of February 2002. For this event, 100 radar datasets, collected between February 20 and 28 are analyzed. These data correspond to three different periods: period A: February 20-21, period B: February 27 and period C: February 26-27. Periods A and B are used for extraction of the bathymetry and period C is used as for calculation of the current field.

The wind speed for the 10-day period of data acquisition was stronger than 8 m/s (75% of the data) the directional wind window is southwest to west, figure 4.8-1. The basic meteorological statistics during the radar sampling are presented in table 4-3 and the time series are illustrated in figure 4.8-2. The mean wind speed is 17.3 m/s, 14.2 m/s and 15.4 m/s during periods A, B and C respectively.

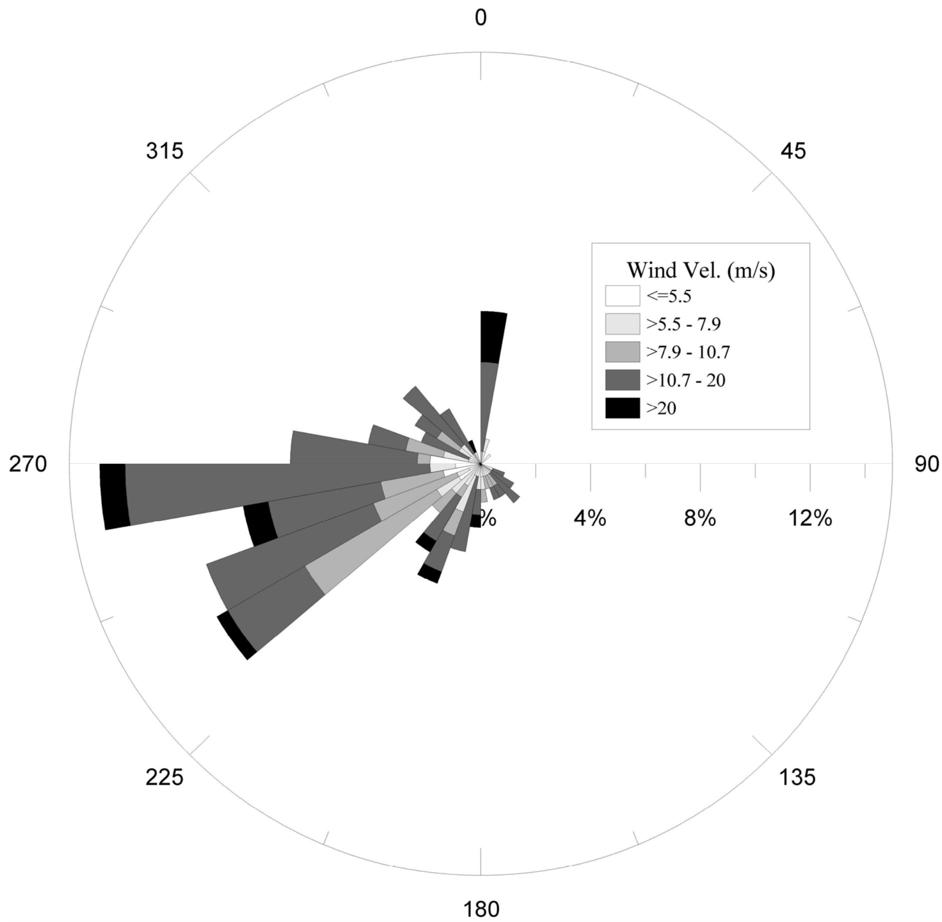


**Figure 4.8-1. Wind plot (polar histogram) for the 10 days before and during the acquisition of radar data. The data were acquired every 6 sec by the meteorological station mounted on the radar mast and averaged to 10-minute intervals.**

**Table 4-3 Synoptic presentation of the wind conditions during the observation periods.**

| | Period A | Period B | Period C |
|---|---|---|---|
| Minimum Wind Speed (m/s) | 11.1 | 10.3 | 8.7 |
| Maximum Wind Speed (m/s) | 22.3 | 16.5 | 24.7 |
| Mean Wind Speed (m/s) | 17.3 | 14.2 | 15.4 |
| Wind Direction | N | SW | W |

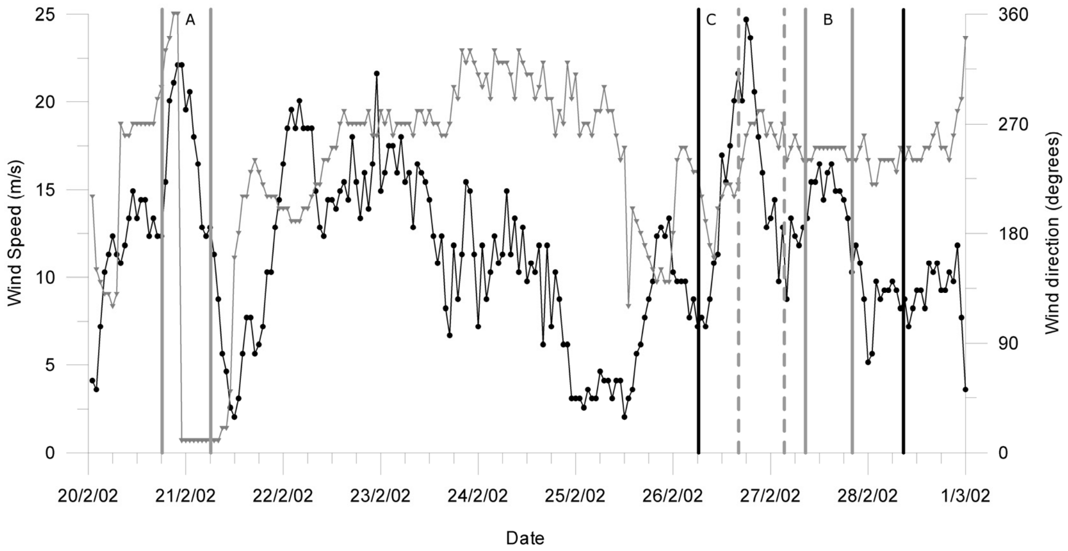


**Figure 4.8-2. Time series of hourly average wind speed (black line) and wind direction (gray line) for the 10-day period during radar observations; the four gray perpendicular solid lines indicate the periods of radar observation for the two succeeding bathymetries (periods A and B), the dashed gray lines indicate the period of radar observation for the bathymetry grid for the current field estimation (period C) during the period indicated with the perpendicular solid black lines.**

During the 10 days of the experiment, the air pressure exhibited significant variability; the maximum air pressure was 1015 hPa and the minimum 965 hPa, figure 4.8-3. During data acquisition of period A the air pressure increased approximately 25 hPa, during period B it was constant at approximately 990 hPa and during period C it increased approximately 15 hPa. Over the period of current field observation a low-pressure system trespassed, causing a rapid decrease in the air pressure of 20 hPa in 10 h followed by a rapid increase of approximately 20 hPa in 7 h, figure 4.8-4. During the last 26 h of the current field observation, the air pressure presented a small variability of 5 hPa. The response of the sea surface to the meteorological conditions was approximately 1.5 m, 2.4 m and 1.6 m significant wave height during the acquisition periods A, B and C respectively.

The water level was monitored at two nearby positions, in Westerland and in List Port, both of the time series have the same behavior, the minimum tidal range is 1.1 m and the maximum 2 m, the full tidal cycle is approximately 12.3 h the impact of meteorological conditions is obvious, figure 4.8-5. On February 26 the ebbing phase was prevented; which is clear in both time series, hence the flooding phase lasted 18 h. The correlation of the water level with air pressure proved that the decrease of the air pressure caused the continuous flooding. After stabilization of the air pressure, the normal behavior of the tidal cycle was reestablished, figure 4.8-6. The open question is the response of the current field at the mouth of the tidal inlet.

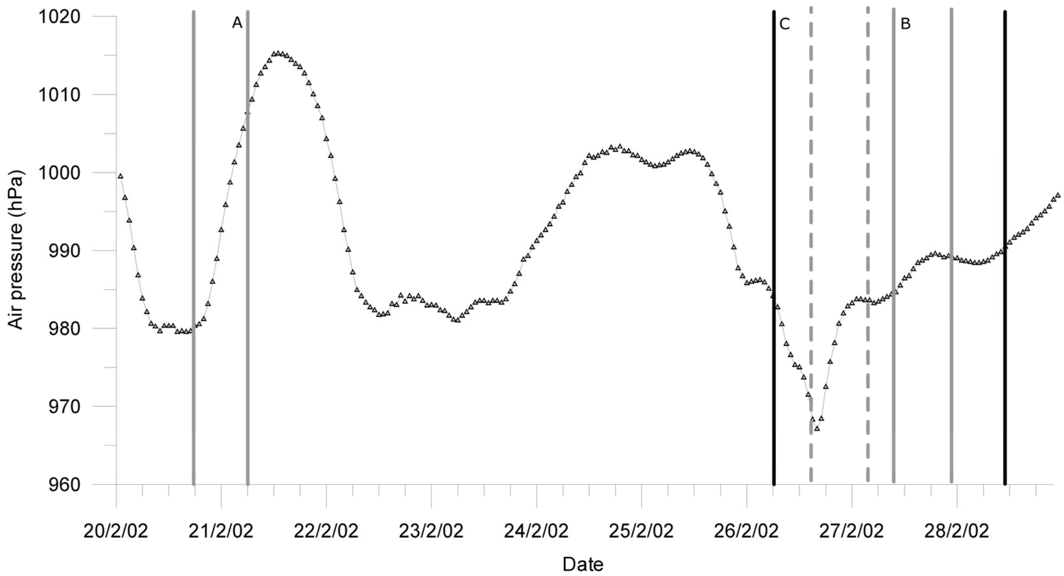


**Figure 4.8-3. Time series of the hourly average air pressure for the 10-day period during the radar observations; the four gray perpendicular solid lines indicate the periods of radar observation for the two succeeding bathymetries (periods A and B), the dashed gray lines indicate the period of radar observation for the bathymetry grid for the current field estimation (period C) within the period indicated with the perpendicular solid black lines. Data source: SWA/DWD.**

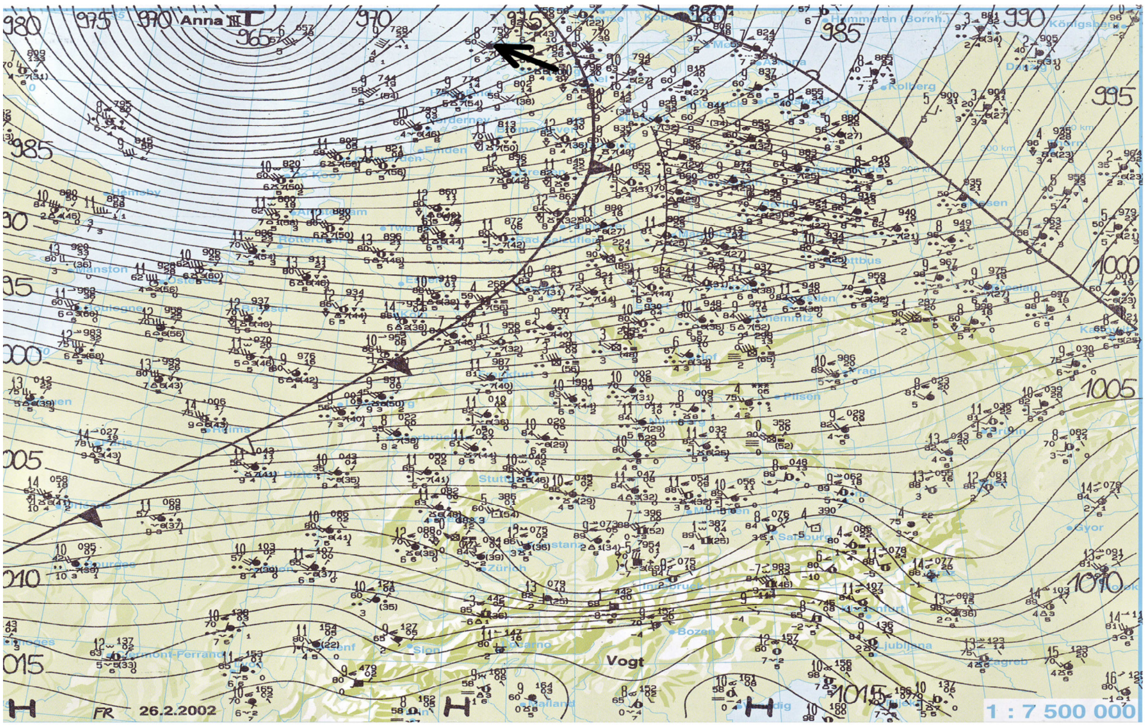


**Figure 4.8-4. Hindcast of the air pressure February 26, 2002. The black arrow indicates the area of investigation. The low pressure front crossed the German Bight over the next 6 hours. Source: Berliner Wetterkarte (BWK).**

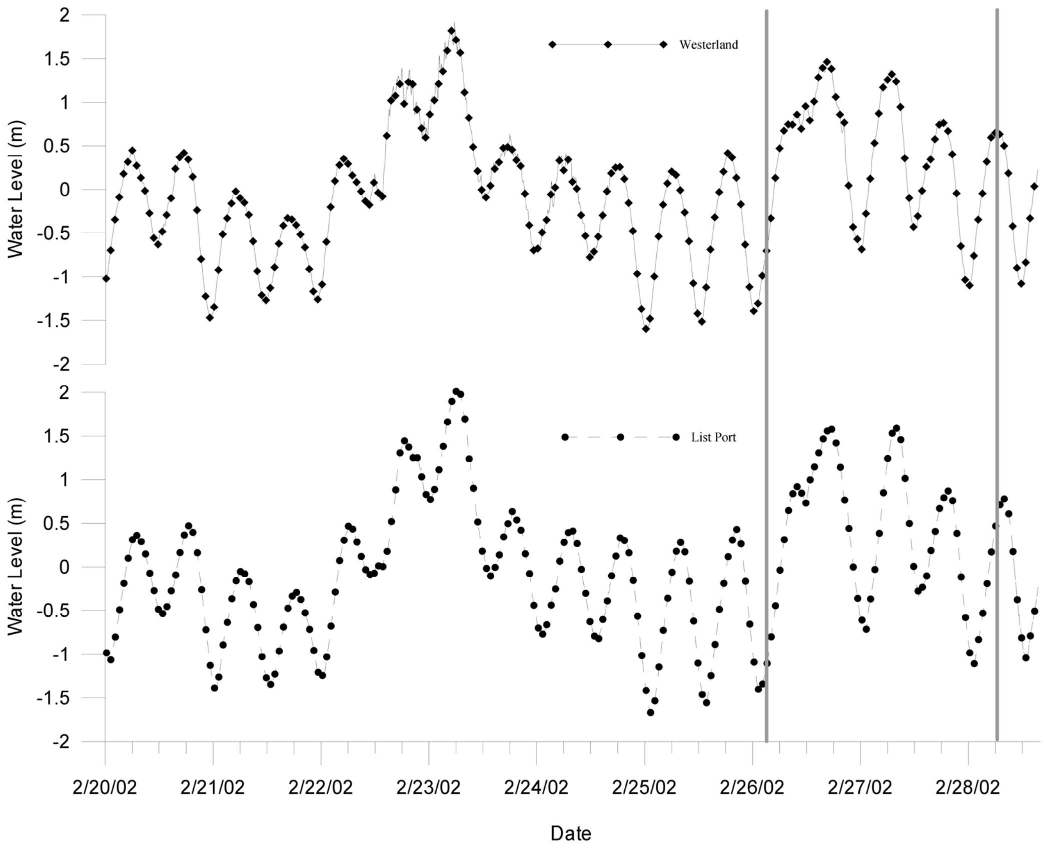


**Figure 4.8-5 Time series of the hourly average water level for the 10-day period during radar observations, the solid line with diamonds was measured on the west side of the island (Westerland) and the dashed line in the Wadden sea (List Port). The two gray perpendicular solid lines indicate period C of the radar data acquisition.**

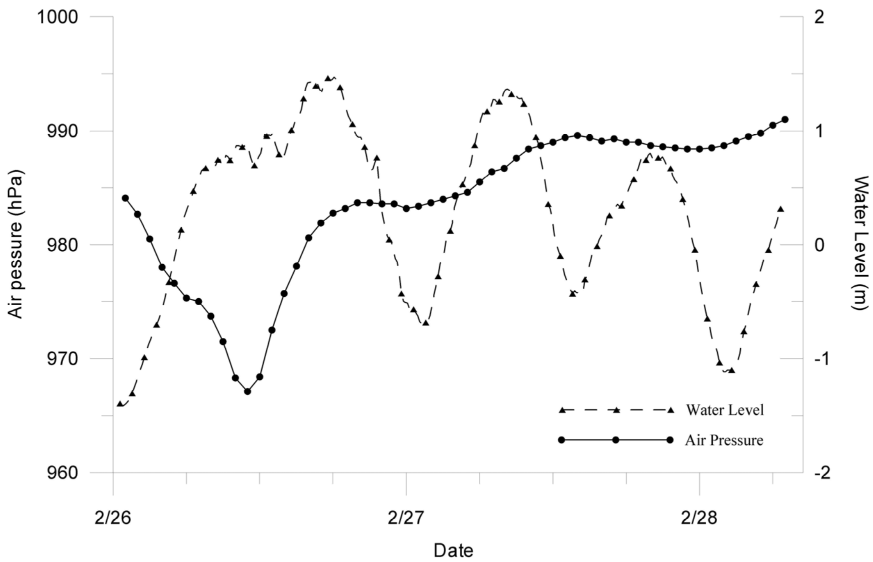


**Figure 4.8-6. Time series of the water level (dashed line) and the air pressure (solid line). The decrease of air pressure prevented the ebb, the stabilization of the air pressure restored the normal tidal cycle.**

### 4.8.3 Bathymetric survey

To identify the storm impact on the bathymetry of the tidal channel, periods A and B have been analyzed and compared. For both periods, a 12-hour time series (a tidal cycle) of the DiSC calculated depths of each grid cell have been averaged; therefore the initial and final bathymetries are available, figures 4.8-7 and 4.8-8. Depth contours are given with a 1 m interval. The deeper transverse channel at the center of the image is identified as a shipping way that is also shown on nautical charts. To determine a common reference, the tidal gauge measurements extended by the tide calendar were used. The difference of the average sea levels between the two periods is approximately 0.4 m; for this reason the value 0.4 m has been assumed as the difference from the common reference level. For the investigation of the position of the sediment deposition and erosion during the storm, a cross-section connecting the two shallowest points and crossing the main channel, was taken into consideration, figure 4.8-9, from O1 to O2.

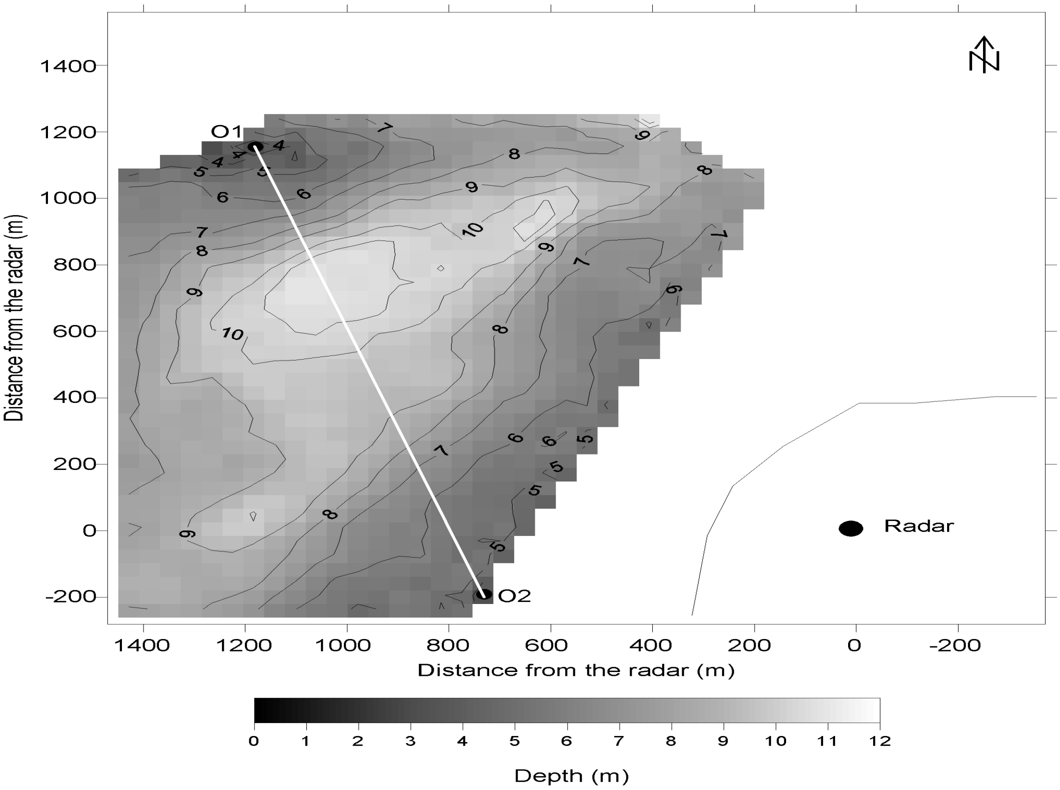


**Figure 4.8-7. DiSC Average bathymetry over 12 h of the area of investigation during the initial phase of the storm, 20th of February 2002 (Period A). The line connecting points O1 and O2 is the cross section of figure 4.8-9.**

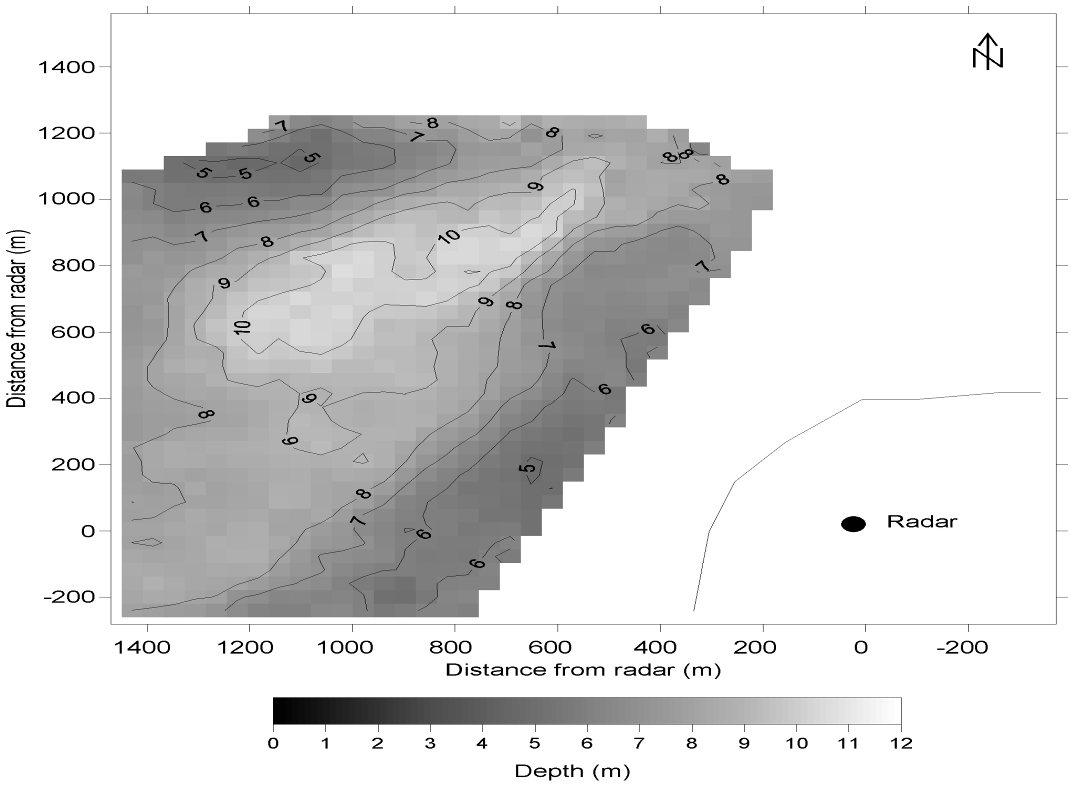


**Figure 4.8-8. DiSC average bathymetry over 12 hours in the area of investigation during the initial phase of the storm on February 28, 2002 (period B). It has the same water level as figure 4.8-7.**

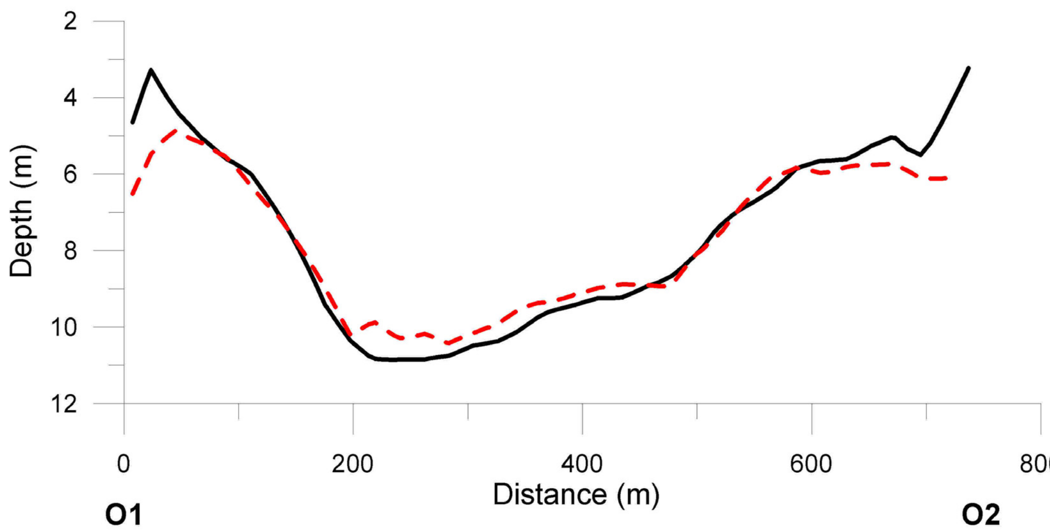


**Figure 4.8-9. Cross-sections of the estimated depth for periods A and B, from point A to point B, see figure 4.8-7.**

The mean difference of the sediment volume during the two periods is approximately 50700 $m^3$. The accuracy of the above results has been calculated to the accuracy as estimated by validation of the method ±7-10% per cell, Flampouris et al. (2008b), so the uncertainty of the estimation of the sediment volume is ± 5000 m$^3$.

### *4.8.4 Current Field*

The wave field was observed by radar over 46 h at 30 min intervals and the current field has been extracted using DiSC with a spatial resolution of 40 m; a typical example is in figure 4.8-10 and the same dataset with spatial resolution of 80 m is in figure 4.8-11. At the beginning of the observations, the current field had an abnormal behavior, the flooding lasted for more than 12 h, as a response to the trespassing of the low pressure front. Afterwards, with a stabilization of the air pressure, it exhibited the normal, known behavior with a period of approximately 13 h, figures 4.8-12 and 4.8-13 respectively. The illustrated current roses are indicative for the whole area and the available data has the same resolution as the results (40 m x 40 m), but are plotted only for five positions at hourly intervals to be obvious during the tidal phase. The current direction and speed of all five points are illustrated in figure 4.8-14; hence the impact of synergy of air pressure and wind on the current field is observable.

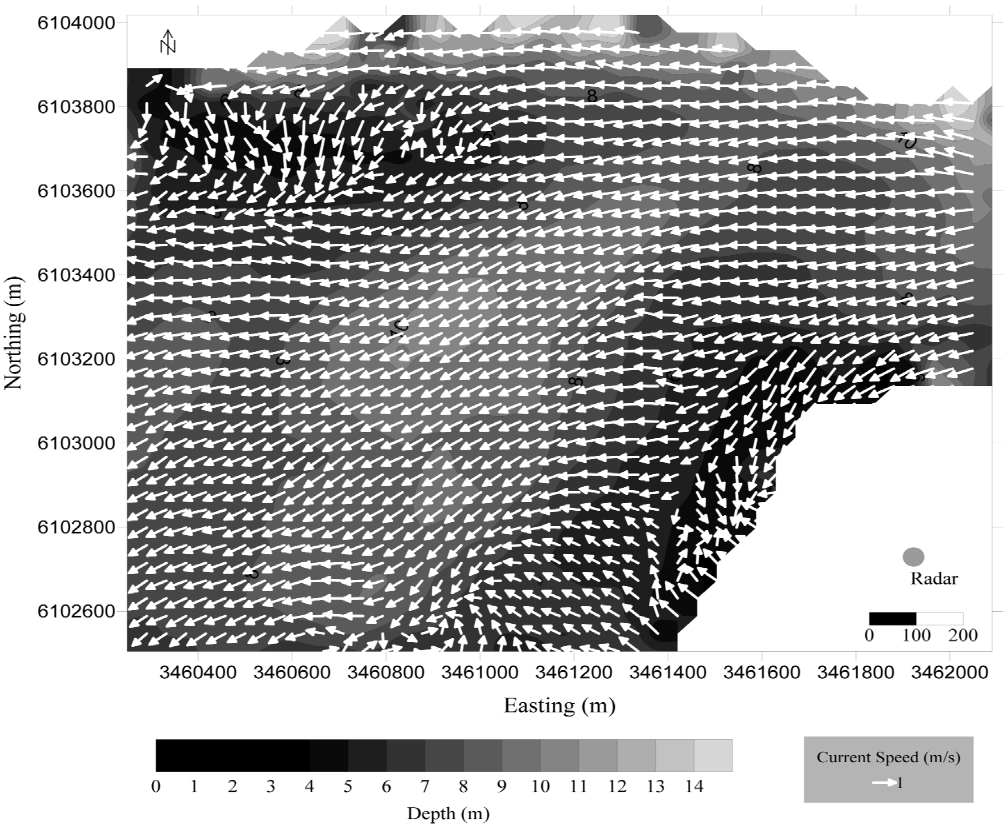


**Figure 4.8-10. Current field during ebbing with native spatial DiSC resolution (40 m x 40 m).**

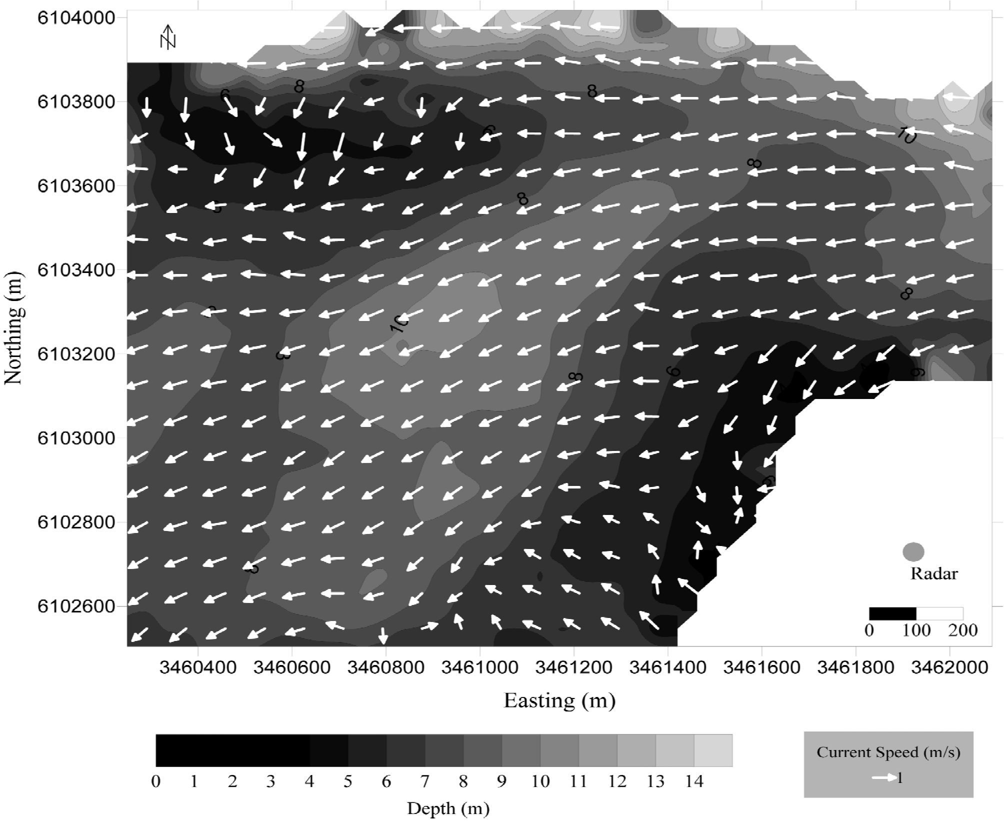


**Figure 4.8-11. Current field during ebbing with spatial resolution (80 m x 80 m).**

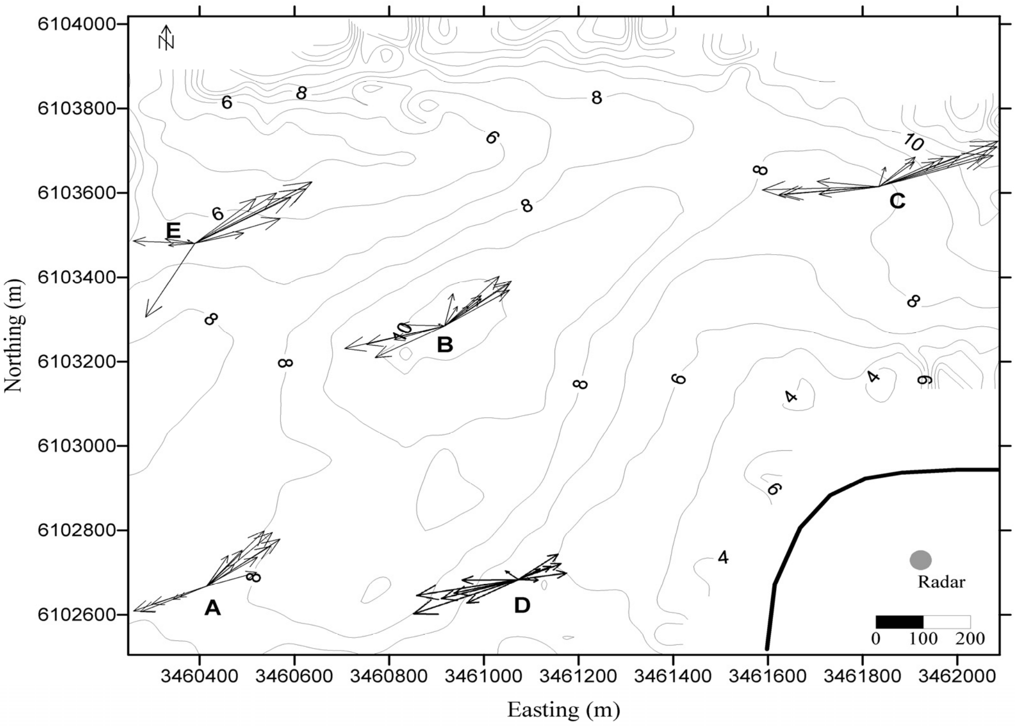


**Figure 4.8-12. Tidal current roses for a tidal cycle at five selected points in the Lister Land Tief Inlet. Arrow lengths represent the DiSC current velocities during normal tidal conditions.**

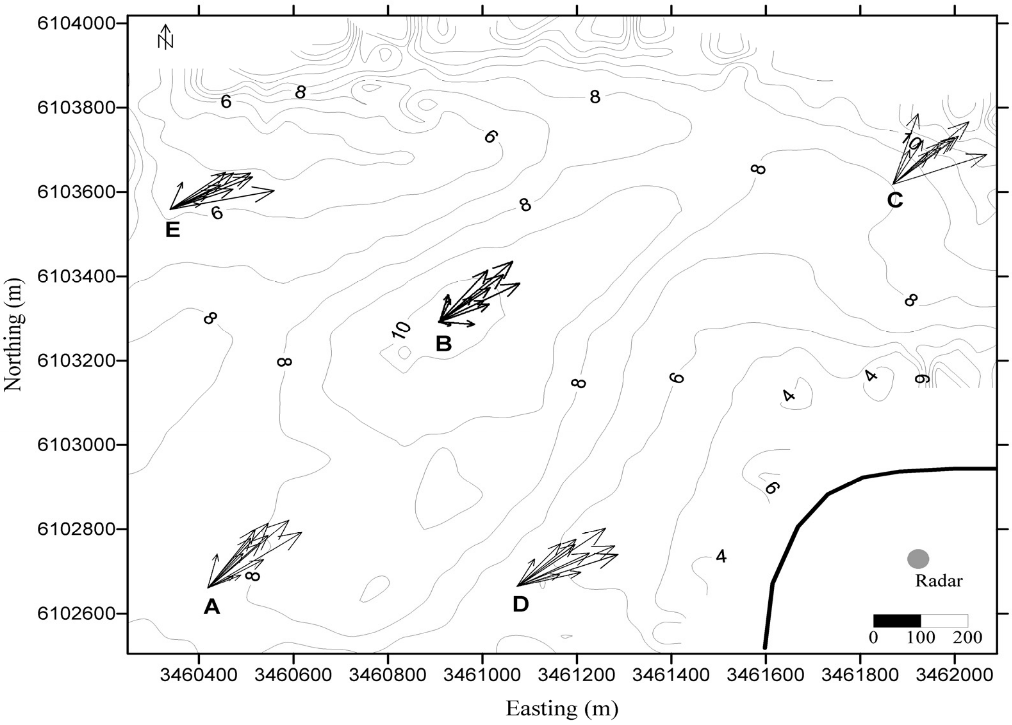


**Figure 4.8-13 Tidal current roses for a tidal cycle at five selected points in the Lister Land Tief Inlet. Arrow lengths represent the DiSC current velocities during the trespassing of the front.**

### *4.8.5 Discussion*

The main products of the present investigation are an estimation of the bathymetry during severe meteorological conditions and the effects of a low pressure on the water circulation in the coastal areas.

#### 4.8.5.1 Bathymetry

The estimated bathymetries, figures 4.8-7 and 4.8-8, illustrate the geomorphological features of the seabed and offer strong evidence for the mechanisms of sediment motion in the area of investigation during a storm. The area of results could be separated into three distinct sub-areas, near the shore (southeast), the channel and the shoaling (northwest), according to the basic geomorphological characteristics.

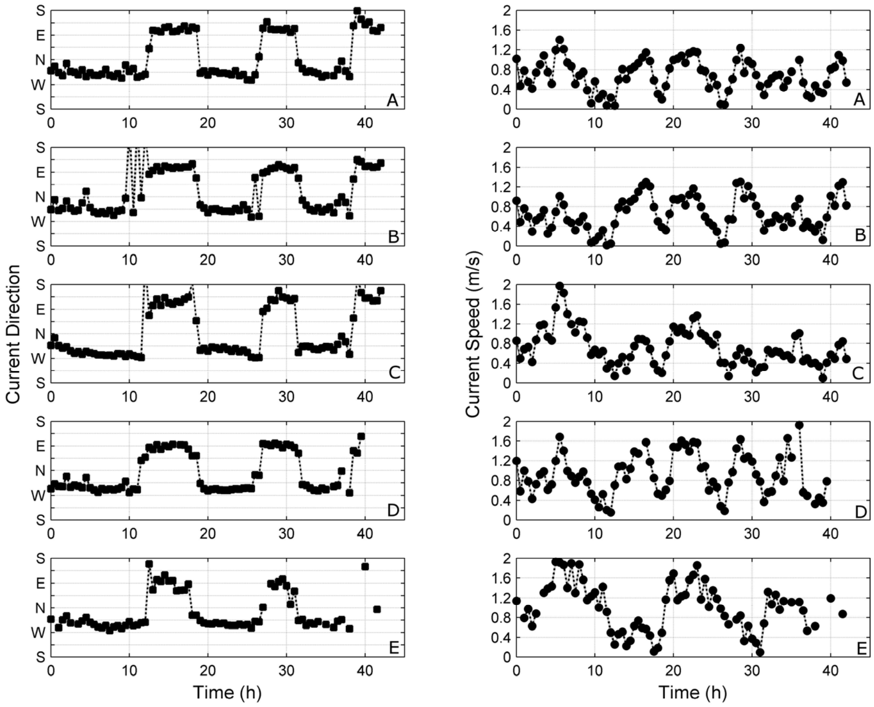


**Figure 4.8-14. Time series of the current direction and speed for the points A-E, see figure 4.8-12. At all points, for the first 13 hours only ebbing is observed.**

The minimum depth retrieved by DiSC is approximately 4 m, which is the limit of the method, due to the spatial resolution of the radar and the wave conditions; at its core is the linear dispersion relation, which is not a valid assumption over the shoalings. The area of investigation is on the eastern coast of the North Sea, where the fetch for the development of the waves is large enough for the creation and propagation of long waves, which have the additional effect of the wind during the storm. These waves, which indicate the bathymetric and current field information, break in shallow areas. This affects the microwave imaging of the waves and the assumed wave model is no longer applicable.

A comparison of the bathymetries between periods A and B (the first and the last phases of the 10-day storm) demonstrates that there is appreciable sediment accretion in the channel of approximately 0.5 m. More specifically, during period A, the spatial pattern of the depth is uniform and well formed. Whereas during period B, the influence of the storm is obvious; the bathymetry of the channel presents discontinuities and the isodepth patches in the channel are no longer uniform. The nearshore geomorphological structures have propagated from south to north as an effect of the dominant wind and wave conditions, which is most obvious at the northern part where the channel has narrowed.

The sources of accumulated sediment are probably the shallower areas in the south near to the shore and at the shoaling in the northwest, where there is erosion, exceeding in some cases 1 m, figure 4.8-9. The source of the sediment could not be from north of the area of investigation, because there is a second deep channel where the sediment has only accumulated. The quantity of the missing sediment is less than that deposited in the channel; hence it is assumed that the general sediment motion from south to north was boosted by the storm. Nearshore, on the northeastern side, the underwater spit embayed by the isoline at 7 m has been propagated during the storm and similarly the geomorphological feature on the northwestern side. In the west, during the first period there is a shoal (approximately 3 m depth), which was eroded approximately 2 m during the storm.

### 4.8.5.2 Current field

An important achievement of the present investigation is the acquisition of a spatial time series of the current field during storm conditions and its correlation with the air pressure forcing. The temporal resolution of the result is 30 min over 46 h with spatial 40 m and covers an area of 4 km$^2$.

The snapshot of the current field during the ebbing, figure 4.8-10, demonstrates the impact of the seabottom morphology on the current. The effect of the shoal in the northwest and the nearshore is to increase the current speed (as expected from the continuity) and also the circular water motion around it. It must be stressed here that the observation of this phenomenon is only possible due to the high resolution of the observation; even observations with half resolution (80 m) are not enough to demonstrate it, figure 4.8-10.

During the normal conditions of period C, after restoration of the normal tidal cycle, figure 4.8-12, and the period between, time steps 40 and 64 in figure 4.8-14 and figure 4.8-15, the strongest currents are in the shallow areas (points E and D) with a maximum speed 1.9 m/s and the speed is less with 1.2 m/s in the channel (points A and B). At the northeastern end of the channel (point C), where it is narrower, the maximum current speed is approximately 2 m/s and the minimum monitored 0.2 m/s during slack water. The effect of the depth on the current direction is determined; a characteristic example is south of the northwest shoal (point

E) where the current is parallelized by the geological structure. In the channel the current direction is the same as the orientation of the inlet. The flooding lasted 7 h and the ebbing 6 h; the current speed was higher during ebbing.

During the trespassing of the low air pressure system, period C, figure 4.8-13 and the period between the 1$^{st}$ and the 13$^{th}$ hours (time steps 1 and 25) in figures 4.8-14 and 4.8-15, the current field was monitored; the flooding lasted 13 h. During the period of the missing ebbing, the current velocity is low, approximately 0.5 m/s, which agrees with the water level measurements. During all the other periods, the current speed had similar variations under normal conditions. The maximum speed depends on the position of the measurement and varies between 1.2 m/s and 2 m/s, which was observed close to the shoaling (points A and E) and the minimum was in the channel. The directional spread of the velocity was maximum 70 degrees, but the mean direction depended on the location. A comparison of the water levels, figure 4.8-6, with the DiSC results has proved the identification of the tidal period; variability of the current speed during the whole observation period does not exceed the 0.25 m/s from time step to time step. During the abnormal conditions, the variability of the current speed correlates with a conflict between the normal tide and the impact of the low pressure. In addition, the wind stress seems to have an impact on the variability of the current speed, e.g. the increase of wind speed during time steps 8-11 (4 h-6 h), caused a peak of the current speed in time step 14. Similarly, a variation in the wind direction influences the current vector in time steps 70 to 75. Local variability in the wind field will not affect the vertically integrated current values that are calculated by DiSC.

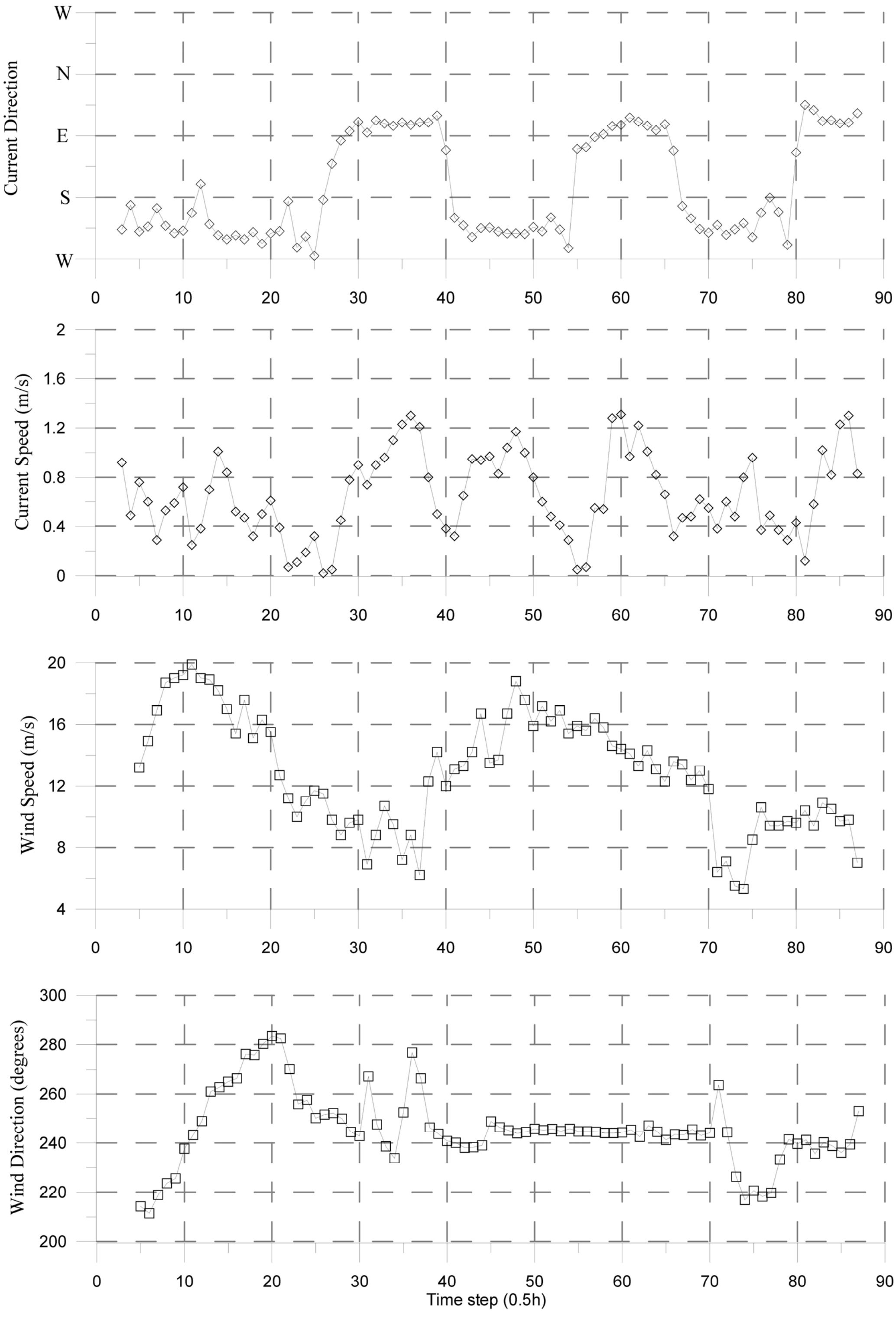


**Figure 4.8-15. Time series of the current vector at point B and of the wind vector at the radar mast.**

### 4.8.6 Conclusions

This part of the study achieves a bathymetric and current field monitoring of a coastal area during storm conditions, with high resolution in time and in space, by making observations using a ground-based X-band nautical radar and applying the Dispersive Surface Classificator; a spatial survey that is almost impossible to obtain with typical in-situ measurements.

The bathymetric survey proved the impact of the severe meteorological conditions on the sediment dynamics in the tidal inlets. The 10 days of storm caused the movement of 5-10% of the annual sediment budget for the area. The observation of the current field illustrates the local current features are caused mainly by the bathymetry and probably the local wind vector. In addition, this is the first time that the "inverted barometer" effect on the current field of the coastal area has been observed as a time series.

The two phenomena, and their combination, the variability of sediment dynamics and the non-monitored effect of the air pressure and the local bathymetry on the current field, proved that modeling assumptions, such as an invariable bathymetric grid and neglecting the direct air pressure gradient, could negatively affect the comprehension, description and results of hydro- and sediment- dynamic modeling in the littoral zone.

# CHAPTER 5

# 5 Monitoring of the littoral wave field propagation

The whole of chapter 4 provides concrete proof of the need for a precise mathematical description of the wave field in the littoral zone. It also proved that the inverse application of a valid wave theory, in combination with field data, can provide accurate bathymetry and current field observations. In addition, knowledge of the mechanism of wave field propagation contributes to coastal protection and integrated management. In this context, that of monitoring with a horizontally polarized and dopplerized X-band radar of the propagating wave field in the littoral zone over an uneven sea bottom, its transformation and wave breaking are presented in the current chapter.

## 5.1 Microwave radar imaging of the ocean surface

In chapter 3, the principles of microwave imaging of the sea surface were summarized. In the following two paragraphs, the literature about a normalized radar cross-section and Doppler velocity observations of the wave field under low grazing angles is reviewed. It is known that the four properties of the radar system and its installation, radar frequency, polarization, grazing angle and resolution cell size, have significant impact on radar measurements, due to their interconnections and influence on imaging of the sea surface under different oceanographic conditions. In this investigation, the radar operation frequency was set to X-band, the polarization to horizontal and the resolution cell size is known; the radar measurements took place under LGA and the radar cross-section was calibrated, but mainly the Doppler information is used. For this reason, the literature review focuses on studies with coherent radars, horizontally polarized and imaging at a low grazing angle.

### *5.1.1 Literature review of microwave imaging of sea waves at low grazing angle (LGA)*

This section reviews the research on sea-surface monitoring with dopplerized, C, X and Ku (4-18 GHz) band radars with horizontal polarization and low grazing angles ($1^o$ -$10^o$); the exceptions to this are mentioned. Pidgeon (1968) performed a series of nearshore experiments where the Doppler characteristics of radar sea return were measured. The horizontal polarization Doppler shift is dependent on the wave height and the wind velocity together, on the angle between the wind and wave direction and the radar propagation direction and is directly related to the motion of the surface layer of the sea. The mean Doppler shift of the radar sea return for horizontal polarization is approximately twice as high as the Doppler shift for vertical polarization for the same or similar wind and wave conditions; the same ratio of velocities calculated from horizontal and vertical polarizations have been reported by Stevens et al. (1999); similar results occurred for Valenzuela and Laing (1970), who modified the composite surface theory for LGA. Kalmykov and Pustovoytenko (1976) observed at low grazing incidence that a significant portion of the backscatter of horizontally polarized energy is produced by the crests of the ocean waves and explained a scattering model including a combination of composite surface and wedge scattering; details for the wedge model by Lyzenga et al. (1983). Moreover, for horizontal polarization, relatively stable backscatter signals, called bursts, are observed on top of the signals scattered by the capillary waves. The most significant results towards the end of 1970s are summarized by Valenzuela (1978a), Valenzuela (1978b) and Hasselmann et al. (1978).

The littoral observations of Lewis and Olin (1980) with X-band and simultaneously with video cameras, boosted microwave remote sensing in the surf zone, due to the fact that they described the spikes of the sea clutter and correlated them with whitecaps during stormy conditions and also with wave breaking. Those initial observations and their conceptual models have had a great impact on ongoing research. A characteristic of the spikes is the large decorrelation time (of the order of seconds) when compared to that of typical radar scatter (a few milliseconds), the same conclusion was reached also by Trizna (1991). At the time of the experimental setup both polarizations were used, the polarization ratio was unusually high, a fact that nowadays is accepted and observed many times, e.g. Frasier et al. (1998), Liu et al. (1998). They explained their results by assuming that the surface of the broken wave advects with the underlying water of the wave to be electromagnetically very rough, due to droplets and foam. This explanation is supported by the results of Ericson et al. (1999) and Coakley et al. (2001) who studied the presence of turbulent disturbances on the rolling surface of a stationary breaking wave and their relation with radar backscatter. Melief et al. (2006) analyzed coherent radar sea clutter data, which were compared with radar sea clutter models, by examining the power, polarization and velocity of the sea clutter. It was shown that these quantities, especially the velocity, are good measures of many physical properties of the ocean surface, wave breaking and steepening, jet formation and disruption. Furthermore, it was shown that these physical properties match well with sea clutter models. Sea clutter is found to consist of two components, a diffuse background, characterized by low values of backscattered power, HH/VV polarization ratio and Doppler velocity, and a number of spiking events, which possess higher power, polarization ratio and velocity. The background is reasonably well modeled by tilt-modulated Bragg scattering, whereas the spikes may be associated with the scattering on steepened and/or breaking waves. Moreover, it is shown that the influence of microbreakers has to be taken into account to explain the relatively high polarization ratio.

One of the first efforts to simulate the Doppler spectral characteristics of radar sea scatter for low grazing angles, based on the two-scale model for radar scatter, was made from Trizna (1985). The model failed for horizontal polarization, but he examines the impact of the Bragg scatterers, of the orbital velocity, the Stokes drift currents and the wind drift on the Doppler spectra, by expanding the conceptual model of Pidgeon (1968) and of Mel'nichuk and Chernilrov (1971). A similar approach was taken by Savchenko (1988), assuming that the Doppler spectrum can be achieved by using the simplest trochoidal profile, permitted the successful evaluation of the sea wave parameters as monitored by an X-band radar with horizontal polarization.

Lee et al. (1995b) presented data from backscattering experiments at microwave frequencies conducted off the west coast of Scotland in the summer of 1991. Using a dual-polarization X-band coherent scatterometer, time-resolved backscattering from ocean waves at a range of grazing angles was measured. In their results the dependency of the Doppler spectra to the grazing angle is defined. Peak separation between vertical and horizontal polarizations was resolved, the separation was more discreet at low grazing angles ($6^{o}$) and the identification of Bragg scattering from non-Bragg scattering was possible. Non-Bragg scattering is dominant in providing returns for the horizontal polarization; the same features of Doppler spectra were also observed and modeled by Plant (1997). The spiking events were once more observed and were related to the breaking events, but not uniquely.

Based on the same data, Lee et al. (1995a), investigated the issue of scattering mechanisms by studying the lineshapes of the backscattered microwave power spectra. It was found that spectral lineshapes can be decomposed into physically meaningful basis functions that are Gaussian, Lorentzian or Voigtian and this approach was expanded to breaking waves Lee et al. (1998a) and Lee et al. (1998b); Walker (2000) developed a similar model, but based only on the Gaussian distribution for each of the modeled phenomena. In addition it was proven that the breaking waves provide the major contribution to non-Bragg backscatter; the Doppler frequency of those scatterers is less than the fundamental wave phase speed, Lee et al. (1996). Lee et al. (1999) summarized their overall conclusions from the already mentioned studies; at small grazing angles the non-Bragg scattering is due to the fast scatterers generated by the wave breaking, and with increasing wave steepness and surface roughness; in this case the mechanisms of multiple scattering and multi-path interference become increasingly important. Applying the same concept, Caponi et al. (1999) developed a relatively simple model; the radar module computes the backscattering as an accumulation of Bragg response from every tilted facet of the reconstructed surface, except for those locations where hydrodynamic conditions leading to wave breaking are detected, where it was assumed that backscattering occurs in a quasi-specular, polarization-independent fashion. The simulated Doppler spectra reproduced the peak separation phenomenon observed in field measurements at very low-grazing angles and also showed a behavior similar to the field data when the grazing angle is increased and the range-versus-time intensity reproduced the observed polarimetric characteristics.

This series of convincing studies by Lee motivated several groups to conduct experiments in wave tanks with LGA, different types of wave breakers, with or without foam or wind; and subsequently to model the backscatter mechanisms. The results of the tank experiments demonstrated mainly features that had already observed in previous investigations, spikes, shift of the Doppler peaks between horizontal and vertical polarization. For truth on the ground, optical imagery has been used in most cases. The main contribution of these experiments was made to further clarify the backscatter mechanisms, Fuchs et al. (1999), Sletten et al. (1996), Sletten and Wu (1996), Dano et al. (2001b), Dano et al. (2001a), Ericson et al. (1999), Walker et al. (1996), Plant et al. (1999), Sletten et al. (2003), Lamont-Smith et al. (2007), Hwang et al. (2008b) and Hwang et al. (2008a). Dano et al. (2001a; Dano et al. (2001b) focus on spilling and plunging breakers over a range of incidence and azimuth angles using several different radar systems, the backscatter mechanism was assumed specular. Fuchs et al. (1999) also studied LGA backscattering from laboratory plunging breakers using simultaneous radar and optical imaging systems. Sletten et al. (2003) demonstrated that for the spilling breaker, over 90% of the horizontally polarized radar backscatter is generated during the initial stages of breaking by a small bulge near the wave crest. The Doppler velocity associated with this energy is very close to that of the phase speed of the dominant wave in the water wave packet. For the plunging breaker, the initial feature on the crest generates a lower percentage of the total backscattered energy. For the spilling breaker, the agreement between the experimental and numerical results is good, particularly in the Doppler domain. The model was based on the multi-path approach. The plunging breakers have also been studied numerically; West (2002) isolated the crest regions of the waves to remove large-scale multiple back-reflection paths to avoid interference with the breakers, but still the horizontally polarized backscatter significantly exceeds that of vertical polarization.

Lamont-Smith et al. (2007) carried out a number of experiments in two large wave tanks with three different radar systems. The radar frequency, grazing angle, azimuth angle, water wavelength, wave steepness and the breaking wave strength were all varied systematically. The velocity of the peak Doppler power spectral density was found to depend on the phase velocity of the breaking wave in the radar line of sight, but was independent of the radar frequency. The spectral width depended on the phase velocity of the wave, but not on the grazing angle used; this is one of a few studies that focus on the spectral width. The azimuthal dependency is discussed extensively by Lamont-Smith (2008). The contribution of the wave breakers to the radar sea return remains an open question under continuing investigation. Analysis of the field data collected, covering wind speeds from 7 to 15 m/s, grazing angles from 1.4$^o$ to 5.5$^o$ and different levels of background swell influence, found that the breaking effects increase significantly to the Doppler velocity of both polarizations (about 50% faster), enhancing the horizontally polarized backscattering cross-section drastically (with a 10–15 dB increase), but producing only a relatively small change to the vertically polarized cross-section (about a 1–2 dB increase), Hwang et al. (2008b).

### *5.1.2 Nearshore hydrodynamics by coast based Doppler radars*

In 1995, the Focused Phased Array Imaging Radar, FOPAIR, was presented by McIntosh et al. (1995). The radar system provides high-resolution X-band images of the ocean surface and is designed to provide high-speed imagery for short range applications (up to 400 m). As it is vertically polarized, the observations from this system are not comparable with those of present investigation, but it has been used in several experiments from shore with impressive results in different subjects: calculation of directional wave spectra, Frasier and McIntosh (1995), the study of sea spikes, Liu et al. (1998) and Frasier et al. (1998) and the monitoring of the hydrodynamics in the littoral zone, Puleo et al. (2003), Farquharson et al. (2004) and Farquharson et al. (2005). The impact of the wind on the FOPAIR measurements is presented by Moller et al. (2000). Those investigations have strongly influenced thinking about the observation of the nearshore zone by ground based coherent radars. The first results of FOPAIR motivated McGregor et al. (1998), who used a shore-based microwave S-band Doppler radar for the remote sensing of ocean wave propagation over an offshore sand bar. The spatial variation in wave phase with distance along the radar beam direction was used to calculate bathymetry with sufficient accuracy. The tidal cycle variation of water depth and the real-time bathymetry permitted the calculation of ocean wave energy fluxes from the radar velocity data. Those two experimental setups are similar to the experiment presented in this study. Allan et al. (1999) presented one of the first applications of Doppler velocities on the velocity alterations due to the trespassing of an oceanic front, with differences of the velocity in the order of 0.5 m/s. This study extensively discussed several technical details about the analysis and the interpretation of the Doppler data. On the interpretation of Doppler velocities at LGA, Stevens et al. (1999) tried to separate the non-linear features in the wave-resolving microwave radar observations of ocean waves. Their measuring device was an S-band radar. By combining observations with modeling they separated the wave signal from the non-linearity caused by shadowing and also by hydrodynamic modulations, such as tilt modulation, wave breaking and intrinsic wave non-linearity. They also improved the wave height spectrum estimation.

Plant et al. (2005) demonstrated the measurement of river surface currents with several coherent microwave radars, among the systems was a pulsed, dual polarized, Doppler radar called RiverRad, which was used to measure river surface currents from a riverbank. In all cases, the basis for microwave measurement of surface current is the Doppler shift induced in the signal backscattered from the rough water surface. Microwave measurements have been compared with conventional measurements of near-surface currents and found to be accurate to within about 10 cm/s. This publication provided motivation for two further studies. For the first the same radar system was utilized for microwave data collection from the surf zone; the data was for determination of the breakers' characteristics and the development of a composite theory for the backscatter mechanism of breakers, Catalán et al. (2008). The second investigation was implemented by Braun et al. (2008) with a dopplerized X-band nautical radar; in these experiments from a moving ship and shore in a wave-sheltered tidal inlet during low and moderate wind conditions, the focus of the study was on the measurement of the current field. The method, called Radar Doppler Current Profiler, RDCP, was extended by the use of second radar with the same characteristics and provided the full vector of the current surface field, Cysewski et al. (2008).

### *5.1.3 Summary*

Despite 50 years of research there are still open questions about the interaction of electromagnetic microwaves with the sea surface. The basic backscatter mechanism for a high grazing angle is known and extensively investigated, but this is invalid at low grazing angles. The complexity of sea clutter at LGA is derived from its geometrical characteristics and the governing hydrodynamics of the sea surface. The sea echo is characterized by intense spikes in time and space, which are related mainly to the wave breaking and the actual wind and wave conditions. The existence of so many different influencing factors has not permitted an aggregate explanation of the phenomenon, each of the many investigations focus on one specific factor. Therefore, even though all this knowledge exists, there are very few studies of the coastal zone based on dopplerized microwave X-band monitoring. This study focuses on the development of empirical, integrated methods for the quantitative observation of the sea surface hydrodynamics (mean velocity, sea surface waves and wave breakers) in the coastal zone based on the combination of patches of existing knowledge and new methodological achievements.

## 5.2 Experimental Setup

In the first experiments on the littoral wave field observations by Doppler X-band radar, the choice of an area of investigation was an important step. It is known that the bed relief impacts the, already complex, nearshore hydrodynamics, which has a direct impact on the electromagnetic imaging of the sea surface, e.g. Hennings and Herbers (2006). Therefore to reduce the impact of the bathymetry, the west coast of Sylt, close to Ellenbogenberg, was chosen, due to the almost constant slope of the sea bottom, figure 5.2-1, and because it is the highest dune at northern end of Sylt.

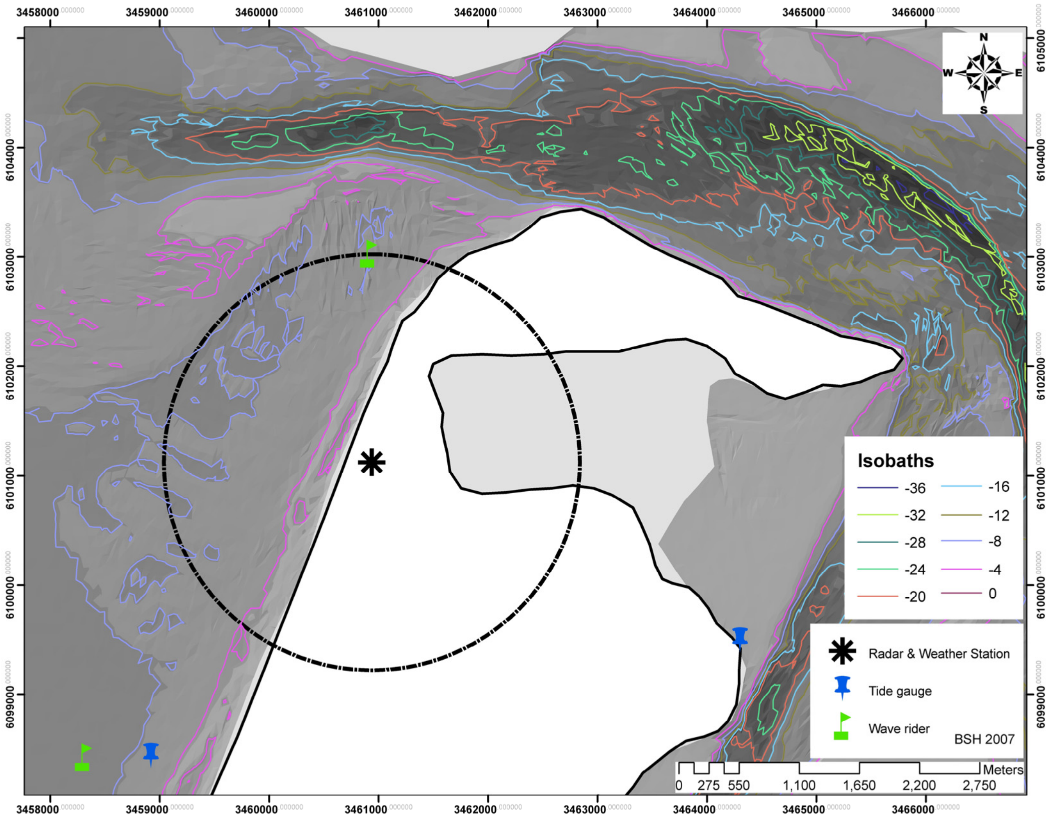


**Figure 5.2-1. Area of investigation and experimental setup. The black star marks the position of the radar (see Figure 5.2-3), the two blue pins the positions of the tidal gauges and the green flags the positions of the wave buoys. The two sensors on the west side of Sylt are moored a few kilometers to the south. The black circle illustrates the area covered by the radar.**

For this part of the investigation, only one radial direction, 265° with respect to the north, is used; the cross section of the bathymetry (based on BSH data) is illustrated in figure 5.2-3.

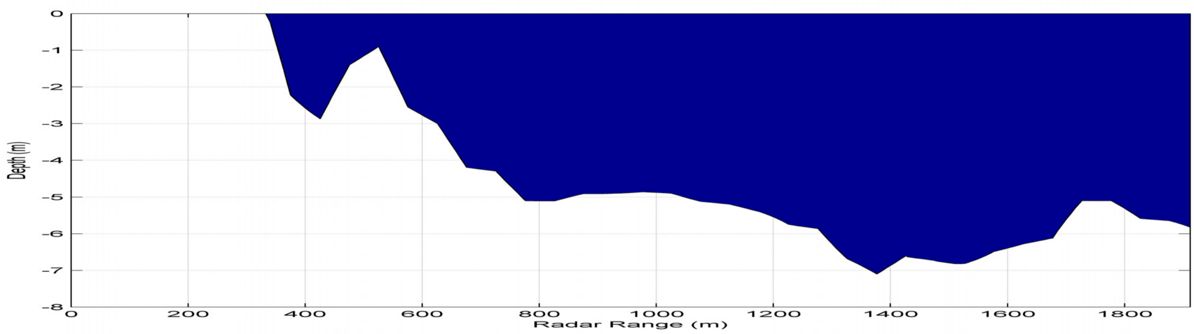


**Figure 5.2-2. Bathymetric cross-section. The 0 m distance corresponds to the radar position and the cross-section is taken facing 265° with respect to north. Data source: BSH, May 2008.**

Due to the impact of the local bathymetry on the wave field, the range has been divided into ten regions; the length of each of them is 150 m, table 5-1. In all the 10 regions, there are local variations of the bathymetry. At regions R2 and R3, there is the main sand bar, where a permanent breaking zone exists. At R5-R6, there is the outer bar, where the wave energy begins to dissipate. Between these two regions, and between R8 and R9, there are two troughs. The separation into regions is used to focus on specific processes in the data interpretation, sections 5.4 and 5.5.

**Table 5-1. The 10 regions that the radar imaging area has been subdivided.**

| Identifier | R1 | R2 | R3 | R4 | R5 |
|---|---|---|---|---|---|
| Distance from the radar(m) | 405-555 | 555-705 | 705-855 | 855-1005 | 1005-1155 |
| Identifier | R6 | R7 | R8 | R9 | R10 |
| Distance from the radar(m) | 1155-1305 | 1305-1455 | 1455-1605 | 1605-1755 | 1755-1905 |

Nevertheless, the complexity of the natural environment requires synergetic monitoring by several systems. In this case, a dopplerized X-band radar, two wave riders, two tidal gauges and a weather station on the radar mast are used. During the experiment, all the measurements were almost synchronous and the data were transmitted to the field operations center in real time. The field station is hosted in an almost operationally autonomous trailer, which is equipped with solar panels, generator and accumulators for a continuous, uninterruptible power supply, figure 5.2-3.

The experiment was conducted during the winters of 2008 and 2009. During the field campaigns several problems occurred. The reasons were that the station itself, as a hardware combination, was a part of the experiment and it was the first time that this setup was used. Due to modifications the radar is a prototype, which had problems due to its technical immaturity. In addition, the severe meteorological conditions had a direct impact on the six different measuring devices and/or their connections to the field station. For this reason, a set of only four days of data, taken February 1-4, 2008, is used for this thesis. In the following paragraph, only details about the radar and the recorded data are presented. For details about the rest of the instrumentation setup see section 4.2.

**Figure 5.2-3. Photograph of the field station and the radar mast, on top of the Ellenbogenberg dune. The radar is mounted approximately 34 m above the NN.**

### *5.2.1 Radar*

The basic instrument is an X-band, single polarized (horizontal transmitting-horizontal receiving) radar, with an antenna length of 5 ft, which was developed based on a commercial nautical radar by a cooperation between GKSS and the Electrotechnical University of St. Petersburg in Russia, Ziemer (2002).

The wavelength of the electromagnetic signal is $\lambda_{rad} = 3cm$. The main modification of the nautical system was making the transmitter–receiver module coherent to detect Doppler frequency shifts in 254 cells (7.5 m each, thus the theoretical range of radar is 1905 m) along a radial beam. A dual-channel linear amplifier, a dual-channel analog/digital (A/D) converter block, and a control unit to trigger the transmitter, steer the antenna, and transfer the data to the computer were added to the basic instrument. The diagram in figure 5.2-4 illustrates the components of the radar system. The radar was operated with a pulse repetition frequency (PRF) of 1000 Hz. The system is controlled by a PC software interface, which triggers the control unit and receives and stores the digitized complex radar signal.

Detection of the phase of the transmitted signal allows detection of the phase shift of the received signal. The two intermediate amplifiers IF1 and IF2 provide a high-resolution conversion of the signal separated for the near and far ranges. The transmitted electromagnetic pulse produced by a magnetron does not fulfill the demanded frequency stability. Therefore, an intended leakage of the transmitter signal is guided through a circulator and an IF amplifier. By triggering the A/D converter early enough, the leakage of the transmitter signal is passed through 60 MHz IF frequency amplifiers and can be stored as initial values in the series of range bins of the received signal. The phase shift is detected between the stored mirror of the transmitted pulse and the string of the received signal bins. The frequency stability of the IF amplifier guarantees the demand for stability. The hardware and the software are designed to enable a permanent registration of the signal. Thus, the only limiting quantity is the size of the hard disk on which the data are stored and the memory of the computational system for the data analysis, Braun et al. (2008).

The position, the height and the view direction of the radar antenna are determined by a differential global positioning system, DGPS. The radar is mounted on a 16 m mast on the top of a sand dune that is 18 m above NN, so the position of the antenna is 34 m above NN. The exact position of the radar in global coordinates is 3460939 m easting and 6101123 m northing in the Gauss–Krüger coordinate system. The grazing incidence angle varies between $1^{o}$ and $5^{o}$, depending on the distance from the radar; therefore the radar measurement is considered as a low grazing angle measurement.

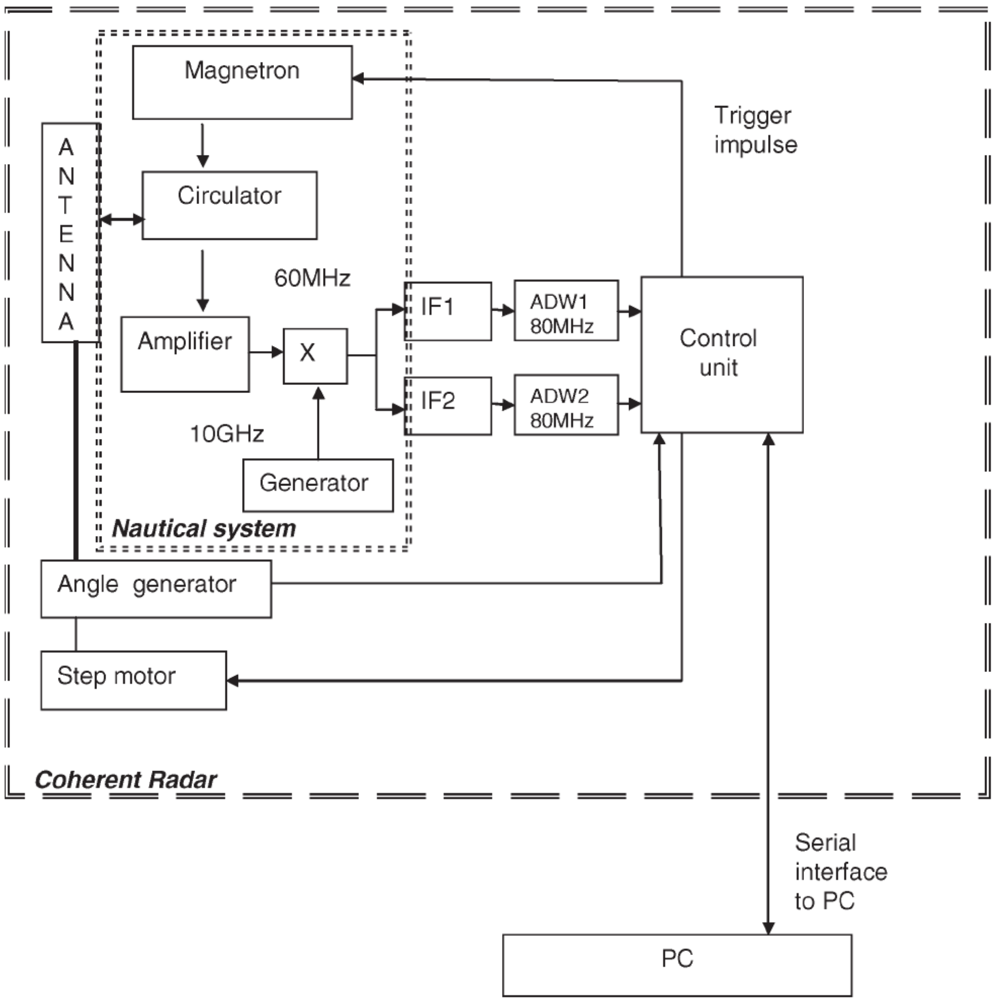


**Figure 5.2-4. Diagram of the Dopplerized radar. The magnetron unit of the nautical system was retained. To record the phase of the transmitted signal, this was A/D converted and stored before the received signal was converted and stored, Braun et al. 2008.**

Throughout the experiment the statistical parameters (significant wave height, peak wave direction and the peak spread, of the wave field at the two points) were transmitted in real time. Based on the recorded wave direction of both wave riders and knowledge of the local bathymetry, the radar antenna was steered against the wave propagation direction and three cross-sections of backscattered radar power in the arc of the directional spread of the wave field were obtained. Each of the beams lasts approximately 10 min. The data are delivered in terms of received power for two different channels and were converted into normalized radar cross-sections, $\sigma_0$, paragraph 5.4.1. In addition, the two channels are combined for the calculation of the Doppler shift, paragraph 5.4.2.

### *5.2.2 Response of radar data to low backscattered signal*

During the imaging of the wave field by the Doppler radar the combined effect of shadowing and storing of instrument noise when the signal is low influence the quality of radar data for oceanographic purposes. The imaging of the sea wave field by ground based X-band radar is a complex process. As described in section 3.4, it is considered there are four physical processes that modulate the RCS: shadowing, tilt modulation, hydrodynamic modulation and wind modulation. It is proven and commonly accepted that shadowing must be seriously included whenever the sea is viewed at grazing angles smaller than the RMS slope of the sea surface, Wetzel (1990b). Assuming that the geometrical optics are valid, there is a sharp transition between sea surface that is illuminated or not, in this investigation this concept is obscure, because the recorded data are continuous and there is not a well-defined power threshold for the shadowing.

At microwave frequencies, the noise the target echo signal competes with is usually generated within the receiver itself. It is generated by thermal agitation of the conduction electrons in the ohmic portion of the receiver input stages. As this is the first time that this specific radar system is used, the base level of noise in the data is examined. In addition, to clarify how it is recorded with a minimum effect from the sea state, a 5-minute radar dataset was acquired in February 20, 2009, during low wind conditions of 2-3 m/s and minimal swell. Figure 5.2-5 is a range-time-intensity (RTI) plot of the measurement, the intensity has a range dependent behavior, which is illustrated as lines parallel to the time axis and is time independent. That structure in the data is the result of the low reflected power and of the radar response. Therefore, the recorded time series represents mainly the noise of the instrument itself. The faint, diagonal lines in the figure are related to the propagation of scatterers towards the radar; the level of the signal of both of them is of the same order.

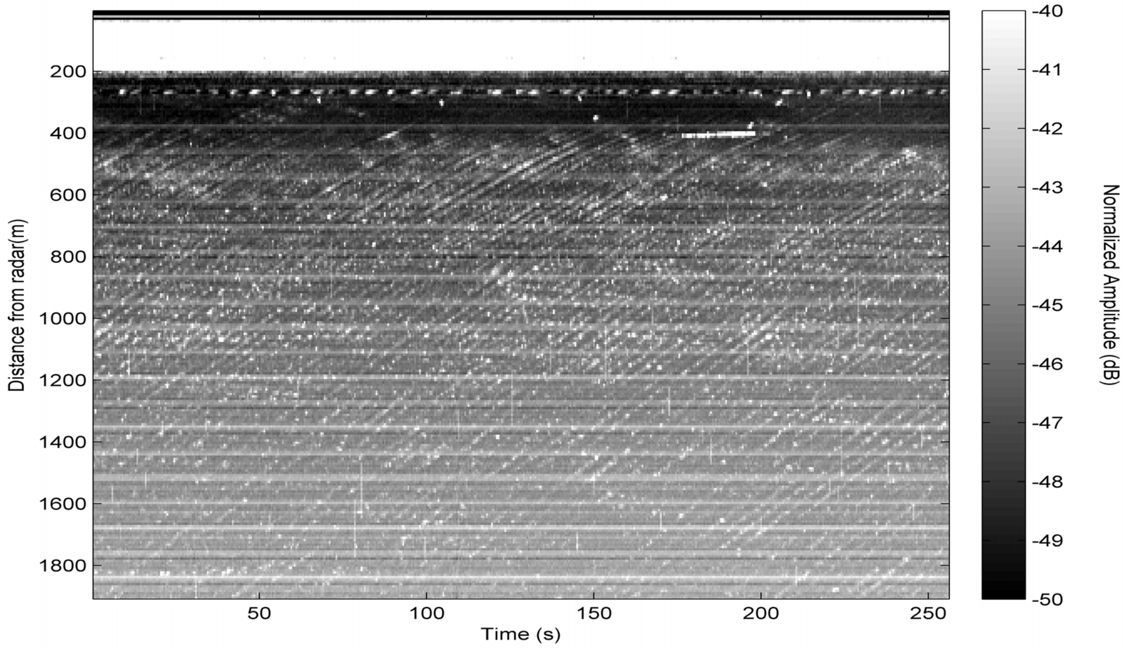


**Figure 5.2-5. Range-Time-Intensity plot. The data were acquired during low wind and low wave conditions. The time-independent lines are hardware artifacts that are excluded during the analysis.**

Under stormy conditions, the measured wave lengths vary between 60 m and 100 m and the measured wave period is maximum 12.5 s. The length of the radar footprint is 7.5 m, therefore under average experimental conditions approximately 10% of the main wave component is illuminated during 0.5 s. It has already been mentioned that the grazing angle of sea surface monitoring varied between 1 and 5 degrees. This has a direct impact on the imaged wave. For a representative wave with the experimental conditions of $L = 100m$ and $H = 2m$, approximately the 50% of the wave is illuminated with a 5° grazing angle and only 20% with a 2° grazing angle; the rest is shadowed, figure 5.2-6.

The hardware-induced structures in the data exist when the level of the signal is low, therefore, even during a storm the recorded signal has this behavior in the shadowed areas; in the time series of the raw data, this appears as zero values in the complex signal. The frequency of the low is close to the Nyquist frequency and they generate many harmonic peaks, therefore extremely high values of the Doppler velocity are calculated. To avoid the interference of the combined effect, two different methodologies are presented for their separation in section 5.4.5.

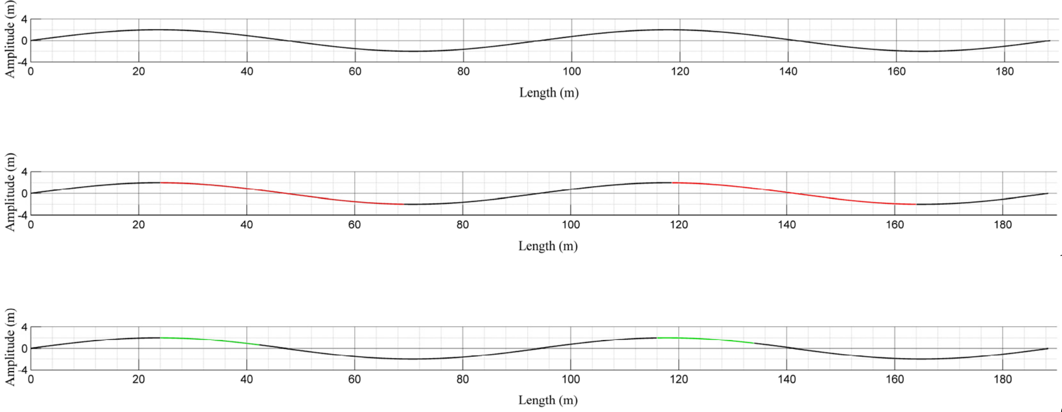

a
b
c

**Figure 5.2-6. Microwave imaging of a sea surface wave with $L = 100m$ and $H = 2m$ for 3 different grazing angles: a. $\theta_g = 90^o$ the whole wave is imaged; b. $\theta_g = 5^o$ only the red area is imaged and $\theta_g = 2^o$ only the green area is imaged.**

## 5.3 Oceanographic conditions

During the experiment, the wind conditions varied between 8 m/s and 22 m/s and the wind direction varied between SW and NW, figure 5.3-1. Data acquisition started during the severest wind conditions, therefore it is considered that the wave field during the experiment was fully developed. The maximum recorded value of significant wave height was approximately 3 m for the nearshore wave rider, which is an extreme value at that position. The wave direction was mainly western, during the lower wind conditions on February 3. The tide direction modifies the recorded wave direction, therefore the data from the offshore wave buoy are used. The significant wave height varied between 0.8 m and 3 m, figure 5.3-2.

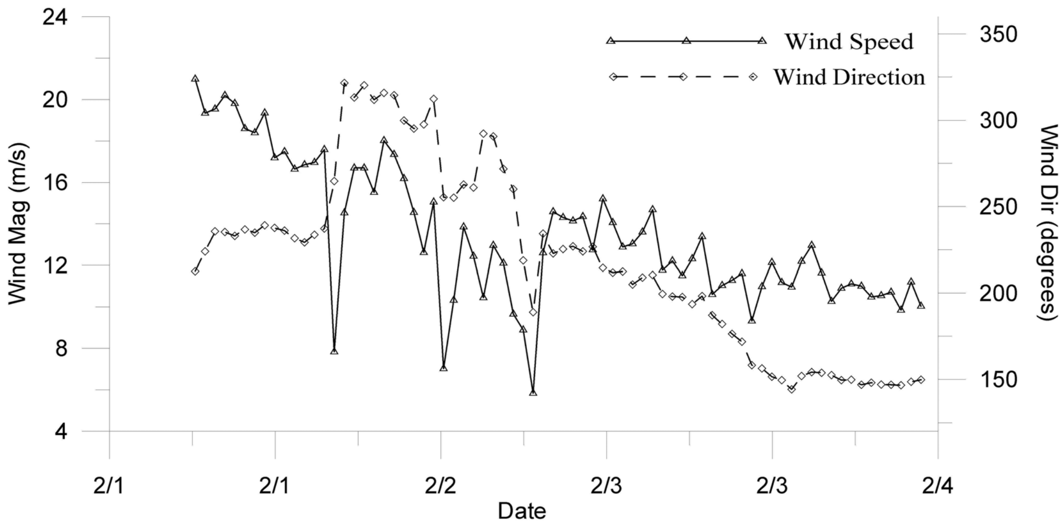


**Figure 5.3-1. Hourly wind speed averaged over 10 minutes and direction during the radar data acquisition of the field experiment.**

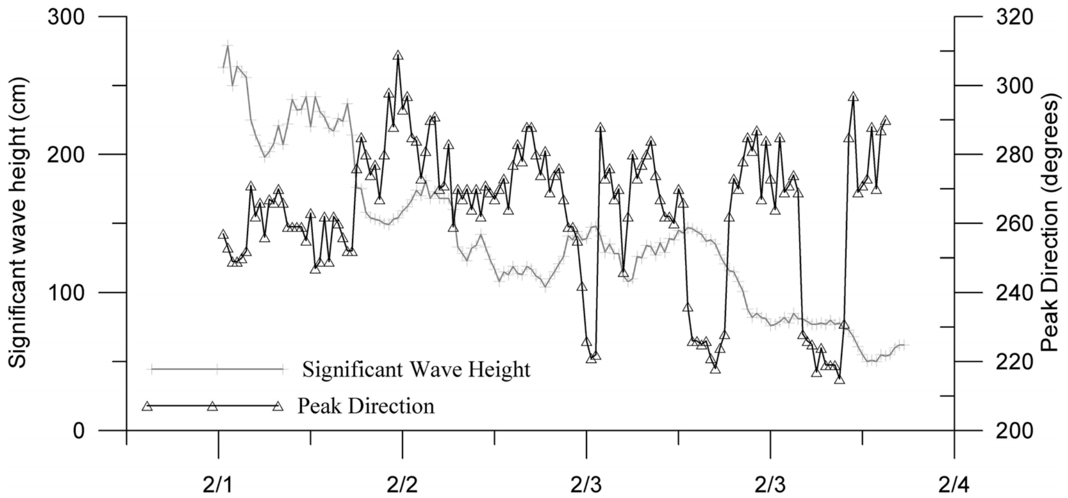


**Figure 5.3-2. Significant wave height and wave peak direction by the wave rider in the area of radar range during radar data acquisition, impacted by the bathymetry under low tide conditions.**

During the experiment, the tidal period was approximately 12.5 h and the tidal range approximately 2 m, figure. 5.5-3. An impressive characteristic of the tidal record is that the absolute difference between the recorded maximum and minimum for the three days is 3.5 m, which is an extreme value.

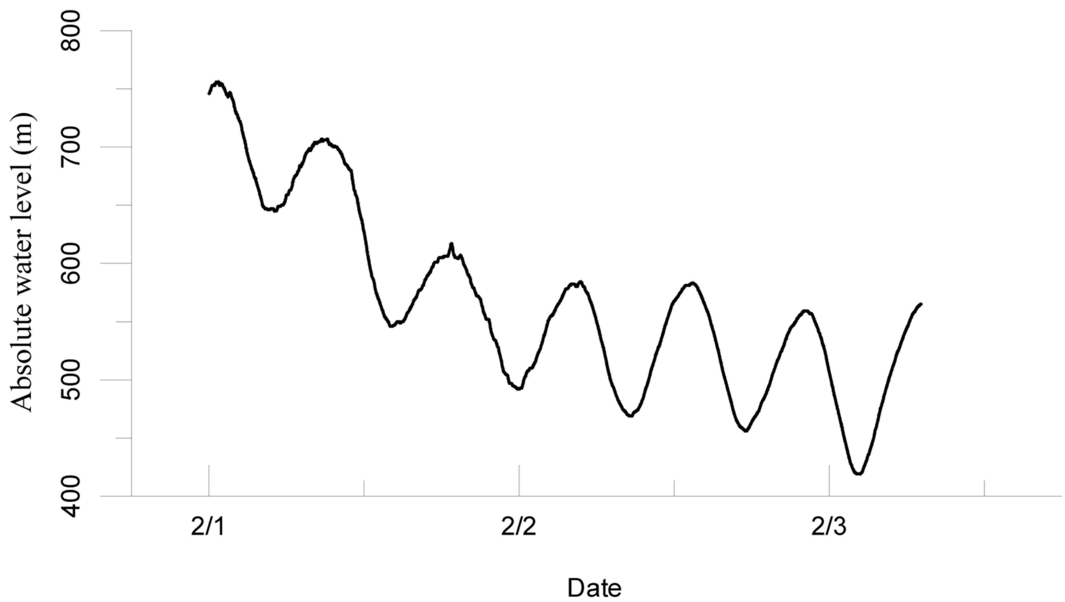


**Figure 5.3-3. The tide signal from the tidal gauge in Westerland, 9 nm to the south, the time shift was calculated by the astronomic tidal prediction.**

## 5.4 Radar data processing

Due to the complexity of the monitored phenomena and the radar data themselves, a series of algorithms, selection and separation filters were established and applied to solve problems related to the quality of the data and to enable the extraction of useful oceanographic information. The current section includes the main algorithms that were developed and applied to the data. Analysis of the radar data is a complicated multi-stage process. In this investigation, the Normalized Radar Cross Section is calculated, the time series of the Doppler velocities for the whole range of the radar is analyzed and the average in time of Doppler velocities is calculated, figure 5.4-1.

### *5.4.1 Calculation of the Normalized Radar Cross Section*

The received signal of a marine radar system is delivered in terms of an uncalibrated intensity scale; this parameter is inappropriate for the determination of a relation between the radar intensity and the Doppler velocities as a function of distance and the local bathymetry, because the acquired quantity is not normalized and also not comparable with data recorded under different conditions and settings. In addition, the internal components of the radar

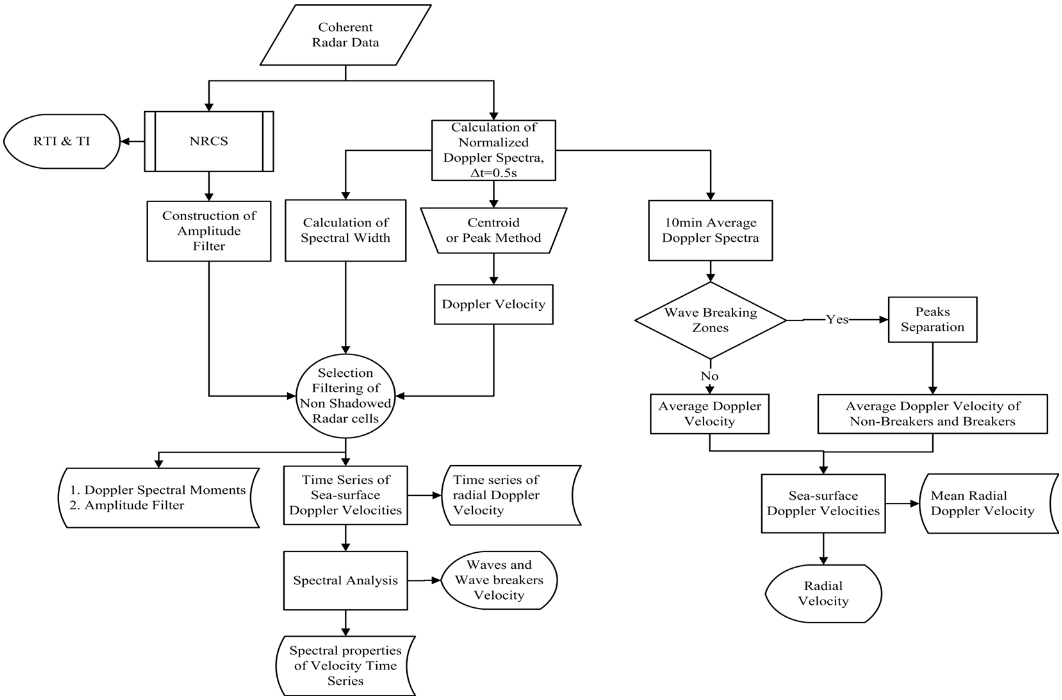


**Figure 5.4-1. Flowchart of coherent radar data processing. This is an extended version of the right branch of the flowchart in figure 1.6-1. The NRCS and the Doppler velocity of the sea surface are analyzed with the goal of monitoring the actual sea state.**

(circulator, amplifier, mixer, control unit) impact the performance of the system, as it includes system dependent parameters such as losses and amplification characteristics. Therefore, it is essential to perform a calibration of the transfer function between the received intensity index and the actual received power at the antenna, Gommenginger et al. (2000).For the calculation of normalized radar cross sections, the method of direct etalon is applied. The fundamental concept of the method is a comparison of the backscattered power of each object in range with the backscattered power obtained from a target with a known radar cross-section. An application of the method is not normally used in nautical radars, because they are constructed to detect the position of objects and not their cross section. In this case, to avoid multi-scattering of the ground, the positions of the reflector have been set in the shadowed areas behind the coastal sand dunes; therefore the backscattered signal is clear and direct.

In section 3, the radar equation (3.1) was given and based on this, the normalized radar cross section is calculated: $\sigma_0$, the ratio of the scattered power to the incident power, defines the surface backscatter coefficient for a unit area of sea surface; this is taken as a measure of the sea surface roughness. This allows a comparison between the pixels. Therefore, the data have been calibrated with reflectors of known reflectivity per unit area, $\sigma_r$, and at known distance from the radar $R_r$. For the normalization, two assumptions are taken into account.

The first is that the gain $G_t$ can be approximated to the maximum antenna gain:

$$G_t = G \tag{5.1}$$

The effective aperture $A_e$ represents the performance of the antenna in reception. The antenna's effective aperture is related to the maximum gain of the antenna by:

$$A_e = \frac{G\lambda_{rad}^2}{4\pi} \tag{5.2}$$

Where $\lambda_{rad}$ is the wavelength of the radar radiation (m). Thus, replacing (5.1) and (5.2) in (3.1) leads to:

$$P_r = \frac{P_t G^2 \lambda^2}{(4\pi)^3} \times \frac{\sigma_r}{R_r^4} \tag{5.3}$$

The measured amplitude of the complex signal of the reflector $U_r = \sqrt{U_{\mathrm{Re}}^2 + U_{\mathrm{Im}}^2}$ is related with the received power through the relation:

$$P_r = \frac{U_r^2}{R_\Omega} \tag{5.4}$$

Where $R_\Omega$ is the resistance of the radar system. By replacing the equation (5.4) into (5.3)

$$U_r = \mathrm{K}\frac{\sqrt{\sigma_r}}{R_r^2} \tag{5.5}$$

Where $\mathrm{K} = \sqrt{\frac{P_t G^2 \lambda^2 R_\Omega}{(4\pi)^3}}$; all the actual values of the multiplicands are unknown, but the value of $\mathrm{K}$ is calculated from the equation (5.5) and the field data, acquired for calibration of the radar cross section.

For each grid cell ($i$), the equation (5.5) is valid, the calculation of the absolute radar cross section $\sigma_i$ is equal to:

$$\sigma_i = \frac{U_i^2 R_i^2}{K^2} \tag{5.6}$$

and the normalized radar cross section $\sigma_{0_i}$ for each grid cell ($i$), the area covered by one pulse, is given by

$$\sigma_{0_i} = \frac{\sigma_i}{S_i} \tag{5.7}$$

Where $S_i = 0.5\phi\left[R_i^2 - \left(R_i - \frac{\tau_p c_s}{2}\right)^2\right]$ (5.8)

$S_i$ is the radiated area without antenna height correction. Since the difference is in the order of centimeters, $\tau_p = 50ns$ is the pulse width, $\phi = 0.0192$ in radians is the width of the antenna diagram and $c_s$ is the speed of light in m/s.

### 5.4.2 *Reflector measurements*

During February 2009, a field campaign for calibration took place. A corner reflector with three square-plains was used, having a calculated radar cross-section of $100\,m^2$. Measurements were taken from two different points in the shadow region of the radar, table 5.2. It was not possible to define the reflection of point 1, therefore only point 2 was used for the calculation of K, by substitution in the equation (5.5) $K = 1142420$ Vm. The raw radar data of the reflector are illustrated in figure 5.4-1. In figure 5.4-2, the NRCS of the same dataset is presented. The red stars in both cases demonstrate the backscattered energy from the reflector. The theoretical value $\sigma_0$ of the reflector is 0 dB; in this case there is a slight deviation of approximately 3 dB.

**Table 5-2. Acquired data for the calculation of the calibration constant K.**

| | Easting Coordinate in GK (m) | Northing Coordinate in GK (m) | Height above MSL (m) | Distance from the radar (m) | Average amplitude (Rel. Un.) |
|---|---|---|---|---|---|
| Point 1 | 6101417 | 3460870 | 2 | 303.7 | Corrupted |
| Point 2 | 6100675 | 3460566 | 1.2 | 583.8 | 18700 |
| Radar | 6101123 | 3460939 | 34 | - | - |

This deviation probably derives from the conditions during field measurements, e.g. reflection also from the DGPS antenna. Nevertheless, this discrepancy lies within the technical range of variability and has a value that is expected from field measurements.

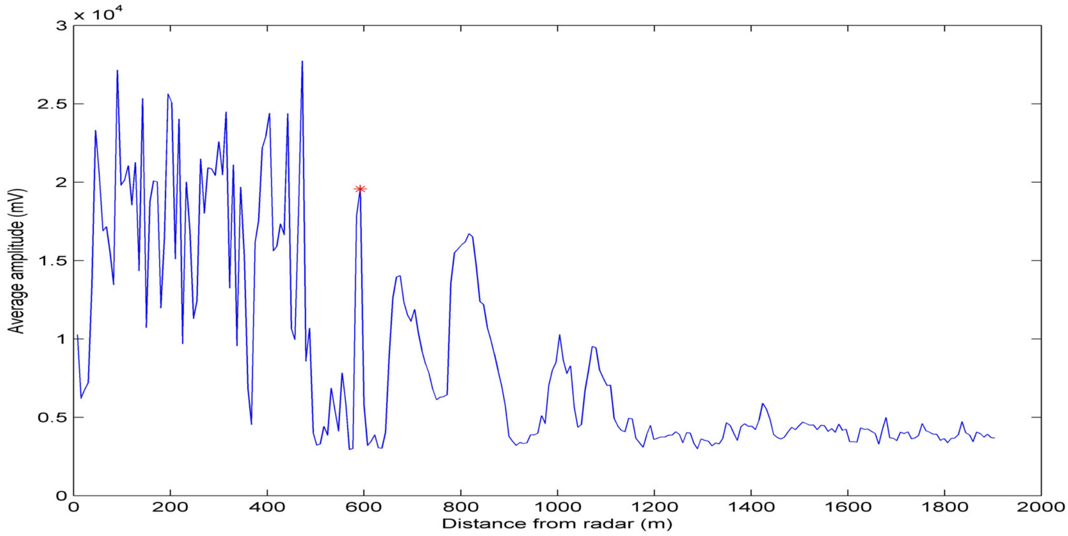


**Figure 5.4-2. Average radar cross section that are used for the calibration; the red star corresponds to the amplitude of the reflector.**

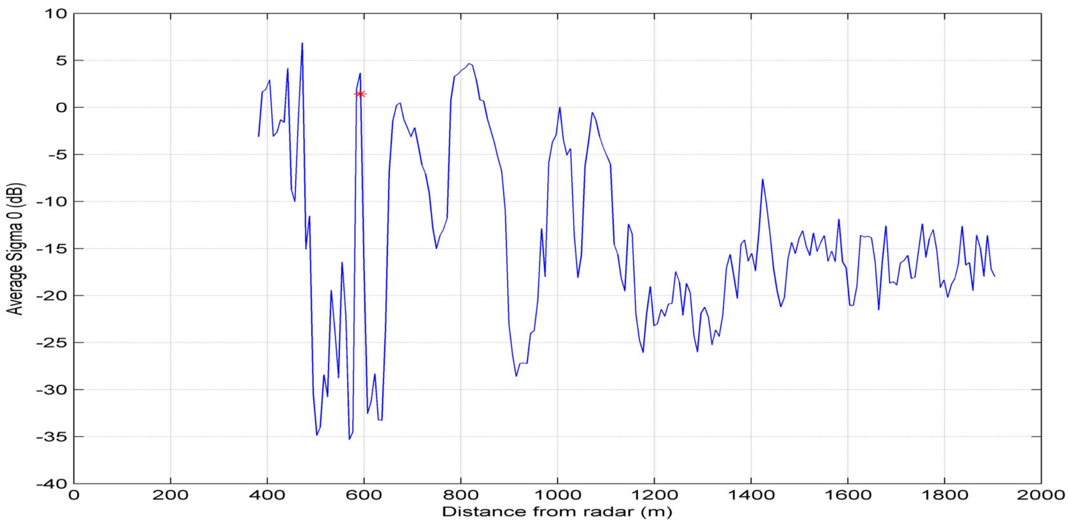


**Figure 5.4-3. Normalized radar cross-section of the same dataset as figure 5.4-2. The red star corresponds to the NRCS of the reflector and the expected theoretical value is 0 dB.**

### 5.4.3 Doppler velocity

The main advantage of coherent radar systems is the determination of the Doppler spectra. In this study it is calculated individually every 0.5 s as well as for the average Doppler spectrum over the whole duration of the measurement of 10 min. Many scatterers contribute to the Doppler measured in a radar pixel, producing a power weighted spectrum of Doppler velocities. The scattering-object velocity is obtained from the measured Doppler frequency given by

$$f_D = \frac{2}{\lambda}\cos\theta_g (u_w \pm u_c \pm u_{orb} \pm c_p) \qquad (5.9)$$

where $\lambda$ is the wavelength of the transmitted pulse, $\theta_g$ is the scatterometer local grazing angle, $u_w$, $u_c$, $u_{orb}$ and $c_p$ refer to wind drift, current velocity, orbital wave motion, Lee (1977), and the speed of the scattering object on the water surface, respectively. In this conceptual approximation, the surface tilt is ignored. The plus and minus signs refer to the contributions from approaching or receding scatterers, respectively, because in this case it is considered that all the scatterers approach the coast and the radar is mounted in fixed position. It is considered that the effect of the current velocity on the waves has been minimized from the experimental setup. Lange and Huehnerfuss (1978) have shown that a good approximation to the wind drift is 2.6-5.5% of the wind speed; Lee et al. (1995b) applied 3%, as it provided the best agreement to their data, in this case we take the same factor as Tomczak (1964), 4.1%, due to the fact that during his experiments the wind velocities were similar to the measurements of this investigation.

From the equation (5.9), the expected Doppler shift could be produced by four different possible scatterers, which are imaged as four different peaks. The variability of the natural system and background noise could produce complicated radar data without clear peaks corresponding to the monitored phenomena. Therefore, the methodology for the calculation of Doppler velocity always presents an open scientific question.

### 5.4.4 Calculation of the Doppler velocity

The fundamental idea behind the calculation of radial Doppler velocity, without examining the physical background, is summarized in the following equation:

$$v_r = \frac{\lambda_{rad}}{2\cos\theta_g} f_D \tag{5.10}$$

Therefore, the estimation of a representative Doppler frequency, $f_D$, for the ongoing phenomena is the main requirement. In general, this subject is not broadly discussed, because it is either assumed that several peaks of the Doppler spectra exist or it is a concealed detail of the data analysis or even, in a few cases, it is considered a trivial step in the analysis, because the authors invariantly use the same method in all their research.

A time series of Doppler velocities are formed by computing consecutive instantaneous Doppler shifts over a series of pulses, Allan et al. (1998). A number of techniques have been published for the computation of the Doppler frequency, including the finite difference instantaneous frequency estimator, McLaughlin et al. (1995); the covariance moment estimation technique, Frasier and McIntosh (1995) and Jessup et al. (1991); tracking the peak of the short-time Fourier transform, Ebuchi et al. (1993); tracking the peak of the cross Wigner-Ville time-frequency distribution, Allan et al. (1999); and applying Hilbert transformation on the each radar pulse and calculating the temporal derivative, e.g. Hwang et al. (2008b).

In this case, a similar methodology as Ebuchi et al. (1993) and as used by Braun et al. (2008), is applied. The Doppler frequency is estimated from the centroid of the Doppler spectrum $S_D(f)$ around the position of the peak frequency. The centroid is defined as:

$$f_D = \frac{\sum f S_D(f)}{\sum S_D(f)} \tag{5.11}$$

The physical meaning of the Doppler centroid is defined as the power weighted sum of the Doppler shifts of individual scatterers in a radar pixel. By substituting the Doppler frequency from the equation (5.11) to the equation (5.10), the Doppler velocity is calculated.

Radar data are complex values and from 262144 successive radar pulses, corresponding approximately to 256 s. For the calculation of the Doppler spectra, a Fast Fourier Transformation is applied on chunks of 512 radar pulses, each approximately 0.5 s. The frequency resolution of the resulting spectra is $\Delta f = 1.95 Hz$ and the Nyquist frequency is $f_{Nyq} = 512 Hz$. The Nyquist frequency corresponds to the velocity of 7.5 m/s with a bin size of 2.9 cm/s. In this case, because the radar is shore based and the waves propogate towards the coast, the velocity of the wave crests detected by the radar is only positive and the negative values correspond to aliased frequencies, therefore the Doppler spectra are unwrapped by simply moving the negative parts to the upper end of the spectrum.

In the first step of data analysis, the data are smoothed with a median filter with span of 8 bins, which does not affect the statistical properties of the spectra. In the next step, the signal to noise ratio is calculated for each frequency, in the case that the ratio is lower than 1.2, the spectral density is set equal to 0, figure 5.4-4. Based on the peak position of the spectrum and the centroid, the Doppler velocities are calculated; all the results are geocoded.

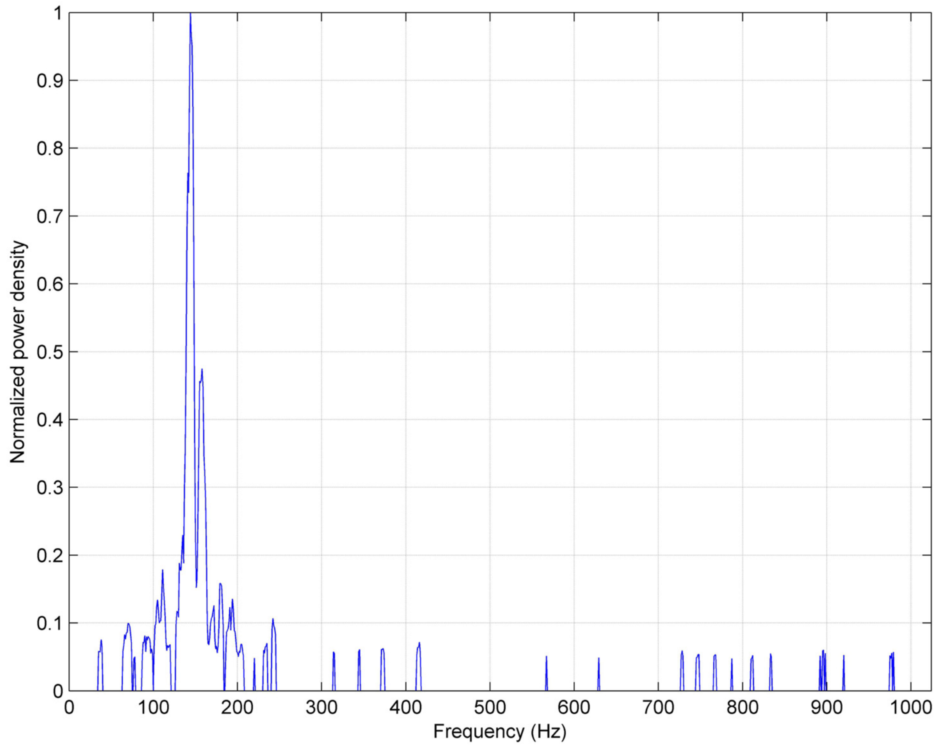


**Figure 5.4-4. Example of a normalized Doppler spectrum after smoothing and subtraction of noise.**

### *5.4.5 Selection filter of individual spectra*

Due to the effect of shadowing and the storing of the instrument noise in the time series of raw data, as was discussed in section 5.2.2, there are gaps in the recorded signal. The amplitude of these points is equal or tends to zero, figure 5.4-5; therefore higher harmonics exist in the resulting spectra, which outflank the frequency of the backscattered signal. To filter out these ambiguous velocities, two different methods were followed.

The first method is applied in the time domain. The number of naught signal values in each time chunk is counted and the chunks with more than 20% missing values are excluded and the FFT is applied to the remaining data.

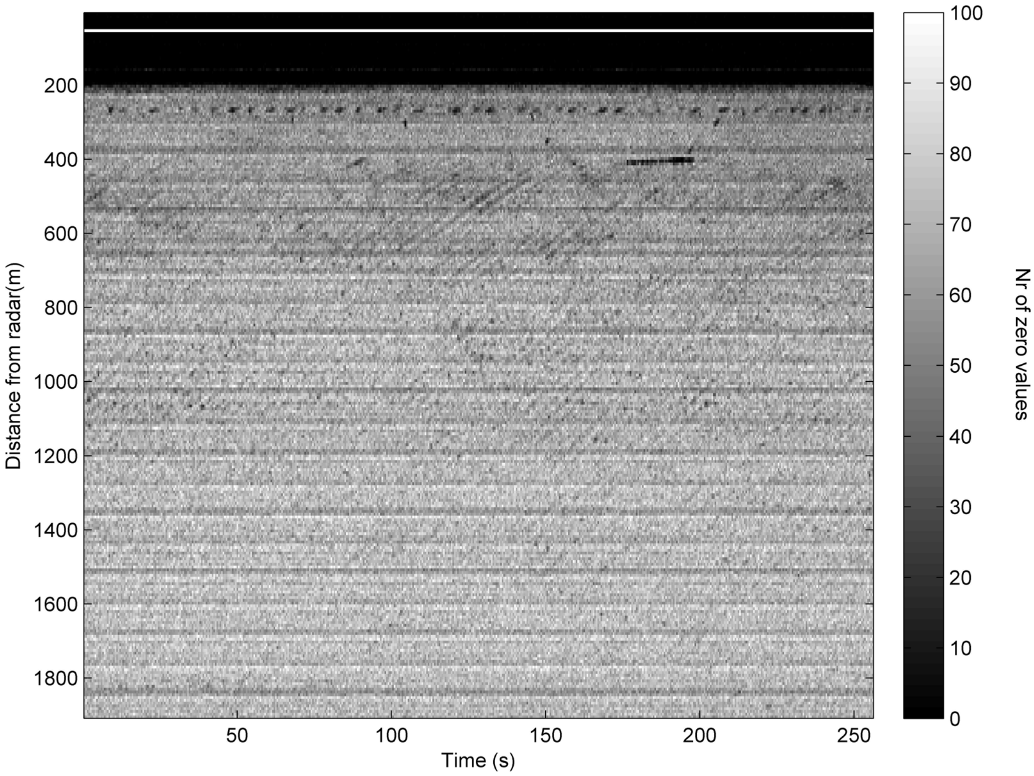


**Figure 5.4-5. The number of zeros in the same dataset with figure 5.2-5. The wind and wave conditions during this data acquisition are low.**

For the second approach, the filtering is performed in the frequency domain. The moments of the Doppler spectra are calculated and based on these the properties of the spectra are evaluated. The asymmetry is examined through the skewness, peakedness, kurtosis and the width of the spectra through several width indicators, which have been adapted for sea wave spectra studies, Prasada Rao (1988). The most robust are the following

$$qp = \frac{2\Sigma f S_D^2}{(\Sigma S_D)^2} \tag{5.12}$$

$$\varepsilon = \sqrt{\frac{\Sigma S_D \cdot \Sigma f^4 S_D - \Sigma f^2 S_D}{\Sigma S_D \cdot \Sigma f^4 S_D}} \tag{5.13}$$

In $qp$, the second moment is of the higher order that is utilized and at the $\varepsilon$ the fourth order. The use of the higher order significantly impacts the stability of the quantity as it takes into consideration the tail behavior of the spectrum, therefore $qp$ is used for the filtering of the data; the threshold is set to 0.3.

In figure 5.4-6, the performance of the filtering in the time domain and in the frequency domain is compared and the relation of the two quantities with the Doppler velocities is illustrated. The performance of the two strategies is almost identical and the influence of shadowing is increased with distance from the radar; therefore the numbers of available data is reduced, figure 5.4-7.

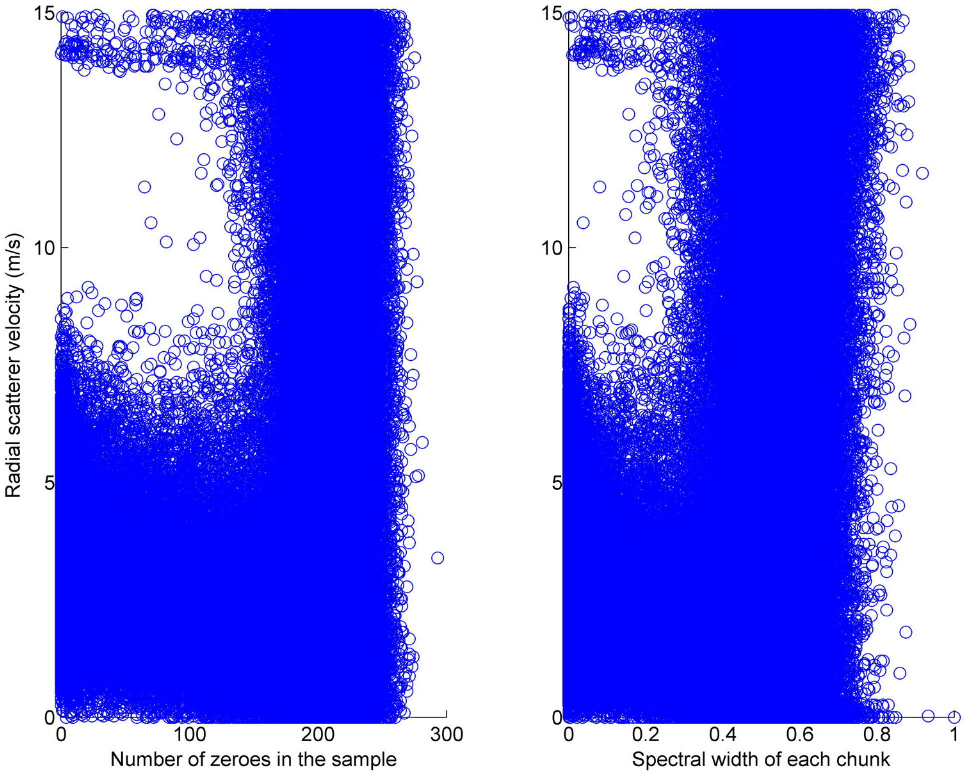


**Figure 5.4-6. Scatter plots of the numbers of missing values in the data (critical value 120) and of the spectral width criterion, qp, (critical value 0.35) as a function of the Doppler velocity. Both of these approaches have a similar performance.**

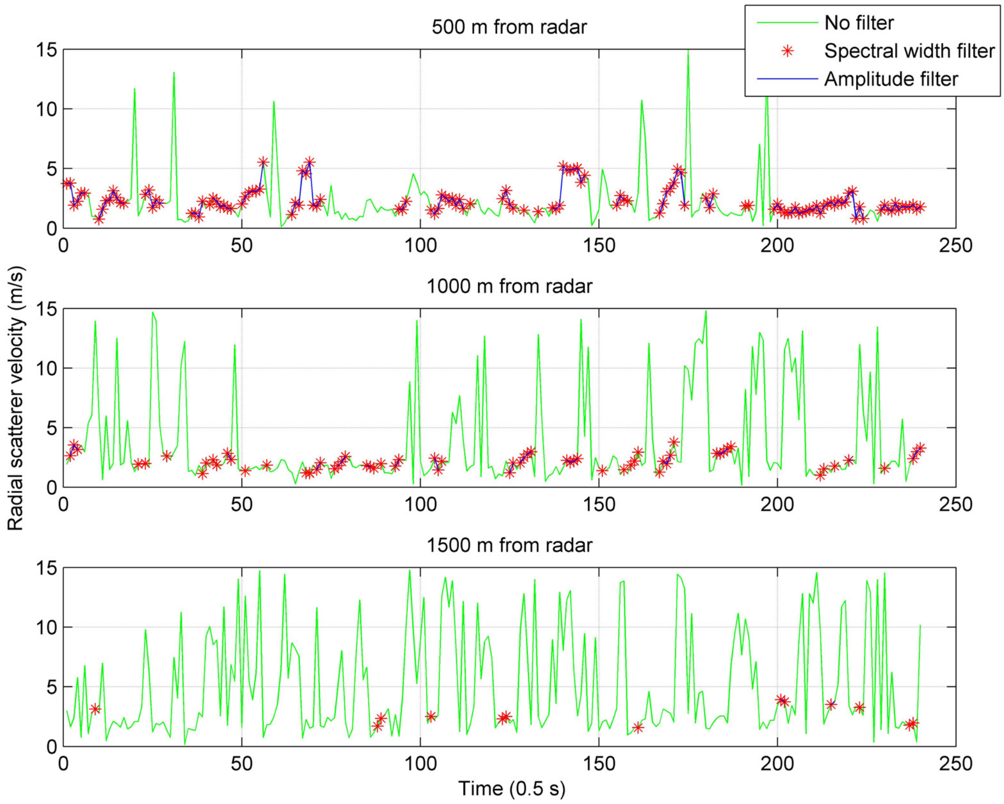


**Figure 5.4-7. Three 2-min intervals of consecutive 0.5 s radial scatterer velocity estimates, computed by tracking the peak of the each Doppler spectrum (the green line), the red stars and the blue line are the velocities filtered in by the spectral width (red stars) and the existence of values (blue line).**

### *5.4.6 Separation of multiple peaks in the Doppler spectra*

The Doppler spectra are the sum of the frequency shifts of different phenomena, equation 5.9. In case the two phenomena have velocities of a different order of magnitude, for instance in this study by waves and wave breakers, multiple peaks appear in the Doppler spectra. This is useful for the measurement of the radial velocity of each phenomenon and for their separation. In the literature review, section 5.1, it was mentioned that a determination of the wave breakers is possible by three different methods: the NRCS, the Doppler velocity and the polarization ratio, only the first two are applicable in this thesis. Therefore, the scientific task is to separate the velocities of breaking from non-breaking wave features, for this reason, a pyramid feature segmentation algorithm was applied.

A pyramid representation is a type of multi-scale signal representation. Figuratively speaking, the base of the pyramid is the original (with the highest resolution) signal and the top of the pyramid represents the coarsest signal. At each pyramid level, the resolution is decreased by a factor of two. Pyramids are calculated by successive application of smoothing and subsampling by a factor of two. The pyramid scheme applied in this study is a Gaussian, based on spectral low-pass filtering, Burt (1984). The steps of a Gaussian pyramid are as follows:

1. Smoothing the original signal, in this case with a median filter.
2. Subsampling of the smoothed signal by picking up every second value; the resulting second pyramid level has half the resolution of the original signal.
3. Repeating the two first steps n times, until that the peaks are clearly defined.

To calculate the Doppler velocities the same process as in section 5.4.4 is followed.

## 5.5 Sea waves backscattering in the littoral zone

Microwave scattering from a propagating wave field is an extended subject of investigation, both in the laboratory and the field. Previously the focus of researchers has mainly been on deep water waves. This is because of the complexity of the surf zone, where several different phenomena take place (wave field propagation, wave breaking, tide- and wave-generated currents), which cause complicated backscattering.

A few studies do focus on the littoral zone, Haller and Lyzenga (2003), Puleo et al. (2003), Farquharson et al. (2005), Catalán et al. (2008). The common problem in all of those experiments is determining the stages of wave breaking. The source of the problem is the lack of instrumentation providing ground truth. Video data, which is what is usually collected, have the problems that they only operate during daylight and detect only foam, the existence of which proves that a wave broke, but not the breaking of the actual wave; it is known that foam increases the backscattering. The use of in-situ devices is almost impossible, as the provided point measurements cannot reveal the ongoing spatial processes; however Farquharson et al. (2005) compared radar sea surface Doppler velocities with sea bottom based subsurface ADCP velocities.

Therefore, in this and the following sections, the investigation focuses on the separation of non-breaking and breaking waves, based on their backscattering characteristics, backscattered power and the Doppler characteristics of nearshore waves while they propagate, under different geophysical conditions. The algorithms described in the section 5.4 were applied to the data collected during the field experiment, section 5.2. The results of the analyses are presented, in particular the normalized radar cross sections, the Doppler velocity and their joint distributions and all these observations are interpreted with the use of in-situ measurements of wind, waves, currents and bathymetry. From the eighty available datasets, only four (from the six, the selection criterion is the antenna steering direction) were chosen to represent different wave conditions, the significant wave height in the illustrated cases ranges from 2 m to 5 m and the wave field propagates towards the shore. The wave propagation direction is from westerly ($260^{o}$ – $270^{o}$) and the radar is steered against this direction, table 5-3.

### *5.5.1 Radar images*

The series of figures 5.5-1 – 5.5-6 shows the range-time images (RTI) of a normalized radar cross section, $\sigma_0$, and the associated Doppler velocity, $v_r$, in the direction of wave propagation, the steering direction of the radar is known from the timestamp, in the title of each plot.

The position $r = 0\,\mathrm{m}$ is the base of the radar mast and $t = 0\,\mathrm{s}$ is the moment of the measurement start time, the grid cell has length $\Delta r = 7.5\,\mathrm{m}$ and the time step is $\Delta t = 0.5\,\mathrm{s}$; the definition of the axes is common for all the plots. The NRCS values vary from -60 dB to approximately -20 dB. The breaking zone starts at $r_{br_{HW}} = 650\,\mathrm{m}$, during high water and at $r_{br_{LW}} = 850\,\mathrm{m}$ during low water, where a sand reef exists. The remaining energy of the waves finally dissipated at $r_{br_{BCH}} = 450\,\mathrm{m}$, which is the shore. At the first breaking zone, the reflectivity from the sea surface increase to values above -35 dB and at the second above -20 dB. The large NRCS features are obvious at both breaking zones. The eliminated values (white color) correspond to the shadowed areas; the remaining values correspond to the wave crests. In addition, the area between the coast and the first breaking zone, it is less shadowed. This is due to the different grazing angle, the backscattering of the LGA, as has been proved several times, for a review Wetzel (1990a), for radars with HH polarization, the geometric shadow is a good approximation.

**Table 5-3. Summary of the wind and wave conditions measured during the radar data acquisition for the selected six datasets.**

| Date and time of data acquisition | Id. No. | Water level | Hs | Wave Dir. | $T_p$ | Wind speed $U_{10}$ |
|---|---|---|---|---|---|---|
| | | m | M | $^{o}$TN | s | m/s |
| 2/1/2008 13:34:58 | A245 | -1.1 | | | | |
| 2/1/2008 13:43:45 | A255 | -1.13 | 5 | 265 | 11.8 | 18.0 |
| 2/1/2008 13:52:31 | A265 | -1.13 | | | | |
| 2/1/2008 15:52:33 | B265 | -0.53 | 4.1 | 266 | 11.1 | 16.7 |
| 2/1/2008 21:52:33 | C265 | -0.15 | 2.9 | 268 | 11.1 | 14.3 |
| 2/3/2008 01:52:35 | D265 | -1.65 | 2.1 | 271 | 7.7 | 13.4 |

The range-time of the Doppler velocity images (RTV) show values spanning the full unwrapped velocity range from 0 m/s to 10 m/s; the positive Doppler velocities represent the motion of the sea surface towards the radar. The velocity, same as the NRCS, has a distinct structure, where the existing values correspond to wave crests and the missing values to the troughs. From those individual wave signatures, the celerity of the imaged waves is calculated based on a discrimination of the shadowed and non-shadowed areas, table 5-4; the non-shadowed areas correspond to the wave crests.

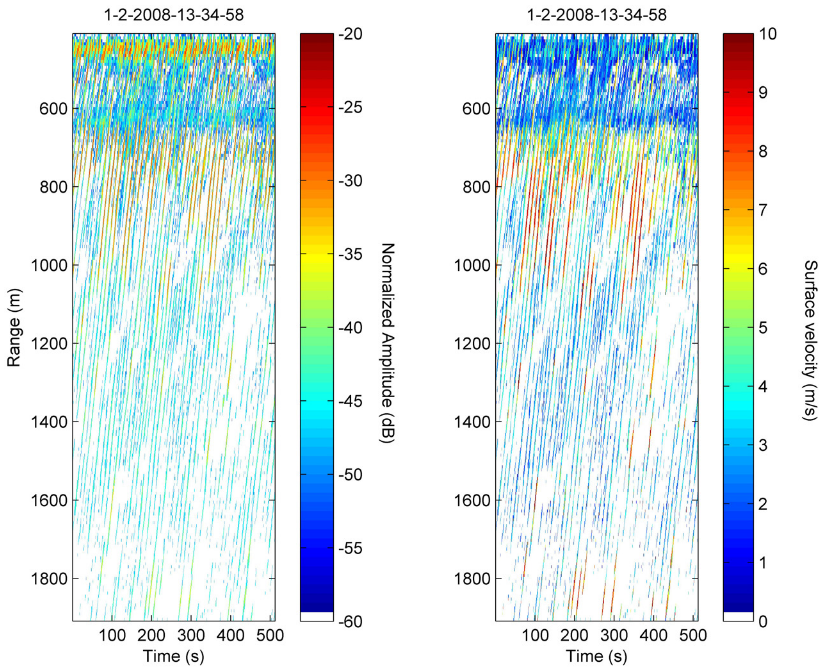


**Figure 5.5-1. Range-Time- Intensity and Range-Time- Doppler velocity plots of dataset A245 ($H_S$=5 m).**

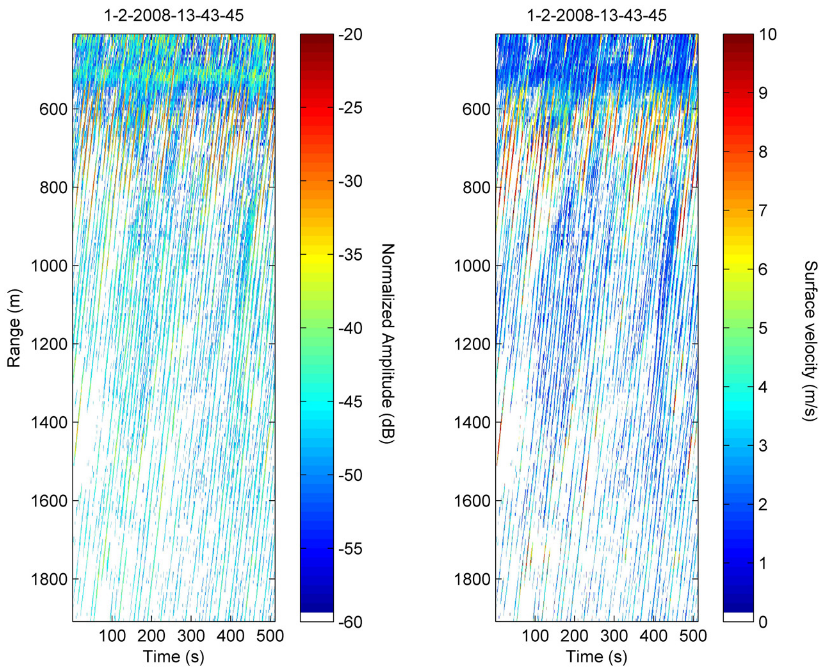


**Figure 5.5-2. Range-Time- Intensity and Range-Time- Doppler velocity plots of dataset A255 ($H_S$=5 m).**

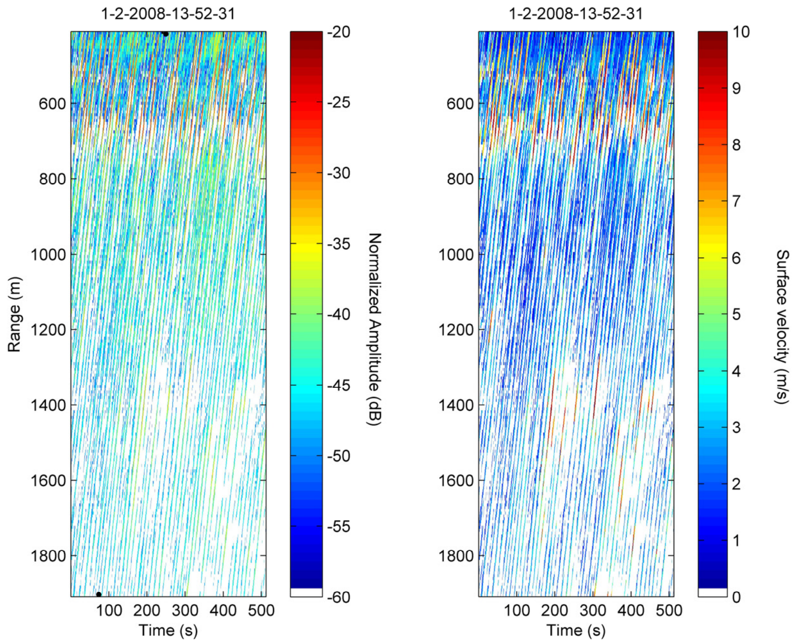


**Figure 5.5-3. Range-Time-Intensity and Range-Time-Doppler velocity plots of dataset A265 ($H_S$=5 m). The black dots illustrate the beginning and the end of the individual wave plotted in figure 5.5-7.**

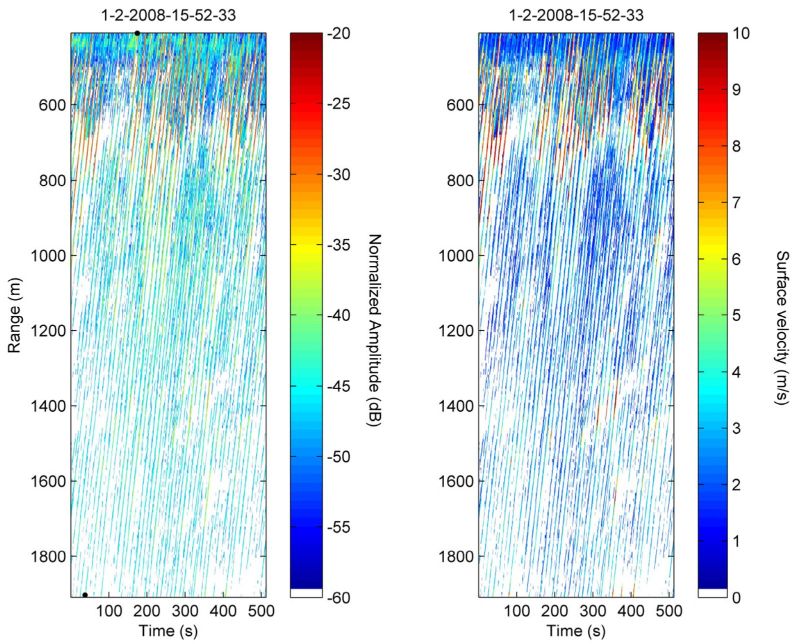


**Figure 5.5-4. Range-Time-Intensity and Range-Time-Doppler velocity plots of dataset B265 ($H_S$=4.1 m). The black dots illustrate the beginning and the end of the individual wave plotted in figure 5.5-8.**

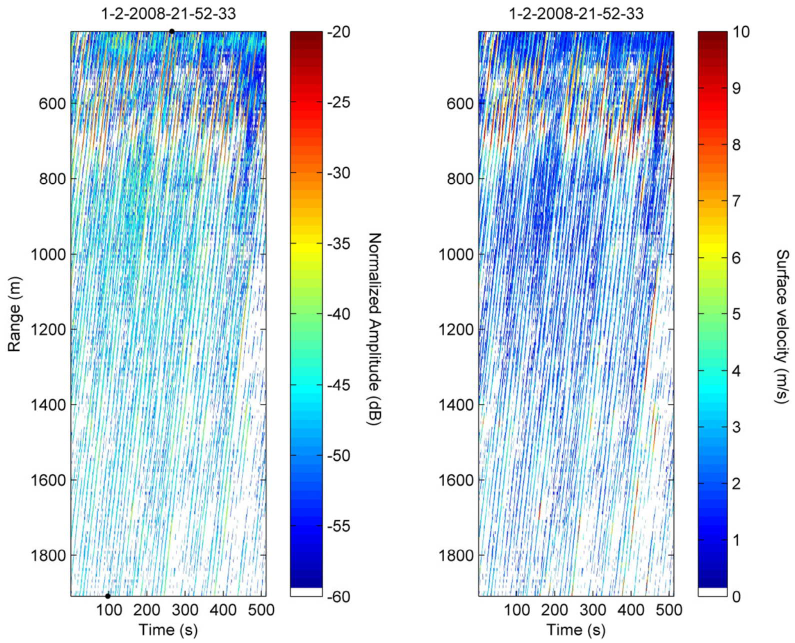


**Figure 5.5-5. Range-Time-Intensity and Range-Time-Doppler velocity plots of dataset C265 ($H_S$=2.9 m). The black dots illustrate the beginning and the end of the individual wave plotted in figure 5.5-9.**

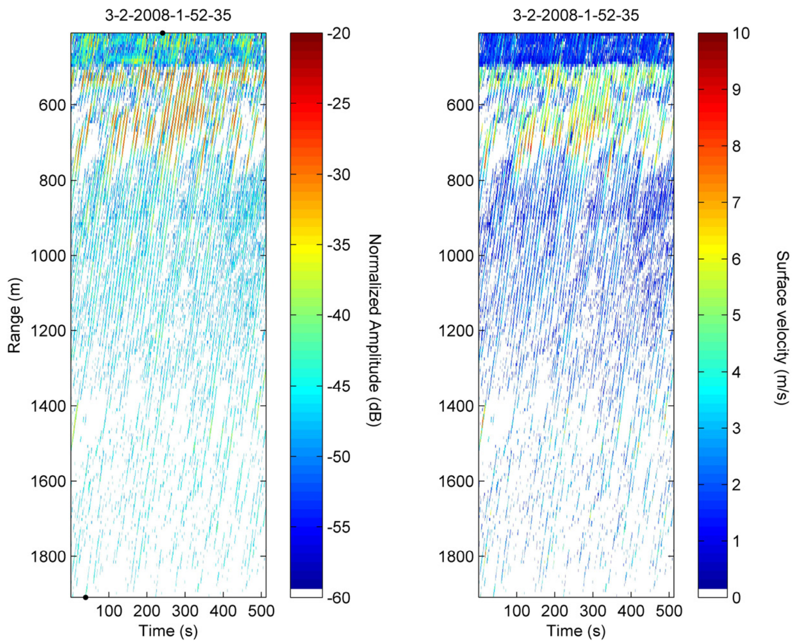


**Figure 5.5-6. Range-Time-Intensity and Range-Time-Doppler velocity plots of dataset D265 ($H_S$=2.1 m). The black dots illustrate the beginning and the end of the individual wave plotted in figure 5.5-10.**

For each line, the velocity is calculated by determining the position, in range and time, of the nearest and more distant non-shadowed radar cells; therefore a mean celerity for the whole radar range is calculated. The celerity extracted from the individual signatures depends, also, on the angle between the components of the celerity in the antenna's facing direction. This is proven from the set of samples of A, which covers an angle of $20^{o}$ and the difference between A245 and A265 is 0.8 m/s.

The celerity from the radar imaged structures and the open sea buoy measurements were compared. The difference between the two independent measurements is in the order of 0.5 m/s, except the case D265, $H_s = 2$ m, where the difference is higher than 1 m/s. There are two reasons for this discrepancy. The first source of error is because the radar beam can not be always perpendicular to the wave crest. The second source of error is the calculation of a mean value for the whole range; the wave signatures are tilted after the breaking zone, therefore the celerity is reduced; this is clearer in figure 5.5.3, where the wave height is about 5 m.

**Table 5-4. Comparison of the phase velocities calculated from the imaged wave crests and from the buoy measurements.**

| Id. No. | Phase velocity from scatterers m/s | Phase velocity from buoy m/s |
|---|---|---|
| A245 | 9.33 | 9.76 |
| A255 | 8.90 | 9.76 |
| A265 | 8.52 | 9.76 |
| B265 | 9.37 | 9.72 |
| C265 | 8.92 | 9.27 |
| D265 | 7.20 | 8.20 |

The RTI figures demonstrate the existence of high values (ranging between -40dB to -25dB) of the NRCS on the top of crests, at a random place and time. It is interesting to investigate the scattering characteristics according to the source, i.e. waves and breaking waves. It is known that the foam has an important role in the backscatter mechanism, but due to a lack of in-situ data, it is considered part of the wave breaking.

As a first step in the analysis, four characteristic profiles of the individual wave signature, one for each dataset are illustrated in figures 5.5-7-5.5-10 and the $\sigma_o$ is directly correlated with the Doppler velocities by the color scale and the bathymetry. Only 50% of the data has been plotted for better visualization, without influencing the scientific content of the plots. The sea wave height is important for the imaging of the wave field; for A265, $H_s = 5\text{m}$, the waves are imaged for the whole range of the radar; in contrast for D265, $H_s = 2m$, the waves are imaged almost for half the radar range. In addition, the width of the peaks differs at the different positions and also for the different energy conditions. A265 peaks outside the breaking zone spanning about 25 m and decaying to about 15 m in the breaking zone. Similarly, the width of the peaks for D265 in the breaking zone is approximately 10 m. The width of B265 and C265 is approximately 18 m and 22 m, respectively. The variation of the peak width is due to the different length of the waves under the different oceanographic conditions and the percentage of the imaged wavelength, which is related with the grazing angle. Under all conditions, the backscattering intensity of the propagating waves in the deeper areas, where it is assumed that the waves are not breaking, ranges from approximately -40dB to -60dB; this is in accordance with Farquharson et al. (2005).

In table 5.5 the calculations of wave breaking depth during the data acquisition, based on the relation $H/d_b = 0.78$, are tabulated. This relation is derived for a solitary wave traveling over a horizontal bottom, McCowan (1891), but it is commonly used in engineering practice as a first estimate of the breaker index. There are several similar empirical and semi-empirical relations for monochromatic waves, but in this experiment an irregular sea is monitored. Therefore, incipient breaking may occur over a wide zone as individual waves of different heights and periods reach their steepness limits. Thornton and Guza (1983), suggested that the breaking wave height is related to the depth, with $H_{S,b} = 0.6 d_{S,b}$. The calculated breaking depth values are comparable with the instantaneous sea water level; therefore the tidal phase should be taken into consideration; the A265 and B265 data were acquired 1 h before and 1 h after low water, C265 were acquired at high water and D265 were acquired 2 h after high water. The importance of the actual sea level is obvious in the 5.5-9, that during high water there is a significant backscatter signal for the whole surf zone, from the main sand bar to the shore. However, with the assumption that the $d_b$ and $d_{S,b}$ values are the two limits of the breaking zone, augmentation of the normalized radar cross section could be interpreted as the wave increase in steepness and the first stage of the wave breaking.

The depth of the first peak ($d^1_{-40dB}$), over -40 dB, in all the cases appears in the range of theoretical breaking depth. For A265, the $d^1_{-40dB}$ is significantly less than the $d_{S,b}$ due to the fact that the waves are high enough to break in areas deeper than the area covered by the radar.

**Table 5-5. The actual $H_s$, corresponding wave breaking depths, dB and $d_{S,b}$ and the radar deduced wave breaking.**

| Id. No. | $H_s$ | $d_b$ | $d_{S,b}$ | $d^1_{-40dB}$ |
|---|---|---|---|---|
| | m | M | m | m |
| A265 | 5.0 | 6.4 | 8.3 | 6.9 |
| B265 | 4.1 | 5.2 | 6.9 | 5.5 |
| C265 | 2.9 | 3.7 | 4.8 | 5.1 |
| D265 | 2.1 | 2.7 | 3.5 | 4.1 |

The remaining three datasets have breaking depth values relatively close to the observed depth of the first peak. The rest of the peaks are related also with the breakers; as has already been mentioned the wave field is composed of several waves with different characteristics, so they break at different depths. This sequence of breaking-related phenomena is illustrated clearly by D265, where there are four distinct events, with $\sigma_0 \geq -40\text{db}$. The four zones where those events appear are directly related to significant changes, $O(1)\,\text{m}$, in the local bathymetry.

For the four different energetic wave conditions, the sand bar 500 m from the radar is the common zone, where the highest values of $\sigma_0$, -25dB, are recorded. The length of this zone depends on the wave height. For A265, the zone has a length of 200 m. For B265 the zone is separated into two shorter zones of 150 m. For C265, the zone has a length of 300 m, which demonstrates that the waves start breaking over the sand bar, but the scatterers (shorter breaking waves or foam) are propagating as far as the shore. For the case D265, the four zones vary from 50 m to 100 m, which illustrate that the process that causes high backscattering is also brief.

Moreover, in the figures 5.5-7-5.5-10, the velocity information is given as a color scale. In all four cases there are common characteristics. Outside of the breaking zones, the measured Doppler velocities range from 2.5 m/s to 3.5 m/s depending on the actual wave conditions and the local depth. In the breaking zone, the velocity exceeds 12 m/s; this value is related with the wave height and also, as it corresponds to the high values of NRCS due to wave breaking, is close to the phase velocity. Similar results on the Doppler velocity of wave breakers have been reported by Farquharson et al. (2005). The subject is more extensively analyzed in section 5.6.

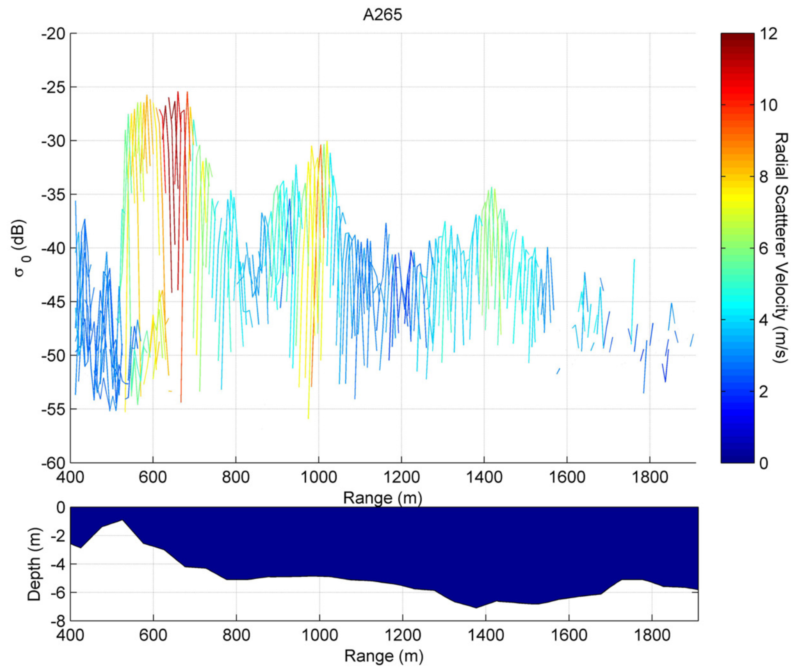


**Figure 5.5-7. Normalized radar cross section for a single wave. The color scale corresponds to the radial Doppler velocity. Dataset: A265.**

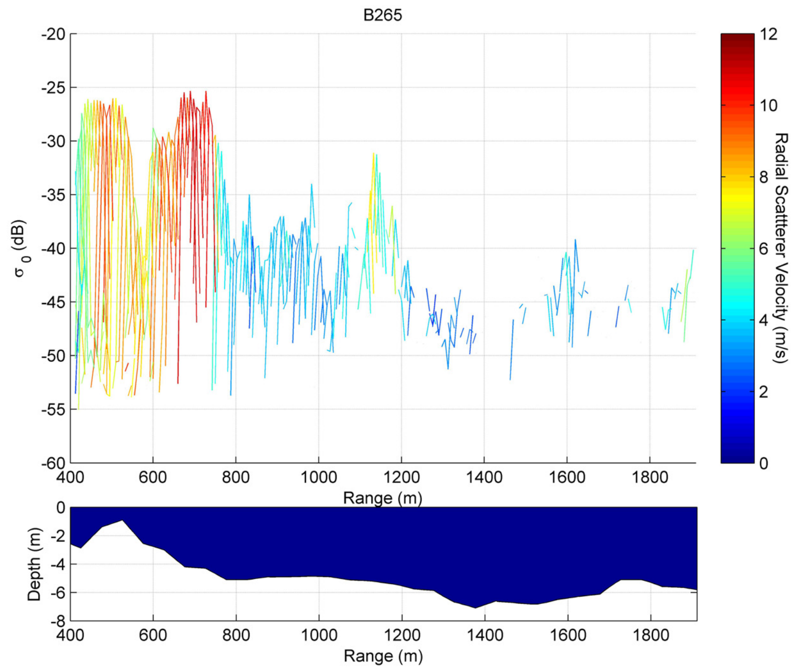


**Figure 5.5-8. Normalized radar cross section for a single wave. The color scale corresponds to the radial Doppler velocity. Dataset: B265.**

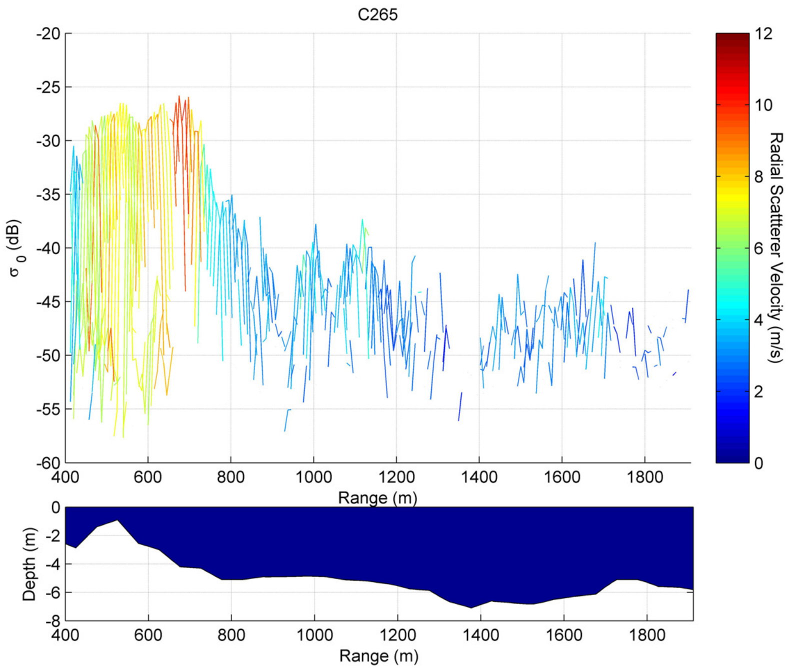


**Figure 5.5-9. Normalized radar cross section for a single wave. The color scale corresponds to the radial Doppler velocity. Dataset: C265.**

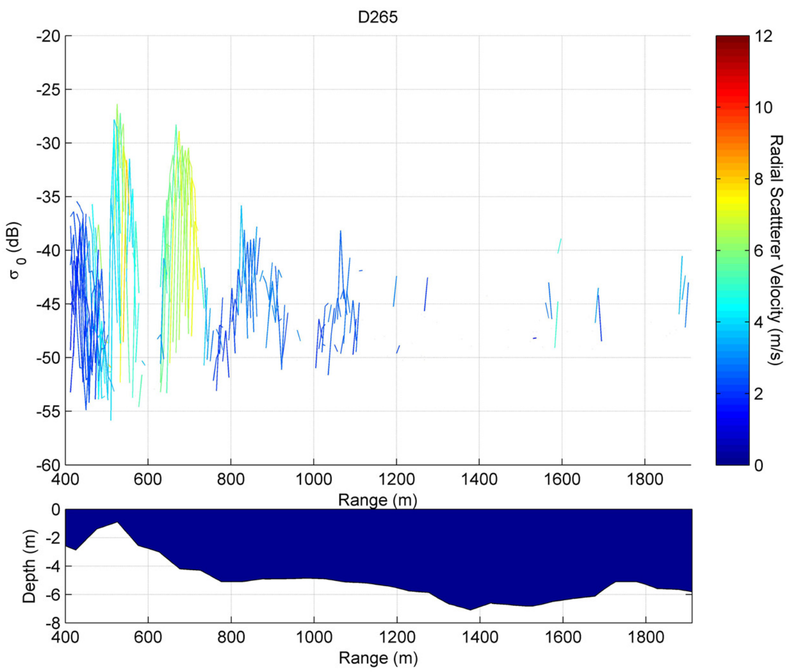


**Figure 5.5-10. Normalized radar cross section for a single wave. The color scale corresponds to the radial Doppler velocity. Dataset: D265.**

To summarize the previous observations, the statistics of the whole range of time series datasets are calculated. The histograms of the NRCS for the whole radar range were computed with a 4 dB bins width, figure 5.5-11. The data from the different wave conditions follow a similar frequency distribution. The histograms from all the cases show two peaks. The first covers 40% of the data and lays within a narrow set of backscattered power, approximately -48 dB, the second smaller peak is at the bin of -28 dB. Due to the fact that the phase of wave evolution (propagating wave, breaker, foam) is unknown, histograms for each 150 m have been calculated, thus the backscattered energy may be correlated to the impact of the bathymetry on the wave field and not with the actual ongoing processes, figures 5.5.12-5.5.15. For all the histograms, a median was defined, because it is less prone to be affected by the presence of expected outliers.

The peak in most of the cases is at histogram bin -46 dB to -50 dB, independent of the wave conditions, which is also proved by the median, which ranges from -44 dB to -50 dB. There is only one exception in the R1-R3 of the B265 data set, where the peak of the distribution is shifted to a lower $\sigma_o$, at bin -54 dB. Since the radar setup and the signal processing focus on wave crests and it is considered that $\sigma_o \approx -48\,\mathrm{dB}$ corresponds to scatterers from the NRCS of non-breaking waves, which was also proven in the previous paragraphs. Most of the histograms are positively skewed, because the majority of the samples concentrates on the left side and have relatively few high values. The left side tail of the distribution is short, due to hardware limitations and detection sensitivity of low signals.

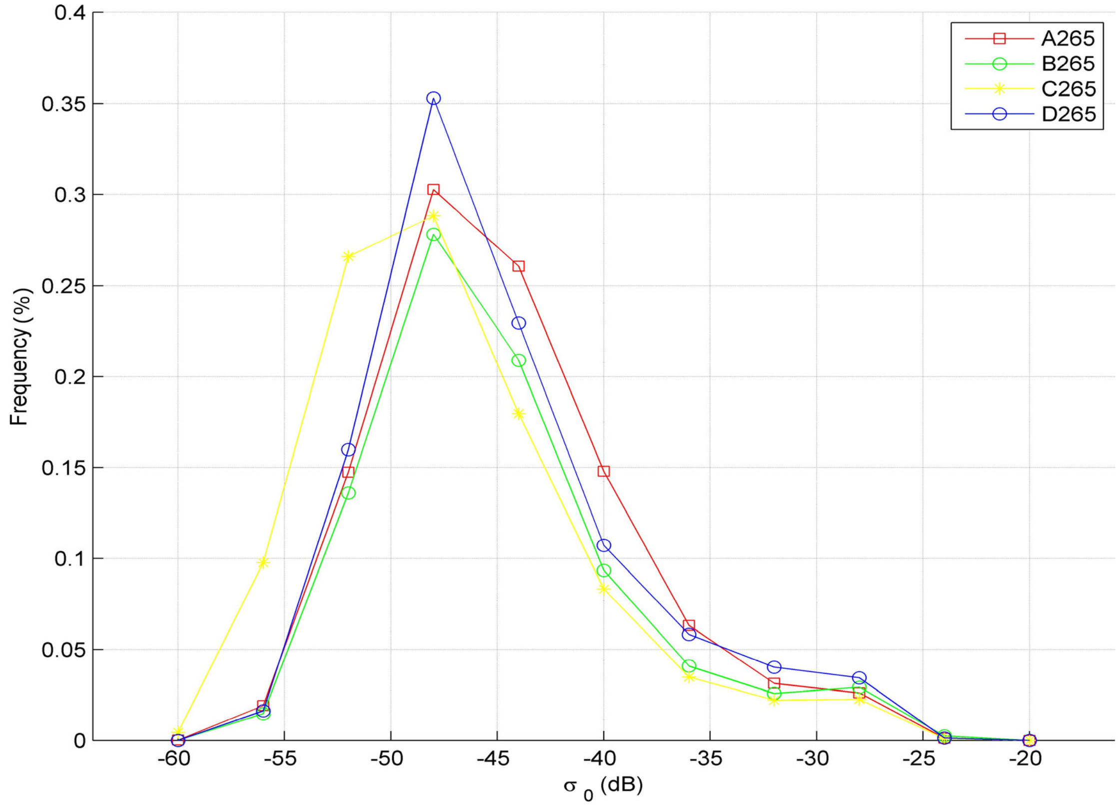


**Figure 5.5-11. Histograms of the normalized radar cross section for the four different energetic conditions.**

At the breaking zone (R1-R3) for all four wave conditions, the distribution of the NRCS has two peaks; the first is in the frequency bin -48 dB and the second peak in the bin at -28 dB. Despite the two peaks, the remaining values of $\sigma_o$ have an almost uniform distribution, for example R2 at C265. This kind of distribution is characteristic for a mixed wave surface, where waves, wave breakers and foam exist simultaneously. Catalán et al. (2008), using an HH polarization, reported median values for breaking waves $\sigma_o \approx -24\,\mathrm{dB}$, for steep waves $\sigma_o < -45\,\mathrm{dB}$ and for foam presented similar distributions to the one is the breaking zone in this investigation, their ground truth was based on optical data.

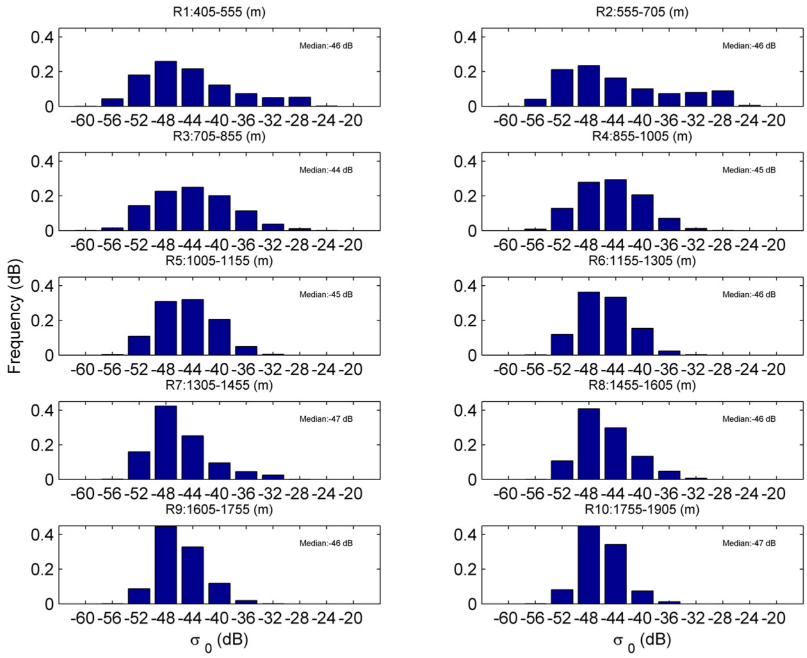


**Figure 5.5-12. Histograms of normalized radar cross section. Top left is the nearest to the shore and bottom right the furthest, the separation into sub-regions is every 150 m and according to local bathymetry. Dataset: A265.**

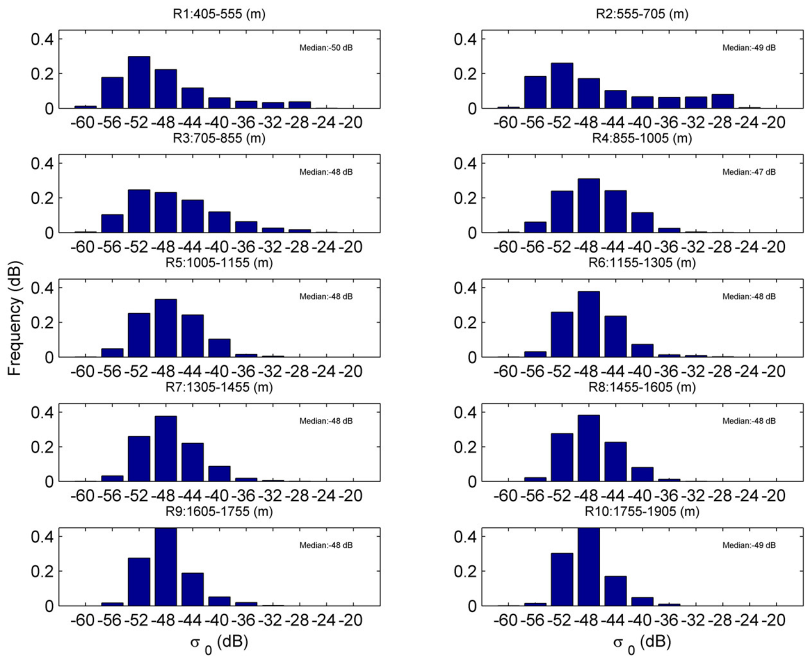


**Figure 5.5-13. Histograms of normalized radar cross section. Top left is the nearest to the shore and bottom right the furthest, the separation into sub-regions is every 150 m and according the local bathymetry. Dataset: B265.**

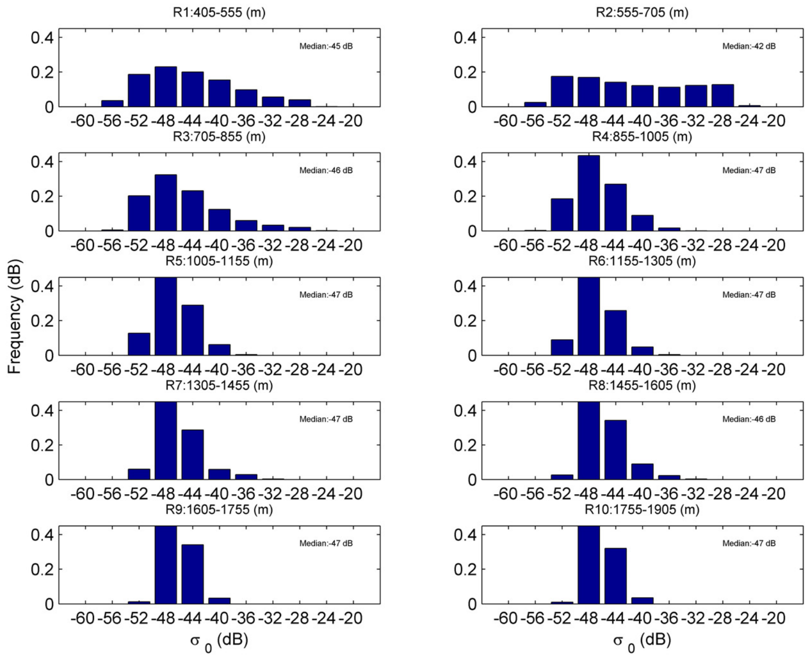


**Figure 5.5-14. Histograms of normalized radar cross section. Top left is the nearest to the shore and bottom right the furthest, the separation into sub-regions is every 150 m and according to local bathymetry. Dataset: C265.**

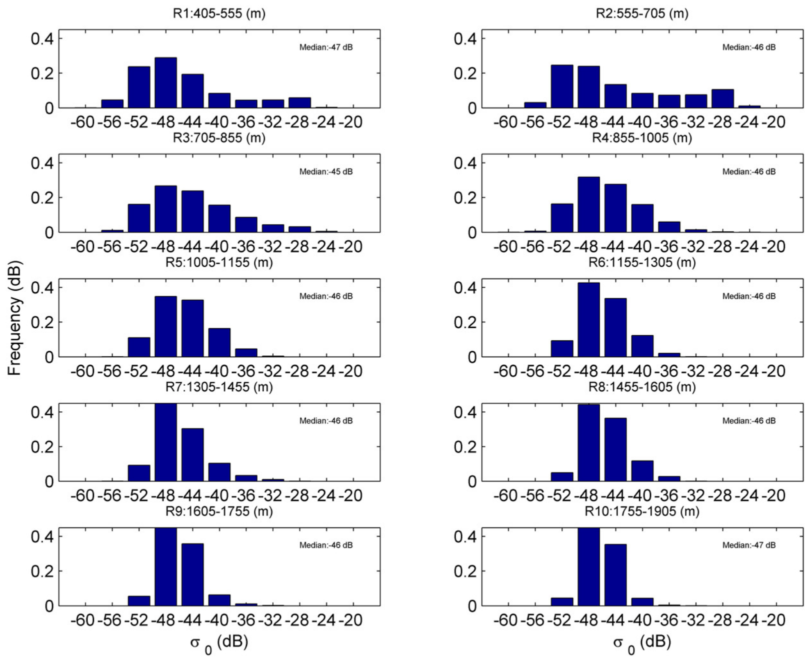


**Figure 5.5-15. Histograms of normalized radar cross section. Top left is the nearest to the shore and bottom right the furthest, the separation into sub-regions is every 150 m and according to local bathymetry. Dataset: D265.**

Moreover, all the data sets have been checked with the Kolmogorov-Smirnov test, the Lilliefors test and normal probability plots, if they come from the Gaussian distribution at a significance level of 0.05; in all cases the normality hypothesis was rejected. A rejection of normality was expected, because the imaging at LGA is a strongly non-linear phenomenon, but the normal probability plots revealed that the distribution of the $\sigma_o$ at R4 of A265 and B265 could be considered weakly Gaussian, appendix C. The frequency distributions of the remaining data sets become narrower as a function of distance from the radar and the significant wave height. Characteristic examples are the distributions of R9 and R10 of C265 and D265, where more than the 80% of the data is concentrated in two frequency bins of the histogram. The shape of the frequency distributions is similar to the shape of the distributions by Trizna (1991), who fitted the Wigner-Ville distribution, but that kind of study is out of the scope of this thesis.

The figures 5.5-16 - 5.4-19 illustrate the backscattered power as a function of the ground-based radar grazing angle. The grazing angle is a geometrical property of the radar, which defines the illuminated distance. The result shows similar trends to those indicated by the analysis of the histograms. Both median and mean values of the NRCS are independent of the grazing angle; the median $\sigma_o$ values are approximately -45 dB for A265, B265, D265 and -48 dB for C265. Therefore, the intensity of the backscattering is also independent of the grazing angle; the $\sigma_o$ value of the dominant sea surface scatterers ranges from -48 dB to -45 dB.

The deviations from the linear trend are caused by the phenomena related to wave breaking. In all four datasets, there is a clear threshold of grazing angle, over which the values of the $\sigma_o$ increase. The $\theta_g$ threshold ranges from $2^o$ to $3^o$ for the four different wave conditions and corresponds to the R3 and R4 sub-areas, where $\sigma_o$ represents where the waves break. This relation is clearly illustrated in D265, figure 5.5-19; in this case the median and the mean increase up to -38 dB with $3^o \leq \theta_g \leq 3.5^o$ and $\theta_g \approx 4^o$, which correspond to the two clearly narrow peaks in figure 5.4-10. The significant conclusion of this analysis is that the NRCS is independent from the grazing angle, but depends on the ongoing hydrodynamic phenomena. The combination of the scatter plots with histograms of the NRCS and a determination of the breaking zone from the wave measurements, shows that for values of $\sigma_o > -38\,\text{dB}$, the radar imaged phenomena are related to the breaking of the waves.

All the foregoing remarks are illustrated in figure 5.5-20, where the percentage of the $\sigma_o > -38\text{dB}$ is illustrated for all different wave conditions and for the ten sub-areas that the radar range has been divided into. This plot demonstrates the frequency of pixels related to the wave breaking process during ten minutes of the observation. As the distance from the radar decreases and the waves shoal there is a gradual increase of the maxima NRCS. In all four different wave conditions, values higher than $-38\text{dB}$ occur more frequently in R2, where the sand bar exists and the majority of the wave energy is expected to be dissipated. For the datasets A265 and B265 (with a significant wave height of 5 m and 4 m respectively), approximately 25% of the recorded data have intensities higher than -38 dB. The first peak of their distribution is broad, because it covers areas R6 to R1. The gradual augmentation of the percentage demonstrates the gradual evolution of the wave field transformations in the breaking zone. The second peak lays between R6 and R8, where the actual depth is of the same order as the calculated $d_b$. For the case C265 (with a 3 m significant wave height) the peak is again at R2 and only 20% of the recorded data have intensities higher than -38 dB. The peak is narrower than for A265 and B265 and it covers the area from R4 to R1. In the remaining sub-areas the distribution is almost uniform and approximately 3%. In the case D265 (with a 2 m significant wave height), more than 35% of the radar data in R2 are related with wave breakers. This distribution has the narrowest peak of all the cases, from R3-R1; the rest of the distribution is uniform with small deviations from approximately 1%.

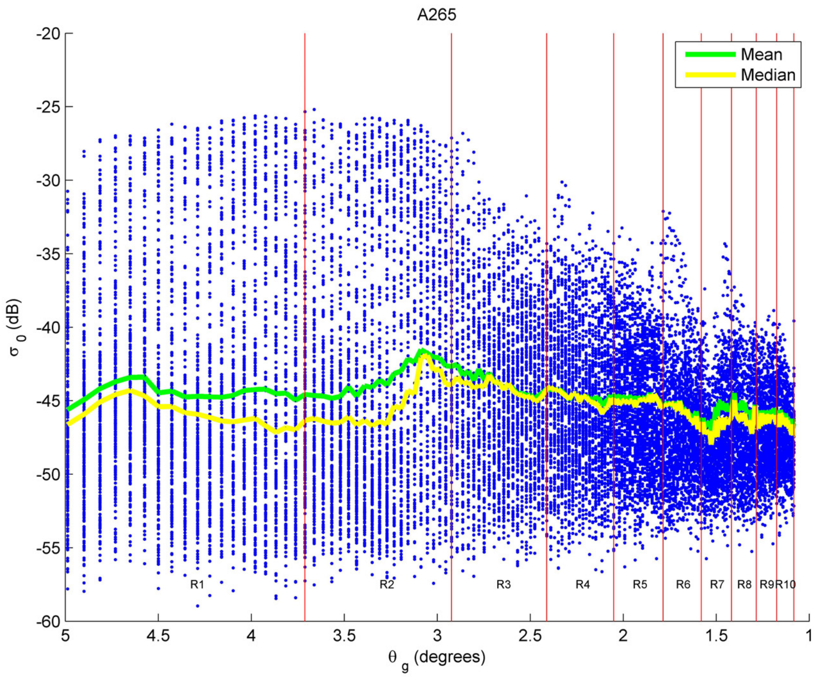


**Figure 5.5-16. Grazing angle dependency of backscatter power. Green and yellow lines correspond to the mean and median of NRCS for each grazing angle. The vertical red lines indicate the sub-areas of the radar beam. Dataset: A265.**

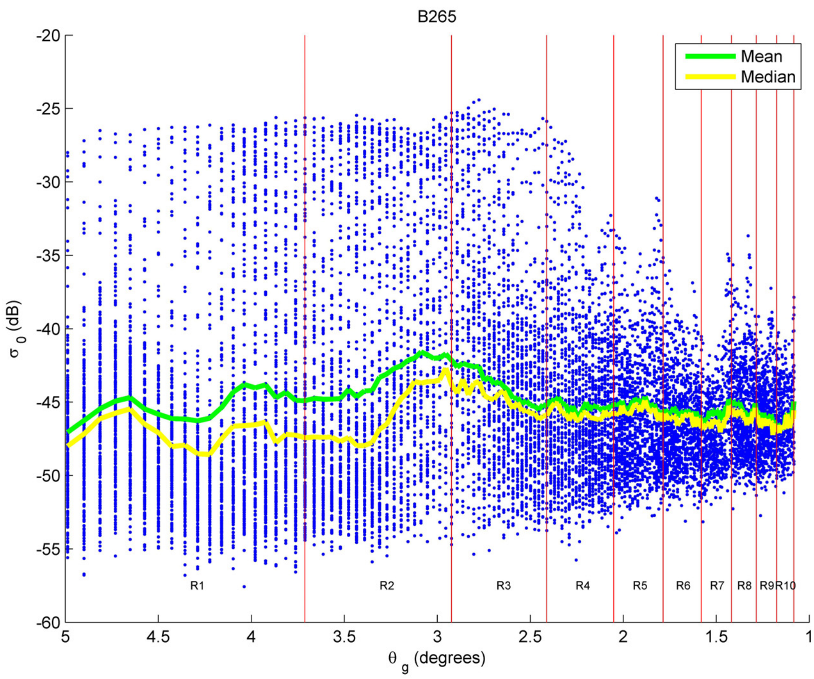


**Figure 5.5-17. Grazing angle dependency of backscatter power. Green and yellow lines correspond to the mean and median of NRCS for each grazing angle. The vertical red lines indicate the sub-areas of the radar beam. Dataset: B265.**

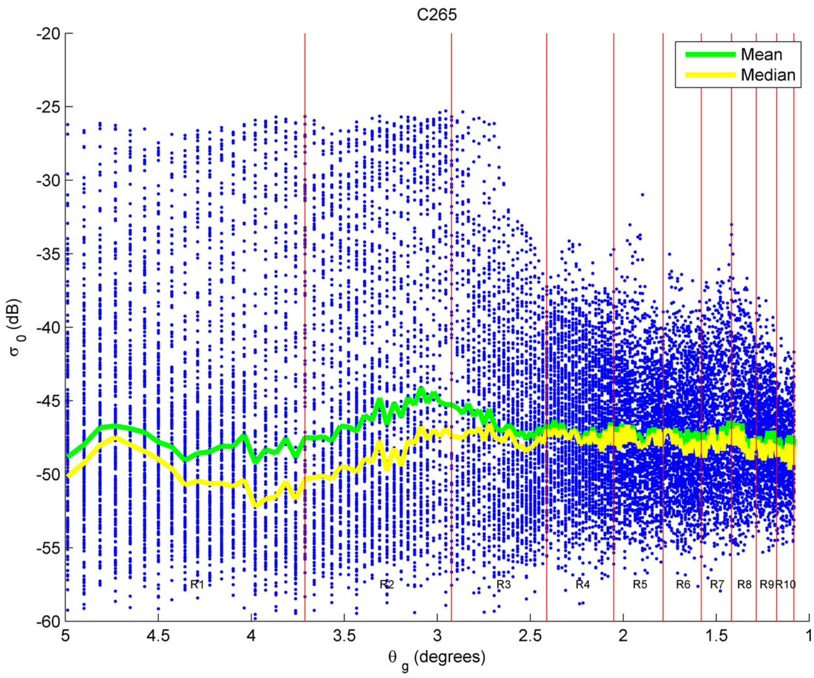


**Figure 5.5-18. Grazing angle dependency of backscatter power. Green and yellow lines correspond to the mean and median of NRCS for each grazing angle. The vertical red lines indicate the sub-areas of the radar beam. Dataset: C265.**

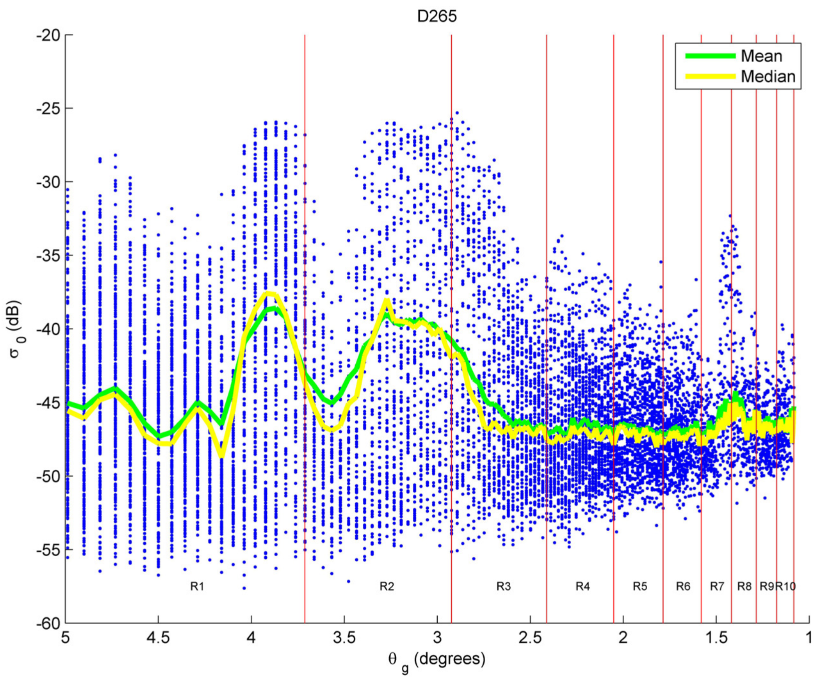


**Figure 5.5-19. Grazing angle dependency of backscatter power. Green and yellow lines correspond to the mean and median of NRCS for each grazing angle. The vertical red lines indicate the sub-areas of the radar beam. Dataset: D265.**

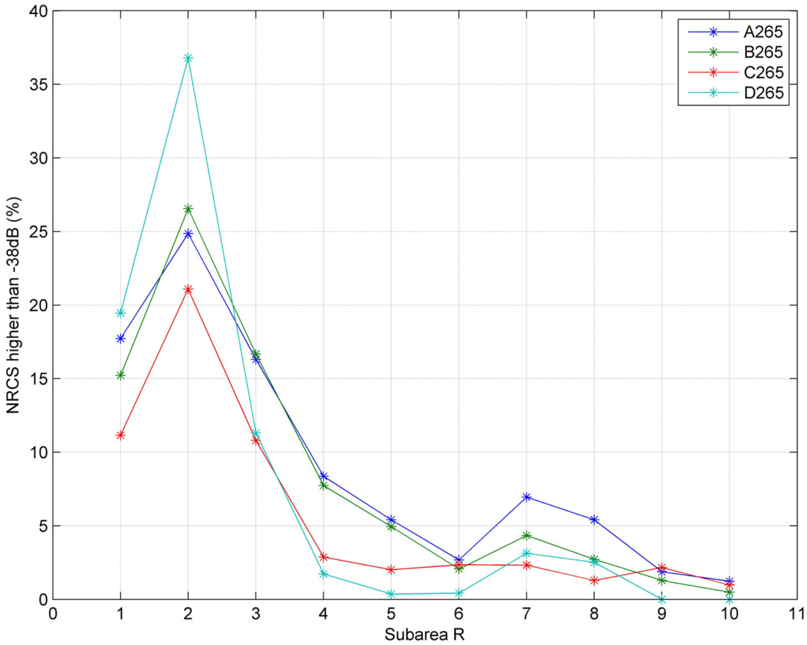


**Figure 5.5-20. Spatial distribution among the 10 sub-areas of backscattered power higher than -38dB, which corresponds to wave-breaking related phenomena. With lower wave conditions, D265, high intensity is measured concentrated over the sand bar.**

Farquharson et al. (2005) showed an excellent correlation between the decay in wave height and the maximum bore NRCS as waves progressed onshore. Catalan (2008) concluded that active breaking has a weak inverse dependency on grazing angle, which is a weak increase of NRCS as the grazing angle decreases. In the current section, it proves that the backscatter intensity of propagating waves is independent of wave height ($2\,\mathrm{m} \le H_S \le 5\,\mathrm{m}$) and grazing angle ($1^o \le \theta_g \le 5^o$); with approximately -45 dB. The wave breaking process, steepening of the wave, actual breaking and foam increases the $\sigma_0$ by about 20 dB. With the available data for different wave energy conditions, it proves that backscattering of the breaking is also independent of wave height and grazing angle, because the mean, median and maximum of $\sigma_0$ in all the different datasets and the different wave breaking in the same dataset is approximately -25 dB.

## 5.6 NRCS and Doppler velocity

In section 5.5 a normalized radar cross section was investigated and extensively discussed in connection with ongoing hydrodynamic processes. It proved that there is a well-defined threshold of $\sigma_o$, above which the imaged process is related to wave breaking. In this paragraph, the Doppler velocity of the sea surface will be discussed. The Doppler velocities of a propagating wave field are expected to be a combination of water particle orbital velocity, scatterer phase velocity, surface current and wind friction velocity. The Doppler velocity of the wave breakers is expected to be in the same order of the phase velocity of sea waves. These two characteristics of radar images, NRCS and Doppler velocity, and their combination are utilized for classification of the monitored processes.

Joint histograms of the NRCS and the Doppler velocities were computed for the radar images of the four different wave conditions and for the 10 sub-areas that the range has been divided into, figures 5.6-1 -5.6-4. The bin size of the NRCS is set to 4 dB and the bin size of the Doppler velocity is 0.4 m/s. In all sub-areas of the four different wave conditions, there is a main peak at the bin of -48 dB, already shown in the one dimensional histograms, which corresponds to a Doppler velocity range from approximately 1.6 m/s at R1 and R2 up to 2.6 m/s at the most distant regions, R8-R10. In the breaking zones, R1-R3, there is a second cluster at the bin $\sigma_o = -24\,\mathrm{dB}$, the appearance of which depends on the wave height; the peak becomes smaller as significant wave height decreases. This effect is clearly illustrated at R7 for A265, where this peak appears 0.5 km before the breaking zone and at R3 for D265, where a second peak occurs. The Doppler velocities that correspond to the second peak are higher in the furthest breaking zone. At R3 of datasets A265, B265 and C265, the velocity ranges approximately from 7.5 m/s to 9 m/s, at R2 from 6 m/s to 7.5 m/s and at R1 is less than 6 m/s. A similar behavior is also seen in D265 at R2, where the second peak of the histogram corresponds to 5.5 m/s.

The first peak of the histograms, $\sigma_o \approx -48\,\mathrm{dB}$, satisfies the assumption that corresponds to propagating waves, as the NRCS is independent of the distance and appears to be an almost conservative quantity, even in the breaking zone. The second proof is that the radial speed depends on the general wave conditions and is reduced over the sand bar. By using these two quantities, it is possible to determine the mean velocity of sea surface scatterers, which is related to the actual wave, sea surface and current conditions. The second peak of the histograms, $\sigma_o \approx -24\,\mathrm{dB}$, appears at Doppler velocities that are higher than the summation of water particles orbital velocities and current field velocity, but in the same order of magnitude as the phase velocity of the waves.

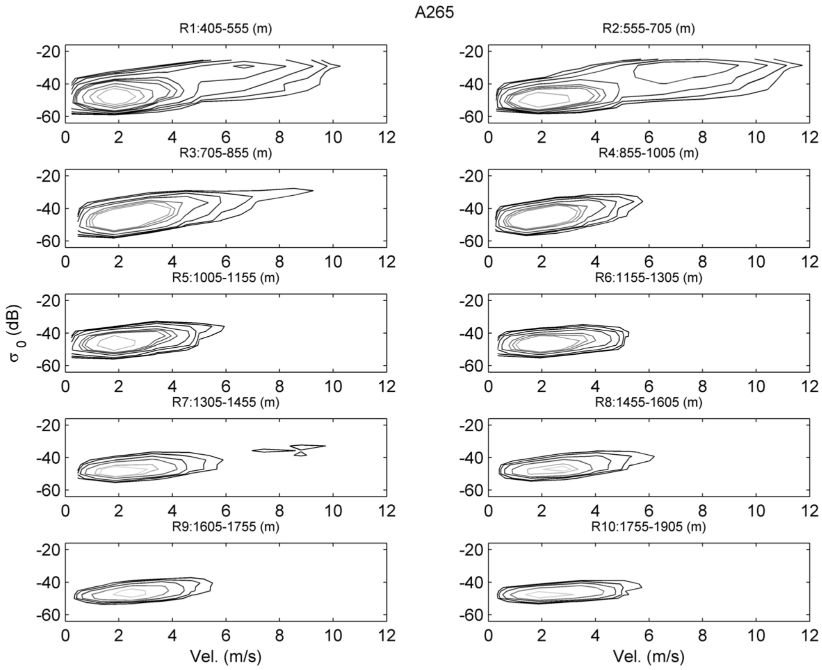


**Figure 5.6-1. Contour plots of joint histograms of NRCS and Doppler velocity from dataset A265 for all sub-areas. The bin size of the NRCS is set to 4 dB and the bin size of the Doppler velocity is set 0.4 m/s.**

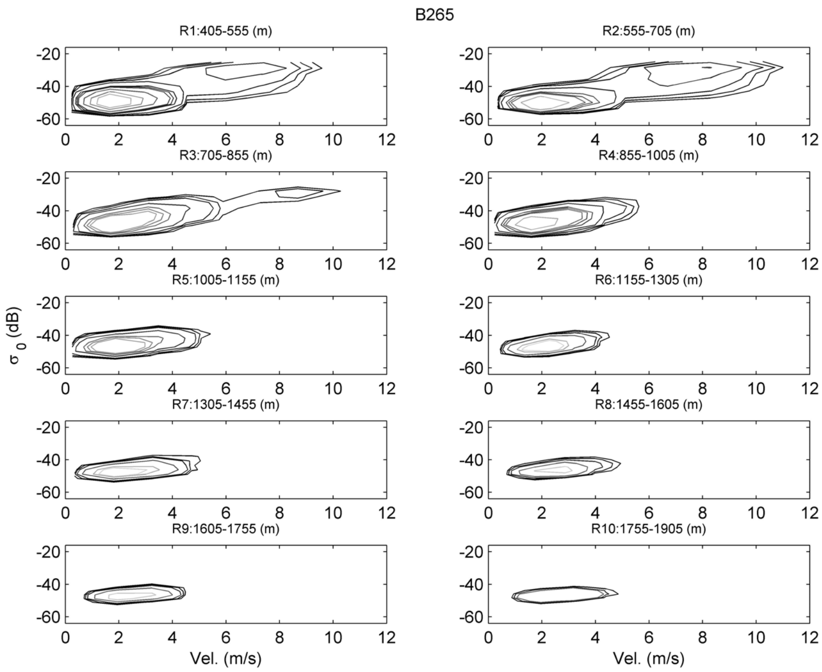


**Figure 5.6-2. Contour plots of joint histograms of NRCS and Doppler velocity from dataset B265 for all sub-areas. The bin size of the NRCS is set to 4 dB and the bin size of the Doppler velocity is set 0.4 m/s.**

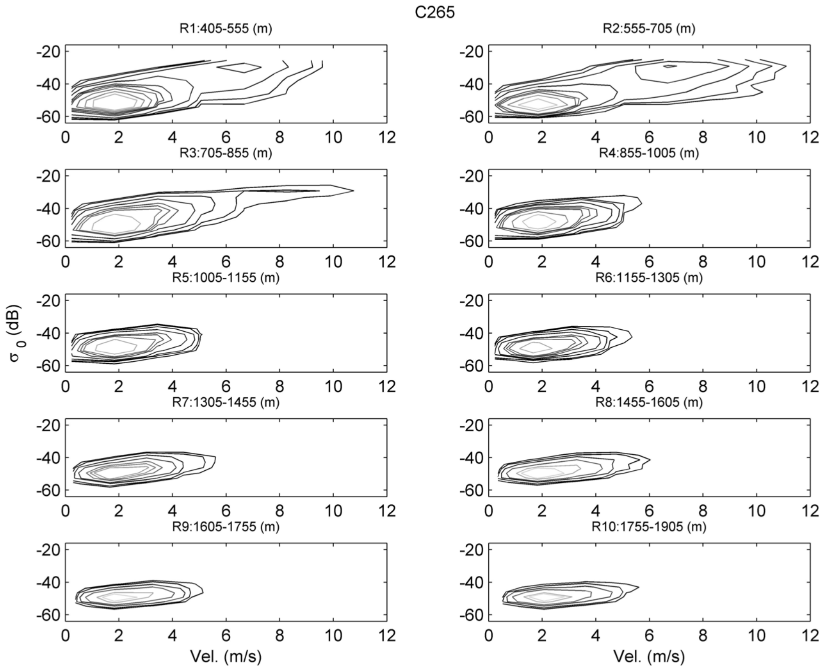


**Figure 5.6-3. Contour plots of joint histograms of NRCS and Doppler velocity from dataset C265 for all sub-areas. The bin size of the NRCS is set to 4 dB and the bin size of the Doppler velocity is set 0.4 m/s.**

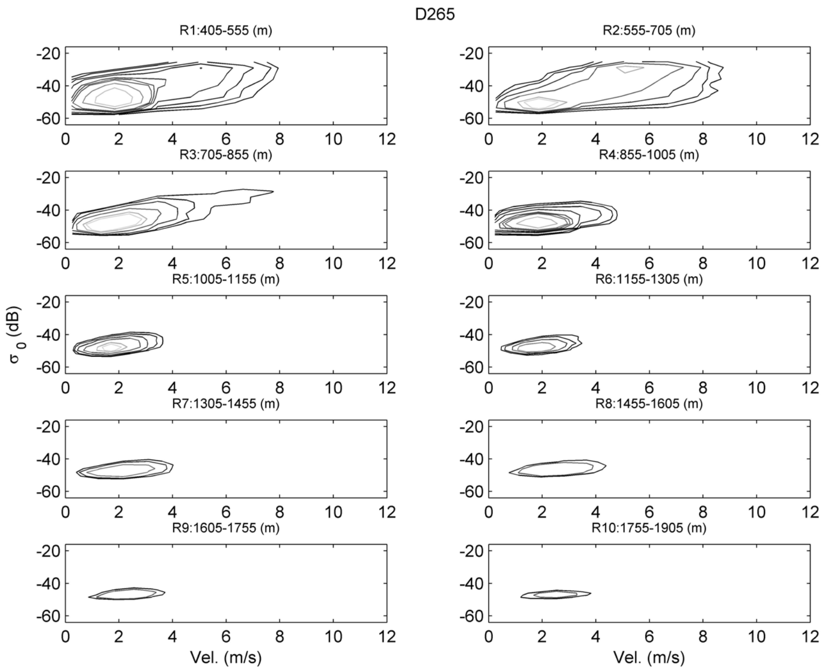


**Figure 5.6-4. Contour plots of joint histograms of NRCS and Doppler velocity from dataset D265 for all sub-areas. The bin size of the NRCS is set to 4 dB and the bin size of the Doppler velocity is set 0.4 m/s.**

## 5.7 Average Doppler velocities in time

In this section, the measured Doppler velocities for the four different conditions, figures 5.5-3- 5.5.6, are averaged and analyzed for their basic components. The direct product of the analysis is a set of 200 simultaneous time series of the horizontal velocity of the scatterers on the water surface in the coastal zone, with a spatial resolution of 7.5 m. The time series of 10 min intervals with gaps due to the filtering were averaged, figure 5.7-1.

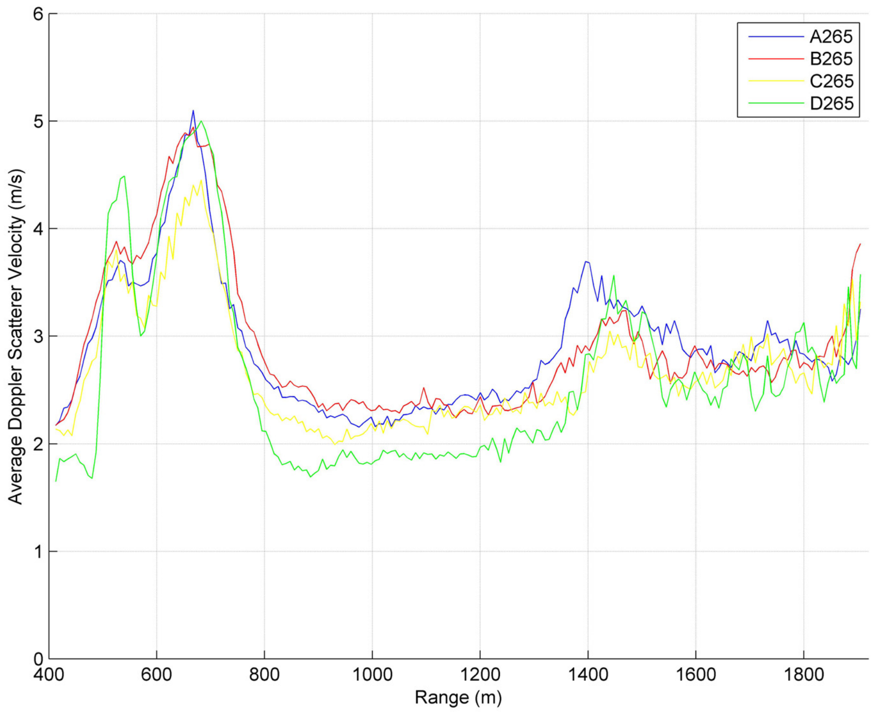


**Figure 5.7-1. 10-minute average Doppler velocities of the four different wave cases for the whole range of the radar beam.**

The impact of the bathymetry is obvious: at the isobath of 2 m on the sand reef, the waves break and the mean velocity of the scatterers is almost the double that in the homogeneous areas. After the reef, towards the shore, the velocity is reduced and again increases on the second sand bar; the same features are also observed with the average over time. In both cases, the factor of velocity increase is approximately 2-2.5 in comparison with measurements outside the breaking zone. The general spatial trend of the velocity, outside the breaking zones illustrates a decrease of velocity when coming closer to the shoreline. As long as all the imaging effects are neglected, this observation could be interpreted as wave energy decay due to bottom friction; this is discussed more extensively in section 5.9.

Assuming the scattering-object velocity in the water frame of reference obtained from the Doppler frequency is the sum of the wind drift velocity, the current velocity including the orbital motion and the speed of the scattering object, in the following paragraphs, the measured radial velocities are qualitatively evaluated. For the validation, a range of radar bins between 900 m and 1100 m from the radar, are used, because this area has an almost homogeneous sea bottom and there are the fewest gaps in the time series of the Doppler velocity in comparison with the time series further seaward.

It was previously mentioned that during the experiment the wind velocity and wave heave were recorded by in-situ instruments. In table 5.6, the wind drift velocity at 10 m height on the coast is tabulated; the assumption is that the wind field is homogeneous. In addition, the maximum horizontal water particle velocity has been calculated based on the significant wave height of the nearest wave rider, at a depth of 5.5 m. Doppler shift due to the current is not considered, because the radar was directed into the propagation direction of the wave field, so the Doppler effect of currents on the waves is not observable.

**Table 5-6. Validation of Doppler radial velocities, $v_r$, with the in-situ measurements of the wind drift velocity, $u_w$ and the maximum horizontal particle velocity, $u_{orb}^{List}$.**

| Id. No. | $v_r$ 900 m-1100 m m/s | $u_w$ m/s | $u_{orb}^{List}$ m/s | $v_r - u_w - u_{orb}^{List}$ m/s |
|---|---|---|---|---|
| A265 | 2.3 | 0.88 | 1.49 | -0.07 |
| B265 | 2.46 | 0.72 | 1.73 | 0.01 |
| C265 | 2.05 | 0.62 | 1.71 | -0.24 |
| D265 | 1.94 | 0.57 | 1.00 | 0.37 |

The result of the validation, the final column in table 5-6, shows that the measured Doppler velocity is composed of the sum of wind drift velocity and the orbital velocity. The differences, in the cases of the higher waves, A265 and B265, are in the order of few centimeters. In the cases of lower wave conditions the difference is in the order of a few decimeters. The discrepancy lies within a geophysical range of variability and probably an elimination of the Doppler effect of the currents on the waves from the radar data is not absolutely effective. Furthermore, for this comparison the wave data from List West were used. As already commented on for figure 5.3-2, when the wave height is low, the wave buoy measurement is impacted by tidal conditions and probably the wave buoy measurement had a reduced accuracy. Nevertheless, this validation does prove that extraction of maximum orbital velocity is possible by coherent radar measurements.

## 5.8 Time series analysis of radar Doppler velocities

In this section, the spectra of radial velocities for the four different energetic conditions were estimated by applying a time series analysis on the detected Doppler velocities. The time series values correspond to the maximum velocities of the sea waves imaged by the radar, therefore the high values of wave breakers in the breaking should be interpreted as spectra for breaking waves. The total length of the time series is 1024 samples (512 s), the gaps in the time series of the velocities have been filled with a zero value. Fast Fourier Transformation is applied using a Bartlett window. The length of the window is 128 samples, corresponding to 64 s. Degrees of freedom are calculated according to the relation $DoF = 3N / M$ , where $N$ is the total number of samples and $M$ the number of samples per window segment, Jenkins and Watts (1968). Therefore, theoretically, each individual spectrum has 48 degrees of freedom, but it is impossible to define the exact number of degrees due to an introduced uncertainty from gap filling; the percentage of missing values indicates a measure of the uncertainty introduced. Figures 5.8-1-5.8-4 illustrate the evolution of the sea surface kinetic energy: the last 2000 m as the wave field approaches the coast under four different wave conditions. This is the first time in the bibliography that a series of 200 simultaneous wave-related spectra are calculated for a propagating wave field. The bandwidth between the independent samples is approximately $\Delta f = 0.016\,\mathrm{Hz}$ and the first non-zero frequency is at 0.032 Hz.

The four examples demonstrate similar features; a basic observation is about the range (or equivalently the grazing angle) and wave height dependency of the radar wave imaging. The percentage of the missing values in the time series, approximately 10% close to the shoreline and 90% in most distant radar cells, is a function of the distance from the radar, figures 5.8-1-5.8-4, right plot. In addition, the numbers of missing values have two local maxima (at 600 m and 780 m) that are related to the effect of the sand bar on the waves. Due to the bathymetric gradient, the waves become steeper and higher, increasing the shadowing effect and thus a smaller area of the waves is illuminated. Therefore, the local maxima of the gaps are behind the shoals and not over them. In an area between 850 m and 1000 m, approximately 50% of the data is missing, which confirms the imaging concept described in section 5.2.

The velocity spectra have their main peak in a narrow frequency bandwidth for the whole range, on and around which the main part of the energy is concentrated. The main peaks along the radar radius are at frequencies 0.11 Hz, 0.095 Hz, 0.095 Hz and 0.13 Hz, for A254, B265, C265 and D265, respectively. Despite the relatively large $\Delta f$, the peaks are invariant outside the breaking zone, but also exist in the breaking zone. The spectra are considered as narrow, they are positively skewed and their bandwidth depends on the wave and wind conditions. Secondary peaks of the spectra appear, as is expected from previous investigations with buoy wave measurements, Ochi (1998). The second frequency peaks are at 0.19 Hz, 0.11 Hz, 0.19 Hz and 0.21 Hz for A254, B265, C265 and D265, respectively. The B265 case also has a third peak at 0.17 Hz. The existence of the secondary peaks and the long right hand tail of the distributions demonstrate the impact of non-Gaussian processes, such as wave breaking, on the spectra.

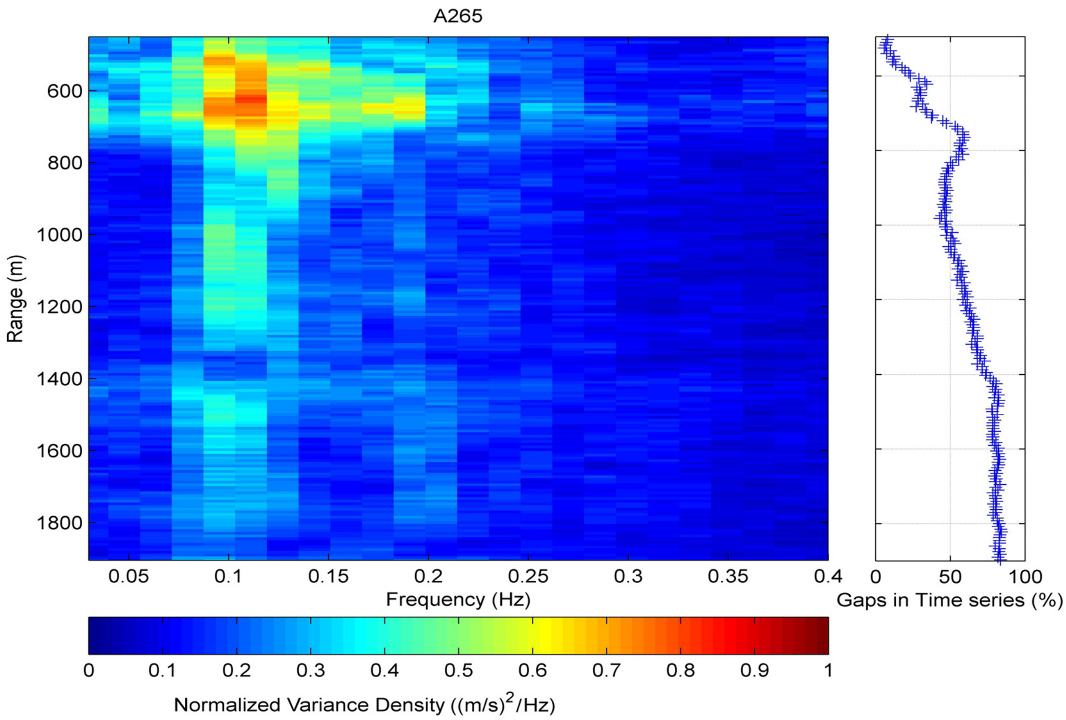


**Figure 5.8-1. Left: Spectra of Doppler velocity time series for 512 s of the whole radar range, the spatial resolution is 7.5 m. Right: Percentage of missing values in velocity time series for each radar grid cell. Dataset: A265**

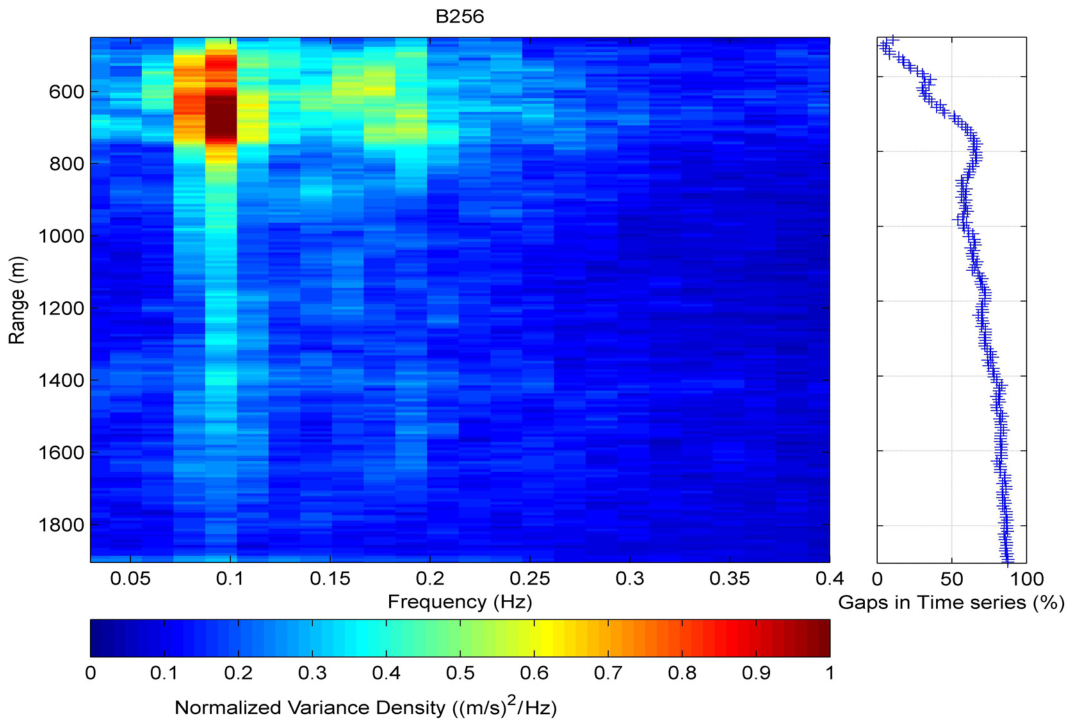


**Figure 5.8-2. Left: Spectra of Doppler velocity time series for 512 s of the whole radar range, the spatial resolution is 7.5 m. Right: Percentage of missing values in velocity time series for each radar grid cell. Dataset: B265.**

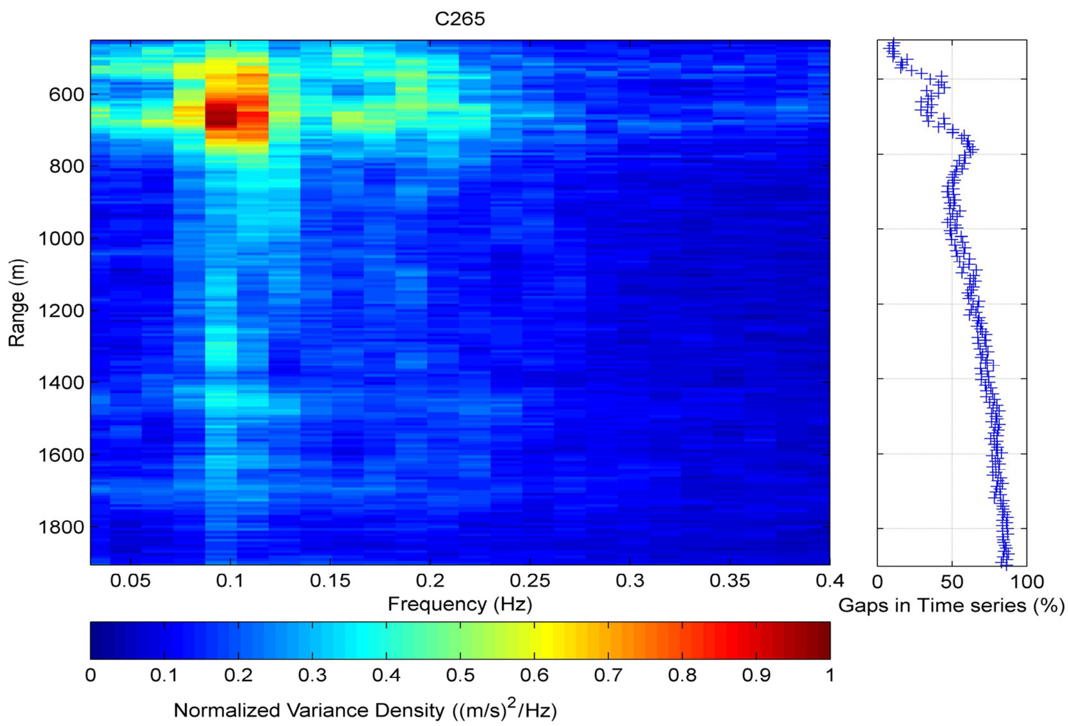


**Figure 5.8-3. Left: Spectra of Doppler velocity time series for 512 s of the whole radar range, the spatial resolution is 7.5 m. Right: Percentage of missing values in velocity time series for each radar grid cell. Dataset: C265.**

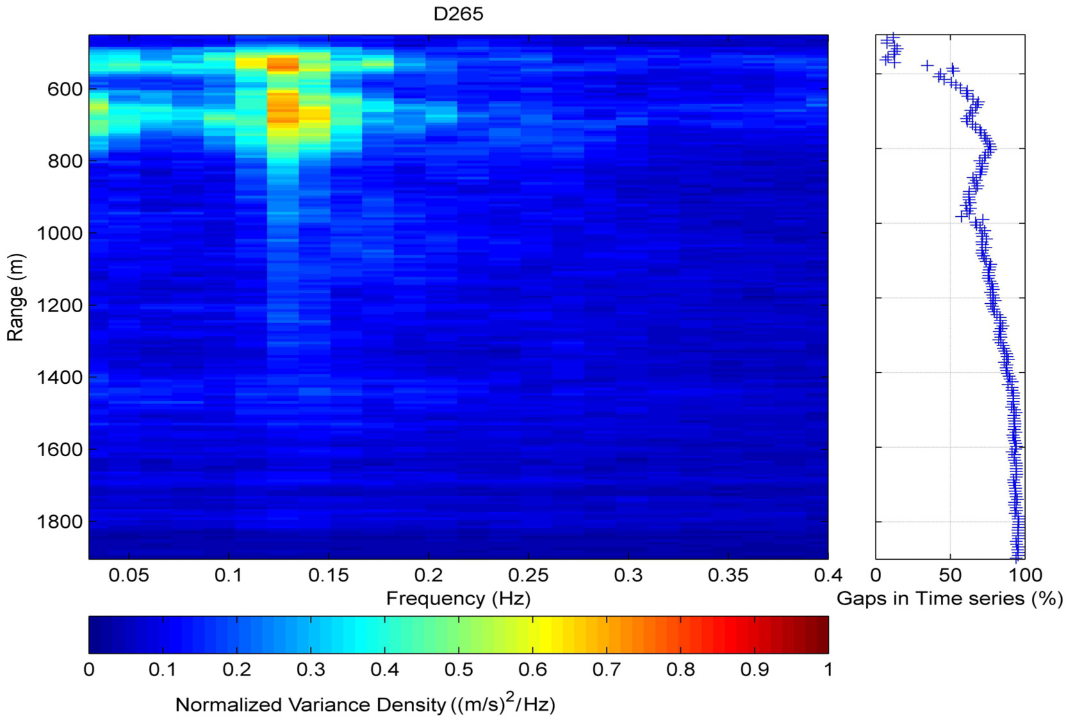


**Figure 5.8-4. Left: Spectra of Doppler velocity time series for 512 s of the whole radar range, the spatial resolution is 7.5 m. Right: Percentage of missing values in velocity time series for each radar grid cell. Dataset: D265.**

A validation of measurements is implemented for the available wave rider data. In this comparison, the radar time series of the horizontal velocity of one radar cell at distance 975 m from the radar is utilized. By assuming the validity of the linear theory, that the measured Doppler velocities correspond to the maximum horizontal particle velocity and having information about the local depth, the radial velocities are transferred into instantaneous heave and a fast Fourier transformation with the same options as before were applied. The time series of this grid cell has been chosen, because it is outside the breaking zone and has the maximum number of available measurements, more than 50%. For the comparison the time series of the deep water buoy are used. The sampling period of the buoy is 0.78125 s, which is larger than the calculated radar sampling period of 0.5 s. Therefore, the wave rider measurements were converted by applying a linear interpolation between the measured values: a fast Fourier transformation was applied, a Bartlett window used and the degrees of freedom for the spectra occurring are exactly 48.
The resulting spectra of both measurements are illustrated in figures 5.8-5-5.8.-8. The blue line corresponds to the radar and the red line to the buoy measurements; the $\Delta f$ for both is $0.016\,\mathrm{Hz}$ . Despite the same properties of the spectra they have not been calculated from

simultaneously acquired data. There is a time shift of 20 min, due to the data acquisition schedule. The wave rider acquired data for the first 30 min of each hour, whereas the radar was acquiring data for the second half of each hour. Thus validation is taking place with time series that were acquired with a time lag and the wave rider measurement has been transferred in space.

The black line corresponds to the spectrum of the shadow mask. Since the shadow mask is defined as a binary time series that is constructed based on the Doppler velocity time series, the existence of a value in the time series of Doppler velocities corresponds to 1 and a lack of measurement (shadow) corresponds to zero. As has already been proved, Seemann (1997), and applied operationally in WaMoS, e.g. Reichert et al. (1999a), the peak frequency of an imaged wave field is extracted from the spectrum of shadow mask of a microwave image. In this case, only one radar footprint is examined and here it proves it conserves the property. Hence, a spectral analysis of the time series of Doppler velocities provides equivalent information to a spectral analysis of the shadow mask.

The demonstrated spectra from the radar data for all the different wave conditions have a common characteristic; the tails of the distribution tend to the value of the energy 0.1 $m^2$/Hz and not to zero. This is the impact of a non-linear part of the analyzed quantity and has been discussed for decades in several scientific fields, e.g. Kim and Powers (1979). In those time series, there are two interacting sources of the non-linearity: The propagation of the waves over an uneven sea bottom and the imaging of the wave field are both non-linear processes. They both result in the gaps in the radar time series, which have been filled with a constant value of zero. The impact of this non-linearity is illustrated clearly in D265, figure 5.8-8, which has about 30% of measurements and where the energy density of the peak frequency is approximately at the same level as the energy density of the rest of the frequencies. This effect of the non-linear wave field has been shown by Ochi and Ahn (1994).

In cases B265 and D265 the peak frequency of the two time series is identical, at frequency bins $0.087\,\mathrm{Hz} < f \le 0.10\,\mathrm{Hz}$ and $0.119 Hz < f \le 0.135\,\mathrm{Hz}$ respectively. For cases A265 and C265, the peak frequency of the radar time series is shifted one bin towards the higher frequencies. While in A265, the peak frequency of the radar ranges $0.103 Hz < f \le 0.119\,\mathrm{Hz}$ and the peak frequency of the buoy ranges $0.087\,\mathrm{Hz} < f \le 0.103\,\mathrm{Hz}$. Similarly with C265, where the peak frequency of the radar ranges $0.087\,\mathrm{Hz} < f \le 0.10\,\mathrm{Hz}$ and the peak frequency of the buoy ranges $0.072\,\mathrm{Hz} < f \leq 0.087\,\mathrm{Hz}$. Thus, it proves that the spectra based on radar data determine the same peak frequencies as the time series spectra from the wave rider. The energy density of the wave rider spectra, in cases A265, B265 and D254, is approximately 40% less than the energy density of the radar spectra at the peak frequency. For C265, the energy density of the two spectra is approximately equal at the peak frequency, but the peak of the radar time series is almost twice as broad; the energy density around the peak frequency is 44% higher that the energy density around the peak of the wave rider spectrum. From this comparison, the effects of the currents on the wave measurements by the radar, which can change the energy intensity in the spectra, Hedges (1987), is assumed negligible. This assumption is based on the data acquisition strategy of steering the radar beam against the direction of wave propagation to detect the maximum Doppler frequency shift only due to the waves.

Despite the few available datasets, it shows that the radar Doppler measurements can provide unique information about wave energy propagation with high spatial, 7.5 m, and temporal, 0.5 s, resolutions and illustrates the transformations of the waves in the surf zone. The quantitative comparison of the spectra from radar agrees with the wave spectra from different wave conditions presented in the bibliography and demonstrates that radar deduced spectra include information about the wave field in the shallow areas and also about wave breaking spectral characteristics.

Therefore, it is possible to utilize the Doppler radar measurements for systematic monitoring of the wave field. The condition to elicit the provided information is to define a transfer function between the measured velocity and the ongoing oceanographic phenomena. For the establishment of the transfer function, just these few datasets prove that the radar imaged phenomena have the same peak frequency and there is an almost constant relation between the different energy intensity of the spectra of the two independent measurements. However, with only the available information at present, no generalization of the method is possible for several reasons. There was in-situ measurement only at one point, which is outside the radar radius and has a time lag, so it is impossible to extend the function for the whole radar range. Moreover, the available data are very few datasets: four datasets have been demonstrated, but the applicable datasets are less than ten. Finally, it has been proven and is generally accepted, that the minimum temporal length of wave measurements for the calculation of reliable wave spectra has to be approximately 15 min; in this case the radar measurements last only 8.5 min. Despite these three disadvantages of the experiment, the data analysis provides extremely strong indications for further research in the subject, which could enhance the wave monitoring and reveal the mechanisms of the wave evolution in the coastal zone.

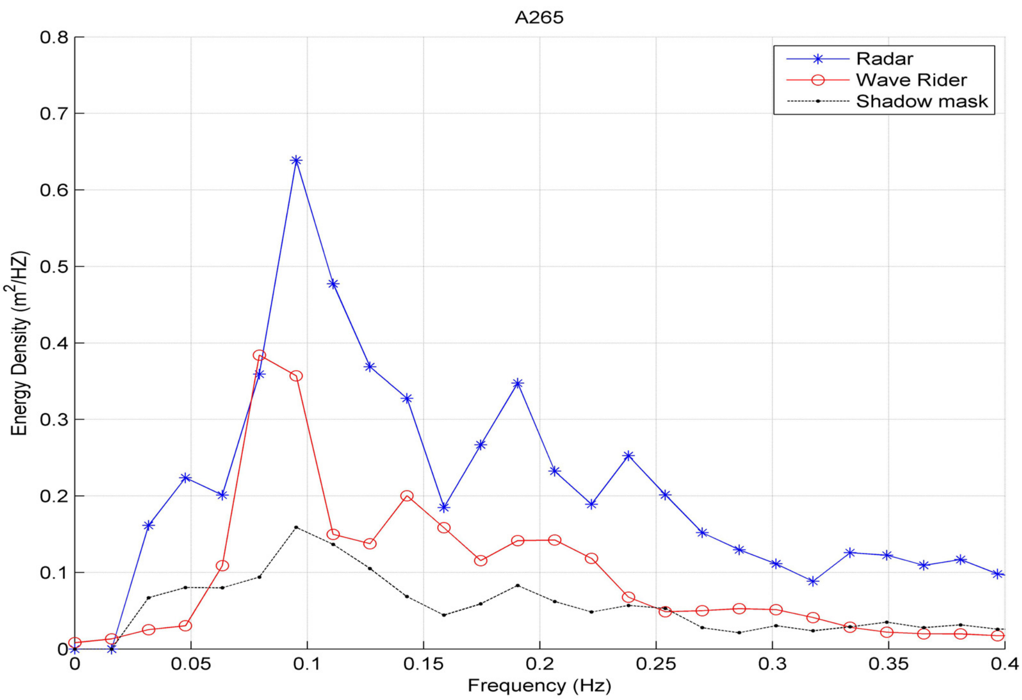


**Figure 5.8-5. Spectra of offshore buoy heave (red line), of radar extracted heave for the grid cell 975 m from the radar (blue line) and of the shadow mask for the same grid cell (black line). Dataset: A265, 975 m from the radar.**

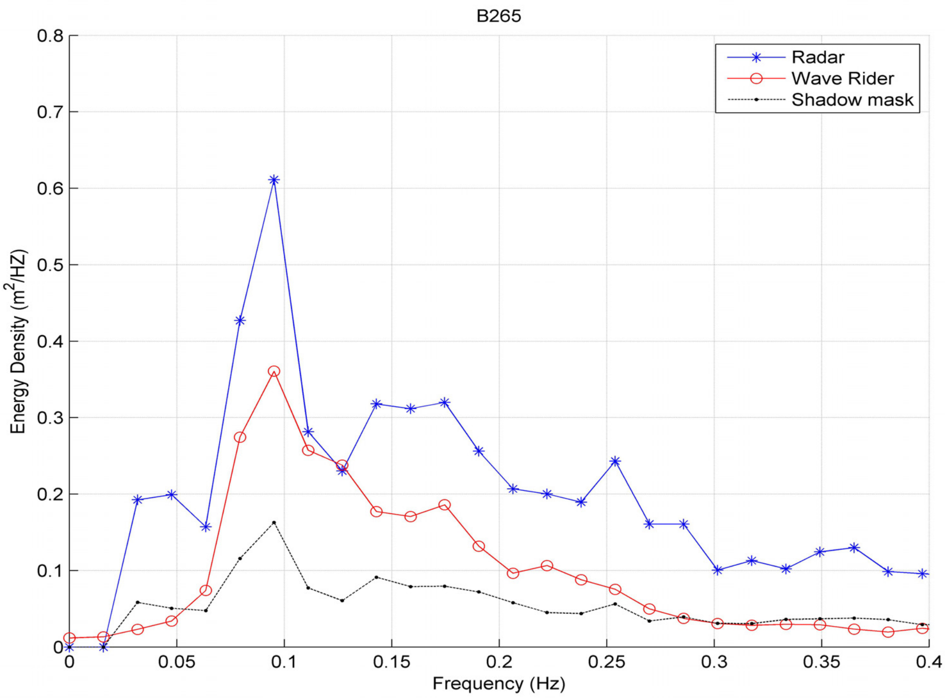


**Figure 5.8-6. Spectra of offshore buoy heave (red line), of radar extracted heave for the grid cell 975 m from the radar (blue line) and of the shadow mask for the same grid cell (black line). Dataset: B265, 975 m from the radar.**

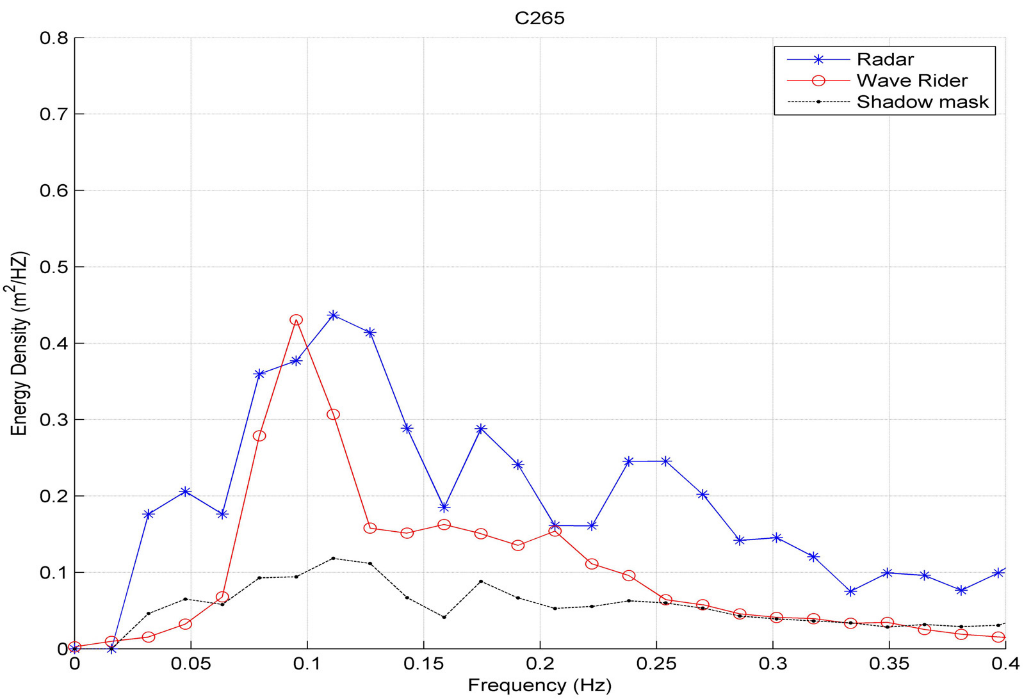


**Figure 5.8-7. Spectra of offshore buoy heave (red line), of radar extracted heave for the grid cell 975 m from the radar (blue line) and of the shadow mask for the same grid cell (black line). Dataset: C265, 975 m from the radar.**

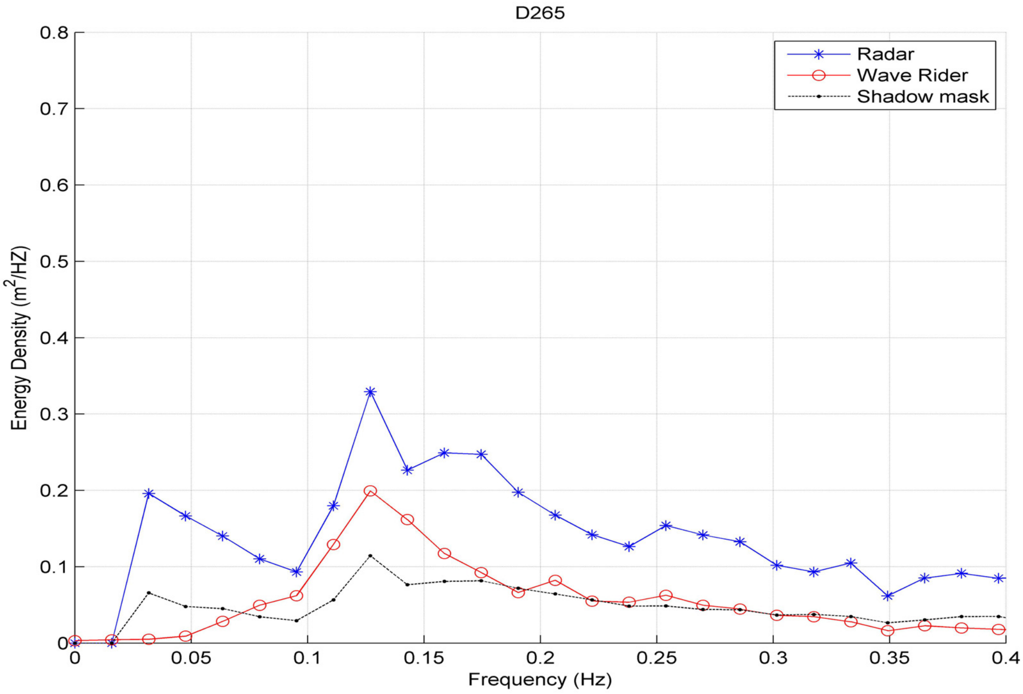


**Figure 5.8-8. Spectra of offshore buoy heave (red line), of radar extracted heave for the grid cell 975 m from the radar (blue line) and of the shadow mask for the same grid cell (black line). Dataset: D265, 975 m from the radar.**

## 5.9 Mean Doppler spectra

The final step of data analysis is the averaging of the 0.5 s Doppler spectra series for the whole period of each dataset, approximately 10 min. The spatial evolution of the mean Doppler spectra provides the mean sea surface velocity for the whole range of the observation. In section 5.6, it was proven that the propagating, non-breaking waves have a velocity in the range of 2 m/s; the order of the breaking waves velocity is 3 to 4 times faster, so these two conditions of the waves are separated and the surface velocity is monitored along the radar beam.

The separation is based on the conclusions of the joint histograms. In that section it was proved that, in the breaking zone, there are two main clusters. The first cluster, which exists at the bin of -48 dB and 2 m/s velocity, is present for the whole range of the radar beam. The second cluster, which appears at the histogram bin of -24 dB and 8 m/s, is proven it is related to wave breaking. The NRCS of the second cluster is several times higher than the first cluster. Therefore in the average Doppler spectrum, the second peak of breakers suppresses the first peak. Thus, the Doppler spectra have only one peak, which contradicts the observations of the joint histograms, left plot at figures 5.9-1-5.9-4. To weight the backscattering from the non-breaking and breaking waves, each individual Doppler spectrum has been normalized with its maximum value and afterwards they have been averaged. In both cases, the spectra have been normalized after the averaging, middle plot in figures 5.9-1-5.9-4. To make the difference between the averaged spectra from the different processing of the data obvious, examples of both of them have been plotted in the right plot of figures 5.9-1-5.9-4 and the bathymetry is illustrated in addition. In these sets of figures for the four different wave conditions, the range distribution of the mean Doppler spectra is illustrated. Due to our interest being the velocity of the scatterers (and not the frequency shift), on the x-axis the Doppler velocity is plotted, as described at the paragraphs 5.4.3 and 5.4.4.

For all four different wave conditions, there are common characteristics. The color scale demonstrates the normalized spectrum distribution. Closer to 1 is the value that more often appears, so the reddish values correspond to the mean dominant velocities of the sea surface during measurement. The average Doppler spectra, leftmost plot, illustrate the spatial distribution of velocity, which is dominated by wave propagation outside the breaking zone. Their common feature is a slow reduction of velocity as the waves propagate towards the shore (all the velocities are positives), which becomes clearer in the normalized average Doppler spectra, second from left. The most varied of the radar spectra are concentrated within a narrow range of velocities. As the waves begin to break, the velocity distribution of the radar cells broaden and in the area (400 m - 800 m) where the breakers are dominant, the peak of the spectrum has moved towards the higher velocities, at the order of wave celerity. These are similar results to the conclusions of Lee et al. (1999), who did not interpret the second peak, the wave breakers. Moreover, in their case, the power of the second peak in comparison with the first peak is significantly lower. In this study, it is clear that the second peak is many times higher than the first one, as the probability of the waves to break is much higher in the breaking zone than randomly in the ocean. The broadness of the Doppler spectra is explained by Coakley et al. (2001), who concluded that the width of the Doppler spectra of the wave breakers depends on the motion of the roller, which is observed to move up and down the wave and to have velocity deviations in the order of 2 m/s, which is similar to this investigation; the breakers-related peaks are also broader than the peaks from the propagating waves.

The effects of normalization prior to averaging are obvious in the common plot of the two differently derived spectra: outside of the breaking zone, the main peak is of the same velocity, but in the breaking zone there is a clear separation. The velocity of the peak from normalized spectra is reduced, but remains at the same order of magnitude.

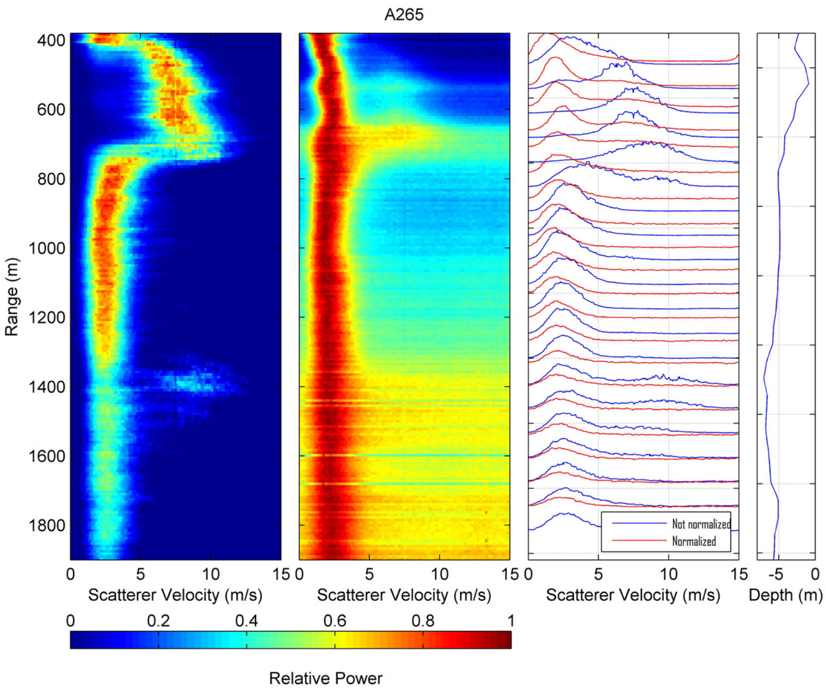


**Figure 5.9-1. Left: Normalized mean Doppler velocity distribution for each radar cell and for the whole radar range, equivalent to the mean Doppler spectra. Center: Normalized mean Doppler velocity distribution of the already normalized individual Doppler spectra for each radar cell and for the whole radar range. Right: Comparison between the results of the two different processing procedures and correlation with the underlying bathymetry. Dataset: A265.**

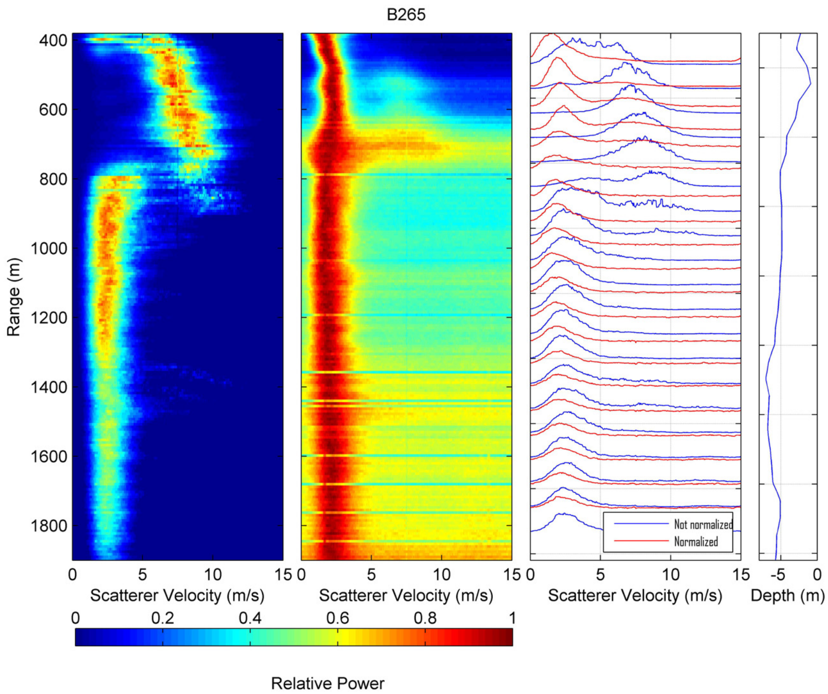


**Figure 5.9-2. Same key as caption of figure 5.9-1. Dataset: B265.**

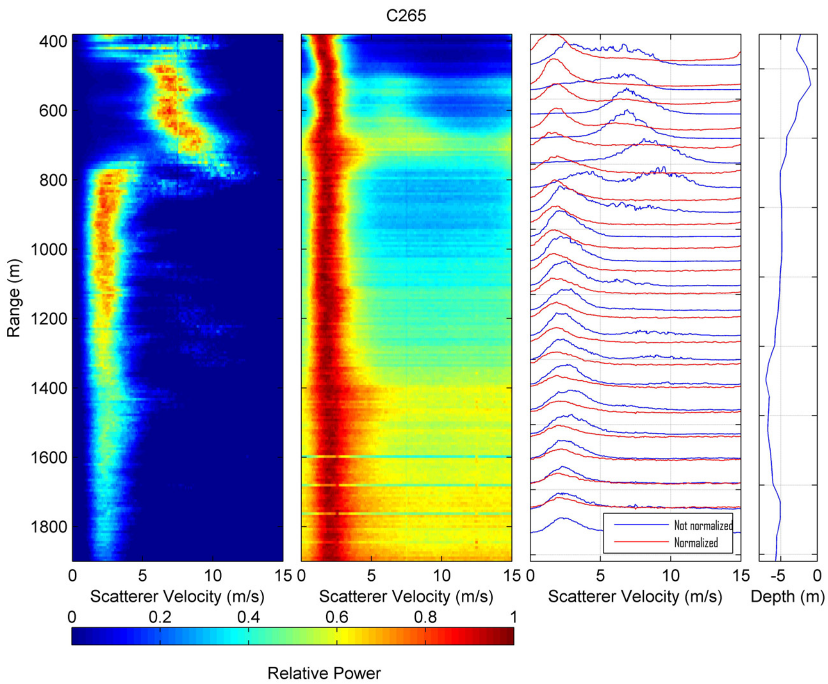


**Figure 5.9-3. Same key as caption of figure 5.9-1. Dataset: C265.**

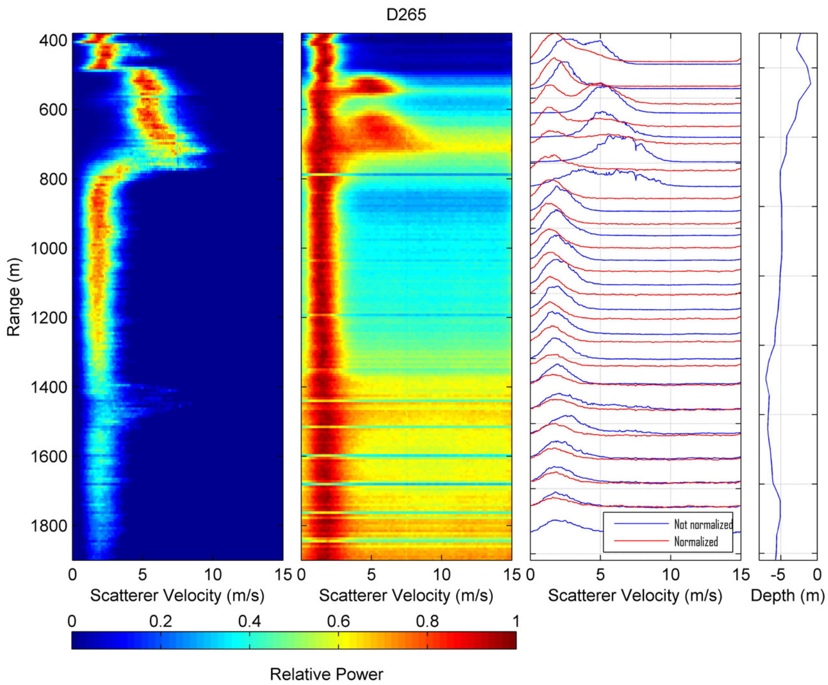


**Figure 5.9-4. Same key as caption of figure 5.9-1. Dataset: D265.**

By establishing a concrete method for the determination of the waves velocity, a calculation of the wave energy is possible and based on that the wave energy dissipation can be estimated. For the calculation of wave energy the wind drift velocity has been subtracted from the radial velocity and the result has been transferred to heave, similar to section 5.8. For the calculation of the energy, the equation: $E = \frac{1}{2}\rho g\left(\frac{H}{2}\right)^2$ is applied, Boccotti (2000), energy per square meter of the sea surface. The results for three distances (nearest to the shore, outside of the breaking zone, furthest possible offshore) from the radar and for the four different wave conditions are tabulated in table 5-7.

The results prove that the dissipated energy of the wave field between the further seaward radar cell and the closest to the shoreline depends on the actual wave conditions. For dataset A265, which was acquired during the most severe wave conditions ($H_s$ =5 m), 87% of the wave energy is dissipated during the last 1.5 km towards the coast; 46% of the wave energy dissipated by the bottom friction and random breakers and the remaining 41% in the breaking zone. For dataset D265 ($H_s$ = 2 m) more than 80% of the wave energy is lost over the last 1.5 km towards the shore, but only 35% of the energy is dissipated outside the breaking zone and more than the 45% in the breaking zone. The results from the two other datasets, B265 and C265, acquired when the significant wave height was 4 m and 3 m respectively, straddle the results of A265 and D265.

The results from estimation of the wave energy and its decay confirm and extend the conclusion from analysis of the normalized radar cross-section, figure 5.5-20; where it proved that the lower the wave the closer it breaks to the sand bar than to the shore. In this section, it proves, with independent measurements, that the lower the wave height the more energy is released on the sand bar.

**Table 5-7. Estimated wave energy for three radar grid cells, based on the measured radial Doppler velocities and percentages of the dissipated energy between the same points.**

| Id. No. | Wave energy ($J/m^2$) | | | Dissipated energy (%) between | |
|---|---|---|---|---|---|
| | Nearshore (475 m) | Outside breaking zone (975 m) | Offshore (1990 m) | Offshore & nearshore | Offshore & breaking zone |
| A265 | 3446 | 14003 | 26064 | 87 | 46 |
| B265 | 3923 | 13975 | 24271 | 84 | 42 |
| C265 | 3280 | 12365 | 21793 | 85 | 43 |
| D265 | 2511 | 8386 | 12928 | 81 | 35 |

# 6 Summary, conclusions and outlook

This dissertation has presented a study on microwave scattering from sea waves in the littoral zone. The motive behind this study is that ground based microwave remote sensing is a relatively inexpensively established tool that combines the benefits of in-situ sensors and remote sensing; by providing time series with high sampling frequency of area-wide phenomena, such as the wave field propagation. It has been shown and already used operationally, that microwave remote sensing provides wave related parameters over a relatively large domain, but also on the local scale. This investigation extends these applications and the potential applicability of ground based remote sensing to the inverse modeling of the wave field for determination of local bathymetry and current field, chapter 4, and to the estimation of the deterministic and stochastic properties of individual waves and the wave field as it propagates over and interacts with an inhomogeneous sea bottom, chapter 5. To achieve progress in this subject, different analytical techniques were developed, integrated with existing ones and applied to interpret the radar measurements. Based on the analysis and the results, the following conclusions are drawn and ideas for future development are generated.

## 6.1 Inversion of the wave field for the monitoring of the bathymetry and current field

The determination of bathymetry based on an inversed modeling of the wave group has been under investigation over the last decade, mainly by two groups worldwide. In this study both methods, DiSC and Bell’s, have been applied. Within the scope of this investigation, the objectives were validation of a linear version of DiSC and the modified solitary inversion by Bell’s method by their comparison with a non-linear extension of the DiSC and an oceanographic application of the method for monitoring the bathymetry and current field during a storm.

The two first objectives have been fulfilled with a similar approach. The performance of both methods was examined by comparison with echosoundings and by analyzing the same radar data with similar methodologies; the imaged area is inhomogeneous, there are two deep channels and sand reefs. The accuracy of a linear version of DiSC over the whole area is higher than 90%, but it decreases to 50% over steep sea bottom slopes and in the deeper areas where the waves are not impacted by the local depth. Bell's method has approximately 80% accuracy, which is independent of the local bathymetric gradient, but it decreases in the deeper areas as well. The main difference between the two methods is an inversed wave model; it assumes linear wave dispersion for the DiSC and modified linear dispersion with the solitary theory for Bell's method. A comparison of the two methods demonstrates differences with two levels of implementation and efficiency for the determination of the bathymetry. Since the two algorithms have been implemented by two different groups at different test sites, there are significant differences. The error of one grid cell of DiSC is spatially correlated only with one neighboring grid cell, on the contrary, the error of the Bell's method has a significant correlation with several neighboring grid cells and it propagates in the occurred bathymetric grid. A comparison on their performance shows that their common source of error is the physical limitation due to the wave length and bathymetric gradient decreases the accuracy of the DiSC, but does not impact the accuracy of the Bell's. Due to the assumed models, the DiSC performs better in deeper and homogeneous areas than Bell's method, which performs better in the shallower areas.

Due to the promising results of this comparison and of other publications in which different non-linear wave theories have been inverted for the determination of local bathymetry, DiSC is extended by three non-linear wave theories; which is the third objective of the study. Two of them are composite models and extensions of linear theory, modified by the solitary theory (the same as Bell's method), CHB, and a modified fifth order Stokes theory, CKD. The third model is a modified cnoidal model for shallow water, MCN. Their application shows that the MCN presents significant results only in the very shallow areas, where it performs better than the other three models. Linear, CHB and CKD have similar accuracies of approximately 80% - 90%. The linear model is more accurate in the deeper areas, but the CHB and CHD are impacted less by the sea bottom gradient and have higher accuracy than the linear model in the shallower areas.

In summary, the lesson from both comparisons is that selection of the appropriate wave model should be based on the specific characteristics of the area under investigation; for instance, in very shallow areas, the waves should be inverted with a non-linear theory for the determination of bathymetry. In addition, a similar performance of linear and modified linear approaches suggests the adaptation of one of these models and tuning of the algorithm. Based on the overall experience, for a strand plain coastal area the most suitable model is the linear, because inversion has the minimum calculation cost, but delivers a similar accuracy. Therefore, for monitoring of the storm in February 2002, the linear version of DiSC was applied.

This application, the fourth objective of the investigation, illustrates clearly the effect of a severe storm on the local bathymetry. Over a period of ten days, 50000 $m^3 \pm 10\%$ of sediment migrated, which is approximately 8% of the annual movement of sediment. In parallel, the current field was monitored with the same instrument and is also output by DiSC. Therefore, the normal tidal current conditions and the impact on the current field of a low pressure front trespassing were monitored. With typical in-situ instrumentation, observations of the bathymetry and current field are impossible to implement under such meteorological conditions with such high spatial and temporal resolution. This example confirms an excellent microwave remote sensing application by demonstrating the high potential of this tool for coastal monitoring.

## 6.2 Monitoring of the littoral wave field propagation

The monitoring of the wave field by a coherent X-band radar system, horizontally polarized and directed against the wave propagation direction revealed some scientific information about the backscattered signal, but mainly about the ongoing hydrodynamic phenomena in the littoral zone. Since this is one of the few experiments in which this kind of data were acquired to extract oceanographic knowledge, it was essential beforehand to integrate existing analytical methods with new ideas. Therefore, there are both important algorithmic innovations and oceanographic results.

In the methodology, the fifth objective to be fulfilled, there are two main achievements. The first innovation is a separation of the illuminated areas from the shadowed areas for the calculation of Doppler velocity. It proved that the signal of the shadowed areas is of the same order as the noise of the radar system and it has a high temporal variation, which generates Doppler velocities in the order of twice the Nyquist frequency. A separation is achieved by two independent methods: in the temporal domain by examining the stored intensity, and in the frequency domain by examining the width of the Doppler spectra; the two methods have equivalent results. Even though the effect of the shadow is known and extensively investigated, it is systematically ignored, e.g. Satake et al. (2009), introducing bias and calculation of the Doppler velocities to be extremely high to have any physical meaning. The second methodological innovation is the identification of the number of the peaks in the Doppler spectra and the adaption of peaks separation based on a pyramid-feature segmentation algorithm. Thus, the separation of different scatterers velocities is implemented. This algorithm is well-established and well-known, Burt (1984), but it is the first time that has been used successfully in this kind of analysis.

From an observation of the wave field, there are important oceanographic conclusions with regards to the wave propagation and wave breaking related phenomena; the last two objectives of the study to be fulfilled. An indirect calculation of the phase velocity based on the rate of appearance in time and space of scatterers, is validated and proven as accurate. In all four wave conditions there is an overestimation of the order of 10%, which arose by the calculation of only one value for the whole radar range and also by the projection effect, in the case of wave imaging at an angle.

The radar radius was divided into ten subareas, in order to define in detail the governing properties of the coastal environment and observing system. The backscattering intensity of propagating waves is almost constant and ranges from -50 dB to -40 dB, which is independent of the grazing angle. Wave breaking related phenomena, wave steepness, breakers and foam, increase the backscattered intensity, with a maximum value of approximately -16 dB and a mean value of approximately -24 dB. Since a sand reef dominates wave breaking, an identification of a relation between the grazing angle and the intensity is impossible. The distribution of NRCS proved strongly non-Gaussian, except for cases with a larger grazing angle outside the breaking zone, where the NRCS follows weak non-Gaussian distribution. The littoral zone scattering was also analyzed using joint histograms of NRCS and Doppler velocities that are measured for each pixel in the radar images. Two main clusters in the distributions were shown. The first cluster includes radar grid cells with low NRCS and low Doppler velocity; which is present in the whole radar range. In all cases, the velocity depends on the wave height and the wind drift; both of them are different in the four demonstrated cases. The calculation of radial velocity spectra proves that the peak frequency remains almost constant for the whole radar range, but the energy density depends on the actual wind and wave conditions as well as the existence or absence of wave breaking phenomena. By assuming the validity for the equation of horizontal particle velocity for transitional depth, the radial velocity transferred into heave and its spectrum has been estimated for the radar data outside the permanent breaking zone. In comparison with buoy measurements, it proved that the spectra of both data and shadow mask have an identical peak frequency with the wave heave spectra. Moreover, the power density of the peak frequency was proven to be approximately 40% higher than that the measured by the buoy, independent of the dominant wave conditions. This is a strong indication of the applicability of the calibration of each footprint of the radar, acting as an independent wave measuring device.

The second cluster of the joint histograms demonstrates pixels with high NRCS and high Doppler velocities. Those distributions appear mainly at depths where wave breakers were expected to be observed; in the case of a 5 m significant wave height, they appear at four different spots from the radar and only once when the $H_s$ is equal to 2 m. The backscatter intensity is about -28 dB and the corresponding velocity approximately equal to the phase velocity of the waves, which is that expected of wave breakers. A distribution of velocity over the breaking zone is the following: At the beginning, the velocity increases, reaches a maximum value and then there is a fast decay of the observed horizontal velocity which probably corresponds to the different phases of the wave breaking: steepening, breaking and foaming. Due to the lack of in-situ data, this remains a reasonable assumption. By knowing the threshold over which wave breaking is expected to be observed, the number of breaking-related events during the observation period is measured for each sub-region. The higher waves dissipate their energy along the whole radar range and finally break on the sand reef, as opposed to the smaller waves, which release their energy by breaking directly on the submerged sand bar or even closer to the shoreline; the observed breaking events are 15% more for the case of a 2 m significant wave height, D265, than the case of a 5 m significant wave height, A265. The integration of those observations and the adaptation of the algorithm for separation of the velocities in the same spectrum, permit the calculation of dissipated energy due to bottom friction by calculating the reduction of kinetic energy along the radar radius. In this experiment, it proved that approximately 35% to 45% of the wave energy is dissipated due to random wave breakers and bottom friction, while approximately 40% to 45% is lost in the breaking zone.

In this section, it is proven that the monitoring of the wave field by ground based radar provides quantitative oceanographic information, even in the challenging littoral environment. It is possible to determine the sea surface velocity and to analyze it to component velocities, to measure the wave breaking events and based on those quantities, to estimate the wave energy decay.

## 6.3 Outlook

In the previous sections, 6.1 and 6.2, the two initial scientific questions were answered. In the context of further research, amelioration of the methods and their application the following approaches are suggested.

The conclusion of this study signifies the completion of a decade of fruitful research to invert wave propagation for the determination of the bathymetry and the current field. This is the second doctorate dissertation, after Senet (2004), and there are more than ten publications focused on this subject. The Dispersive Surface Classificator has been brought to its final version. The signal processing algorithm, the inversion algorithm, and the suitability of selected wave models have been extensively tested. Therefore, DiSC may now be considered an oceanographic instrument. With this perspective, the system forms part of the Coastal Observation System for Northern and Arctic Seas (COSYNA), Riethmuller et al. (2009), and is applied quasi-operationally for the bathymetric monitoring of coastal areas with high bathymetric variation. The remaining task is the universal acceptance of DiSC and an extended deployment and application of the system, which will answer the open questions and probably generate more.

Although this study provides a concrete methodology for monitoring the littoral wave field with Dopplerized radar and illustrates significant results, further research in the field is essential. A calibration and validation of the Doppler velocity spectra requires an array of wave probes parallel to the radar beam, thus a virtual array of wave buoys could be calibrated and provide more than 200 simultaneous and independent wave measurements. In addition, a comparison of radar Doppler velocities with sea bottom current meters, e.g. acoustic Doppler velocimeters, would contribute to a more precise separation of the horizontal velocity components and clarify in detail the waves’ transformation and the wave breaking mechanisms. Moreover, a simultaneous monitoring of the same area with optical sensors and/or with radar systems horizontally and vertically polarized would help discriminate between the different sea surface backscattering features.

A concrete remark of the present investigation is that ground-based X-band remote sensing should be considered a multipurpose oceanographic tool with established applications and great potential for further development. It has already been applied to determine the significant wave height and wave direction, e.g. WaMoS, Ziemer (1995), for the retrieval of the ocean wind field, Dankert et al. (2003), for the measurement of the current field during low wind and wave conditions, e.g. Plant et al. (2005) and Braun et al. (2008), during severe oceanographic conditions, the extraction of the local bathymetry, Senet et al. (2008) and the present investigation, as well as wave field transformations and wave breaking in the coastal zone, e.g. Farquharson et al. (2005) and the present study. All these quantities, phenomena and conditions, dominate the coastal environment. Therefore, an open issue is the integration of all the different data acquisition strategies and analytical algorithms under a common platform; for instance the adoption by DiSC of the instantaneous dispersion relation occurring from the Doppler measurements, for the determination of the bathymetry. This would make the ground based remote sensing a powerful tool, which covers all the essential measurements of the coastal environment, it will reduce the monitoring cost, it will extend calibration and validation of coastal hydrodynamic models and will boost the data assimilation of the prediction models. Thus, quantities required by coastal engineering, such as bottom shear stress and the probability of wave breaking, could be calculated more precisely or even measured, thereby enhancing the efficiency of coastal protection.

## References


Ahrendt, K., 2001. Expected effect of climate change on Sylt island: results from a multidisciplinary German project. Climate Research, 18(1-2): 141-146.

Alamsyah, N., 2008. Identification of geomophological dynamics from bathymetric time series acquired by radar, GKSS-Forschungzentrum Geesthacht GmbH · Geesthacht.

Allan, N., Trizna, D.B. and McLaughlin, D.J., 1998. Numerical comparison of techniques for estimating Doppler velocity time series from coherent sea surface scattering measurements. Radar, Sonar and Navigation, IEE Proceedings -, 145(6): 367-373.

Allan, N., Trump, C.L., Trizna, D.B. and McLaughlin, D.J., 1999. Dual-polarized Doppler radar measurements of oceanic fronts. Geoscience and Remote Sensing, IEEE Transactions on, 37(1): 395-417.

Alpers, W. and Hasselmann, K., 1978. The two-frequency microwave technique for measuring ocean-wave spectra from an airplane or satellite. Boundary-Layer Meteorology, 13(1): 215-230.

Alpers, W. and Hasselmann, K., 1982. Spectral signal to clutter and thermal noise properties of ocean wave imaging synthetic aperture radars. International Journal of Remote Sensing, 3: 423-446.

Alpers, W. and Hennings, I., 1984. A Theory of the Imaging Mechanism of Underwater Bottom Topography by Real and Synthetic Aperture Radar. J. Geophys. Res., 89.

Alpers, W., Ross, D. and Rufenach, C.J.G.R., 1981. On the detectability of ocean surface waves by real and synthetic aperture radar. Journal of Geophysical Research, 86 6481-6498.

Anonymous, 2003. Cfloor. Roxar Software Solutions AS, Oslo, pp. Seabed algorithm.

Backhaus, J., Hartke, D., Huebner, U., Lohse, H. and Mueller, A., 1998. Hydrographie und Klima im Lister Tidebecken. In: C. Gaetje and K. Reise (Editors), Oekosystem Wattenmeer-Austausch, Transport- und Stoffumwandlungsprozesse. Springer, Heidelberg, pp. 39- 54.

Barrick, D.E., 1968. Rough surface scattering based on the specular point theory. IEEE Trans. Antennas Propagat., AP-16: 449-454.

Battjes, J.A. and Janssen, J.P., 1978. Energy loss and set-up due to breaking of random waves, Proceedings 16th Conference on Coastal Engineering. Am. Soc. Civ. Eng., New York, pp. 569-587.

Bell, P., J. Williams, S. Clark, B. Morris and A. Vila-Concejo, 2004. Nested Radar Systems for Remote Coastal Observations. Journal of Coastal Research SI39: 5.

Bell, P.S., 1999. Shallow water bathymetry derived from an analysis of X-band marine radar images of waves. Coastal Engineering, 37(3-4): 513-527.

Bell, P.S., 2008a. Mapping shallow water coastal areas using a standard marine X-band radar. In: H. Atkinson (Editor), Hydro8. The Hydrographic Society UK, Liverpool.

Bell, P.S., 2008b. Mapping the bathymetry of the Dee estuary using wave inversions of marine radar image sequences, Ocean Sciences Meeting. American Society of Limnology and Oceanography, American Geophysical Union, The Oceanography Society and Estuarine Research Federation, Orlando, pp. 498.

Boccotti, P., 2000. Wave mechanics for ocean engineering. Elsevier oceanography series, 64. Elsevier, Amsterdam.

Booij, N., 1981. Gravity waves on water with non-uniform depth and current. PhD Thesis, University of Technology., Delft

Borge, J.C.N., Reichert, K. and Dittmer, J., 1999. Use of nautical radar as a wave monitoring instrument. Coastal Engineering, 37(3-4): 331-342.

Borge, J.N., Ziemer, F., Seemann, J. and Senet, C., 1998. Overcome of the Nyquist in frequency in nautical radar measurement of wave fields, 17th OMAE Conference.

Boussinesq, J., 1872. Theorie des ondes et des resous qui s propagent le long d' un canal rectangulaire horizontal, en communiquant au liquide contenu dans ce canal des vitesses sensiblement pareilles de la surface au fond. Journal de Math. Pures et Appl., 17: 55-108.

Braun, N., Ziemer, F., Bezuglov, A., Cysewski, M. and Schymura, G., 2008. Sea-Surface Current Features Observed by Doppler Radar. Geoscience and Remote Sensing, IEEE Transactions on, 46(4): 1125-1133.

Brown, W., Munk, W., Snodgrass, F., Mofjeld, H. and Zetler, B., 1975. MODE Bottom Experiment. Journal of Physical Oceanography, 5(1): 75-85.

BSH, 2009. Seegangsstatistik der Messstationen in der Deutschen Bucht Bundesamt für Seeschifffahrt und Hydrographie.

Burt, P., 1984. The pyramid as structure for efficient computation. In: A. Rosenfeld (Editor), Multiresolution Image Processing. Springer Series in Information Science. Springer, pp. 6-35.

Caponi, E.A., Lake, B.M. and Yuen, H.C., 1999. Hydrodynamic effects in low-grazing angle backscattering from the ocean. Antennas and Propagation, IEEE Transactions on, 47(2): 354-363.

Catalán, P., Haller, M., Holman, R. and W., P., 2008. Surf zone breaking wave identification using marine radar, 31st ICCE ASCE, Hamburg.

Catalan, P.A. and Haller, M.C., 2008. Remote sensing of breaking wave phase speeds with application to non-linear depth inversions. Coastal Engineering, 55(1): 93-111.

Cherry, J.A., 1994. Distortion analysis of weakly nonlinear filters using volterra series, Ottawa.

Chorin, A.J. and Marsden, J.E., 2000. A Mathematical Introduction to Fluid Mechanics. Texts in Applied Mathematics 4.

Chowdhury, M., 2007. Assessment of water flow and the impact on sediment motion in a tidal channel of north Sylt basing on radar observation, Christian Albrecht University of Kiel, Kiel.

Coakley, D.B. et al., 2001. Electromagnetic scattering from large steady breaking waves. Experiments in Fluids, 30(5): 479-487.

Cooley, J. and Tuckey, J., 1965. An algorithm for the machine calculation of complex Fourier series. Mathematics of Computation, 19: 297-301.

Cysewski, M., Ziemer, F. and Schymura, G., 2008. First Experiences and Application for Radar Doppler Current Profiler. In: H. Atkinson (Editor), Hydro8. The Hydrographic Society UK, Liverpool.

Cysewski, M.C., 2003. Radarscanning in der Hydrographie Diploma Thesis, HafenCity Universität, Hamburg, 96 pp.

Dankert, H., 2004. Measurement of waves, wave groups and wind fields using nautical radar-image sequences University of Hamburg, Hamburg.

Dankert, H., Horstmann, J. and Rosenthal, W., 2003. Ocean wind fields retrieved from radar-image sequences. J. Geophys. Res., 108.

Dano, E.B. et al., 2001a. Radar backscatter from mechanically generated transient breaking waves. II. Azimuthal and grazing angle dependence. Oceanic Engineering, IEEE Journal of, 26(2): 201-215.
Dano, E.B., Lyzenga, D.R. and Perlin, M., 2001b. Radar backscatter from mechanically generated transient breaking waves. I. Angle of incidence dependence and high resolution surface morphology. Oceanic Engineering, IEEE Journal of, 26(2): 181-200.
Dean, R.G. and Dalrymple, R.A., 2004. Coastal Processes with Engineering Applications Cambridge University Press
Dette, H.H., Peters, K. and Newe, J., 1998. MAST III-SAFE Project: Data Documentation, Large Wave Flume Experiments '96/97, Leichtweiss-Institute, Technical University Braunschweig.
Dickman, S.R., 1988. Theoretical Investigation of the Oceanic Inverted Barometer Response. J. Geophys. Res., 93.
Dietz, C. and Heck, H.-L., 1952. Geologische Karte von Deutschland, Insel Sylt, Kiel, Landesanstalt für Angewandte Geologie.
Dingemans, M.W., 1997. Water wave propagation over uneven bottoms. Advanced Series on Ocean Engineering, 13. World Scientific, River Edge.
Doddy, P. et al., 2004. Living with coastal Erosion in Europe - Sediment and Space for Surtainability, Results from the Eurossion Study, Luxembourg.
Doodson, A.T., 1924. Meteorological perturbations of sea level and tides. Geophysical Supplement Monthly Notices of the Royal Astronomical Society, 124.
Dronkers, J., 2005. Dynamics of coastal systems. Advanced Series on Ocean Engineering, 25. World Scientific, New Jersey, London 519 pp.
Dugan, J., Piotrowski, C. and Williams, J., 2003. Water depth and surface currentretrievals from air-borne optical measurements of surface gravity wave dispersion. Journal of Geophysical Research - Oceans, 106(C8): 16 903-16 915.
Ebuchi, N., Kawamura, H. and Toba, Y., 1993. Physical Processes of Microwave Backscattering From Laboratory Wind Wave Surfaces. J. Geophys. Res., 98.
Elachi, C. and Brown, W., Jr., 1977. Models of radar imaging of the ocean surface waves. Oceanic Engineering, IEEE Journal of, 2(1): 84-95.
Ericson, E.A., Lyzenga, D.R. and Walker, D.T., 1999. Radar backscatter from stationary breaking waves. Journal of Geophysical Research, 104 29679- 29695.
Ernstsen, V. et al., 2006. Precision of high-resolution multibeam echo sounding coupled with high-accuracy positioning in a shallow water coastal environment. Geo-Marine Letters, 26: 141-149.
Evmenov, V.F., Kozhukhov, I.V., Nichiporenko, N.T. and Khulop, G.D., 1973. Test of the radar method of defining ocean wave elements. Fluid Mechanics - Soviet research, 2(5): 141-145.
Farquharson, G., Behn, M., Perkovic, D., Culcuoglu, Z. and Frasier, S.J., 2004. Microwave radar remote sensing of surface currents in the nearshore region, Geoscience and Remote Sensing Symposium, 2004. IGARSS '04. Proceedings. 2004 IEEE International, pp. 1160-1163.
Farquharson, G., Frasier, S.J., Raubenheimer, B. and Elgar, S., 2005. Microwave radar cross sections and Doppler velocities measured in the surf zone. J. Geophys. Res., 110.

Flampouris, S., Bell, P.S. and Ziemer, F., 2009a. Überwachung der Bathymetrie durch Invertierung der Propagation von Schwerewellen, Symposium Geoinformationen für die Küstenzone, Hamburg.

Flampouris, S., Seemann, J. and Ziemer, F., 2009b. Sharing our experience using wave theories inversion for the determination of the local depth, OCEANS 2009-EUROPE, 2009. OCEANS '09., pp. 1-7.

Flampouris, S., Seemann, J. and Ziemer, F., 2010. Observation of littoral hydrodynamics by ground based Dopplerized X-band Radar, Ocean Sciences Meeting, Portland.

Flampouris, S. and Ziemer, F., 2006. Comparison of bathymetric changes observed by radar on different time scales, SeaTech Week, Brest.

Flampouris, S., Ziemer, F. and Schymura, G., 2008a. High temporal and spatial resolution monitoring of the bathymetry and current field in coastal areas by using ground based X-band radar, Ocean Sciences Meeting, Orlando.

Flampouris, S., Ziemer, F. and Seemann, J., 2007. Survey of bathymetry and current fields by radar image series acquired by shore based x-band radar, Geoscience and Remote Sensing Symposium, 2007. IGARSS 2007. IEEE International, pp. 3579-3582.

Flampouris, S., Ziemer, F. and Seemann, J., 2008b. Accuracy of Bathymetric Assessment by Locally Analyzing Radar Ocean Wave Imagery (February 2008). Geoscience and Remote Sensing, IEEE Transactions on, 46(10): 2906-2913.

Flampouris, S., Ziemer, F. and Seemann, J., 2008c. Observation of storm impact on the bathymetry and the current field in local scale by radar. Submitted.

Flampouris, S., Ziemer, F. and Seemann, J., 2009c. Observing littoral waves by doppler radar, IGARSS, Capetown

Frasier, S. and McIntosh, R., 1995. Three dimensional spectra of X-band Doppler radar backscatter from the ocean surface, IEEE International Geoscience and Remote Sensing Symposium, pp. 1370-1374.

Frasier, S.J., Liu, Y. and McIntosh, R.E., 1998. Space-time properties of radar sea spikes and their relation to wind and wave conditions. J. Geophys. Res., 103.

Fu, L.-L. and Pihos, G., 1994. Determining the response of sea level to atmospheric pressure forcing using TOPEX/POSEIDON data. J. Geophys. Res., 99.

Fuchs, J., Regas, D., Waseda, T., Welch, S. and Tulin, M.P., 1999. Correlation of hydrodynamic features with LGA radar backscatter from breaking waves. Geoscience and Remote Sensing, IEEE Transactions on, 37(5): 2442-2460.

Galal, E.M. and Takewaka, S., 2008. Longshore migration of shoreline mega-cusps observed with X-band radar. Coastal Engineering Journal, 50(3): 247-276.

Gibbard, P.L., Boreham, S., Cohen, K.M. and Moscariello, A., 2005. Global chronostratigraphical correlation table for the last 2.7 million years. Boreas 34

Gommenginger, C.P., Ward, N.P., Fisher, G.J., Robinson, I.S. and Boxall, S.R., 2000. Quantitative Microwave Backscatter Measurements from the Ocean Surface Using Digital Marine Radar Images. Journal of Atmospheric and Oceanic Technology, 17(5): 665-678.

Goodman, J., 1976. Some fundamental properties of speckle. J. Opt. Soc. Am., 66: 1145-1150.

Gronlie, O., 1995. Microwave Radar Directional Wave Measurements - MIROS Results. 32, WMO Geneva.

Guenther, H. and Rosenthal, W., 1995. A wave model with a nonlinear dissipation source function, 4th International Workshop on Wave Hindcasting and Forecasting, pp. 138-147.

Haller, M.C. and Lyzenga, D.R., 2003. Comparison of radar and video observations of shallow water breaking waves. Geoscience and Remote Sensing, IEEE Transactions on, 41(4): 832-844.

Hara, T. and Plant, W., 1994. Hydrodynamic modulation of short windwave spectra by long waves and its measurement using microwave backscatter. Journal of Geophysical Research, 99: 9767-9784.

Hasan, G.M.J. and Takewaka, S., 2007 Observation of a stormy wavefield with X-band radar and its linear aspects. Coastal Engineering Journal (CEJ), 49 (2): 149 - 171.

Hasselmann, K., 1971. Determination of ocean wave spectra from {D}oppler radio return from the sea surface. Nature Physical Science, 229: 16-17.

Hasselmann, K. et al., 1978. Radar measurements of wind and waves. Boundary-Layer Meteorology, 13(1): 405-412.

Hasselmann, K. and Hasselmann, S., 1991. On the nonlinear mapping of an ocean wave spectrum into a synthetic aperture radar image spectrum. J. Geophys. Res. , 96: 10 713 -10 729.

Havlicek, J. and Bovik, A., 1995. AM-FM models, the analytic image, and nonlinear demodulation techniques. TR-95-001, Laboratory for Vision Systems, University of Texas, Austin.

Havlicek, J., Bovik, A. and Chen, D., 1973. AM-FM Image modeling and Gabor Analysis, Visual information representation, Communication, and Image processing. Optical Engineering, pp. 391-398.

Havlicek, J., Harding, D. and Bovik, A., 1996. The multicomponent AM-FM image representation. IEEE Trans. on Image Processing, 5: 1094-1100.

Havlicek, J., Harding, D. and Bovik, A., 2000. Multodomensional quasi-eigenfunction approximations and multicomponent AM-FM models. IEEE Transactions on Image Processing 9: 227-242.

Hayes, M.O., 1979. Barrier island morphology as a function of tidal and wave regime. In: S.P. Leatherman (Editor), Barrier Islands,. Academic Press, New York, pp. 1-27.

Headland, J.R. and Chu, H.L., 1984. A numerical model for refraction of linear and cnoidal waves, 19th International Conference on Coastal Engineering, Houston.

Heathershaw, A.D., Blackley, M.W.L. and Hardcastle, P.J., 1979. Wave direction estimates in coastal waters using radar. Coastal Engineering, 3: 249-267.

Hedges, T.S., 1976. An empirical modification to linear wave theory. Proceedings of the Institution of Civil Engineers, 61 (2): 575-579

Hedges, T.S., 1987. Combinations of waves and current:s an introduction. Proceedings Institution of Civil Engineers, 82: 567-585.

Hedges, T.S., 1995. Regions of validity of analytical wave theories. Proc. Instn Civ. Engrs Wut., Marit. & Energy, 112,(111-114).

Hedges, T.S., 2009. Discussion of "A function to determine wavelength from deep in to shallow water based on the length of the cnoidal wave at breaking" by J.P. Le Roux. Coastal Engineering, 56(1): 94-95.

Hennings, I., 1990. Radar Imaging of Submarine Sand Waves in Tidal Channels. J. Geophys. Res., 95.

Hennings, I., 1998. An historical overview of radar imagery of sea bottom topography. International Journal of Remote Sensing, 19: 1447-1454.

Hennings, I. and Herbers, D., 2006. Radar imaging mechanism of marine sand waves at very low grazing angle illumination caused by unique hydrodynamic interactions. J. Geophys. Res., 111.

Hennings, I., Herbers, D., Prinz, K. and Ziemer, F., 2004. On waterspouts related to marine sandwaves. In: G.T. Hulscher S., Idier D. (Editor), Marine Sandwave and River Dune Dynamics International Workshop, University of Twente, Enschede, The Netherlands, pp. 351.

Herbers, T.H.C., Elgar, S., Guza, R.T. and O'Reilly, W.C., 2006. Surface gravity waves and nearshore circulation. DUCK94 Experiment Data Server: SPUV Pressure Sensor Wave Height Data. U.S. Army Corps of Engineers.

Hessner, K. and Bell, P., 2009. High resolution current & bathymetry determined by nautical X-Band radar in shallow waters, OCEANS 2009-EUROPE, 2009. OCEANS '09., pp. 1-5.

Hessner, K., Reichert, K. and Dannenberg, J., 2006. 2D Surface Elevation Measurements by means of X-band Radar, 9th International Workshop on Wave Hindcasting and Forecasting, Victoria, BC, Canada.

Hirakuchi, H. and Ikeno, M., . 1990 Wave direction measurement using marine X-band radar, 22nd ICCE, Delft, pp. 703-715.

Holland, T.K., 2001. Application of the linear dispersion relation with respect to depth inversion and remotely sensed imagery. Geoscience and Remote Sensing, IEEE Transactions on, 39(9): 2060-2072.

Holman, R. and Stanley, J., 2007. The history and technical capabilities of Argus. Coastal Engineering, 54.

Hoogeboom, P. and Rosenthal, W., 1982. Directional wave specta in radar images, IGARSS. IEEE.

Hwang, P.A., Sletten, M.A. and Toporkov, J.V., 2008a. Analysis of radar sea return for breaking wave investigation. J. Geophys. Res., 113.

Hwang, P.A., Sletten, M.A. and Toporkov, J.V., 2008b. Breaking wave contribution to low grazing angle radar backscatter from the ocean surface. J. Geophys. Res., 113.

Hyunjun, K. and Johnson, J.T., 2002. Radar image study of simulated breaking waves. Geoscience and Remote Sensing, IEEE Transactions on, 40(10): 2143-2150.

Irani, G., Gotwols, B. and Bjerkaas, A., 1986. The 1978 Ocean Wave Dynamics Experiment, Optical and In Situ Measurement of the Phase Velocity of Wind Waves, Wave Dynamics and Radio Probing of the Ocean Surface. Plenum Press, pp. 165-179.

Jaehne, B., Haussecker, H. and Geissler, P., 1999 Spatial and Fourier Domain, Handbook of Computer Vision and Applications Signal Processing and Pattern Recognition. Academic Press, pp. 35-66.

Jenkins, G.M. and Watts, D.G., 1968. Spectral analysis and its applications. Holden-Day series in time series analysis. Holden-Day, San Francisco.

Jessup, A.T., Melville, W.K. and Keller, W.C., 1991. Breaking Waves Affecting Microwave Backscatter 1. Detection and Verification. J. Geophys. Res., 96.

Jonsson, I.G., 1990. Wave-current interactions. In: B. Le Mehaute and D.M. Hanes (Editors), Ocean engineering science. John Wiley & Sons, Inc., New York.

Kakoulaki, G., 2009. Study of the interraction between the current field and structures in the bathymetry in a tidal inlet, Christian Albrechts University, Kiel.

Kalmykov, A.I. and Pustovoytenko, V.V., 1976. On Polarization Features of Radio Signals Scattered From the Sea Surface at Small Grazing Angles. J. Geophys. Res., 81.

Kappenberg, J., Fanger, H.-U. and Mueller, A., 1998. Currents and suspended Particulate matter in tidal channels of the Sylt- Rømø basin. Senckenbergiana maritima, 29: 93-100.

Kim, Y.C. and Powers, E.J., 1979. Digital Bispectral Analysis and Its Applications to Nonlinear Wave Interactions. Plasma Science, IEEE Transactions on, 7(2): 120-131.

Kirby, J.T. and Dalrymple, R.A., 1986. An approximate model for nonlinear dispersion in monochromatic wave propagation models. Coastal Engineering, 9(6): 545-561.

Koester, R., 1974 Geologie des Seegrundes vor den Nordfriesischen Inseln Sylt und Amrum. Meyniana 24 27-41.

Korteweg, D.J. and DeVries, G., 1895. On the change of form of long waves advancing in a canal, and on a new type of long stationary waves. Phil. Mag, , 39: 422-443.

Krishen, K., 1971. Correlation of radar backscatter cross-sections with ocean wave height and wind velocity. Journal of Geophysical Research., 76: 6528-6539.

Lamont-Smith, T., 2008. Azimuth dependence of Doppler spectra of sea clutter at low grazing angle. Radar, Sonar & Navigation, IET, 2(2): 97-103.

Lamont-Smith, T., Waseda, T. and Rheem, C.K., 2007. Measurements of the Doppler spectra of breaking waves. Radar, Sonar & Navigation, IET, 1(2): 149-157.

Lange, P. and Huehnerfuss, H., 1978. Drift Response of Monomolecular Slicks to Wave and Wind Action. Journal of Physical Oceanography, 8(1): 142-150.

Le Roux, J.P., 2007. A function to determine wavelength from deep into shallow water based on the length of the cnoidal wave at breaking. Coastal Engineering, 54(10): 770-774.

Lee, P.H.Y., 1977. Doppler measurements of the effects of gravity waves on wind-generated ripples. Journal of Fluid Mechanics Digital Archive, 81(02): 225-240.

Lee, P.H.Y. et al., 1995a. Power spectral lineshapes of microwave radiation backscattered from sea surfaces at small grazing angles. Radar, Sonar and Navigation, IEE Proceedings -, 142(5): 252-258.

Lee, P.H.Y. et al., 1995b. X band microwave backscattering from ocean waves. J. Geophys. Res., 100.

Lee, P.H.Y. et al., 1996. Dependence of polarimetric Doppler spectra on breaking-wave energy, Geoscience and Remote Sensing Symposium, 1996. IGARSS '96. 'Remote Sensing for a Sustainable Future.', International, pp. 2201-2203 vol.4.

Lee, P.H.Y. et al., 1999. What are the mechanisms for non-Bragg scattering from water wave surfaces? Radio Sci., 34.

Lee, P.H.Y. et al., 1998a. Scattering from breaking gravity waves without wind. Antennas and Propagation, IEEE Transactions on, 46(1): 14-26.

Lee, P.H.Y., Barter, J.D., Lake, B.M. and Thompson, H.R., 1998b. Lineshape analysis of breaking-wave Doppler spectra. Radar, Sonar and Navigation, IEE Proceedings -, 145(2): 135-139.

Lewis, B.L. and Olin, I.D., 1980. Experimental study and theoretical model of high-resolution radar backscatter from the sea. Radio Sci., 15.

Lindhorst, S., Betzler, C. and Hass, H.C., 2008. The sedimentary architecture of a Holocene barrier spit (Sylt, German Bight): Swash-bar accretion and storm erosion. Sedimentary Geology, 206(1-4): 1-16.

Liu, Y., Frasier, S.J. and McIntosh, R.E., 1998. Measurement and classification of low-grazing-angle radar sea spikes. Antennas and Propagation, IEEE Transactions on, 46(1): 27-40.
Louters, T. and Gerritsen, F., 1995. The riddle of the sands, National Institute for Coastal and Marine Management, Rijkswaterstaat, The Hague.
Lyzenga, D.R., Maffett, A.L. and Shuchman, R.A., 1983. The Contribution of Wedge Scattering to the Radar Cross Section of the Ocean Surface. Geoscience and Remote Sensing, IEEE Transactions on, GE-21(4): 502-505.
Massel, S.R., 1996. Ocean surface waves: Their physics and prediction. Advanced Series on Ocean Engineering 11 World Scientific, Singapore, New Jersey, London, Hong Kong.
Mattie, M.G. and Lee, H., D., 1978. The use of imaging radar in studying ocean, 16th ICCE. ASCE, pp. 174-189.
McCowan, J., 1891. VII. On the solitary wave. Philosophical Magazine Series 5, 32(194): 45 - 58.
McGranahan, G., D. Balk, and B. Anderson., 1999. Climate change and the risk of settlement in the low elevation coastal zone, World Bank, Washington, DC.
McGregor, J.A., Poulter, E.M. and Smith, M.J., 1998. S band Doppler radar measurements of bathymetry, wave energy fluxes, and dissipation across an offshore bar. J. Geophys. Res., 103.
McIntosh, R.E., Frasier, S.J. and Mead, J.B., 1995. FOPAIR: a focused array imaging radar for ocean remote sensing. Geoscience and Remote Sensing, IEEE Transactions on, 33(1): 115-124.
McLaughlin, D.J., Allan, N., Twarog, E.M. and Trizna, D.B., 1995. High resolution polarimetric radar scattering measurements of low grazing angle sea clutter. Oceanic Engineering, IEEE Journal of, 20(3): 166-178.
McNinch, J.E., 2007. Bar and Swash Imaging Radar (BASIR): A Mobile X-band Radar Designed for Mapping Nearshore Sand Bars and Swash-Defined Shorelines Over Large Distances. Journal of Coastal Research, 23(1): 59-74.
Mel'nichuk, Y.U. and Chernilrov, A.A., 1971. Spectra of radar signals from sea surface for different polarizations. Izvestia, Atmos. Oceanic Phys, 7: 28-40.
Melief, H.W., Greidanus, H., van Genderen, P. and Hoogeboom, P., 2006. Analysis of sea spikes in radar sea clutter data. Geoscience and Remote Sensing, IEEE Transactions on, 44(4): 985-993.
Moller, D., Mourad, P.D. and Prasier, S.J., 2000. Field observations of radar backscatter from the ocean surface under low wind speed conditions. J. Geophys. Res., 105.
Moore, R., 1985. Radar sensing of the ocean. Journal of Oceanic Engineering, 10: 84-112.
Mueller, M.J., 1980. Handbuch ausgewählter Klimastationen der Erde. Forschungsstelle Bodenerosion der Universität Trier., Trier.
Munk, W.H. and MacDonald, G.J., 1960. The Rotation of the Earth: A Geophysical Discussion. Cambridge University Press, New York, 323 pp.
Ochi, M.K., 1998. Probability distributions of peaks and troughs of non-Gaussian random processes. Probabilistic Engineering Mechanics, 13(4): 291-298.
Ochi, M.K. and Ahn, K., 1994. Probability distribution applicable to non-Gaussian random processes. Probabilistic Engineering Mechanics, 9(4): 255-264.
Oost, A.P. and Boer, P.L.d., 1994. Sedimentology and development of barrier islands, ebb-tidal deltas, inlets and backbarrier areas of the Dutch Wadden Sea. Senckenbergiana maritima, 24 65-115.

Oppenheim, A.V. and Lim, J.S., 1981. The importance of phase in signals. Proceedings of the IEEE, 69(5): 529-541.
Oudshoorn, H.M., 1961. The use of radar in hydrographic surveying In: J.W. Gohnson (Editor), 7th Conf. Coast. Eng. ASCE, pp. 59-76.
Peregrine, D.H., 1967. Long waves on a beach. Journal of Fluid Mechanics Digital Archive, 27(04): 815-827.
Pidgeon, V.W., 1968. Doppler Dependence of Radar Sea Return. J. Geophys. Res., 73.
Pierson, W.J., Neumann, G. and James, R.W., 1955. Practical methods for observing and forecasting ocean waves by means of wave spectra and statistics. 603, US Navy Hydrographic Office.
Pinet, P.R., 1999. Invitation to oceanography. Jones & Bartlett Pub, Sudbury, Massachussetts, 555 pp.
Piotrowski, C. and Dugan, J., 2002. Accuracy of bathymetry and current retrievalsfrom airborne optical time-series imaging of shoaling waves. IEEE Trans. Geosci. Remote Sens, 40(12): 2606-2618.
Plant, W., 1977. Studies of backscattered sea return with a CW, dual-frequency,<tex>X</tex>-band radar. Oceanic Engineering, IEEE Journal of, 2(1): 28-36.
Plant, W.J., 1997. A model for microwave Doppler sea return at high incidence angles: Bragg scattering from bound, tilted waves. J. Geophys. Res., 102.
Plant, W.J., Keller, W.C. and Hayes, K., 2005. Measurement of river surface currents with coherent microwave systems. Geoscience and Remote Sensing, IEEE Transactions on, 43(6): 1242-1257.
Plant, W.J. et al., 1999. Bound waves and Bragg scattering in a wind-wave tank. J. Geophys. Res., 104.
Ponte, R.M., 1994. Understanding the relation between wind- and pressure-driven sea level variability. J. Geophys. Res., 99.
Prandle, D., 2000. Operational oceanography -- a view ahead. Coastal Engineering, 41(1-3): 353-359.
Prandle, D. et al., 2000. Tide, wave and suspended sediment modelling on an open coast -- Holderness. Coastal Engineering, 41(1-3): 237-267.
Prasada Rao, C., 1988. Spectral width parameter for wind-generated ocean waves. Journal of Earth System Science, 97(2): 173-181.
Proudman, J., 1929. he effects on the sea of changes in atmospheric pressure. Geophysical Supplement Monthly Notices of the Royal Astronomical Society, 2(4): 197-209.
Puleo, J.A., Farquharson, G., Frasier, S.J. and Holland, K.T., 2003. Comparison of optical and radar measurements of surf and swash zone velocity fields. J. Geophys. Res., 108.
Reichert, K., Hessner, K. and Dittmer, J., 1999a. Wamos II: An operational wave monitoring system, Oceanology International '99,.
Reichert, K., Hessner, K., J.N. Borge and Dittmer, J., 1999b. Wamos II: A radar based wave and current monitoring system, ISOPE '99. 3, pp. 139-143.
Reichert, K., Hessner, K. and Lund, B., 2007. Coastal applications of X-band radar to achieve spatial and temporal surface wave monitoring, OCEANS 2007 - Europe, pp. 1-6.
Ridderinkhof, H., 1989. Tidal and residual flows in the western Dutch Wadden Sea III: Vorticity balances. Netherlands Journal of Sea Research, 24(1): 9-26.

Riethmuller, R., Colijn, F., Krasemann, H., Schroeder, F. and Ziemer, F., 2009. COSYNA, an integrated coastal observation system for Northern and Arctic Seas, OCEANS 2009-EUROPE, 2009. OCEANS '09., pp. 1-7.

Romeiser, R., Alpers, W. and Wismann, V., 1997. An improved composite surface model for the radar backscattering cross section of the ocean surface 1. Theory of the model and optimization/validation by scatterometer data. Geophysical Research, 102: 25237-25250.

Ross, J.C., 1854. On the effect of the pressure of the atmosphere on the mean level of the ocean. Philosophical Transactions of the Royal Society of London, 144: 285-296.

Ruessink, B.G., Bell, P.S., van Enckevort, I.M.J. and Aarninkhof, S.G.J., 2002. Nearshore bar crest location quantified from time-averaged X-band radar images. Coastal Engineering, 45(1): 19-32.

Salomons, W. et al., 2005. The Catchment to Coast Continuum, Coastal Fluxes in the Anthropocene, pp. 145-200.

Satake, M., Kawamura, S., Shusse, Y., Nakagawa, K. and Iguchi, T., 2009. Ocean surface backscattering at extremely low grazing angles observed by C-band polarimetric doppler weather radar, IEEE International Geoscience & Remote Sensing Symposium, Cape Town.

Savchenko, A.K., 1988. Measurement of some sea-surface parameters by X-band coherent radar. Radiophysics and Quantum Electronics, 31(6): 461-465.

Schneggenburger, C., Guenther, H. and Rosenthal, W., 1997. Shallow water wave modeling with nonlinear dissipation. Deutsche Hydrographische Zeitschrift / German Journal of Hydrography, 49(23): 14.

Schwarzer, K., 1984. Das Morsum-Kliff und seine Ausbreitung unter den nördlich vorgelagerten Wattsedimenten. In: E.T. Degens, G. Hillmer and C. Spaeth (Editors), Exkursionsführer Erdgeschichte des Nordsee-und Ostseeraumes. Geologisch-Paläontologisches Institut der Universität Hamburg, Hamburg pp. 251-282.

Sedlacek, S., 2007. Flächenhafte Abschätzung der Bodenschubspannung im Flachwasser mittels Dopplerradar University of Hamburg, Hamburg, 127 pp.

Seemann, J., 1997. The structure of wave number frequency spectra from radar image sequences of the sea surface, Geesthacht : GKSS, 172 pp.

Seemann, J. and Senet, C., 1999. make_carth_radar.pro. GKSS, V2T, Geesthacht, pp. Calculation of a cartesian image sequence by using the polar image sequence

Seemann, J., Senet, C., Dankert, H., Hatten, H. and Ziemer, F., 1999. Radar image sequence analysis of inhomogeneous water surfaces, SPIE'99 Conference - Applications of Digital Image Processing XXII, pp. 536-546.

Seemann, J., Senet, C. and Ziemer, F., 2000a. Local Analysis of Inhomogeneous Sea Surfaces in Coastal Waters Using Nautical Radar Image Sequences. In: G. Sommer, N. Krüger and C. Perwass (Editors), Mustererkennung 2000, 22. DAGM-Symposium. Springer, Berlin, pp. 179-186.

Seemann, J., Senet, C.M., Wolff, U., Hatten, H. and Ziemer, F., 2000b. Hydrographic parameter maps retrieved from nautical radar image sequences of inhomogeneous water surfaces, Geoscience and Remote Sensing Symposium, 2000. Proceedings. IGARSS 2000. IEEE 2000 International, pp. 1898-1900 vol.5.

Seemann, J., Senet, C.M., Wolff, U. and Ziemer, F., 2000c. Nautical X-band radar image processing: monitoring of morphodynamic processes in coastal waters, OCEANS 2000 MTS/IEEE Conference and Exhibition, pp. 1329-1335 vol.2.

Seemann, J. and Ziemer, F., 1995. Computer simulation of imaging ocean wave fields with a marine radar, OCEANS '95. MTS/IEEE. Challenges of Our Changing Global Environment. Conference Proceedings., pp. 1128-1133 vol.2.

Sekine, M. and Mao, Y., 1990. Weibull Radar Clutter. Peter Peregrinus Ltd., London.

Senet, C. et al., 1999a. Image sequence analysis of water surface waves in a hydraulic wind wave tank, SPIE'99 Conference - Applications of Digital Image Processing XXII, pp. 148 -158.

Senet, C. et al., 1999b. Optical image sequence analysis and interpretation of the water surface in a multidirectional wave tank and its application in coastal engineering, 2nd International Symposium on Operationalization of Remote Sensing.

Senet, C., Seemann, J. and Ziemer, F., 2000a. Hydrographic parameter maps deduced from CCD image sequences of the water surface supplemented by in-situ wave gauges, IEEE International Geoscience and Remote Sensing Symposium 2000, pp. 843-846.

Senet, C.M., 2004. Dynamics of dispersive boundaries: The determination of spatial hydrographic-parameter Maps from optical sea-surface image sequences, University of Hamburg, Hamburg, 183 pp.

Senet, C.M. et al., 1999c. Optical image sequence analysis and interpretation of stationary and instationary wave fields, Geoscience and Remote Sensing Symposium, 1999. IGARSS '99 Proceedings. IEEE 1999 International, pp. 387-389 vol.1.

Senet, C.M. and Seemann, J., 2002a. Studie I: “State of the Art”, GKSS Research Center GmbH, Geesthacht.

Senet, C.M. and Seemann, J., 2002b. Studie II: “Validation”, GKSS Research Center GmbH, Geesthacht

Senet, C.M., Seemann, J., Flampouris, S. and Ziemer, F., 2008. Determination of Bathymetric and Current Maps by the Method DiSC Based on the Analysis of Nautical X-Band Radar Image Sequences of the Sea Surface (November 2007). Geoscience and Remote Sensing, IEEE Transactions on, 46(8): 2267-2279.

Senet, C.M., Seemann, J. and Ziemer, F., 2000b. Dispersive surface classification: local analysis of optical image sequences of the water surface to determine hydrographic parameter maps, OCEANS 2000 MTS/IEEE Conference and Exhibition, pp. 1769-1774 vol.3.

Senet, C.M., Seemann, J. and Ziemer, F., 2000c. Hydrographic parameter maps deduced from CCD image sequences of the water surface supplemented by in-situ wave gauges, Geoscience and Remote Sensing Symposium, 2000. Proceedings. IGARSS 2000. IEEE 2000 International, pp. 843-846.

Senet, C.M., Seemann, J. and Ziemer, F., 2001. The near-surface current velocity determined from image sequences of the sea surface. Geoscience and Remote Sensing, IEEE Transactions on, 39(3): 492-505.

Sha, L.P., 1989. Sand transport patterns in the ebb-tidal delta off Texel Inlet, Wadden Sea, The Netherlands. Marine Geology, 86(2-3): 137-154.

She, J. and al., e., 2004. Optimal Design of Observational Networks - ODON. In: W. Cieslikiewicz (Editor), EurOCEAN 2004, European Conference on Marine Science and Technology. European Commission, Galway.

Shuchman, R.A., Lyzenga, D.R. and Meadows, G.A., 1985. Synthetic aperture radar imaging of ocean-bottom topography via tidal-currents interactions: Theory and observations. International Journal of Remote Sensing, 6: 1179-1200.

Shyu, J.-H. and Phillips, O., 1990. The blockage of gravity and capillary waves by longer waves and currents. Journal of Fluid Mechanics, 217: 115-141.

Sistermans, P. and Nieuwenhuis, O., 2004. Isle of Sylt: Isles Scheslwig-Holstein (Germany)-a Case Study of European Initiative for Sustainable Coastal Erosion Management (Eurosion), Amersfoort, The Netherlands, pp. 21.

Skolnik, M., 1990. An introduction to radar. In: S. Merril (Editor), Radar handbook. McGraw-Hill Professional, New York.

Skolnik, M., 2001. Introduction to radar systems. Electrical Engineering Series. McGraw-Hill International editions, New York, 772 pp.

Sletten, M.A., Trizna, D.B. and Hansen, J.P., 1996. Ultrawide-band radar observations of multipath propagation over the sea surface. IEEE Transactions on Antennas and Propagation, 44.

Sletten, M.A., West, J.C., Liu, X. and Duncan, J.H., 2003. Radar investigations of breaking water waves at low grazing angles with simultaneous high-speed optical imagery. Radio Sci., 38.

Sletten, M.A. and Wu, J., 1996. Ultrawideband, polarimetric radar studies of breaking waves at low grazing angles. Radio Science, 31: 181-192.

Smith, J., 1990. Modulation of short wind waves. In: G. Geernaert, L. and P. W. (Editors), Surface waves and fluxes. Kluwer Academics, pp. 247-284.

Smith, J.M. and Kraus, N.C., 1990. Laboratory study on macro-features of wave breaking over bars and artificial reefs, US Army Corps of Engineers, Waterways Experiment Station.

Spiegel, F., 1997. Zur Morphologie der Tidebecken im Schleswig-Holsteinischen Wattenmeer. In: G.C.E. Research (Editor), Die Küste, pp. 115-142.

Stevens, C.L., Poulter, E.M., Smith, M.J. and McGregor, J.A., 1999. Nonlinear features in wave-resolving microwave radar observations of ocean waves. Oceanic Engineering, IEEE Journal of, 24(4): 470-480.

Stockdon, H.F., Holman, R.A., 2000. Estimation of wave phase speed and nearshore bathymetry from video imagery. Journal of Geophysical Research 105(C9): 18.

Stokes, G.G., 1847. On the theory of oscillatory waves. Trans. Cambridge Phil. Soc. , 8: 441-473.

Stokes, G.G., 1880. On the theory of oscillatory waves, mathematical and physical papers. Cambridge University Press, 1: 225-229.

Svendsen, I.A., 2006. Introduction to Nearshore Hydrodynamics. Advanced Series on Ocean Engineering, 24. World Scientific, River Edge, 744 pp.

Svendsen, I.A. and Buhr Hansen, J., 1976. Deformation up to breaking of periodic waves on a beach, 15th ICCE. ASCE, Hamburg, pp. 477-496.

Takewaka, S., 2005 Measurements of shoreline positions and intertidal foreshore slopes with X-band marine darar system. Coastal Engineering Journal (CEJ), 47 (2/3): 91- 107.

Thornton, E.B. and Guza, R.T., 1983. Transformation of Wave Height Distribution. J. Geophys. Res., 88.

Tomczak, G., 1964. Investigations with drift cards to determine the influence of the wind on surface currents

Tokyo Geophys. Inst. Stud. Oceanogr, 10: 129-139.

Trizna, D., 1985. A model for Doppler peak spectral shift for low grazing angle sea scatter. Oceanic Engineering, IEEE Journal of, 10(4): 368-375.

Trizna, D., 1988. Measurement and interpretation of North Atlantic ocean marine radar sea scatter.
Trizna, D., 2001. Errors in bathymetric retrievals using linear dispersion in 3D FFT analysis of marine radar ocean wave imagery. IEEE - Transaction on Geoscience and Remote Sensing, 39 (11): 2465 - 2469.
Trizna, D.B., 1991. Statistics of low grazing angle radar sea scatter for moderate and fully developed ocean waves. Antennas and Propagation, IEEE Transactions on, 39(12): 1681-1690.
U.N., 1993. Report of the United Nations Conference on Environment and Development. A/CONF.151/26/Re, United Nations, New York.
Ursell, F., 1953. The long-wave paradox in the theory of gravity waves. Mathematical Proceedings of the Cambridge Philosophical Society, 49(04): 685-694.
Valenzuela, G., 1978a. Theories of the interaction for the interaction of electromagnetic and ocean waves - A review. Boundary-Layer Meteorology, 113: 61-85.
Valenzuela, G.R., 1974. The effect of capillary and resonant interaction on the second order Doppler spectrum of radar sea echo. Journal of Geophysical Research, 79: 5031-5037.
Valenzuela, G.R., 1978b. Theories for the interaction of electromagnetic and oceanic waves — A review. Boundary-Layer Meteorology, 13(1): 61-85.
Valenzuela, G.R. and Laing, M.B., 1970. Study of Doppler Spectra of Radar Sea Echo. J. Geophys. Res., 75.
van Dongeren, A. et al., 2008. Beach Wizard: Nearshore bathymetry estimation through assimilation of model computations and remote observations. Coastal Engineering, 55(12): 1016-1027.
Verduin, J., 2004. The European Directory of Initial Ocean-Observing Systems - EDIOS. In: W. Cieslikiewicz (Editor), EurOCEAN European Conference on Marine Science and Technology. European Commission, Galway.
Vogelzang, J., Wensink, G.J., Calkoen, C.J. and Van der Kooij, M.W.A., 1997. Mapping submarine sand waves with multiband imaging radar 2. Experimental results and model comparison. J. Geophys. Res., 102.
Walker, D., 2000. Experimentally motivated model for low grazing angle radar Doppler spectra of the sea surface. Radar, Sonar and Navigation, IEE Proceedings -, 147(3): 114-120.
Walker, D., Lyzenga, D.R., Ericson, E.A. and Lund, D.E., 1996. Radar backscatter and surface roughness measurements for stationary breaking waves. Proceedings of the Royal Society of London Series A, 452 1953-1984.
Walker, J.R., 1976. Refraction of finite-height and breaking waves, 15th international conference on Coastal Engineering. A.S.C.E, Honolulu.
Ward, K., 1988. Compound representation of high resolution sea clutter. Electronics Letters, 17: 561-563.
Werle, B.O., 1998. Directional characteristics of sea-wave scattering observed at low-grazing angles. Antennas and Propagation, IEEE Transactions on, 46(1): 41-44.
West, J.C., 2002. Low-grazing-angle (LGA) sea-spike backscattering from plunging breaker crests. Geoscience and Remote Sensing, IEEE Transactions on, 40(2): 523-526.
Wetzel, L.B., 1990a. Electromagnetic scattering from the sea at low grazing angles. In: G. Geernaert, L. and W. Plant, L. (Editors), Surface waves and fluxes. Springer, Berlin.
Wetzel, L.B., 1990b. Sea clutter. In: S. Merril (Editor), Radar handbook. McGraw-Hill Professional, New York.

Williams, W.W., 1946. The determination of gradients of enemy-held beaches. Geographical Journal, 107: 18.
Wills, T.G. and Beaumont, H., 1971. Wave Direction Measurement Using sea surveillance radars, Royal Aircraft establishment.
Wright, F.F., 1965. Wave observation by shipboard radar. Ocean science and Ocena engineering, 1: 87-105.
Wright, J., 1966. Backscattering from capillary waves with application to sea clutter. Antennas and Propagation, IEEE Transactions on, 14(6): 749-754.
Wright, J. and Keller, W., 1980. Ocean-wave modulation transfer functions from the West Coast experiment. Geographical Research Letters, 85: 4957-4966.
Wunsch, C., 1972. Bermuda sea level in relation to tides, weather, and baroclinic fluctuations. Reviews of Geophysics, 10: 1-49.
Wunsch, C. and Stammer, D., 1997. Atmospheric Loading and the Oceanic "Inverted Barometer" Effect. Rev. Geophys., 35.
Young, I.R., Rosenthal, W. and Ziemer, F., 1985. A Three-Dimensional Analysis of Marine Radar Images for the Determination of Ocean Wave Directionality and Surface Currents. J. Geophys. Res., 90.
Ziemer, F., 1991. Directional spectra from shipboard navigational radar during LEWEX In: R.C. Beal (Editor), Directional Ocean Wave spectra. The John Hopkins University Press, Baltimore and London, pp. 80-84.
Ziemer, F., 1995. An instrument for the survey of the directionality of the ocean wave field, Workshop on Oper. Ocean Mon. Using Surface Based Radars. WMO/IOC, Geneva, Swiss, pp. 81-87.
Ziemer, F., 2002. HYMNE, Hydrographic Monitoring of the Neva Bight. ICA2-CT-2000-10034, GKSS, Geesthacht.
Ziemer, F. and Dittmer, J., 1994. A system to monitor ocean wave fields, OCEANS '94. 'Oceans Engineering for Today's Technology and Tomorrow's Preservation.' Proceedings, pp. II/28-II/31 vol.2.
Ziemer, F. and Rosenthal, W., 1987. On the transfer function of a shipborne radar for imaging the ocean waves, International Geoscience and Remote Sensing Symposium: Understanding the Earth as a System. IEEE, Ann Arbor, pp. 1559-1564.
Ziemer, F. et al., 2004. OROMA - Operational Radar and Optical Mapping in monitoring hydrodynamic, morphodynamic and environmental parameters for coastal management. In: W. Cieslikiewicz (Editor), EurOCEAN European Conference on Marine Science and Technology. European Commission, Galway.
Zimmerman, J.F., 1985. Radar images of the sea bed. Nature, 314: 224-226.

# Appendix

## A. Method of Dispersive Surface Classificator

### A.1. Predecessor of DiSC: the global method

Several attempts have been made to determine hydrographic parameters from nautical radar or optical (video) image sequences, such as the near-surface current-velocity vector, the water depth and the calibrated full directional wavespectra.

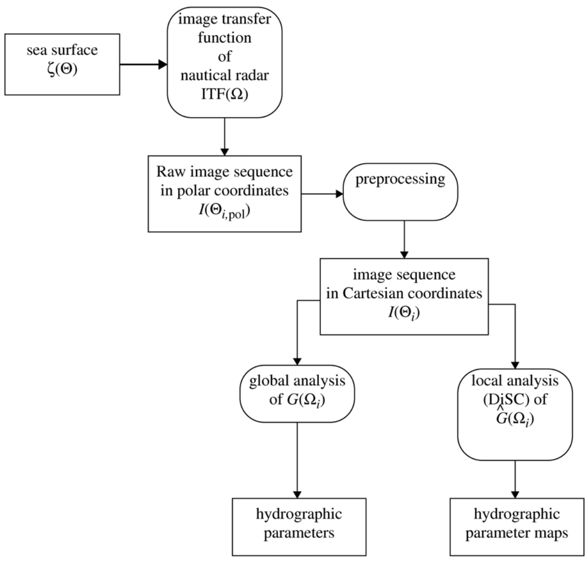


**Figure A-1. Global method and DiSC: an overview. The relation between the continuous spatio-temporal sea-surface elevation, $\zeta(\Theta)$, and nautical radar image sequence is described by the image transfer function, IFT(Ω).The image sequence acquisition system yields image sequences in polar coordinates, $I(\Theta_{i,pol})$. The discrete raw-image sequences are transformed to image sequences given in Cartesian coordinates, $I(\Theta_i)$ .To retrieve global hydrographic parameters the global analysis is performed on the discrete 3D gray-level variance spectra, $G(\Omega_i)$ ,of the image sequence. For spatial hydrographic parameter maps, the local method DiSC is performed on discrete complex-valued 3D spectra, $\hat{G}(\Omega_i)$ ,where by the phase information the spatial structure of the images sequences is preserved.**

The methods used to date, here called the ‘global method’, are based on the analysis of gray-level variance spectra calculated by the squared modulus of a 3D Fast-Fourier Transformation (3D FFT) performed on the image sequences, figure A-1. The 3DFFT in terms of image processing is a global operator. Therefore stationarity and homogeneity of the wave field must be fulfilled. In contrast DiSC only requires homogeneity at the spatial scale of one wavelength (local homogeneity), e.g. the local wavenumbers should not vary too much over this spatial scale.

## A.2. Introduction to DiSC

In shallow waters, where the water depth is much smaller than the main wavelength of the sea state, wave fields become inhomogeneous due to spatially variable bathymetries. Local changes of the wave field, containing the local bathymetry information and shearing currents therefore must be taken into account. For the bathymetry deduction, mainly long waves with high directional distribution are required.

In the following brief description, a newly developed algorithm is given, which analyses image sequences of dynamic dispersive boundaries and used to determine physical parameters on a local spatial scale.

The local analysis method, which allows the analysis of inhomogeneous image sequences of a dynamic and dispersive surface has been labeled DiSC (Dispersive Surface Classificator). In contrast to the global method, DiSC is based on

- preservation of the complex-valued 3D FFT image spectrum,
- filtering techniques of complex spectrum to separate the wave signal from noise, in contrast to the global method that the power spectrum is filtered
- directional and dispersion separation of the complex-valued spectrum into spectral bins at 2D wavenumber planes of constant frequency,
- 2D inverse Fast Fourier Transformation(2D $FFT^{-1}$) of the spectral bins, yielding complex-valued, one-component spatial maps in the spatio-frequency domain,
- calculation of spatial maps of local wavenumbers from the one-component images of constant frequency,

- composition of the one-component local wavenumber maps of constant frequency to local 3D spectra and
- calculation of spatial hydrographic-parameter maps from the local 3Dspectra.

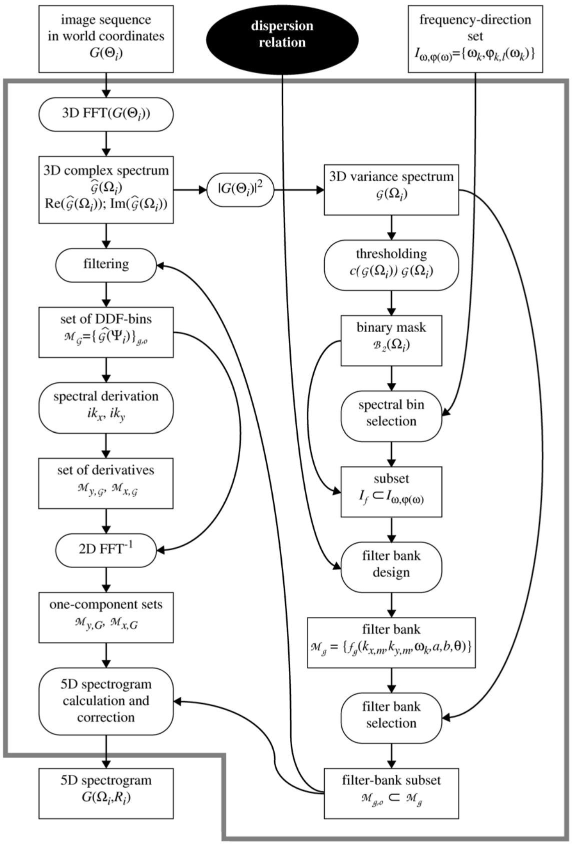


**Figure A-2. Scheme of the procedural and data flow of DiSC**

Here DiSC is applied to nautical radar image sequences of water surface waves in coastal waters acquired from land-based stations. The algorithm delivers results in form of spatial hydrographic-parameter maps (i.e. spatial maps of the water depth and the near-surface current) Seemann et al. (1999), Seemann et al. (2000b), Seemann et al. (2000c), Seemann et al. (2000a). In addition to being used on nautical radar image sequences, DiSC has been applied to optical image sequences acquired with CCD-cameras in hydraulic wave tanks Senet et al. (1999a), Senet et al. (1999c), Senet et al. (1999b), Senet et al. (2000a), Senet et al. (2000b). An overview of the imaging and the image-sequence processing chain, constituting DiSC, is given in figure A-2.

## A.3. Assumptions of DiSC

*1) Stationarity:* The image process analyzed by DiSC has to be stationary. Stationarity implies the temporal invariance of a signal, $G$. Assuming stationarity, DiSC can treat the spatial Fourier decomposition of the distinct frequency components independently,

$$\hat{G}_w(R_i, \omega_w) = \sum_{n=1}^{N} \hat{G}_w(Y_{i,\omega_w}) \cdot e^{i\vec{k}_n \vec{r}} , \tag{A.1}$$

with the complex-valued spatial image, $\hat{G}_w$, at constant frequency, $\omega_w$ , and the $k_x - k_y$ plane, $Y_{i,\omega}$.

*2) Validity of the multi-component AM–FM image model:* For inhomogeneous images the amplitudes or the spatial phase gradients (i.e. the local wavenumber vectors) vary. This information is only implicitly included in the coefficients of the Fourier decomposition (A.1). To enable explicit analysis, the spatial Fourier decomposition is transformed to an image representation, composed of a superposition of 2D jointly amplitude-frequency-modulated, locally coherent, analytic signals (multi-component AM–FM image model Havlicek et al. (1973), Havlicek and Bovik (1995.) and Havlicek et al. (2000)

$$\hat{G}_w(R_i) = \sum_{l=1}^{L} \Lambda_{w,l}(R_i) \cdot e^{i\Phi\omega,l(R_i)} \tag{A.2}$$

The AM-FM Model is the abbreviation of the Amplitude and Frequency Modulation. The model is applicable to sea surface waves or image sequences of it, where both amplitude and frequency modulations occur.

## A.4. Input Parameters

A 3D image sequence, $G(\Omega_i)$, to be analyzed, is the input dataset required for DiSC. Further, a set,

$$I_{FD} = \{\omega_w, \phi_{w,l}(\omega_w)\} \tag{A.3}$$

of user-defined frequency–direction sets to define anchor positions for the spectral filter bank in the 3D $\Omega$-domain, which is used for spectral separation are required. In (A.3) $\omega_w$ locates a

$Y_{i,\omega}$ domain at frequency $\omega_w$, chosen for filtering. In each of these $Y_{i,\omega}$ domains, sets of directions $\phi_{w,l}$ are predefined. Indices are $w = 1,...,W$ and $l = 1,...,L$.

## A.5. The algorithm

The global analysis method is based on spectral filtering and the analysis of the real-valued 3D gray-variance spectra, $G(\Omega_i)$. The spectral phase, which contains information on the local image structure Oppenheim and Lim (1981), is not used. For the determination of physical parameters on a local spatial scale, the spatial structure of the image sequence here is recovered from the complex-valued 3D spectra, $\hat{G}(\Omega_i)$. The core of the local-analysis method is a decomposition of the complex-valued 3D image spectra, followed by a 2D $\mathrm{FFT}^{-1}$ into the spatio-frequency $R_i - \omega$ domain. A DiSC overview is given in Fig.4. The method includes algorithm steps described in the succeeding sections.

*1) 3D Fast Fourier Transformation:* A discrete 3D Fourier Transformation (3D DFT) can be achieved by decomposition into 1D DFTs. A 3D DFT can be decomposed into 1D DFTs because the kernel is separable. A 3D DFT using the world-and spectral coordinates has the form

$$\hat{G}(\Omega_i) = \frac{1}{MNO}\sum_{k=0}^{M}[\sum_{l=0}^{N}(\sum_{m=0}^{O} I_{m,l,k}(\Theta_i)V_O^{-wt})V_N^{-ly}]V_M^{-kx} \quad (A.4)$$

where M, N, and O are the numbers of the $\Omega_i$ coordinates $k_{x,m}, k_{y,n}, \omega_w$ and

$$V_{[M|N|O]} = \exp(\frac{2\pi i}{[M \mid N \mid O]}) \quad (A.5)$$

The result of (A.4) is a discrete complex-valued image spectrum $\hat{G}(\Omega_i)$ of the 3D domain $\Omega_i = (k_{x,m}, k_{y,n}, \omega_w)$. The spatio-temporal extension $X \otimes Y \otimes T$ determines the discrete grid resolution of the 3D spectrum:

$$\Delta k_x = \frac{2\pi}{X},\ \Delta k_y = \frac{2\pi}{Y} \text{ and } \Delta\omega = \frac{2\pi}{\mathrm{T}} \quad (A.6)$$

The discrete grid resolution of the spatio-temporal image sequence determines the spectral extensions (i.e.the Nyquist criteria):

$$\Delta k_{x,\mathrm{N}_y} = \frac{\pi}{\Delta x} \text{ and } \Delta k_{y,\mathrm{N}_y} = \frac{\pi}{\Delta y} \text{ and } \omega_{\mathrm{N}_y} = \frac{\pi}{\Delta y} \quad (A.7)$$

To apply the FFT algorithm in the context of the DiSC method smearing in the wavenumber domain due to spectral leakage in the frequency domain should be avoided. This limitation appears for short times series resulting in the spectral signal of the sea state being smeared to the adjacent frequency bins. The same happens in the wavenumber domain. As the spectral signal is located on the dispersion shell, for short time series the smearing in the frequency domain to the adjacent bins results in a smearing in the wavenumber domain more than is supposed by spectral leakage alone. To overcome this limitation the following inequalities should be valid:

$$\Delta\omega < C_G \cdot MIN(\Delta k_x, \Delta k_y) \quad (A.8)$$

and accordingly

$$T > \frac{2\pi}{C_G \cdot MIN(\Delta k_x, \Delta k_y)} \quad (A9)$$

A detailed overview of continuous and discrete Fourier Transformations can be found in Jaehne et al. (1999 ). The 3DFFT used in this work is based on the FFT algorithm of Cooley and Tuckey (1965). Examples of the usage of a 3D FFT on image sequences of the sea surface with video or CCD cameras are given by Irani et al. (1986); for X-Band Doppler Radars an example is given by Frasier and McIntosh (1995).

*2) Spectral Decomposition:*

The aim of the spectral decomposition of the spectral signal of the inhomogeneous wave field is the division of the signal into one-component images containing separated and therefore analyzable parts of the wave field. The spectral decomposition technique DDF-S (Directional Dispersion Frequency-Separation) is based on the combination of

- a frequency separation (taking a $k_x - k_y$ slice of the 3D wavenumber-frequency spectrum, and
- a directional-wavenumber band pass filter in the $k_x - k_y$ centered on the dispersion shell (dispersion filtering),

yielding a spectral DDF bin. The principle of DDF-S is outlined in figure A-3.

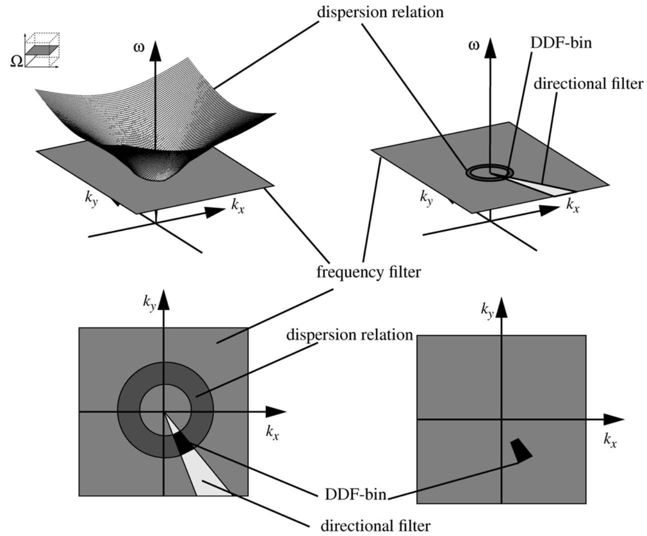


**Figure A-3. Schematic of Directional - Dispersion- Frequency Separation (DDF-S). The result of the DDF-S is a DDF bin.**

Dispersion filtering is required because of the non linearity of radar imaging of the sea surface waves. The nonlinear modulation transfer function (MTF) can be expanded in a Volterra series, Cherry (1994), creating sum- difference- and harmonic signals in addition of the linear fundamental mode in the radar image spectrum, figure A-4. The linear (fundamental) mode is selected by dispersion filtering. The remaining spectral smearing is caused by the inhomogeneity of analyzed area.

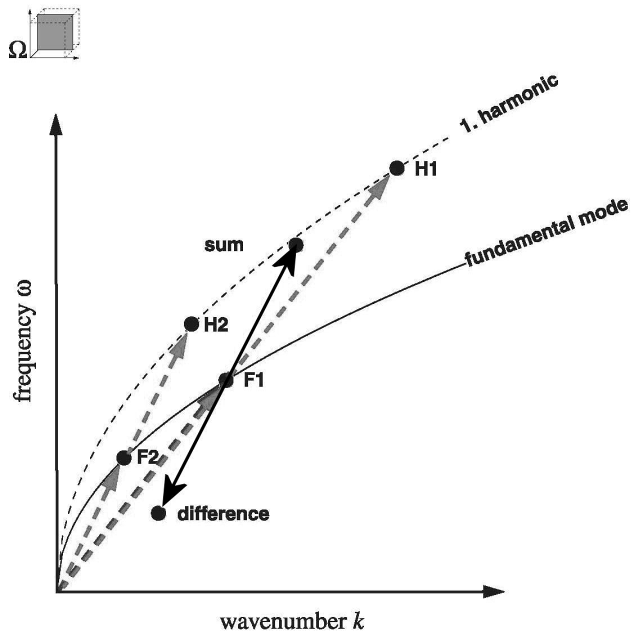


**Figure A-4. Non linear image spectrum given in a 2D $k - \omega$ section of the 3D $\Omega$-domain: Linear dispersion relation (solid line), first harmonic dispersion relation (dashed line), sum and deference structures (bullets).**

*3) Inverse 2D FFT:* Complex-valued one-component images are calculated by transforming the filtered $Y_{i,\omega}$-planes of the 3D image spectrum into the spatial domain, using a 2D FFT$^{-1}$:

$$\hat{I}_{w,l}(R_i) = 2DFFT^{-1}(MTF_{w,l} \cdot \hat{G}_w(Y_i)) \qquad \text{(A.9)}$$

where $MTF_{w,l}$ indicates the MTF of a spectral filter. Complex-valued gradient images are calculated with (A.9) by multiplying $\hat{G}_w(Y_i)$ with the MTF of the derivative overator, $i\vec{k}$ :

$$\nabla_R \hat{I}_{w,l}(R_i) = 2DFFT^{-1}(i\vec{k} \cdot MTF_{w,l} \cdot \hat{G}_w(Y_i)) \qquad \text{(A.10)}$$

The spectral decomposition and inverse 2DFFT yields complex-valued spatial one-component images. These complex-valued one-component images are illustrated as power and phase of a separated part of the wave field.

*4) Calculation of local wavenumbers:* Determination of spatial maps of local-wavenumber vectors is achieved using the phase of the complex-valued one-component images. Initially an approximate version of the Multiple-Signal Classification algorithm Frasier and McIntosh (1995) was used to estimate local wavenumber vectors. More efficient, with regard to computer run time, is a local-wavenumber estimation method developed by Havlicek et al. (1996) to characterize textures of single images. In addition to the complex-valued one-component images, the method utilizes the gradient one-component images. The method provides complex-valued wavenumber vectors $\vec{k}_{w,l}$. The real part of $\vec{k}_{w,l}$ is equal to the spatial phase gradient $\partial\phi_l/\partial x, \partial\phi_l/\partial y$ and defines the real-valued local wavenumber vector. The imaginary part is equal to the normalized gradient of the local amplitude defining the local-bandwidth vector.

*5) Calculation of hydrographic parameter maps:* In chapter 2 the dependency of the dispersion relation, $\tilde{\omega}(\vec{k}, u_c, d)$, on the near-surface current, $u_c$, and the water depth, $d$, is described.

In the gray-level variance spectrum, $G_0(\Omega_i)$, the linear portion of signal energy of the waves, $G_0(\Omega_i)$, is localized on the dispersion shell of surface waves $\tilde{\omega}(\vec{k})$. The sum of the sensor's velocity, $\vec{u}_s$ (i.e.ship velocity), and the near-surface ocean's current, $\vec{u}_c$, deforms the dispersion shell due to the Doppler-frequency shift, $\omega_D$.

A first approach to determine the near-surface current,

$$\vec{u}_c = \vec{u}_e - \vec{u}_s, \qquad \text{(A.11)}$$

was presented by Young et al. (1985), in which a least-squares fitting technique was introduced and was applied to image sequences acquired by a nautical radar. The least-squares technique is based on the idea that the theoretical dispersion shell is fitted to the linear portion (fundamental mode) of the spectral signal of the imaged waves, $G_S(\Omega_i)$.

This least-squares fitting technique has been improved in accuracy 1) by considering the spectral signal found at higher harmonics of the dispersion shell; 2) by taking into account aliasing effects generated due to temporal under-sampling, because of the slow antenna rotation time of a nautical radar ($O$(2s)) Seemann and Ziemer (1995), Borge et al. (1998); and 3) by establishing a reliable error-estimation model.

The accuracy of technique, its limits, and its adaptability are described and discussed by Senet et al. (2001). It is now possible to perform current and wave measurements from fast-moving

vessels. The method is implemented in the operational product WaMoS II (Wave Monitoring System) based on nautical radars Reichert et al. (1999a)and Reichert et al. (1999b).
The method used in this work is based on a quasi-Newton method to find the global minimum of the cost function:

$$f(u_x, u_y, d) = \sum_{l=0}^{L-1} (\sqrt{g\vec{k}_l \tanh(\vec{k}_l d)} + k_{x,l} u_x + k_{y,l} u_y - \omega_l)^2 \qquad \text{(A.12)}$$

where $u_x$, $u_y$ (components of the near-surface current) and $d$ water depth) are the unknowns. The index, $l$, counts the elements of the set of spectral coordinates, $k_l$, $k_{x,l}$, $k_{y,l}$ and $\omega_l$, which are selected in the 3D image spectrum. The dispersion relation $\tilde{\omega}(\vec{k}_l, \vec{u}_c, d) = \sqrt{g\vec{k}_l \tanh(\vec{k}_l d)} + k_{x,l} u_x + k_{y,l} u_y$ is linearly dependent on $u_x$ and $u_y$ and non-linearly dependent on $d$. The spectral coordinates are selected by a threshold criterion

$$M_0 = \{(k_{x,l}, k_{y,l}, \omega_l) \mid \frac{G(k_{x,l}, k_{y,l}, \omega_l)}{MAX(G)(k_{x,l}, k_{y,l}, \omega_l)} > \varepsilon_S\} \qquad \text{(A.13)}$$

where $M_0$ is the subset of spectral-coordinates et selected by the normalized criterion $\varepsilon_S$, which discriminates the linear spectral signal from noise and other signal structures. In (A.13) $k_l$ is the modulus of the wavenumber vector:

$$k_l = \sqrt{k_{x,l}^2 + k_{y,l}^2} \qquad \text{(A.14)}$$

The spectral-coordinate set, $M_0$, defined in (A.13), is represented as a sorted vector with the indices $l = 0,...,L-1$ where $L-1$ is the number of selected spectral coordinates.
An iterative algorithm is performed by a quasi-Newton minimization method for nonlinear functions. After the first guess, where the linear spectral coordinates, $M_0$, are selected, the locations of the fundamental mode dispersion shell, $\tilde{\omega}_0$, and of the p$^{th}$ harmonics, $\tilde{\omega}_p$, are approximately known. The number of regression coordinates is the n increased iteratively by taking the spectral coordinates of higher harmonics into account.
The results of DiSC are bathymetry and current-vector maps. In the given case DiSC has been calculated on boxes of 16 pixel× 16 pixel, e.g. 109 m × 109 m, but at the current analysis the box is 6 pixel × 6 pixel, 42m × 42m. Each of these boxes contains one water depth value and on current vector.

## B. Calculation of the $c_p$ for Bragg scattering

If the speed of the scattering object is associated with the underlying waterwave, then $c_p$ is the phase speed of the water wave given by

$$c_p = \left( \frac{g}{k_w} + \frac{\gamma}{\rho} k_w \right)^{0.5} \tag{B.1}$$

where $g$ is the gravitational acceleration, $\gamma$ and $\rho$ are the water surface tension and density, respectively, and $k_w$ is the associated wavenumber. For Bragg scattering,

$$k_w = k_b \equiv \frac{4\pi \cos\theta_g}{\lambda} \tag{B.2}$$

is the Bragg-resonant wavenumber in water.

## C. Normal test plots of the NRCS

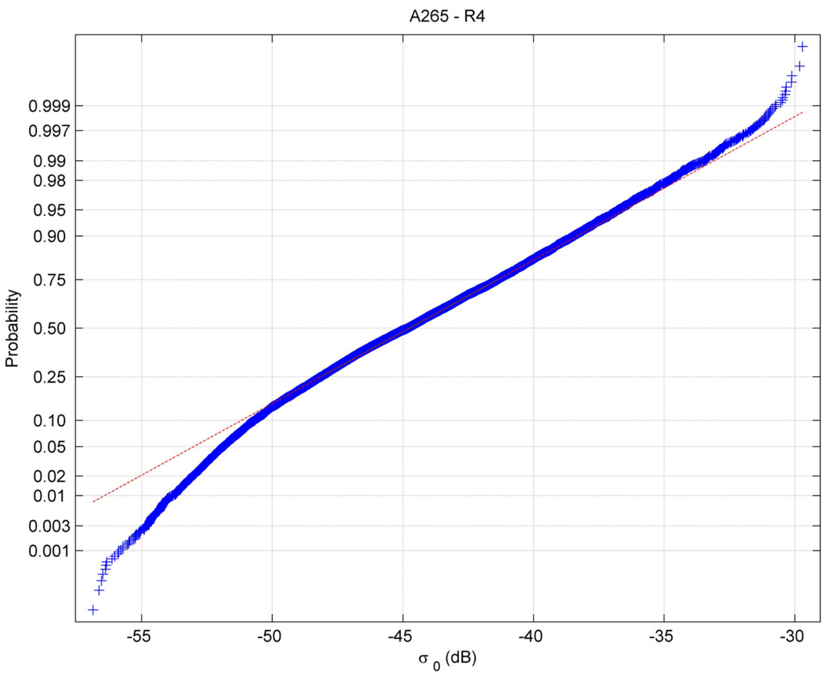


**Figure C-1. Normal probability plot of dataset A265-R4.**

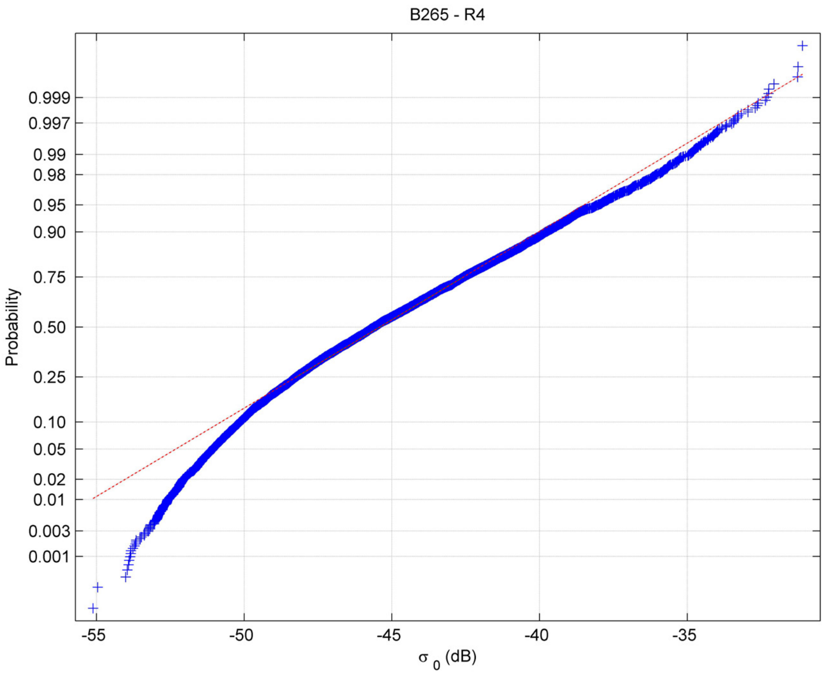


**Figure C-2. Normal probability plot of dataset B265-R4.**